

**A STUDY ON THE EFFECT OF TRANSITION METAL
DOPANTS IN CERIA PRASEODYMIUM CATALYST FOR
SOOT OXIDATION ACTIVITY AND ITS KINETICS**

Thesis

Submitted in partial fulfilment of the requirements
for the degree of

DOCTOR OF PHILOSOPHY

By

SUNAINA S PATIL

Reg.No. 197062 197CH001



**DEPARTMENT OF CHEMICAL ENGINEERING
NATIONAL INSTITUTE OF TECHNOLOGY KARNATAKA,
SURATHKAL, MANGALORE - 575 025**

JULY 2023

**A STUDY ON THE EFFECT OF TRANSITION METAL
DOPANTS IN CERIA PRASEODYMIUM CATALYST FOR
SOOT OXIDATION ACTIVITY AND ITS KINETICS**

Thesis

Submitted in partial fulfilment of the requirements

for the degree of

DOCTOR OF PHILOSOPHY

By

SUNAINA S PATIL

Reg.No. 197062 197CH001

Under the Guidance of

Dr. HARI PRASAD DASARI

Associate Professor



**DEPARTMENT OF CHEMICAL ENGINEERING
NATIONAL INSTITUTE OF TECHNOLOGY KARNATAKA,
SURATHKAL, MANGALORE - 575 025**

JULY 2023

DECLARATION

By the Ph.D. Research Scholar

I hereby *declare* that the Research Thesis entitled **A Study on the effect of Transition Metal dopants in Ceria Praseodymium Catalysts for Soot Oxidation Activity and its Kinetics** which is being submitted to the **National Institute of Technology Karnataka, Surathkal** in partial fulfillment of the requirements for the award of the Degree of **Doctor of Philosophy** in **Chemical Engineering Department** is a *bonafide report of the research work* carried out by me. The material contained in this Research Thesis has not been submitted to any University or Institution for the award of any degree.

197062 197CH001, SUNAINA S PATIL

Department of Chemical Engineering
National Institute of Technology Karnataka, India

Place: NITK-Surathkal

Date: 21 July 2023 .

CERTIFICATE

This is to *certify* that the Research thesis entitled **A Study on the effect of Transition Metal dopants in Ceria Praseodymium Catalysts for Soot Oxidation Activity and its Kinetics** submitted by **SUNAINA S PATIL** (Register Number: 197062 197CH001) as the record of the research work carried out by her, is *accepted as the Research Thesis submission* in partial fulfillment of the requirements for the award of the degree of **Doctor of Philosophy**.



Dr. Hari Prasad Dasari

Associate Professor

Research Guide

(Name and Signature with Date and Seal)



Chairman - DRPC

(Signature with Date and Seal)

Head of the Department
विभागाध्यक्ष

Department of Chemical Engineering
रसायनिक अभियांत्रिकी विभाग

National Institute of Technology Karnataka - Surathkal
राष्ट्रीय प्रौद्योगिकी संस्थान कर्नाटक, सुरात्कल
P.O Srinivasnagar, Mangalore - 575025 Karnataka
पी.ओ. श्रीनिवासनगर, मंगलौर - ५७५०२५, कर्नाटक

ACKNOWLEDGMENT

Firstly, I sincerely thank my research supervisor **Dr. Hari Prasad Dasari**, for his enthusiasm, patience, motivation, and continuous support throughout my work. His guidance helped me through the process of research and writing this thesis. He made my Ph.D. journey marvelous and unforgettable by providing his friendly assistance and valuable time, which helped me understand the concepts very well.

I wish to express my sincere thanks to **Prof. Prasad Krishna, Director (Additional-charge)**, and **Prof. Karanam Umamaheshwar Rao (Former Director)** for providing the necessary permissions and allowing me to use the infrastructure on the institute premises.

I would also like to thank **Dr. P.E. Jagadeeshbabu**, Head of the Department, Chemical Engineering Department, NITK; **Dr. Prasanna B. D and Dr. Hari Mahalingam** (former Head of the Department) for providing me the opportunity to carry out my research work and permitting me to utilize the facilities in the department. I am grateful to **Prof. Vidya Shetty** (Dean Academic) for all the administrative and academic support throughout my research .

I want to thank my Research Progress Assessment Committee (RPAC) members: **Dr. Chinta Sankar Rao and Dr. Beneesh. P. B** (Chemistry Department), DRPC Secretaries: **Dr. Gangamma and Dr. Hari Mahalingam**, for valuable suggestions and evaluation during the research progress of the work. Their recommendations were also helpful in carrying out the work successfully.

I sincerely thank **Prof. G Srinikethan, Prof. M.B. Saidutta and Dr. Keyur Raval** for constant moral support and encouragement during my Ph.D. journey. Also, I thank all other faculties, staff, and research scholars of the Department of Chemical Engineering and other departments of NITK Surathkal.

My honest thanks to the non-teaching staff of the Department of Chemical Engineering, especially **Mrs. Bhavyashree, Mrs. Sandhya, Mr. Sadashiva, Mrs. Thrithila Shetty, Mr. Jnaneshwara G K, Mrs. Vijetha, Mr. Mahadeva, Mr. Suresh, Mr. Harish, Mrs. Ashwija and Mrs. Shashikala.**

The present work is funded by **SERB CRG Project (CRG/2020/000425)** and partially by **SERB IMPRINT Project (IMP/2018/00318)**. I want to extend my gratitude to **Science and Engineering Research Board, India**, for providing the fund that helped to carry out the research on time.

I would also like to express my gratitude to the **Central Research Facility, NITK**, for providing XRD data, Raman Spectroscopy data, FE-SEM-EDAX data, and BET Surface area and pore volume data. I thank **Prof. Sathyanarayan, Chairman-CRF, NITK**, for providing the permissions and opportunity to utilize the CRF facilities. Special thanks to **Mr. Akash Gupta, Ms. Disha S, Mrs. Pratheeksha Bhat, and Mr. Pradeep**, who helped me facilitate the characterization data. I also acknowledge **SAIF STIC, Cochin**, for facilitating **UV-Vis/DRS data**. Also, I would like to thank **MRC, MNIT Jaipur** for rendering **XPS analysis data**.

I sincerely convey my thanks to my fellow teammates and alumni of the “Energy and Catalysis Materials Laboratory Research Team” Mr. Lakhanlal, Mr. Rahul Kumar Shirasangi, Mrs. Gouramma Pattanashetti, Mr. Atmuri Shourya, Ms. Madhura D R, Dr. Anjana PA, Dr. Irfana Shajahan, Mr. Avinash Suresh Nayak, Ms. Maya R, Mr. Aasif Ahmed Wagay, Ms. Debashreetha Singha, Ms. Pranathi S, Mr. Srijith, Mrs. Anugraha, Ms. Kirthi Rajvanshi, Ms. Ashmitha Das, Mr. Akhil Vijay, Ms. Chaitra Shenoy, Mr. P. Govardhan and undergraduate students especially Ms. Sahana Naik, Ms. Shwetha Ganiger, Ms. Priyanka R, Ms. Shreya K, Ms. Supreetha, Mr. Sukesh, Mr. Srikar, Mrs. Nivedita Reddy and Ms. Parvathi Nair who were part of research team without their kind support and help, this research journey would be difficult.

I sincerely thank **Dr. Harshini Dasari** and **Ms. Veda Alankritha** for their friendly support and for always being as a family throughout my journey. I also thank **Dr. Maheswata Lenka** for the friendly support. My very profound gratefulness to my parents, **Mr. Shivasharan S Patil and Mrs. Nirmala S Patil**; my father in law **Mr. B. Pundalika Marathe**; my mother in law **Mrs. Usha P Marathe**; my siblings **Mrs. Soumya S Patil and Dr. Sourabh S Patil**, My other family members **Mr. Maruthi Mudhol, Mr. Vishwanath Nayak , Mrs. Shrinidhi , Baby Ditya and Baby Tanishka**, cousins, friends, and relatives.

Finally, I must precisely express my gratitude to my husband, **Dr. Shriram P Marathe**, for encouraging and inspiring me throughout my years of study.

This journey would not have been possible without all your support.

Thank you.

Sunaina S Patil

Dedication

*I dedicate my dissertation to my supervisor, who helped me begin and complete this long and
challenging journey,*

To all my teachers who led me to the world of knowledge and wisdom,

To my loving parents for providing the best possible education,

&

To my husband, family, and friends for all their encouragement and inspiration.

ABSTRACT

The catalytic descriptors (lattice oxygen, metal-oxygen bond strength, host structure, redox capability, multi-functionality of active sites, site isolation, and phase cooperation) govern the heterogeneous oxidation reactions. The present study aims to explore the catalytic descriptors that govern the soot oxidation activity of transition metal doped Ceria-Praseodymium catalyst system and its kinetics thereof. The transition metal (0 to 20 mol %) doped Ceria-Praseodymium catalysts (Copper doped Ceria-Praseodymium, Cobalt doped Ceria-Praseodymium, Iron doped Ceria-Praseodymium, Manganese doped Ceria-Praseodymium and Chromium doped Ceria-Praseodymium) were successfully synthesized by Solution Combustion Method and characterized by X-Ray Diffraction, Raman Spectroscopy, Scanning Electron Microscopy, X-Ray Photoelectron Spectroscopy, BET & BJH surface area analysis, and tested for soot oxidation activity and its kinetic study using Thermo-gravimetric analysis.

The 5 mol% Copper doped Ceria-Praseodymium catalyst system showed better soot oxidation activity which is attributed to the better reactive planes and chemisorbed oxygen species compared to other Copper-doped Ceria-Praseodymium catalyst system and Ceria-Praseodymium catalyst system. 5 mol% Cobalt doped Ceria-Praseodymium catalyst system showed better soot oxidation activity among the Co doped Ceria-Praseodymium catalysts, and the descriptors controlling the catalytic activity are phase cooperation (solid-solution formation) and better redox properties compared to Co-CP and CP catalyst systems. The descriptors controlling the soot oxidation activity of the Iron doped Ceria-Praseodymium catalyst system are (secondary phase formation and redox properties), and the 5 mol % Iron-doped Ceria-Praseodymium catalyst system showed better soot oxidation activity. In Manganese doped Ceria-Praseodymium catalyst system, the 5 mol% Manganese-doped Ceria-Praseodymium catalyst system showed better catalytic activity for the soot oxidation reaction. The descriptors controlling the soot oxidation activity are surface area, crystallite size, active surface adsorbed O^- species, and Mn^{3+}/Mn^{4+} surface concentration. The surface concentration of Cr^{3+} and Pr^{3+} played a significant descriptor role, and Chromium doped Ceria-Praseodymium catalyst system showed better soot oxidation activity than other Ceria-Praseodymium catalyst systems. As the Cr concentration increased, there was a decrease in the Cr^{3+} and Pr^{3+} concentrations in the Chromium-doped Ceria-Praseodymium catalyst system. Compared to all the transition metals doped Ceria-Praseodymium catalysts in the present study 5 mol % Cobalt doped Ceria-Praseodymium catalyst system showed better catalytic activity with lowest T_{50} of $349 \pm 1^\circ C$.

In the transition metal (TM (5 mol%) = Cr, Mn, Fe, Co, and Cu) -doped Ceria-Praseodymium nanofiber catalysts 5 mol% Chromium doped Ceria-Praseodymium nanofiber showed better soot oxidation activity and is attributed to larger average pore size and pore volume and, the nano string diameter is smaller than all other nanofiber catalysts. The kinetic triplets namely activation energy, pre-exponential factor and the reaction models were evaluated.

Keywords: Transition metal dopants, Praseodymium-doped Ceria, XRD analysis, XPS analysis, redox potential, Soot Oxidation Activity.

TABLE OF CONTENTS

SL. NO.	TITLE	PAGE NO.
	ABSTRACT	i
	TABLE OF CONTENTS	ii
	LIST OF FIGURES	vii
	LIST OF TABLES	x
	NOMENCLATURE	xii
1.	INTRODUCTION	1
1.1.	Soot Oxidation	1
1.2.	Soot Oxidation kinetics	3
1.3.	Catalyst Materials	3
1.4.	Synthesis of Nanoparticles	5
1.5.	Scope and objective	7
1.3.	Organization of the Thesis	8
2.	LITERATURE REVIEW	9
2.1	Combustion Synthesis	9
2.2	Soot Oxidation	12
2.3	Kinetic Analysis	24
2.4	Conclusions	27
2.5	Scope of Work and Research Gap	28
3.	MATERIALS AND METHODOLOGY	33
3.1	Materials	33
3.2	Solution Combustion Synthesis	33
3.3	EDTA Citrate Method	35
3.4	Direct Nitrate Calcination Method	35
3.5	Electrospinning Technique	36
3.6	Characterization Techniques	38
3.6.1	X-Ray Diffraction	38
3.6.2	FT-Raman Spectroscopy	39
3.6.3	BET-BJH analysis	39
3.6.4	Field Emission Scanning Electron Microscopy Analysis (FE-	40

	SEM)	
3.6.5	X-Ray Photoelectron Spectroscopy	41
3.7	TGA-FTIR	42
3.8	Soot Oxidation and Kinetic Studies	43
4	EFFECT OF NIOBIUM - DOPED CERIA ON SOOT OXIDATION ACTIVITY	46
4.1	XRD Analysis	47
4.2	Raman Spectroscopy Analysis	49
4.3	SEM Analysis	50
4.4	Soot Oxidation Activity	52
4.5	Conclusions	55
5	EFFECT OF COPPER - DOPED CERIA - PRASEODYMIUM CATALYSTS FOR SOOT OXIDATION ACTIVITY AND ITS KINETICS	56
5.1	X-Ray Diffraction (XRD)Analysis	58
5.2	Raman Spectroscopy Analysis	61
5.3	BET-BJH Analysis	62
5.4	FE-SEM Analysis	64
5.5	XPS Analysis	66
5.6	Soot Oxidation Activity	69
5.7	Soot Oxidation Kinetic analysis	72
5.7.1	Ozawa and KAS method to evaluate activation energy	72
5.7.2	Determination of Pre-Exponential Factor (A)	73
5.7.3	Coats-Redfern (CR) Method	74
5.7.4	Master plot method to evaluate the reaction models	75
5.7.5	Experimental and theoretical kinetic curves construction and comparison	77
5.9	Conclusions	80
6	INVESTIGATIONS OF COBALT-LOADED CERIA - PRASEODYMIUM CATALYSTS FOR SOOT OXIDATION ACTIVITY AND ITS KINETICS	81
6.1	X-Ray Diffraction (XRD)Analysis	81
6.2	Raman Spectroscopy Analysis	83
6.3	BET-BJH Analysis	86
6.4	FE-SEM Analysis	88
6.5	XPS Analysis	90
6.6	Soot Oxidation Activity	94

6.7	Soot Oxidation Kinetics	91
6.8	Conclusion	102
7	EFFECT OF IRON - DOPED CERIA - PRASEODYMIUM CATALYSTS FOR SOOT OXIDATION ACTIVITY AND ITS KINETICS	103
7.1	X-Ray Diffraction (XRD)Analysis	104
7.2	Raman Spectroscopy Analysis	105
7.3	FE-SEM Analysis	107
7.4	BET-BJH Analysis	109
7.5	XPS Analysis	111
7.6	Soot Oxidation Activity	114
7.7	Kinetic Analysis	115
7.7.1	Determination of Activation Energy (E_a) and Pre-Exponential Factor (A)	115
7.7.2	Experimental and Calculated Data Comparison	118
7.8	Conclusion	120
8	EFFECT OF MANGANESE - DOPED CERIA - PRASEODYMIUM CATALYST ON SOOT OXIDATION ACTIVITY AND ITS KINETICS	121
8.1	X-Ray Diffraction (XRD)Analysis	122
8.2	Raman Spectroscopy Analysis	123
8.3	FE-SEM Analysis	123
8.4	BET-BJH Analysis	128
8.5	XPS Analysis	130
8.6	Soot Oxidation Activity	134
8.7	Kinetic Analysis	134
8.7.1	Determination of Activation Energy (E_a) and Pre-Exponential Factor (A)	134
8.7.2	Experimental and Calculated Data Comparison	136
8.8	Conclusion	140
9	THE CATALYTIC EFFECT OF CHROMIUM - DOPED CERIA - PRASEODYMIUM ON SOOT OXIDATION ACTIVITY AND ITS KINETICS	141
9.1	X-Ray Diffraction (XRD)Analysis	141
9.2	Raman Spectroscopy Analysis	143
9.3	FE-SEM Analysis	144
9.4	BET-BJH Analysis	147

9.5	XPS Analysis	149
9.6	Soot Oxidation Activity	152
9.7	Kinetic Analysis	153
9.7.1	Determination of Activation Energy (E_a) and Pre-Exponential Factor (A)	154
9.7.2	Experimental and Calculated Data Comparison	154
9.8	Conclusion	158
10	ELECTROSPUN TRANSITION METAL (TM $(x=0.05)$ = Cr, Mn, Fe, Co, Cu) - DOPED $Ce_{0.9}Pr_{0.1}O_{2-\delta}$ (CP) NANOFIBERS AND ITS SOOT OXIDATION ACTIVITY	160
10.1	Background	160
10.2	XRD and Raman Spectroscopy Analysis	162
10.3	BET-BJH Analysis	165
10.4	FE-SEM Analysis	165
10.5	Soot Oxidation Activity	171
10.6	TGA-FTIR of Soot Oxidation Activity	172
10.7	Conclusions	176
11	CONCLUSIONS	177
11.1	Summary	177
11.2	Conclusions	181
11.3	Future Scope of Work	183
	APPENDIX – I	184
	APPENDIX – II	186
	APPENDIX – III	187
	APPENDIX – IV	188
	APPENDIX – V	189
	APPENDIX-VI	195
	APPENDIX-VII	198
	APPENDIX-VIII	201
	APPENDIX-IX	204
	REFERENCES	207
	PUBLICATIONS	234
	BIODATA	238

LIST OF FIGURES

SL. NO.	TITLE	PAGE NO.
2.1	SEM Micrographs of pulverized GDC powder (Charojrochkul et al. 2012)	10
2.2	Soot Oxidation Activity of CeO ₂ and Pr-Doped CeO ₂ Catalyst (Andana et al. 2018)	17
3.1	Solution Combustion Synthesis Method.	34
3.2	Preparation of Nb-doped Ceria by EDTA – Citrate complex and DNC method.	36
3.3	Electrospinning technique to develop transition metal doped Ce-Pr catalysts	37
3.4	X-Ray Diffraction (XRD - Malvern PAN analytical: Empyrean)	38
3.5	Compact Raman Spectrometer (Renishaw (UK))	39
3.6	BET and BJH analyser (Anton Paar- Autosorb iQ-XR-XR 195364 Quantachrome instruments)	40
3.7	Field Emission Scanning Electron Microscopy (FE-SEM) (Carl Zeiss-Gemini SEM 300)	41
3.8	X-Ray Photoelectron Spectroscopy (Omicron ESCA+ - ultrahigh vacuum)	42
3.9	TGA-FTIR	42
3.9	Thermo gravimetric Analyser (Exstar TG/DTA 6300)	43
4.1	(a) XRD patterns (b) Enlarged (111) planes of Ce _{1-x} Nb _x O _{2-δ} (x = 0,0.03,0.05,0.1,0.2, 0.3 and 1).	47
4.2	Raman Spectra of Ce _{1-x} Nb _x O _{2-δ} (x = 0,0.03,0.05,0.1,0.2, 0.3 and 1)	49
4.3	SEM micrographs of Ce _{1-x} Nb _x O _{2-δ} (x = 0,0.03,0.05,0.1,0.2, 0.3 and 1)	51
4.4	Soot Oxidation Activity of Ce _{1-x} Nb _x O _{2-δ} (x = 0,0.03,0.05,0.1,0.2, 0.3 and 1)	52
5.1	(a) XRD spectra (b) Enlarged view of the (111) plane of CeO ₂ (c) Enlarged view of the (-111) and (111) of CuO planes in Pure Cu, Pr and Cu _x (x=0-0.2) (Ce _{0.9} Pr _{0.1}) _(1-x) O _{2-δ} Catalysts	59
5.2	Raman Spectra of Pure Ce, Cu, and Cu _x (x=0-0.2) (Ce _{0.9} Pr _{0.1}) _(1-x) O _{2-δ} Catalysts	61

5.3	(a) N ₂ -adsorption-desorption isotherm (b) Pore size distribution of Pure Ce, Cu, Pr, and Cu _x (x=0-0.2) (Ce _{0.9} Pr _{0.1}) _(1-x) O _{2-δ} Catalysts	63
5.4	FE-SEM images of Pure Ce, Cu, Pr, and Cu _x (x=0-0.2) (Ce _{0.9} Pr _{0.1}) _(1-x) O _{2-δ} Catalysts	65
5.5	(a) Ce 3d (b) Pr 3d (c) O1s (d) Cu 2p XPS spectra for Cu _x (x=0-0.2) (Ce _{0.9} Pr _{0.1}) O _{2-δ} Catalysts.	67
5.6	Soot Oxidation plots for Pure Ce, Cu, Pr, and Cu _x (x=0-0.2) (Ce _{0.9} Pr _{0.1}) _(1-x) O _{2-δ} Catalysts.	70
5.7	Conversion v/s Temperature plots of pure Ce, Pr, Cu, and Cu _x (x=0-0.2) (Ce _{0.9} Pr _{0.1}) _(1-x) O _{2-δ} Catalysts	78
5.8	(a) Rate vs. Temperature plot (b) Arrhenius plot for pure Ce and Cu _x (x=0-0.2) (Ce _{0.9} Pr _{0.1}) _(1-x) O _{2-δ} Catalysts	79
6.1	XRD spectra of Co _x (x=0-0.2) (Ce _{0.9} Pr _{0.1}) _(1-x) O _{2-δ} Catalysts	82
6.2	Raman Spectra of Co _x (x=0-0.2) (Ce _{0.9} Pr _{0.1}) _(1-x) O _{2-δ} Catalysts	84
6.3	FE-SEM images of Co _x (x=0-0.2) (Ce _{0.9} Pr _{0.1}) _(1-x) O _{2-δ} Catalysts.	87
6.4	(a) N ₂ -adsorption-desorption isotherm (b) Pore size distribution of Co _x (x=0-0.2) (Ce _{0.9} Pr _{0.1}) _(1-x) O _{2-δ} Catalysts	89
6.5	(a) Ce 3d (b) Pr 3d (c) O1s (d) Co 2p XPS spectra for Co _x (x=0-0.2) (Ce _{0.9} Pr _{0.1}) _(1-x) O _{2-δ} Catalysts.	91
6.6	Soot Oxidation plots for Co _x (x=0-0.2) (Ce _{0.9} Pr _{0.1}) _(1-x) O _{2-δ} Catalysts	95
6.7	Experimental and calculated Curves for Co _x (x=0-0.2) (Ce _{0.9} Pr _{0.1}) _(1-x) O _{2-δ} Catalysts.	98
6.8	(a) Rate vs. Temperature plot (b) Arrhenius plot for Co _x (x=0.05-0.2) (Ce _{0.9} Pr _{0.1}) _{1-x} O _{2-δ} Catalysts.	100
7.1	XRD spectra of Fe _x (x=0-0.2) (Ce _{0.9} Pr _{0.1}) _{1-x} O _{2-δ} Catalysts.	104
7.2	Raman Spectra of Fe _x (x=0-0.2) (Ce _{0.9} Pr _{0.1}) _{1-x} O _{2-δ} Catalysts.	107
7.3	FE-SEM images of Fe _x (x=0-0.2) (Ce _{0.9} Pr _{0.1}) _{1-x} O _{2-δ} Catalysts.	108
7.4	(a) N ₂ -adsorption-desorption isotherm (b) Pore size distribution of Fe _x (x=0-0.2) (Ce _{0.9} Pr _{0.1}) _{1-x} O _{2-δ} Catalysts.	110
7.5	(a) Ce 3d (b) Pr 3d (c) O1s (d) Co 2p XPS spectra for Fe _x (x=0-0.2) (Ce _{0.9} Pr _{0.1}) _{1-x} O _{2-δ} Catalysts.	112
7.6	Soot Oxidation plots for Fe _x (x=0-0.2) (Ce _{0.9} Pr _{0.1}) O _{2-δ} Catalysts.	114
7.7	Experimental and calculated Curves for Fe _x (x=0-20)0.1 (Ce _{0.9} Pr _{0.1}) _(1-x) O _{2-δ} Catalysts.	117
7.8	(a) Rate vs. Temperature plot (b) Arrhenius plot for Fe _x (x=0-0.2) (Ce _{0.9} Pr _{0.1}) _{1-x} O _{2-δ} Catalysts.	119
8.1	XRD spectra of Mn _x (x=0-0.2) (Ce _{0.9} Pr _{0.1}) _{1-x} O _{2-δ} Catalysts.	122
8.2	Raman Spectra of Mn _x (x=0-0.2) (Ce _{0.9} Pr _{0.1}) _{1-x} O _{2-δ} Catalysts.	124
8.3	FE-SEM images (a) 500 nm (b) 200 nm of Mn _x (x=0-0.2) (Ce _{0.9} Pr _{0.1}) _{1-x} O _{2-δ} Catalysts.	126-127
8.4	(a) N ₂ -adsorption-desorption isotherm (b) Pore size distribution of Mn _x (x=0-0.2) (Ce _{0.9} Pr _{0.1}) _{1-x} O _{2-δ} Catalysts.	129
8.5	(a) Ce 3d (b) Pr 3d (c) O1s (d) Co 2p XPS spectra for	132

	$Mn_{x(x=0-0.2)}(Ce_{0.9}Pr_{0.1})_{1-x}O_{2-\delta}$ Catalysts.	
8.6	Soot Oxidation plots for $Mn_{x(x=0-0.2)}(Ce_{0.9}Pr_{0.1})_{1-x}O_{2-\delta}$ Catalysts.	135
8.7	Experimental and calculated Curves for $Mn_{x(x=0-20)}(Ce_{0.9}Pr_{0.1})_{1-x}O_{2-\delta}$ Catalysts.	138
8.8	(a) Rate vs. Temperature plot (b) Arrhenius plot for $Mn_{x(x=0.05-0.2)}(Ce_{0.9}Pr_{0.1})_{1-x}O_{2-\delta}$ Catalysts.	139
9.1	XRD spectra of $Cr_{x(x=0.05-0.2)}(Ce_{0.9}Pr_{0.1})_{1-x}O_{2-\delta}$ Catalysts.	142
9.2	Raman Spectra of $Cr_{x(x=0.05-0.2)}(Ce_{0.9}Pr_{0.1})_{1-x}O_{2-\delta}$ Catalysts.	144
9.3	FE-SEM images (a) 500 nm (b) 200 nm of $Cr_{x(x=0.05-0.2)}(Ce_{0.9}Pr_{0.1})_{1-x}O_{2-\delta}$ Catalysts.	145-146
9.4	(a) N_2 -adsorption-desorption isotherm (b) Pore size distribution of $Cr_{x(x=0-0.2)}(Ce_{0.9}Pr_{0.1})_{1-x}O_{2-\delta}$ Catalysts.	148
9.5	(a) Ce 3d (b) Pr 3d (c) O1s (d) Co 2p XPS spectra for $Cr_{x(x=0-0.2)}(Ce_{0.9}Pr_{0.1})_{1-x}O_{2-\delta}$ Catalysts.	150
9.6	Soot Oxidation plots for $Cr_{x(x=0-0.2)}(Ce_{0.9}Pr_{0.1})_{1-x}O_{2-\delta}$ Catalysts.	153
9.7	Experimental and calculated Curves for $Cr_{x(x=0-20)}(Ce_{0.9}Pr_{0.1})_{1-x}O_{2-\delta}$ Catalysts.	156
9.8	(a) Rate vs. Temperature plot (b) Arrhenius plot for $Cr_{x(x=0.05-0.2)}(Ce_{0.9}Pr_{0.1})_{1-x}O_{2-\delta}$ Catalysts.	157
10.1	XRD analysis for T.M _(x=0.05) doped $(Ce_{0.9}Pr_{0.1})O_{2-\delta}$ nanofibers	163
10.2	Raman spectroscopy analysis for T.M _(x=0.05) doped $(Ce_{0.9}Pr_{0.1})O_{2-\delta}$ nanofibers	164
10.3	(a) N_2 adsorption-desorption isotherm (b) Pore size distribution of T.M _(x=0.05) doped $(Ce_{0.9}Pr_{0.1})O_{2-\delta}$ nanofibers	166
10.4	FE-SEM images of TM _(x=0.05) doped $(Ce_{0.9}Pr_{0.1})O_{2-\delta}$ nanofibers (a) (2 μ m) (b) 200nm	169-170
10.5	Soot conversion curves of T.M _(x=0.05) $(Ce_{0.9}Pr_{0.1})O_{2-\delta}$ nanofibers	171
10.6	TGA-FTIR Plots for T.M _(x=0.05) $(Ce_{0.9}Pr_{0.1})O_{2-\delta}$ nanofibers	173-174

LIST OF TABLES

SL. NO.	TITLE	PAGE NO.
2.1	A literature review on various metal oxides synthesized using SCS	11
2.2	Summary of literature review on Soot oxidation activity	15
2.3	T ₅₀ temperature and experimental conditions of various Ce-based catalysts for soot oxidation activity.	20-23
2.4	List of reaction models commonly used to represent solid-state reactions (López-Fonseca et al. 2007)	28
2.5	T ₅₀ temperature, Activation energy, and Pre-Exponential Factor for Soot and Ceria-based Catalysts	29
3.1	List of equations and methods used for kinetic studies.	44
4.1	Physicochemical properties and T ₅₀ of Ce _{1-x} Nb _x O _{2-δ} (x = 0,0.03,0.05,0.1,0.2, 0.3 and 1)	48
4.2	Activation energies obtained for Ce _{1-x} Nb _x O _{2-δ} (x = 0,0.03,0.05,0.1,0.2, 0.3 and 1) by both Ozawa and KAS methods.	53
5.1	Physicochemical properties of Pure Ce, Pr, Cu, and Cu _(x=0-0.2) (Ce _{0.9} Pr _{0.1}) _{1-x} O _{2-δ} obtained from XRD and BET analysis	60
5.2	Reducibility ratio and Surface Oxygen species of Cu _(x=0.05-0.2) (Ce _{0.9} Pr _{0.1}) _{1-x} O _{2-δ} catalyts.	68
5.3	Kinetic triplets and "m" value for Pure Ce, Pr, Cu, and Cu _(x=0.05-0.2) (Ce _{0.9} Pr _{0.1}) _{1-x} O _{2-δ} catalyts.	76
6.1	Physicochemical properties of Co _(x=0-0.2) (Ce _{0.9} Pr _{0.1}) _(1-x) O _{2-δ} and pure Co from XRD and Raman spectroscopy Analysis	85
6.2	BET Analysis and T ₅₀ temperature of Co _(x=0-0.2) (Ce _{0.9} Pr _{0.1}) _(1-x) O _{2-δ} catalyts.	88
6.3	Reducibility ratio and Surface Oxygen species of Co _(x=0-0.2) (Ce _{0.9} Pr _{0.1}) _(1-x) O _{2-δ} catalyts.	93
6.4	T ₅₀ and Kinetic parameters of Co _(x=0-0.2) (Ce _{0.9} Pr _{0.1}) _(1-x) O _{2-δ}	101
7.1	Physicochemical properties of Fe _(x=0-0.2) (Ce _{0.9} Pr _{0.1}) _(1-x) O _{2-δ} from XRD and Raman spectroscopy Analysis.	107
7.2	BET-BJH Analysis of Fe _(x=0-0.2) (Ce _{0.9} Pr _{0.1}) _(1-x) O _{2-δ}	109
7.3	Reducibility ratio and Surface Oxygen species of Fe _(x=0-0.2) (Ce _{0.9} Pr _{0.1}) _(1-x) O _{2-δ} catalyts.	113
7.4	Kinetic triplets and "m" value for Fe _(x=0-0.2) (Ce _{0.9} Pr _{0.1}) _(1-x) O _{2-δ} catalyts.	116
8.1	Physicochemical properties of Mn _(x=0-0.2) (Ce _{0.9} Pr _{0.1}) _(1-x) O _{2-δ} from XRD and Raman spectroscopy Analysis.	125

8.2	BET-BJH Analysis of $Mn_{x(x=0-0.2)}(Ce_{0.9}Pr_{0.1})_{(1-x)}O_{2-\delta}$ catalysts.	130
8.3	Reducibility ratio and Surface Oxygen species of $Mn_{x(x=0-0.2)}(Ce_{0.9}Pr_{0.1})_{(1-x)}O_{2-\delta}$ catalysts.	133
8.4	Kinetic triplets and "m" value for $Mn_{x(x=0-0.2)}(Ce_{0.9}Pr_{0.1})_{(1-x)}O_{2-\delta}$ Catalysts.	137
9.1	Physicochemical properties of $Cr_{x(x=0-0.2)}(Ce_{0.9}Pr_{0.1})_{(1-x)}O_{2-\delta}$ catalysts. from XRD and Raman spectroscopy Analysis.	143
9.2	BET-BJH Analysis of $Cr_{x(x=0-0.2)}(Ce_{0.9}Pr_{0.1})_{(1-x)}O_{2-\delta}$ catalysts.	147
9.3	Reducibility ratio and Surface Oxygen species of $Cr_{x(x=0-0.2)}(Ce_{0.9}Pr_{0.1})_{(1-x)}O_{2-\delta}$ catalysts.	151
9.4	Kinetic triplets and "m" value for $Cr_{x(x=0-0.2)}(Ce_{0.9}Pr_{0.1})_{(1-x)}O_{2-\delta}$ Catalysts.	155
10	Physicochemical properties of $TM_{(x=0.05)}(Ce_{0.9}Pr_{0.1})_{1-x}O_{2-\delta}$ nanofibers obtained from XRD, Raman Spectroscopy, and BET-BJH analysis along with String diameter and T_{50} temperature.	168

NOMENCLATURE:

A - Pre- Exponential Factor (min^{-1})

A_{1.5}- Nucleation and growth model

Am -Avrami Erofeev

α - Extent of Conversion

β - Heating rate (K min^{-1})

CR - Coats Redfern

D₍₁₋₃₎ – (1-3 Dimensional) Diffusion model

DPF- Diesel Particulate Filter

E_a - Activation Energy (kJ mol^{-1})

$f(\alpha)$ - Differential Kinetic Function

EDTA – Ethylene Diamine Tetraacetic Acid

FE-SEM - Field Emission Scanning Electron Microscopy

FWO - Flynn Wall Ozawa

$g(\alpha)$ - Integral Kinetic Function

L₄- Power-law

m - Non Integral Exponent /Avrami integer

KAS - Kissinger Akahira Sunose

O_v – Oxygen vacancies

PM - Particulate Matter

P₁- Phase boundary controlled reaction (contracting linear)

P₂ - Phase boundary controlled reaction (contracting area).

P₃ - Phase boundary controlled reaction (contracting volume).

R - Universal Gas Constant

R₂ - second-order chemical reaction

SCS – Solution Combustion Synthesis

T -Absolute Temperature (K)

T₅₀ - Temperature at which 50% of soot gets oxidized ($^{\circ}\text{C}$)

TGA - Thermogravimetric Analyser

TPR-Temperature Programmed Reduction

XPS – X-ray Photoelectron Spectroscopy

XRD - X-ray Diffraction

CHAPTER 1

INTRODUCTION

Air pollution is a significant challenge worldwide as it creates numerous complications to public health and the environment when toxic components are in excess. The regulations of harmful pollutants are essential to protect the public and the environment. Hence, the Environment Protection Agency (EPA) plays a significant role in regulating policies for toxic emissions. According to EPA, Carbon dioxide (CO₂) alone is responsible for more than 81% of greenhouse gas emissions, and most countries have come forward to reduce the emission of CO₂ and use of Hydro Fluoro Carbons (HFCs) (EPA 2018). The Central Pollution Control Board (CPCB) of India set the standards for Bharat Stage (BS) norms, and it first came into effect in India in 2000 and was altered at every stage. All automobile manufacturers must sell vehicles that mandatorily comply with the norms. The standards target strict guidelines by dropping the permissible levels of pollutants. BS-VI – (2020) was the newest upgrade of the iterated norms set, which allows only 80 mg/km of NO_x, 25 mg/km of particulate matter, and 500 mg/km of CO from diesel vehicles (CPCB 2020).

Another critical pollutant in the air is Particulate Matter (PM), a combination of solid particles and liquid droplets. Inhalable particles of 10 µm diameter are called PM₁₀, and 2.5 µm diameter are called PM_{2.5}. They are generally emitted from construction sites, diesel exhausts, burning crop fields, smokestacks, etc. (2018).

1.1. SOOT OXIDATION

Soot/diesel particulate matter is a common type of PM_{2.5} and is obtained as a by-product due to the incomplete combustion of fossil fuels such as hydrocarbons, coal, etc. It is also commonly found in refineries and motor vehicles exhaust. These microscopic particulates can easily penetrate the lungs and enter the bloodstream when inhaled. It also has a tremendous effect on the environment by acidifying water bodies and is responsible for causing haze/smog (Weidman and Marshall 2012).

Soot formation initiates with the precursors and nucleation of heavy molecules to form particles. The surface growth of particles proceeds by the adsorption of molecules, and then coagulation happens through particle-particle collisions. Soot formation can be reduced by oxidation of the particles, resulting in less harmful products. In the automobile industries, Diesel Particulate Filter (DPF) regeneration is costly and challenging as it involves high temperatures ($\sim 800^{\circ}\text{C}$) and energy. The clogged/ blocked DPF restricts the easy flow of exhaust, and hence pressure drop develops, which may further damage the diesel engine. Thus, within the limitations of particle size restrictions and an engine's life, all particulates should be trapped, and the filter should be regenerated carefully with no toxic byproducts (Van Setten et al. 2001).

Most promising catalysts have been studied which are capable of assisting soot oxidation. Developing novel catalysts for soot oxidation that ensure the least pollution and have high efficiency and reliability with excellent Oxygen storage capacity (OSC) and high surface area is a most challenging task (Durgasri et al. 2014a) (de Leitenburg et al. 1995; Mukherjee et al. 2016; Sudarsanam et al. 2014). The oxidation reaction is initiated by Mars Van Krevelen (MVK)-type mechanism, which suggests that the reaction between Carbon monoxide (CO) and Oxygen (O_2) takes place on the surface of the catalyst (Andana et al. 2016; Aneggi et al. 2005). The three discrete elementary reactions of the MVK mechanism are given below



Here, the metal oxide (MO) loses its active O_2 ; hence, a reduced metal site (M^*) is formed, which cannot further involve in the reaction. The atmospheric gas-phase O_2 chemisorbs on the catalyst's surface to form MO to proceed with CO oxidation. The soot oxidation in DPF with stable catalysts is most important for the present scenario as per requirements of Bharat stage VI (ICCT Policy Update 2016).

Oxygen vacancies play a crucial role in soot oxidation reaction as they facilitate the lattice oxygen diffusion from the bulk to the surface by adsorption-desorption reactions (Bin et al. 2013; Vinodkumar et al. 2015). The above properties would improve soot's catalytic oxidation (Durgasri et al. 2014a).

1.2. SOOT OXIDATION KINETICS

To further understand the soot oxidation kinetics, a mathematical description of particulates' combustion focuses on describing the kinetic triplets—Arrhenius parameters such as pre-exponential factor (A), Activation energy (E_a), and the reaction model. More detailed insight into kinetics and soot oxidation mechanisms may help develop more active or selective soot combustion catalysts and model catalytic converters and regeneration systems (Ganiger et al. 2020). Solid-state reaction kinetic analysis is done to obtain the kinetic triplets. The apparatuses used are flow reactors and thermo-gravimetric analyzers (TGA) (Lee et al., 2013). The kinetic evaluation uses TGA for heterogeneous solid-gas reactions (Chrissafis, 2009). Model-free methods are the most reliable for calculating the E_a of both isothermal and non-isothermal reactions. The model-free methods include methods with and without the integral temperature approximation, and some of these models include Flynn-Wall-Ozawa (FWO) method, the Friedman method, and Kissinger Akahira Sunose (KAS) method (Vyazovkin et al., 2011; Li et al., 2019). The most suitable reaction model is anticipated through the master plot method, which fits the experimental data to theoretical data.

1.3. CATALYST MATERIALS

The main goal of the selected catalyst material should enhance the activity without getting reacted or consumed and be capable of replacing the existing costly noble materials. Ceria (CeO_2) and CeO_2 -based materials have gained massive significance over the decades due to their unique properties and applications in various fields. It induces high OSC (Chavan et al. 2008; Prasad et al. 2012a; Jamshidijam et al. 2014).

CeO₂ has broad applications due to its distinct characteristics and high reactivity to oxygen (Yang et al. 2010). The most critical catalytic properties of CeO₂ are reversible redox properties (Ce^{3+/4+}) along with high oxygen storage capacity (OSC), which aids in enhancing the soot oxidation activity (Hernández-Giménez et al. 2013).

Doping of lanthanides, transition, and noble metals with CeO₂ develops the Oxygen vacancies at the octahedral sites. It creates defects that alter the O₂ diffusion performance and thus gains interest in the area of research. (Chavan et al. 2008; Krishna et al. 2007b; Mukherjee et al. 2016b; Shuang et al. 2015). CeO₂-based catalysts also encourage DPF regeneration by lowering the required temperature to combust the soot. Recently, Ceria-based catalysts have improved the solid-solid contact between the soot and the catalyst (Hernández-Giménez et al., 2013). CeO₂ when doped with rare earth materials and lanthanides such as Praseodymium (Pr) (Krishna et al. 2007a; Mukherjee et al. 2016; Reddy et al. 2009b), Lanthanum (La)(Mukherjee et al. 2016), Gadolinium (Gd)(Anantharaman et al. 2018b; Durgasri et al. 2014a), Samarium (Sm) (Anantharaman et al. 2018d; Sudarsanam et al. 2014b), Neodymium (Nd) (Patil et al. 2019) have shown excellent performance for soot oxidation activity. It has shown an evident reduction in temperature required for soot oxidation compared to undoped/pure CeO₂ and no catalyst (Mukherjee et al. 2016). In most reported works, Ce-Pr has shown tremendous catalytic activity among rare-earth materials (Shuang et al. 2015). The multivalent Pr cation (Pr^{3+/4+}) increases the redox potential of Pr₆O₁₁ due to the high mobility of anion vacancy (Andana et al. 2016; Reddy et al. 2009b).

Researchers have also evaluated the performance of transition metal-doped with CeO₂-based materials such as Manganese (Mn), Zirconium (Zr), Hafnium (Hf), Tin (Sn), Titanium (Ti) for soot oxidation (Anjana et al. 2017) (Jamshidijam et al. 2014) (Mukherjee et al. 2016)(Venkataswamy et al. 2016a). Researchers have also evaluated the performance of Transition Metal (TM) doped with CeO₂-based materials such as Manganese (Mn), Zirconium (Zr), Hafnium (Hf), Tin (Sn), Titanium (Ti) for soot oxidation (Anantharaman et al. 2017; Mukherjee et al. 2016a).

Studies have been carried out for tertiary doping of Ceria-based metals, further increasing the catalytic activity (Dulgheru and Sullivan 2013; Mira et al. 2015; Prasad et al. 2012b)., making the obtained product porous and well dispersed (Varma et al. 2016).

1.4. SYNTHESIS OF NANOPARTICLES

Nanoparticles for soot oxidation application have been synthesized by several techniques, such as the co-precipitation method (Hernández-Giménez et al. 2013; Mahofa et al. 2014; Ranji-Burachaloo et al. 2016; Reddy et al. 2008a; Venkataswamy et al. 2016a), EDTA citrate complex method (Anantharaman et al. 2017, 2018a), Hydrothermal method (Aneggi et al. 2014a; Chingakham et al. 2020; Suárez-Vázquez et al. 2018), Nitrate calcination method (Krishna et al. 2007b), etc.

Solution Combustion Synthesis (SCS) is used extensively to prepare highly pure nanocrystalline powders such as ceramic oxides (Varma and Mukasyan 2004). Metal salts act as oxidizing/reducing agents, and fuels reported for combustion are glycine, sucrose, urea, citric acid, starch, etc. (Varma et al. 2016). In SCS, an exothermic reaction is initiated when the self-ignition temperature of the fuel is attained (Mimani and Patil 2001; Bedekar et al. 2007). SCS produces high-purity, fine, and homogeneous powders with high purity and quick and easy process, saving time and energy (Varma et al. 2016). SCS generates massive gaseous byproducts, leading to a significant product expansion and a fast temperature decrease after the reaction completes, making the obtained product porous and well dispersed (Varma et al. 2016).

Electrospinning Technique (EST) is another effective technique in the current study. It is a simple method to produce highly beneficial nanofibers (Thavasi et al. 2008). EST is used to develop nanofibers with controlled diameter and orientation for various applications (Sasmal and Datta 2019; Thavasi et al. 2008).

Electrospinning is also a widely used technology for nanofiber fabrication with controllable diameter and structure (Bhardwaj and Kundu 2010). The electrospinning technique gained significant attention as it can fabricate nanofibers on a nanometer scale with high quality (CUI et al. 2008; Stegmayer et al. 2022). Unique electrospinning methods can produce nanofibers with porous core-shell or hollow nanofiber structures (Thavasi et al. 2008).

Nanofibers are used in several catalytic applications, such as photocatalysis and oxidation reactions (Stegmayer et al. 2022). Nanofibers in the past decade indicated a favorable impact and represented a key technology for environmental applications (Thavasi et al. 2008). Nanofibers as soot oxidation catalysts are preferred due to increased surface area, eventually leading to enhanced soot and nanofiber contact points (Stegmayer et al. 2022). The fibrous morphology traps and converts soot to a less harmful form at low temperatures by improving the number of contact points (Kumar et al. 2012).

The present work also studies the effect of transition metal (Cr, Mn, Fe, Co, and Cu) dopants in Ce-Pr-based catalysts synthesized by the SCS method on soot oxidation activity. The current study also deals with describing kinetic triplets. Arrhenius parameters such as Pre exponential factor (A), Activation energy (E_a), and the reaction models combinedly, known as the kinetic triplets (Chrissafis 2009; López-Fonseca et al. 2007) are evaluated in the current study. Further, each transition metal doped Ce-Pr nanofiber is generated to study its effect on soot oxidation activity.

1.5. SCOPE AND OBJECTIVES

The scope of the work is to perform studies on the effect of transition metal oxide (Cr, Mn, Fe, Co, and Cu) doping in Ceria Praseodymium catalyst for soot oxidation activity and its kinetic analysis.

The specific objectives of the present study are:

1. Synthesis of transition metal (Cr, Mn, Fe, Co, and Cu) doped Ceria Praseodymium catalysts using Solution Combustion Synthesis.
2. Characterization of synthesized catalysts using XRD, Raman spectroscopy, FESEM-EDS, BET- BJH analysis, XPS, and TG analysis.
3. To perform soot oxidation activity and kinetic studies on the synthesized catalysts.
4. To develop electrospun Transition Metal ((TM ($x=0.05$) = Cr, Mn, Fe, Co, Cu) – doped $Ce_{0.9}Pr_{0.1}O_{2-\delta}$ (CP)) nanofiber catalysts and test soot oxidation activity.

1.6. ORGANIZATION OF THE THESIS

The rest of the thesis is organized as follows:

Chapter 2 provides a literature review of various catalysts studied for soot oxidation and the factors affecting catalytic activity. It also includes the literature based on kinetic studies for soot oxidation activity.

Chapter 3. deals with the materials and methodology adopted for synthesizing the catalysts, characterization techniques, and soot oxidation reaction conditions used in the current study.

Chapter 4 describes the effect of Niobium (Nb) doped Ceria (Ce) as a catalyst for soot oxidation activity.

Chapter 5 comprises the study on Copper (Cu)-doped Ceria-Praseodymium catalysts for soot oxidation activity and its kinetics.

Chapter 6 discusses the investigation of Cobalt (Co) doped Ceria-Praseodymium catalysts for soot oxidation activity and its kinetics.

Chapter 7 deals with the studies on the effect of Iron (Fe) doped Ceria-Praseodymium catalysts on soot oxidation activity and its kinetics.

Chapter 8 presents the studies on the effect of Manganese (Mn) doped Ceria-Praseodymium catalysts on soot oxidation activity and its kinetics.

Chapter 9 deals with the catalytic effect of Chromium (Cr) doped Ceria-Praseodymium catalysts on soot oxidation activity and its kinetics.

Chapter 10 represents the studies on the development of electrospun Transition Metals ((TM ($x=0.05$) = Cr, Mn, Fe, Co, Cu) – doped $Ce_{0.9}Pr_{0.1}O_{2-\delta}$ (CP)) nanofiber catalyst and its effect on soot oxidation activity.

Chapter 11 summarizes the overall conclusion of the results obtained from all the chapters and provides the future scope of research.

CHAPTER 2

LITERATURE REVIEW

2.1. COMBUSTION SYNTHESIS

The combustion synthesis method is very flexible and adaptable for synthesizing a wide range of nano-sized powders. Mimani and Patil synthesized various nano-sized materials and reported that the metal oxides and their composites could be prepared at a very low temperature of < 400 °C. The products were homogenous and crystalline with high surface area and purity (99.99%); the particles obtained were less agglomerated (Mimani and Patil 2001).

The investigation of Chavan and Tyagi establishes the importance of controlling the oxidant-to-fuel ratio in synthesizing mixed oxides (Chavan and Tyagi 2004). The flame wasn't observed during the fuel deficient cases, but the flame temperature of 1486°C and 1788 °C was observed in the case of propellant and excess fuel cases. Kikukawa et al. also studied the effects of the glycine (fuel)/Nitrate (G/N) ratio for the Preparation of spinel-type ferrites by the Glycine-Nitrate-Process (GNP) (Kikukawa et al. 2004). It was found that the crystallite size gradually increases with the increase in the G/N ratio while surface area decreases with an increase in the G/N ratio; hence optimized G/N ratio is essential for combustion studies. Prasad et al. synthesized $\text{Ce}_{0.9}\text{Gd}_{0.1}\text{O}_{1.95}$ powder via GNP with varying G/N ratios (0.1, 0.3, and 0.55). Here glycine complexes with the metal cations to prevent selective precipitation, and also glycine is oxidized by nitrate anions, thereby serving as a fuel for combustion (Prasad et al. 2010). For SCS, several works were reported on various fuels utilized to enhance the powder properties. Esmaeili et al. synthesized MgO nanoparticles using polyethylene glycol and sorbitol as fuel by microwave-induced combustion synthesis method (Esmaeili et al. 2009).

Sharma et al. studied the efficacy of mixed fuel (Urea + glycine) for SCS of alumina. It was reported that urea as a fuel promotes the crystalline character of the product, whereas glycine promotes the amorphous character of the product. Hence, crystallinity can be enhanced easily with a mixed-fuel approach (Sharma et al. 2014).

Charojrochkul et al. studied the effect of fuels for SCS on CeO₂ and GDC nanoparticles. It was reported that the oxides prepared from urea combustion synthesis were more significant as they produced less heat than glycine and citric acid fuels during synthesis. The oxides prepared from urea combustion synthesis had high stability for methane steam reforming. The specific surface area of nanoparticles from citric acid was highest when compared to urea and glycine. In contrast, the particle size was lowest and highest when glycine and urea were used as fuel, respectively (Charojrochkul et al. 2012).

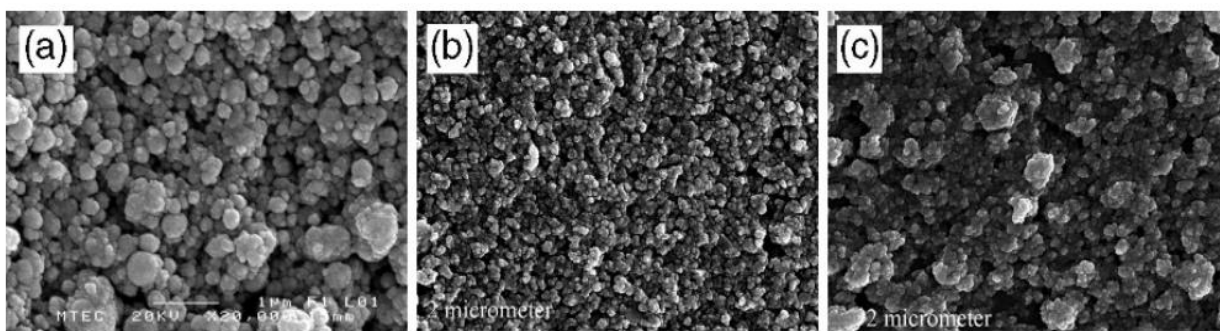


Figure 2.1: SEM micrographs of pulverized GDC powder a) Urea, (b) Glycine, and (c) citric acid (Charojrochkul et al. 2012).

Isabel et al. reported that using starch as fuel results in nonviolent propagation and reduced toxic byproducts. The starch-assisted SCS produces macro-porous metal oxides. With a mixed fuel approach, lattice defects, surface area, crystallite size, and porosity can be altered for the desired product (Isabel et al. 2020). Ansari et al. reported that using glucose as a fuel for SCS for CoTiO₃/CoFe₂O₄, a highly agglomerated product, was obtained, whereas spherical nanoparticles were obtained for maltose and starch as fuel (Ansari et al. 2018). **Table 2.1** summarizes the literature review on metal oxides synthesized using the SCS method.

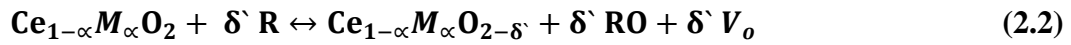
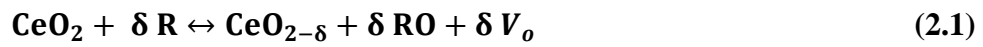
Table 2.1: A literature review on various metal oxides synthesized using SCS.

Material	Fuel	Inference	Reference
YSZ	Glycine	The smoldering mode of combustion took place, and the least amount of residual carbonate species is the one with a G/N ratio of 0.23.	(Kaus et al. 2006)
Eu ³⁺ doped Y ₂ O ₃	Sucrose	Crystallite size: 30–50 nm	(Xu 2006)
Eu ³⁺ doped CaWO ₄	Ammonium nitrate	Crystallite size: 50–100 nm	(Lebedev 2007)
NDC	Glycine	Crystallite size obtained in the range of 10 -35 nm	(Chavan et al. 2008)
Al ₂ O ₃ –ZrO ₂	starch	Reduces the exothermicity of the combustion reaction.	(Tahmasebi and Paydar 2008)
AlN powder	glucose, sucrose, citric acid, & starch.	Fine spherical shape when compared to other fuels	(Qin et al. 2009)
NDC	Glycine	Crystallite size – 11 nm	(Bedekar et al. 2010)
NDC	Urea	Agglomerates increase with increasing dopant content and crystallite size – 20 nm.	(Biswas and Bandyopadhyay 2013)
NDC	Citric acid	Crystallite size obtained in the range of 63 - 68.5 nm	(Kahlaoui et al. 2013)

From the above literature survey, it can be concluded that SCS is an effective method for synthesizing homogeneous products with high purity and yield. It can also be noted that glycine is efficient fuel for SCS when compared to other fuels for obtaining smaller crystallite sizes. Nonviolent combustion can be attained with an optimum lower Fuel/Nitrate ratio.

2.2. SOOT OXIDATION

The reaction of CeO₂ during doping with external dopants has been studied by Trovarelli et al. (Trovarelli et al. 1999) and is given below.



During the redox reaction of CeO₂, an intrinsic vacancy (V_o) is created when a reductant molecule (R = soot) comes in contact, releasing the gaseous product (RO = CO/CO₂). A similar reaction is observed when the isovalent dopant (M) with a certain mole fraction (α) is doped. The oxygen storage can be due to both intrinsic and extrinsic vacancies, where "δ" represents the total oxygen storage capacity due to the redox process induced by a reductant and the additional oxygen storage due to the creation of extrinsic defects, whereas "δ'" is the modified oxygen storage capacity after solid solution formation.

To define the selectivity and activity of metal oxides for oxidation processes, seven descriptors were proposed by Grasselli (Grasselli 2002; Vilé et al. 2016), also known as Grasselli's seven pillars. The descriptors include the redox properties, host structure, Metal-Oxygen bond, Lattice Oxygen, site isolation, phase cooperation, and multi-functionality. Oxygen vacancy formation is also considered the most uncomplicated, and oxygen storage capacity (OSC) can also be regarded as the alternative descriptor (Vilé et al. 2016).

Researchers have evaluated the performance of various catalyst materials, which involve CeO₂ and CeO₂-based materials, due to their unique characteristics and excellent redox nature (Krishna et al. 2007a; Vázquez et al. 2018).

CeO₂ doped with lanthanides and other rare earth materials has been extensively studied and could reduce the required soot combustion temperature much lower than uncatalyzed soot combustion. T₅₀ (The temperature at which 50% conversion is observed) is analyzed from works of literature reported for better comparison with other catalysts.

T₅₀ for pure CeO₂ synthesized by various synthesis techniques is listed in the work reported by Patil and Dasari (Patil and Dasari 2019). Zhang et al. reported T₅₀, which was found to be less for pure CeO₂ nano-rods (368°C) and pure CeO₂ nano-flakes (383°C) synthesized by hydrothermal method (Zhang et al. 2016), followed by pure CeO₂ nanopowder (416°C) synthesized by GNP (Patil and Dasari 2019)

Liang et al. studied the effect of doping Zr on CeO₂ synthesized by the co-precipitation method (Liang et al. 2007). The increased surface area was reported to favor the soot catalytic combustion by providing more redox sites to activate adsorbed oxygen. Similarly, Wu et al. developed Ce_{0.5}Mn_{0.5}O₂ and Ce_{0.5}Zr_{0.5}O₂ as a catalyst by the citric acid sol-gel method for the soot oxidation reaction (Wu et al. 2007). They conveyed that Mn as a dopant presented better catalytic activities than Zr due to the strong interaction between Mn and Ce, promoting oxygen storage/transport capacity. Garci and Atribak studied the catalytic activity of CeO₂, ZrO₂, and Ce–Zr mixed oxides for soot oxidation for both loose and tight contact between the catalyst and soot. It was noted from their work that Ce–Zr mixed oxides had higher BET surface areas and smaller crystal sizes, which enhanced the redox properties (Garci and Atribak 2008).

The catalytic activity studies by Reddy et al. reveal that soot oxidation is enhanced by incorporating Zr⁴⁺ and Hf⁴⁺ into the CeO₂ lattice (Reddy et al. 2008). The hf-doped CeO₂ catalyst exhibited better activity than the Zr-doped CeO₂ due to the high oxygen vacancy creation in the crystal lattice. Reddy et al. indicated that Pr-doped CeO₂ has more surface and bulk oxygen vacancies, redox sites, lattice oxygen mobility, and better thermal stability hence is also found to be a more active catalyst in soot oxidation (Reddy et al. 2009).

Katta et al. also synthesized La-doped CeO₂ and Zr-doped CeO₂ solid solutions by modified co-precipitation method (Katta et al. 2010). It was observed that the O₂ vacancies and the thermal stability of CeO₂ were improved upon doping both transition metal (Zr⁴⁺) and rare earth material (La³⁺). Sudarsanam et al. reported their work on Sm-doped CeO₂ synthesized using the co-precipitation method. It was observed that the oxygen vacancy concentration substantially decreased with increased calcination temperature (Sudarsanam et al. 2014). Their work also concluded that the Sm-doped CeO₂ showed excellent soot oxidation performance compared with pure CeO₂ due to abundant oxygen vacancies and superior BET surface area. Mukherjee et al. carried out soot oxidation studies on CeO₂ doped with various transition and rare earth metals such as Zr, Pr, Hf, Mn, Fe, and La, and the T₅₀ followed the order of Mn < Hf < Pr < La < Fe < Zr < pure CeO₂ (Mukherjee et al. 2016).

Anantharaman et al. synthesized binary metal oxides of CeO₂-Hf using the EDTA-Citrate method (Anantharaman et al. 2018a). It was noticed that the catalytic activity enhanced for (10-30 mol %) CeO₂-HfO₂ and later decreased due to better reducibility and higher oxygen vacancy formation for a lower concentration of Hf into CeO₂. In work reported by Patil et al., Nd was doped with CeO₂, and doping 1% Nd into CeO₂ showed comparatively better activity (Patil et al. 2019). It was reported that surface-active O₂ species (O⁻) and redox potential was high for 1% Nd-doped CeO₂ as detected by the XPS technique. The addition of transition / rare earth dopants to binary metal oxides has also been reported extensively, and the ternary catalyst showed a massive improvement in the catalytic activity comparatively. Table 2.2. summarizes the literature review on the soot oxidation activity of various Ce-based materials.

Table 2.2: Summary of Literature Review on Soot Oxidation Activity.

Material	Method	T₅₀ Temperature (°C)	Reference
CeO ₂	Co-Precipitation	560	Mukherjee et al. 2016
CeO ₂	Modified precipitation method	522	Reddy et al. 2008
CeO ₂	Nitrate precursor calcination	576	Krishna et al. 2007
CeO ₂	EDTA citrate method	530	Anantharaman et al. 2017
CeO ₂	Urea Solution Combustion Synthesis	451	Andana et al. 2016
CeO ₂	Glycine nitrate process	416	Patil et al. 2019
CZr & CPr	Modified co-precipitation method	513 438	Gode et al. 2012
Ce-Sm	co-precipitation method	455	Putla et al. 2014
Ce _{0.75} Zr _{0.25} O ₂ & Ce _{0.16} Zr _{0.84} O ₂	Co-precipitation method	530	Liang et al. 2006
Ce, Ce-Zr & Ce-Hf	Modified precipitation method	522 514 409	Reddy et al. 2008
La - Ce & Zr-Ce	Modified co-precipitation	441 461	Katta et al. 2010

Aneggi et al. studied the influence of Fe, Sm La, Pr, and Tb on Ce-Zr mixed oxides. 5 mol % Fe doped Ce-Zr exhibited lower T_{50} of 389°C due to high surface area (Aneggi et al. 2006). Atribak loaded Yttrium (Y) to Ce-Zr mixed binary oxides, enhancing oxygen vacancy formation with minimum loading and displaying better catalytic performance (Atribak 2009). Similarly, Hernández-Giménez et al. doped Nd to Ce-Zr mixed oxide, and the T_{50} evaluated was low (568°C) for the ternary metal oxides (Hernández-Giménez et al. 2013). In contrast, Ce- Zr and Ce- Nd showed 582 and 610°C, respectively Zr and Nd positively improved redox behavior. Rajvanshi et al. studied the effect of Ni addition to $Ce_{0.9}Pr_{0.1}O_2$ oxide catalysts synthesized by the solution combustion synthesis method, and it was noted that nickel doping positively affects the soot oxidation activity due to increased lattice strain and oxygen vacancies (Rajvanshi et al. 2020).

Apart from various characteristics, properties, and descriptors reported for enhancing the catalytic soot oxidation activity, there are pieces of literature reported on a shape-controlled nanomaterial, which improves the contact between soot and catalyst more efficiently. Chang et al. developed Ag-CeO₂ catalysts to demonstrate the influence of shape-dependent catalytic activity and oxygen vacancies (Chang et al. 2012). Ag-CeO₂ nano-rods and nanocubes were produced by conventional wetness impregnation. The results revealed that the interplay between O₂ vacancies and Ag-CeO₂ interaction depends on the shape of CeO₂ support. Ag can activate the surface lattice oxygen, generate more O₂ vacancies, and promote the reduction of CeO₂ (Chang et al. 2012). Zhang et al. revealed Ceria nano-rods synthesized by the hydrothermal method show better catalytic activity, for which the T_p (peak temperature of soot combustion) is about 500 °C (loose contact) and 368 °C (tight contact mode) (Zhang et al. 2016).

Aneggi et al. synthesized a series of conventional poly-crystalline ceria and single-crystalline ceria nano-rods and nano-cubes by hydrothermal method (Aneggi et al. 2014). The studies reported by Aneggi et al. reveal that the occurrence of more-reactive exposed surfaces positively affects the soot oxidation reaction, with an increase in activity in nano-shaped materials compared with conventional ceria nano-powder. The soot oxidation activity depends on the shape of the ceria nanoparticles, and in addition to the exposed surface, the activity is influenced mainly by the surface area (Aneggi et al. 2014).

Andana et al. studied the effect of the synthesis method for CeO₂ and Pr-doped CeO₂ catalyst for the soot oxidation reaction (Andana et al. 2018). The hydrothermal method and the SCS method were employed for the synthesis of the catalysts. The mixture of nanotubes and nano-rods was obtained by a hydrothermal method which shows better catalytic activity than nano-powder synthesized by SCS, as shown in **Figure 2.2**.

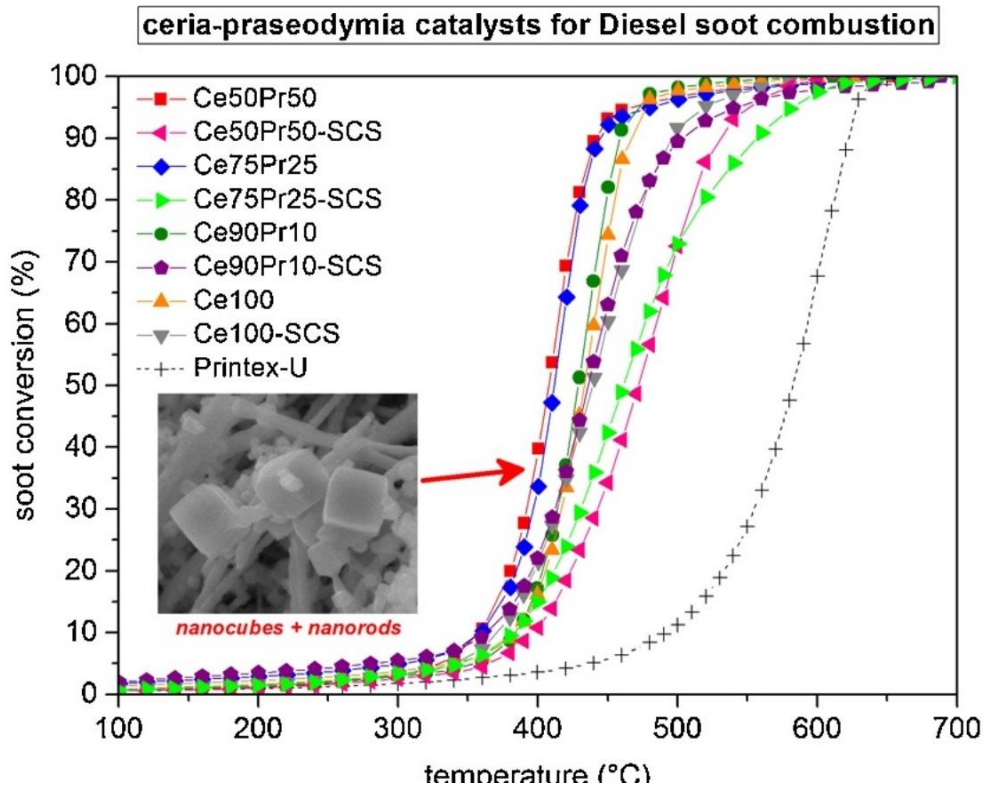


Figure 2.2: Soot oxidation activity of CeO₂ and Pr-doped CeO₂ catalysts (Andana et al. 2018)

Hence, a more shape-dependent catalyst is needed to improve the activity. Electrospinning is another method reported for synthesizing nanofibers (Uslu et al. 2012; Zhang et al. 2010b). Kumar et al. synthesized CeO₂ nanofibers and deposited them on SiC lab-scale and real diesel particulate filters (DPFs) to promote soot combustion (Kumar et al. 2012). The peak temperature (T_p) was in the range of 435-450°C.

Kumar et al. also performed studies on CeO₂ with various sodium hydroxide and citric acid mole ratios (0.3, 0.6, 0.8, and 1.0) and Co-CeO₂ nanofibers (1,5 and 10 wt%) for diesel soot oxidation by co-precipitation and ripening method (Kumar et al. 2012). The synthesized nanofibers improved soot conversion under loose (Tp 460-438°C) and tight contact conditions (Tp 398-410°C) for different CeO₂ nanofibers. Co-CeO₂ improved the soot combustion in the presence of 10% O₂, and the mobility of the O₂ species was enhanced as the cobalt loading was raised. The fibrous morphology can trap and convert soot to non-detrimental form at very low temperatures.

Bensaid et al. worked on fibrous CeO₂ catalysts for soot oxidation, and it was reported that the morphology affects the nature of soot–catalyst contact; it was also concluded that the nanofibers are one of the perfect morphologies for soot combustion as soot particles entrap well in a network of fibers (Bensaid et al. 2013). T₅₀ under various contact conditions were noted to be 372°C (tight), 426°C (prolonged loose), and 533°C (loose), respectively. To improve the soot-catalyst contact conditions and encourage soot combustion.

CeO₂-based catalysts were developed with modified shapes or morphologies for analyzing soot combustion reactions (Miceli et al. 2014). Nanofibers enhance soot and catalyst contact as the number of soot-catalyst contact points plays a significant role in solid-solid catalysis. Nanofibers were reported to trap soot particles at contact points due to their systematic arrangement in the DPF's channels. The T₅₀ for pure CeO₂ nanofibers for loose and tight contact was 555°C and 439°C, respectively. Ag-supported electrospun CeO₂ fibers were developed for soot oxidation (Lee et al. 2018). The diameters ranged from 241–253 nm, and the peak temperatures were reported in the range of 530-495°C (tight contact mode) and 690-468°C (loose contact mode).

The descriptors responsible for oxidation processes are defined by Grasselli (Grasselli, 2002; Vilé et al. 2016). The seven pillars or descriptors were postulated to describe metal oxides' activity and selectivity. The descriptors include host structure, lattice oxygen, metal-oxygen bond, multi-functionality of active sites, phase cooperation, redox ability, and site isolation (Grasselli, 2002; Vilé et al. 2016). The formation of oxygen vacancies or vacancy formation energy has been generally considered the primary descriptor for better reactivity (Farra et al. 2013). For CeO₂-based materials, multiple descriptors control the activity more than a single descriptor, relying on reaction conditions (Vilé et al. 2016, Anantharaman and Prasad, 2019; Patil et al. 2019). Few reporters described BET surface area as critical in enhancing the catalytic activity (Liang et al. 2007; Singhania, 2017).

On the other hand, Liu et al. 2016 reported that the catalyst activity is determined by the number of catalysts–soot contact points than the surface area of the catalyst, while the stability of the catalyst is closely related to the concentration of surface oxygen vacancies. In addition, the active oxygen species (O²⁻, O[·] and O₂²⁻) also play a critical role in determining the catalytic activity (Mukherjee et al. 2016; Patil et al. 2019; Wei et al. 2011). The active oxygen species are referred to as lattice, and surface-adsorbed oxygen species contribute to improving the soot oxidation process (Li et al. 2018). The defects on the surface produced by the oxygen vacancies enhance the active sites to aid the reactions (Malode et al. 2023). The compilation of T₅₀ temperature and experimental conditions of various Ce-based catalysts for soot oxidation activity is provided in **Table 2.3**.

Table 2.3: T₅₀ temperature and experimental conditions of various Ce-based catalysts for soot oxidation activity.

Catalyst	Synthesis method	T ₅₀ (°C)	Experimental conditions	References
Cu-Ce Cu ₅ -VCe Cu ₁₀ -VCe	Wet impregnation method	352 395 370	TGA, air (75 ml min ⁻¹) Heating rate (5 °C min ⁻¹) (Soot: Catalyst =2:8, tight contact)	(Cousin et al. 2007)
Ce Cu-Ce	Citric acid sol-gel method	335 321	Temperature Programmed Oxidation (TPO), 10% O ₂ , N ₂ (500 ml min ⁻¹) Heating rate (20°C min ⁻¹) (Soot: Catalyst =1:10, loose contact)	(Wu et al. 2007a)
CuO-CoO/Ce-Zr	Co-precipitation and impregnation method	363	TGA, air (60 ml min ⁻¹) Heating rate (10°C min ⁻¹) (Soot: Catalyst =1:4, tight contact)	(Reddy and Rao 2009a)
Cu-Ce Cu-CeO ₂ -K	Impregnation method	404 338	TPO, NO, 10% O ₂ , N ₂ (500 ml min ⁻¹) Heating rate (20°C min ⁻¹) (Soot: Catalyst =1:10, loose contact)	(Duan et al. 2010)
Cu-Ce 6-Ba-Cu-Ce 15-Ba-Cu-Ce	Citric acid sol-gel method	433 395 414	TPO, NO, 10% O ₂ , N ₂ (1000 ml min ⁻¹) Heating rate (20°C min ⁻¹) (Soot: Catalyst =1:10, loose contact)	(Lin et al. 2011a)

(Contd.)

Literature Review

Cu-Ce/ZrO ₂ Cu-Ce/SiO ₂ Cu-Ce/Al ₂ O ₃	Deposition-precipitation and wet impregnation	338 409 386	TGA, air (60 ml min ⁻¹) Heating rate (10°C min ⁻¹) (Soot: Catalyst =1:4, tight contact)	(Rao et al. 2011)
Ce _{0.8} Pr _{0.2} O _{2-δ} Ce _{0.75} Zr _{0.25} O _{2-δ}	Modified co-precipitation method	438 513	TGA, air (100 ml min ⁻¹) Heating rate (10°C min ⁻¹) (Soot: Catalyst =1:4, tight contact)	(Thrimurthulu et al. 2012)
5TiO ₂ /Ce-Gd	Deposition co-precipitation method	462	TGA, air (100 ml min ⁻¹) Heating rate (10°C min ⁻¹) (Soot: Catalyst =1:4, tight contact)	(Durgasri et al. 2014b)
Ce-Sm	Co-precipitation method	455	TGA, O ₂ (100 ml min ⁻¹) Heating rate (10°C min ⁻¹) (Soot: Catalyst =1:4, tight contact)	(Sudarsanam et al. 2014b)
Ce Ce _{0.8} Pr _{0.2} O _{2-δ} Ce _{0.8} Zr _{0.2} O _{2-δ} Ce _{0.8} Zr _{0.2} Pr _{0.2} O _{2-δ}	Hydrothermal process	451 457 469 444	Fluidized bed Quartz reactor, 50% air + 50% N ₂ , (100 ml min ⁻¹) Heating rate (5°C min ⁻¹) (Soot: Catalyst =1:9, tight contact)	(Andana et al. 2016)
Ce.Pr	Ammonia co-precipitation method	413	TGA, 10% O ₂ + 90%N ₂ (50 ml min ⁻¹) Heating rate (10°C min ⁻¹) (Soot: Catalyst =1:10, tight contact)	(Fan et al. 2017)

(Contd.)

Literature Review

$Ce_{0.9}Pr_{0.1}O_{2-\delta}$	Solid-phase grinding method	398	TGA, 10% O ₂ , 90%N ₂ (50 ml min ⁻¹) Heating rate (10°C min ⁻¹) (Soot: Catalyst =1:10, tight contact)	(Zhou et al. 2018)
$Ce_{0.9}Gd_{0.1}O_{2-\delta}$ $Ce_{0.9}Sm_{0.1}O_{2-\delta}$	EDTA-Citrate Method	468 480	TGA, air (100 ml min ⁻¹) Heating rate (10°C min ⁻¹) (Soot: Catalyst =1:10, tight contact)	(Anantharaman et al. 2018c)
$Cr_{0.05}Ce_{0.95}$	co-precipitation method	405	TGA, air (100 ml min ⁻¹) Heating rate (10°C min ⁻¹) (Soot: Catalyst =1:10, tight contact)	(Li et al. 2011)
$Cr_{0.1}Ce_{0.9}$	sol-gel method	435	TGA, air (100 ml min ⁻¹) Heating rate (10°C min ⁻¹) (Soot: Catalyst =1:10, tight contact)	(Neelapala and Dasari 2018a)
$Mn_{0.1}Ce_{0.9}$	sol-gel method	368	TPO, NO,10% O ₂ , N ₂ (1000 ml min ⁻¹) Heating rate (20°C min ⁻¹) (Soot: Catalyst =1:10, loose contact)	(Liang et al. 2008)
$Mn_{0.1}Ce_{0.9}$	co-precipitation method	475	TGA, air (100 ml min ⁻¹) Heating rate (5°C min ⁻¹) (Soot: Catalyst =1:4, tight contact)	(Muroyama et al. 2010)

(Contd.)

Study on the Effect of Transition Metal Dopants in Ceria Praseodymium Catalysts for Soot Oxidation Activity and its Kinetics

Literature Review

Mn _{0.1} Ce _{0.9}	impregnation method	415	TGA, O ₂ + N ₂ (100 ml min ⁻¹) Heating rate (20°C min ⁻¹) (Soot: Catalyst =1:10, loose contact)	(Wu et al. 2010)
Mn _{0.2} Ce _{0.8}	co-precipitation method	396	TGA, air (100 ml min ⁻¹) Heating rate (10°C min ⁻¹) (Soot: Catalyst =1:4, tight contact)	(Mukherjee et al. 2016)
Mn _{0.5} Ce _{0.5}	the citric acid complex method	385	TGA, O ₂ + N ₂ (100 ml min ⁻¹) Heating rate (15°C min ⁻¹) (Soot: Catalyst =1:4, tight contact)	(Huang et al. 2020)
CeO ₂ -ZrO ₂ -MnO _x	co-precipitation method	340	TGA, O ₂ + N ₂ (500 ml min ⁻¹) Heating rate (5°C min ⁻¹) (Soot: Catalyst =1:10, tight contact)	(Yao et al. 2020)
Fe _{0.1} Ce _{0.9}	co-precipitation method	513	TGA, air (100 ml min ⁻¹) Heating rate (10°C min ⁻¹) (Soot: Catalyst =1:4, tight contact)	(Mukherjee et al. 2016)
Co _{0.1} Ce _{0.9} Ba _{0.05} CoCe	impregnation method	468 420	TGA, O ₂ + N ₂ (100 ml min ⁻¹) Heating rate (20°C min ⁻¹) (Soot: Catalyst =1:10, loose contact)	(Wu et al. 2010)

2.3. KINETIC ANALYSIS

The mathematical representation of data obtained from the reaction usually includes the kinetic triplet. This kinetic triplet consists of the Arrhenius constant (A), Activation energy (E_a), and the reaction model. López-Fonseca et al. carried out a detailed kinetic study of soot combustion. This study gives a suitable path to evaluate kinetic triplets and lists the reaction models commonly used to represent solid-state reaction kinetics (López-Fonseca et al. 2007).

The work carried out by Lopez-Fonseca et al. confirms the utility of a composite kinetic processing technique based on the complementary use of both the isoconversional method and master-plot methods in ascribing the kinetic triplet of nonisothermal combustion of synthetic porous soot in the air by thermogravimetry method at different heating rates. The advantage of the methodology followed by Lopez-Fonseca et al. is that the activation energy can be obtained from an isoconversional method, and the approximate conversion model can be selected by the master-plot method.

The reaction rate depends on the conversion and is commonly described by the following equation (Vyazovkin et al. 2011).

$$\frac{d\alpha}{dT} = k(T)f(\alpha) \quad (2.1)$$

Where k(T) is the reaction rate constant (min⁻¹), and where f(α) is the reaction model, also called the conversion function, α is the extent of conversion. The general form of the rate equation governing soot oxidation can be expressed using the Arrhenius law.

$$\frac{d\alpha}{dT} = A \exp\left(\frac{-E_a}{RT}\right) f(\alpha) \quad (2.2)$$

Here, A is the pre-exponential factor, E_a is the activation energy, R is the universal gas constant, and T is the absolute temperature.

On integrating equation 2.2 we have:

$$g(\alpha) = \frac{AEa}{R\beta} p(x) \quad (2.3)$$

Where $g(\alpha)$ is the integral degradation model, $x = \frac{Ea}{RT}$ and $p(x)$ is the exponential integral with no analytical solution, to overcome the difficulty, exponential integral has been solved using various methods like series expansion, and approximation methods (Flynn, 1997).

Model-free methods are used to calculate E_a . and the kinetic parameters (E_a and A) depend on the values of conversion (α) and are typically obtained over the range of $0.2 < \alpha < 0.8$. The activation energy (E_a) is obtained by model-free methods such as Flynn-Wall- Ozawa and Kissinger Akhaira and Sunose (KAS) method as reported by (Ozawa 1992; Chandrasekaran et al. 2017 Rajvanshi 2020; Saikia et al. 2017; Shenoy et al. 2019). Employing the Flynn- Wall- Ozawa method (Ozawa 1992), the graph of $\log\beta$ vs. $1/T$ can be plotted. From its slope, E_a can be calculated. The expression for the Ozawa method is as follows.

$$\log\beta + 0.4567 \frac{Ea}{RT} = \text{constant} \quad (2.4)$$

Plotting the $\ln(\beta/T^2)$ vs. $1/T$ gives the E_a value from the slope. The expression for the KAS method is as follows.

$$\ln \frac{\beta}{T^2} = \ln\left(\frac{AEa}{Rg(\alpha)}\right) - \frac{Ea}{RT} \quad (2.5)$$

Equation (2.6) was expressed as integral value “m” if the soot oxidation reaction model follows the A_m model. In contrast, it is not possible for the geometrically contracting model. “m” is considered a non-integral exponent introduced to account for modifying the actual and idealized nucleation and nuclei growth models. When $m = 1$ in the A_m model corresponds to the first-order chemical reaction, $1.5 < m < 4$ corresponds to the nucleation and growth model (Avrami-Erofeev equation).

The following equation is deduced by assuming the “A_m” model and the E_a values obtained by the Ozawa method (López-Fonseca et al., 2007).

$$\ln \frac{\beta R}{E_a} - \ln p(x) = \ln(A) - \frac{1}{m} \ln[-\ln(1 - \alpha)] \quad (2.6)$$

A set of linear lines were observed by plotting $\ln \frac{\beta R}{E_a} - \ln p(x)$ v/s. $\ln[-\ln(1 - \alpha)]$, at various heating rates. The intercept and slope were used to calculate $\ln(A)$ and “m” values, respectively.

One of the most popular non-isothermal model-fitting methods is the Coats–Redfern (CR) method (Ebrahimi-Kahrizangi and Abbasi 2008; López-Fonseca et al. 2005; Saikia et al. 2017) which gives the best linear-fit to determine Arrhenius Factor (A) as well as E_a.

The coats-Redfern method is formalized and utilizes the asymptotic series expansion for p(x) (Ebrahimi-Kahrizangi and Abbasi, 2008). Plotting $\frac{g(\alpha)}{T^2}$ vs. 1/T assists in calculating E_a and A from the obtained slope and intercept, respectively.

The coats-Redfern method is formalized and utilizes the asymptotic series expansion for p(x), and the Equation is given below (Ebrahimi-Kahrizangi and Abbasi, 2008).

$$\ln \frac{g(\alpha)}{T^2} = \ln \left(\frac{AR}{\beta E_a} \left[1 - \frac{2RT}{E_a} \right] \right) - \frac{E_a}{RT} \quad (2.7)$$

Plotting $\frac{g(\alpha)}{T^2}$ vs. 1/T assists in calculating E_a and A from the obtained slope and intercept, respectively.

Literature Review

The master-plot approach compares theoretical master plots, obtained for a wide range of ideal kinetic models, with the experimental master plot (López-Fonseca et al. 2007). We get the following equations using a reference at point $\alpha=0.5$ (López-Fonseca et al. 2007).

$$g(0.5) = \frac{AE\alpha}{\beta R} p(x_{0.5}) \quad (2.8)$$

$$\frac{g(\alpha)}{g(0.5)} = \frac{p(x)}{p(x_{0.5})} \quad (2.9)$$

For a given α , the experimental value of $p(x)/p(x_{0.5})$ and theoretically calculated values of $g(\alpha)/g(0.5)$ are equivalent when an appropriate conversion model is used (López-Fonseca et al. 2007). Graphs of $g(\alpha)/g(0.5)$ and $p(x)/p(x_{0.5})$ are to be plotted for different values of conversion. The plots of $p(x)/p(x_{0.5})$, which coincide with $g(\alpha)/g(0.5)$, will give the approximate reaction model (López-Fonseca et al. 2007).

Table 2.4. lists the reaction models reported by López-Fonseca et al. commonly used to represent solid-state reactions (López-Fonseca et al. 2007). Diffusion is vital in solid-state reactions as it often occurs between crystal lattices. In diffusion processes, the conversion decreases with the thickness of the layer of the product. The one-dimensional (D_1) diffusion model is related to the rate equation for an infinite plate without any shape. The two-dimensional diffusion (D_2) suggests cylindrical particles are, and radial diffusion occurs through a cylindrical shell. The three-dimensional diffusion model (D_3) assumes spherical solid particles. The power-law models (P_1 , P_2 , and P_3) are where the assumed nucleation rate follows a power law, and the growth of nuclei is constant (Fedunik-Hofman and Bayon 2019). **Table 2.5** reports the T_{50} temperature, activation energy, and pre-exponential factor for soot and ceria-based catalysts. The kinetic analysis for the present study for the catalytic soot combustion will be followed according to López-Fonseca et al. (López-Fonseca et al. 2005, 2007).

Table 2.4: List of reaction models commonly used to represent solid-state reactions (López-Fonseca et al. 2007)

Reaction Model	Symbol	Differential kinetic function $f(\alpha)$	Integral kinetic function $g(\alpha)$
Nucleation and growth (Avrami- Erofeev equation)	A1.5	$1.5(1-\alpha)(-\ln(1-\alpha))^{1/1.5}$	$(-\ln(1-\alpha))^{1/1.5}$
Nucleation and growth (Avrami- Erofeev equation)	A2	$2(1-\alpha)(-\ln(1-\alpha))^{1/2}$	$(-\ln(1-\alpha))^{1/2}$
Nucleation and growth (Avrami-Erofeev equation)	A3	$3(1-\alpha)(-\ln(1-\alpha))^{1/3}$	$(-\ln(1-\alpha))^{1/3}$
Nucleation and growth (Avrami- Erofeev equation)	A4	$4(1-\alpha)(-\ln(1-\alpha))^{1/4}$	$(-\ln(1-\alpha))^{1/4}$
Phase boundary controlled reaction (contracting linear)	P1	1	α
Phase boundary controlled reaction (contracting area)	P2	$3(1-\alpha)^{2/3}$	$(1-(1-\alpha)^{1/2})$
Phase boundary controlled reaction (contracting volume)	P3	$2(1-\alpha)^{1/3}$	$(1-(1-\alpha)^{1/3})$
Ginstling-Brounshtein equation	D4	$(2/3)(1-\alpha)^{1/3}[1-(1-\alpha)^{1/3}]^{-1}$	$(1-2\alpha)-(1-\alpha)^{2/3}$
Chemical reaction (first-order)	R1, A1	$1-\alpha$	$(-\ln(1-\alpha))$
Chemical reaction (second-order)	R2	$(1-\alpha)^2$	$(1-\alpha)^{-1}-1$
Power law 1	L1	$4\alpha^{3/4}$	$\alpha^{1/4}$
Power law 2	L2	$3\alpha^{2/3}$	$\alpha^{1/3}$
Power law 3	L3	$2\alpha^{1/2}$	$\alpha^{1/2}$
Power law 4	L4	$(2/3)\alpha^{-1/2}$	$\alpha^{3/2}$
Zhuravlev equation	D5	$(2/3)(1-\alpha)^{5/3}[1-(1-\alpha)^{1/3}]^{-1}$	$[(1-\alpha)^{-1/3}-1]^2$

Table 2.5: T₅₀ temperature, Activation energy, and Pre-Exponential Factor for Soot and Ceria-based Catalysts

Catalyst	T ₅₀ / T _p (°C)	E _a (kJ mol ⁻¹)	A (min ⁻¹)	Reference
10 Ni – Ce – Pr	360	137	-	(Rajvanshi et al. 2020)
95CeO ₂ /5Soot	465	135	3.24× 10 ⁰²	(Zouaoui et al. 2012)
95CeO ₂ /5Soot (O ₂ +NO mixture)	450	59	4.92× 10 ⁰²	(Zouaoui et al. 2012)
Ni-CeO ₂	550	140	-	(Aberkane et al. 2019)
Printex-U+Al ₂ O ₃	582	135	6.70× 10 ⁰⁷	(Ganiger et al. 2022)
Printex-U	594	152	3.59× 10 ⁰⁸	(Ganiger et al. 2022)
Printex-U+SiO ₂	670	190	6.37× 10 ¹⁰	(Ganiger et al. 2022)
CeO ₂	380 465	58 (Nano-rods) 80 (Nanoparticles)	-	(Aneggi et al. 2014a)
5 Ag- Ce - Pr	427	150	-	(Govardhan et al. 2022)
Printex-U	610	175	4.5× 10 ¹⁴	(Nascimento et al. 2015)
CeO ₂ / Printex-U	451	79	3.78× 10 ⁰⁹	(Nascimento et al. 2015)
ZnO/Printex-U	575	104	5.88× 10 ¹⁰	(Nascimento et al. 2015)
ZnO:CeO ₂ /Printex-U (fresh)	420	54	1.14× 10 ⁰⁸	(Nascimento et al. 2015)
ZnO: CeO ₂ /Printex-U (reused)	436	81	2.04× 10 ¹⁰	(Nascimento et al. 2015)

2.4. CONCLUSIONS

From the literature review, the following inferences are obtained:

- Solution combustion synthesis plays a critical role in controlling powder characteristics. Glycine is better fuel for solution combustion synthesis when compared to other fuels like urea and citric acid, and the powder characteristics impact the catalytic activity.
- Transitional metal doping in Ce controls the physiochemical properties, which can control the catalytic activity.
- At least seven fundamental principles or descriptors (lattice oxygen, metal-oxygen bond strength, host structure, redox capability, multi-functionality of active sites, site isolation, and phase cooperation) govern the heterogeneous oxidation catalysis. Transitional metal doping in a ceria-based catalyst system can impact any or some of the seven pillars of selective oxidation catalysis.
- Ceria doped with praseodymium enhances the catalytic activity due to the presence of $\text{Pr}^{4+}/\text{Pr}^{3+}$ oxidation states apart from $\text{Ce}^{4+}/\text{Ce}^{3+}$ oxidation states.
- A detailed study on the impact of transitional metal doping in the Ceria-Praseodymium catalyst system is necessary, as observed from the preliminary literature search. The influence of transitional metal doping in the Ceria-Praseodymium catalyst system has not been fully explored for soot oxidation activity.
- Calculation of kinetic triplet using the model-free methods, master plot method, and model fitting method from non-isothermal thermo-gravimetric data for soot oxidation help the model to regenerate DPFs and determine the catalyst efficiency.
- Soot oxidation activity of the catalyst in the form of nano-powder or nanofibers can differ in their tendency due to the number of contact points between the soot and catalyst and the nature of the generated nanofibers.

Based on the above points from the literature survey, the present objectives of the thesis are framed. The objectives of the thesis address the scope of developing the transitional metal-doped Ceria-Praseodymium catalyst system and are presented in **Chapter 1**. The synthesis methods and characterization tools adopted for analyzing the catalysts and soot oxidation activity study experimental procedures and soot oxidation kinetic data procedures are discussed in detail and are outlined in the next chapter.

2.5. SCOPE OF WORK AND RESEARCH GAP

Increasing population and urbanization also lead to increased industries and motor vehicles. Stringent air quality standards for automobile industries have been considered to eliminate the massive amount of toxic gases. Automobile sectors in India are set to adopt Diesel Particulate Filter with Selective Catalytic Reduction technology as exhaust after-treatment techniques as per BS-VI. This technique reduces the emission of PM₁₀ and PM_{2.5} to acceptable levels. This technique also decreases the regeneration cost for DPFs. Catalysts developed in the recent decade have successfully reduced the soot combustion temperature.

However, there is still a need to replace costly noble metals susceptible to sulphur poisoning. CeO₂-based catalysts have been extensively studied over the past few decades due to their remarkable redox properties and OSC. Doping trivalent lanthanides and transition metals tend to improve catalytic behaviour by increasing O₂ vacancies. Few works on ternary metal oxides are carried out, which has also shown excellent improvement in activity compared to binary metal oxides.

The scope of the current work is to develop and characterize ternary CeO₂-based metal oxides with transition metals as dopants. The need for kinetic study for synthesized catalysts for soot oxidation becomes essential to understand the reaction path and to obtain the kinetic triplets. The kinetic studies on pure soot combustion are reported, but the literature reported is short for catalyst-aided soot combustion reactions. Research on shape-controlled catalysts also dramatically enhances the catalytic performance; nanofibers can trap soot particles and ensure better contact between soot and catalyst. Very little literature has been reported on using electrospun nanofibers for soot oxidation activity in India. Hence, the electrospinning technique will generate nanofibres to compare the synthesized ternary metal oxides for catalytic activity.

CHAPTER 3

MATERIALS AND METHODOLOGY

3.1. MATERIALS

$\text{Ce}(\text{NO}_3)_3 \cdot 6\text{H}_2\text{O}$ (Sigma–Aldrich $\geq 99\%$), $\text{Pr}(\text{NO}_3)_3 \cdot 6\text{H}_2\text{O}$ (Sigma–Aldrich $\geq 99\%$), $\text{Cr}(\text{NO}_3)_2 \cdot 9\text{H}_2\text{O}$, $\text{Mn}(\text{NO}_3)_2 \cdot 4\text{H}_2\text{O}$ (Sigma–Aldrich $\geq 97\%$), $\text{Fe}(\text{NO}_3)_2 \cdot 9\text{H}_2\text{O}$, (Sigma–Aldrich $\geq 99\%$), $\text{Co}(\text{NO}_3)_2 \cdot 6\text{H}_2\text{O}$ (Loba Chemie $\geq 98\%$), $\text{Cu}(\text{NO}_3)_2 \cdot 9\text{H}_2\text{O}$ (Sigma–Aldrich $\geq 98\%$) were used as a precursors. Ammonium niobate (V) oxalate hydrate ($\text{C}_4\text{H}_4\text{NNbO}_9 \cdot x\text{H}_2\text{O}$, Sigma–Aldrich 99.99%) was a precursor to synthesize Niobium oxides. Glycine (99.5%, SRL chemicals) and distilled water were used to synthesize the catalyst via the SCS method (Varma et al. 2016). Citric acid, Ethylene Diamine Tetra Acetic Acid (EDTA, SRL extra pure), Citric acid Monohydrate (SRL extra pure), and Ammonium hydroxide solution (25% Extra pure, Loba Chemie) was the chemical reagent used for the EDTA–Citrate method. Poly Vinyl Pyrrolidone (PVP, Sigma Aldrich 13,00,000 Mw.) was used as a polymer for the electrospinning technique. Printex U soot from Orion Engineered Carbons was used for soot oxidation.

3.2. SOLUTION COMBUSTION SYNTHESIS

The catalyst for the present study was synthesized using Solution Combustion Synthesis (SCS) and is shown in **Figure 3.1**. As per the stoichiometric ratio, the metal (Cr, Mn, Fe, Co, Cu, Ce, Pr) nitrates and fuel (Glycine) were dissolved well in distilled water. The Glycine to Nitrate mole ratio (G/N) was maintained at 0.35. For example, in the case of $\text{Cu}_{x(x=0.1)}(\text{Ce}_{0.9}\text{Pr}_{0.1})_{1-x}\text{O}_{2-\delta}$ (10 Cu-CP); 55.70 g of $\text{Ce}(\text{NO}_3)_3 \cdot 6\text{H}_2\text{O}$; 6.2 g of $\text{Pr}(\text{NO}_3)_3 \cdot 6\text{H}_2\text{O}$; 3.44 g of $\text{Cu}(\text{NO}_3)_2 \cdot 9\text{H}_2\text{O}$ were added to distilled water and well dissolved. Further, 11.98 g of Glycine was added to the same solution.

The solution will then be heated and stirred continuously at 70°C until it turns viscous gel. The gel is transferred to an oven-safe bowl and then kept in a preheated oven at 350°C, where the gel will auto-ignite automatically, and the voluminous product is formed. The obtained powder is calcined at 600 °C for 5 h to remove the impurities. The obtained catalysts were denoted by sample codes provided in **Table A2.1** in Appendix II.

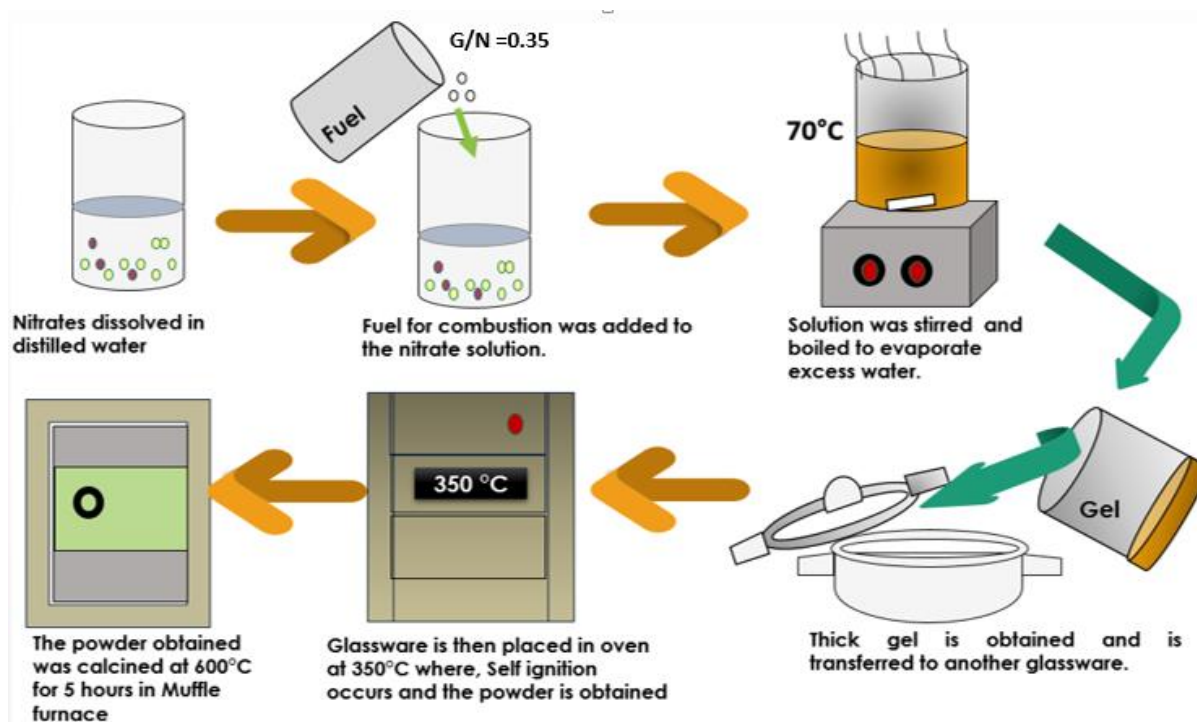


Figure 3.1: Solution Combustion Synthesis method.

3.3. EDTA CITRATE METHOD

CeO_2 , $\text{Ce}_{0.9}\text{Pr}_{0.1}\text{O}_{2-\delta}$ was synthesized using the EDTA citrate method (**Figure 3.2**) (Prasad et al. 2012; Anantharaman et al. 2017). A stoichiometric amount of corresponding metal (Ce and Pr) nitrate was dissolved in distilled water. To this metal nitrate solution, the calculated amount of citric acid is added where the pH of the solution drops. Further, EDTA was added to the same above solution under stirring conditions. The pH of the final solution was maintained at ~ 9 by adding NH_4OH solution along with heating and stirring. The mole ratio 1:1:1.5 for total metal nitrate to EDTA to citric acid was maintained.

Continuous heating of solution results in a thick gel, and further heating in an electric oven at $150\text{ }^\circ\text{C}/24\text{ h}$ produces a black precursor. The obtained solid precursor was undergone two-stage calcination at $300\text{ }^\circ\text{C}/12\text{h}$ and $600\text{ }^\circ\text{C}/5\text{h}$ in a muffle furnace to obtain pure nano-powder.

3.4. DIRECT CALCINATION METHOD

Ammonium Niobate (V) oxalate hydrate (Sigma–Aldrich 99.99%) was used as a precursor to synthesize Niobium oxides by direct calcination method. The resulting samples were manually mixed for different concentrations with CeO_2 using an agate mortar and pestle for 2h. The obtained samples were then calcined at $600^\circ\text{C}/5\text{h}$ to get a pure catalyst.

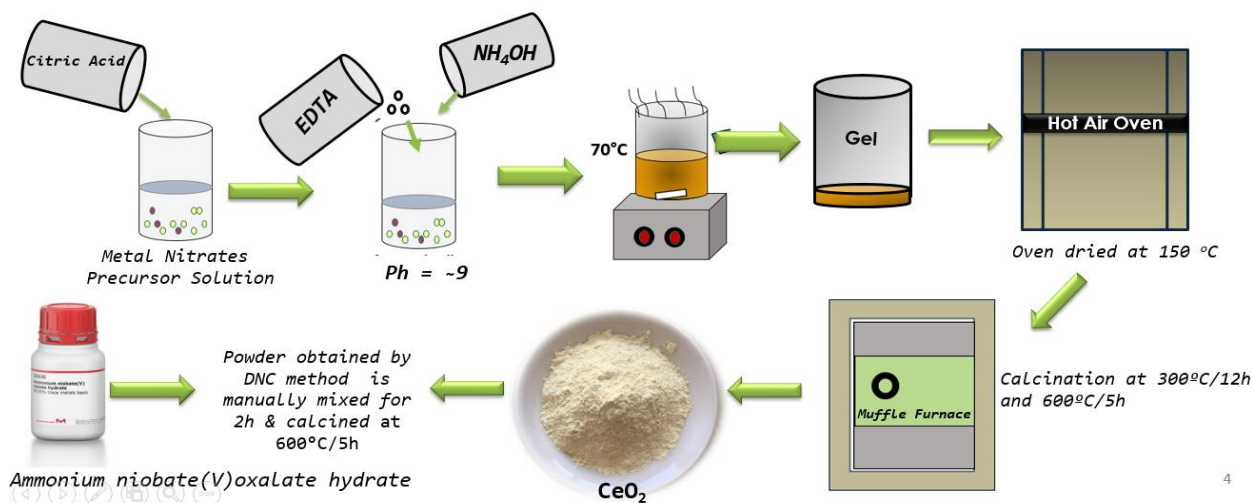


Figure 3.2: Preparation of Nb-doped Ceria by EDTA – Citrate complex and DNC method.

3.5. ELECTROSPINNING TECHNIQUE

Stoichiometric amounts of respective nitrates were used as precursors to synthesize the nanofibres via electrospinning (**Figure 3.3**) and are explained in three steps as follows.

Step 1. Preparation of spinning solution

Ethanol (15 ml) and distilled water (25 ml) were used to dissolve the metal nitrates. The solution was then stirred without heating to dissolve the nitrates. Poly Vinyl Pyrolidone (PVP, 13,00,000 Mw.) was then transferred into the above solution and kept for stirring for 12 h. The solution was then carefully transferred into a 25 ml syringe with a 5 mm dia. needle.

Step 2. Synthesis of nanofibers by electrospinning

The nanofibres were generated in an electrospinning unit (Holmarc-HO-NFES-043C, India). For electrospinning, the voltage was maintained at ~12 kV, and the flow rate of the spinning solution was kept at 700 μ l/h. The distance between the collecting drum and the needle tip was 8 cm.



Figure 3.3: Electrospinning technique to develop transition metal doped Ce-Pr catalysts

Step 3. Collection and calcination of the as-spun nanofibers

The collecting drum speed was maintained at ~ 600 RPM. The obtained as spun nanofibers after ~9 h were then calcined in a muffle furnace at 600 °C/ 5h at a 1 °C/min heating rate.

3.6. CHARACTERIZATION TECHNIQUES

3.6.1. X-Ray Diffraction

An incident X-ray beam meets the crystal lattice, the scattering occurs, and when the scattering of a specific direction is in phase with the scattered rays from other atomic planes, the diffraction occurs. The relation by which the diffraction occurs is known as Bragg's law. The XRD patterns were recorded in Malvern PAN analytical: Empyrean diffractometer (at CRF, NITK Surathkal) in the range of 10 to 80° 2 θ values using Copper (K α radiation; $\lambda=1.54$ Å). The XRD analysis was carried out to identify the crystalline phase, structure, and average crystallite size using Scherrer's equation (Uslu et al. 2012).



Figure 3.4: X-Ray Diffraction (XRD - Malvern PAN analytical: Empyrean)

3.6.2. FT-Raman Spectroscopy

The Raman effect follows when light imposes upon a molecule and interacts with the electron cloud of the bonds of that molecule. The incident photon then excites one of the electrons into a virtual state. FT-Raman spectra were recorded in LabRAM HR Horiba France with a 532 nm laser beam (at CRF, NITK Surathkal).



Figure 3.5: Compact Raman Spectrometer (Renishaw (UK)).

3.6.3. BET-BJH analysis

The most widely used technique for calculating the surface area of fine and porous materials is Brauner-Emmer Teller (BET) method. As per BET theory, N₂ adsorption on the surface is used to determine the surface area. The knowledge about the surface area of macroporous, mesoporous, nonporous solids, and isotherm types can be predicted. Barrett, Joyner, and Halenda's (BJH) method determines the pore size distribution (Thommes et al. 2015).

BET was used to compute specific surface area (S_{BET}) and was determined by Anton Paar- Autosorb iQ-XR-XR 195364 Quantachrome instruments (at CRF, NITK Surathkal).



Figure 3.6: BET and BJH analyser (Anton Paar- Autosorb iQ-XR-XR 195364 Quantachrome instruments)

3.6.4. Field Emission Scanning Electron Microscopy Analysis (FE-SEM)

Field Emission Scanning Electron Microscopy (FE- SEM) was conducted in Gemini SEM 300, Carl Zeiss AG (at CRF, NITK Surathkal). The scanning electron microscope analysis scans the image of the sample surface with a high-energy electron beam. The FE-SEM can obtain high-resolution / magnification images (up to $\times 300000$). SEM coupled with Energy Dispersive X-ray (EDAX) reveals the compositional analysis of the sample. FE-SEM is also the best technique for obtaining the diameter of nanofibers synthesized by the electrospinning technique.



**Figure 3.7: Field Emission Scanning Electron Microscopy (FE-SEM)
(Carl Zeiss-Gemini SEM 300)**

3.6.5. X-Ray Photoelectron Spectroscopy

X-ray photoelectron spectroscopy (**Figure. 3.8.**) is a chemical analysis technique to determine the elements' chemical oxidation, electronic states, and elemental composition on a material's surface (~up to 10 nm). Analysis was performed at room temperature, and the samples in the form of pellets were preserved under ultra-high vacuum conditions, typically less than 10^{-8} Pa. The binding energy of electrons from kinetic energy reflects surface elements' oxidation states. The intensity versus binding energy spectra is plotted, and the deconvoluted peaks are fit. Before the peak fit, the carbon peak correction (~284.3) is done, and the baseline is corrected. The area under the curves is utilized to obtain the reduced species and oxygen species ratios.



Figure 3.8: X-Ray Photoelectron Spectroscopy (Omicron ESCA+ - ultrahigh vacuum)

3.6.6. TGA-FTIR



Figure 3.9. TGA-FTIR (TGA 4000 and Spectrum 2 FT-IR Spectrometer, PerkinElmer, Singapore)

TGA hyphenated system with FTIR (**Figure 3.9**) is used to detect functional groups in gas-phase, IR analysis allows better understanding of the processes observed in the TGA. For oxidation reactions, it is possible to detect the evolution of the functional groups released for gases such as CO₂, CO, etc.

3.7. SOOT OXIDATION AND KINETIC STUDIES

Soot (Printex U, Orion) and catalyst are mixed using mortar and pestle for 30 min under tight contact conditions with a soot: catalyst weight ratio of 1:10. The oxidation reaction occurs in a TGA, and the air is used as a purge gas at a 100 ml/min flow rate. The heating rate for the oxidation reaction is maintained at 10 °C/min, and the heating rate is varied for kinetic studies at 5, 10, 15, and 20 °C/min. The reaction is carried out from room temperature to 600°C. Weight loss of soot with temperature difference is analyzed and converted in terms of conversion (%), and T_{50} is noted.



Figure 3.10: Thermo gravimetric Analyser (Exstar TG/DTA 6300)

The detailed kinetic analysis for soot combustion reactions is studied from the literature (López-Fonseca et al. 2007, Sharma et al. 2012, and Ganiger et al. 2022). The mathematical representation of data obtained from the reaction is usually the kinetic triplet (E_a , A , and the conversion reaction model). The list of equations used in the current study for estimating the kinetic parameters and plots is compiled in **Table 3.1** and the expressions are discussed in Chapter 2.

Materials and Methodology

Table 3.1. List of equations and methods used for kinetic studies.

SI No.	Method /Model/Equation	Equation	Plots	
			Y-axis	X-axis
1	FWO method	$\text{Log } \beta + 0.4567 \frac{Ea}{RT} = \text{constant}$	$\log \beta \text{ (K min}^{-1}\text{)}$	$1/T \text{ (K}^{-1}\text{)}$
2	KAS Method	$\ln \frac{\beta}{T^2} = \ln \left(\frac{AEa}{Rg(\alpha)} \right) - \frac{Ea}{RT}$	$\ln \frac{\beta}{T^2} \text{ (K/ min } \times \text{K}^2\text{)}$	$1/T \text{ (K}^{-1}\text{)}$
3	Master Plot method	$g(\alpha) = \frac{AEa}{\beta R} p(x)$ $\frac{g(\alpha)}{g(0.5)} = \frac{p(x)}{p(x_{0.5})}$ $p(x) = \frac{\exp(-x)}{x}$ $x = \frac{Ea}{RT}$ $p(x) = \frac{\exp(-x)}{x} \cdot \frac{(x^3 + 18x^2 + 86x + 96)}{(x^4 + 20x^3 + 120x^2 + 240x + 120)}$ (4 th Degree of approximation to the exponential integral function.)	$\frac{g(\alpha)}{g(0.5)}$	Conversion (α)
4	Am Model	$\ln \frac{\beta R}{Ea} - \ln p(x) = \ln A - \frac{1}{m} \ln [-\ln (1 - \alpha)]$	$\ln \frac{\beta R}{Ea} - \ln p(x)$	$\ln [-\ln(1 - \alpha)]$
5	CR Method	$\ln \frac{g(\alpha)}{T^2} = \ln \left(\frac{AEa}{R\beta} \left[1 - \frac{2RT}{Ea} \right] \right) - \frac{Ea}{RT}$ $g(\alpha) = (-\ln(1 - \alpha))^{1/m}$	$\ln \frac{g(\alpha)}{T^2}$	$1/T \text{ (K}^{-1}\text{)}$
6	Calculated conversion curves	Conversion = $1 - \exp(-g(\alpha)^m)$ $g(\alpha) = \frac{AEa}{\beta R} p(x)$	Conversion (α)	Temperature ($^{\circ}\text{C}$)
7	Arrhenius and Rate Equation	$k = A e^{-\frac{Ea}{RT}}$ $\frac{d\alpha}{dT} = k f(\alpha)$ $f(\alpha) = m(1 - \alpha)(-\ln(1 - \alpha))^{1/m}$	$\frac{d\alpha}{dT}$	Temperature ($^{\circ}\text{C}$)
			$\ln(k)$	$1/T \text{ (K}^{-1}\text{)}$

A Study on the Effect of Transition Metal Dopants in Ceria Praseodymium Catalysts for Soot Oxidation Activity and its Kinetics

The E_a value is obtained by isoconversional model-free methods such as Ozawa and KAS method (Ozawa, 1992, López-Fonseca et al. 2007). This method involves measuring the temperature (T), corresponding to the fixed conversion value, at different heating rates ($\beta = 5, 10, 15,$ and 20 K min^{-1}). The E_a value is obtained from the slope of the plots. If the E_a value shows no variation at different heating rates, a single-step reaction arises; otherwise, it leads to complex or multiple reactions (Ozawa, 1992).

The pre-Exponential Factor is determined by A_m method, wherein by assuming the A_m model and considering E_a value calculated by the Ozawa method, A set of linear lines is obtained in A_m plots, which A and m values can be attained from the intercept and slope respectively.

The reaction model for solid–gas reactions can be obtained using the master plot method. Master plots are referenced to the theoretical curves, dependent on the kinetic model but independent of kinetic parameters. From the master plot method, choosing a single model for solid–gas reactions is impossible; hence, the model-fitting method is used to select appropriate models. The reaction model with the best linear fit comparing the experimental with the calculated will provide the best suitable and ultimate solid–gas reaction mechanism (López-Fonseca et al., 2007). The Coats–Redfern (CR) integral method has been applied to several solid-state models to calculate the kinetic behavior. CR method for evaluating E_a and A values has been used in the kinetic study of thermal decomposition.

Comparing the experimental and calculated thermoanalytical curves at constant heating rates measures the adequate consistency of the kinetic triplets evaluated. The curves are reconstructed to confirm that the most suitable reaction model was selected at different heating rates.

CHAPTER 4

EFFECT OF NIOBIUM - DOPED CERIA ON SOOT OXIDATION ACTIVITY

Most metal-doped with CeO₂ reported in various works enhanced the catalytic activity significantly (Anantharaman et al. 2018a; Anantharaman 2018b; Devaiah et al. 2015; Patil and Dasari 2019a; Patil et al. 2019a; Reddy et al. 2008a; Shuang et al. 2015a; Vinodkumar et al. 2015). On the other hand, a few metal oxides doped with CeO₂ did not considerably reduce the temperature required for soot combustion compared to pure CeO₂ catalyst (Atribak 2009; Neelapala and Dasari 2018a).

In the case of CO oxidation activity conducted by Kim et al. 2017 on various metal oxide catalysts involving CeO₂ and rare earth metals doped CeO₂, pure CeO₂ performed better than the doped samples. They also interpreted that the ionic radius of the dopant used also plays a critical descriptor in enhancing the catalytic activity (Kim et al. 2017). CeO₂ doped with RE metals with different ionic radii results in differences in structure and properties.

Niobium (Nb) is known for its hydrophilic properties and high acid strength on the surface (Okuhara 2002). Niobium is used as a catalyst for various hydrolysis reactions (Pengpanich et al. 2005), NO_x reduction (Okuhara 2002), and soot oxidation in diesel exhaust (Braga et al. 2007; Pengpanich et al. 2005). The present chapter focuses on synthesizing and characterizing Niobium-doped Ceria oxides prepared by EDTA-DNC method and their effect on soot oxidation activity (Ce_{1-x}Nb_xO_{2-δ}: x = 0 to 0.30).

4.1. XRD ANALYSIS

XRD patterns for pure Ce and Nb-Ce series are displayed in **Figure 4.1 (a)**. The diffraction peaks correspond to the planes (111), (200), (220), (311), (222), (400), (331), and (422) of fluorite structure of CeO₂ for all Nb-doped Ce, and pure Ce samples (Salavati et al. 2009). The dominant diffraction peaks for planes [(001), (100), (101), (002), (110), (102), (201), and (112)] correspond to pure Nb samples. The peaks obtained match well with the orthorhombic structure of NbO, wherein oxygen surrounds Nb atoms in an octahedral form (Raba et al. 2016). It was noticed that the peaks related to Nb were not observed in the Nb-doped Ce samples. It can also be observed from **Figure 4.1 (b)** that the 2θ value slightly shifts towards a lower range with the increase of Nb content as the ionic radius of Nb (0.64Å) is lesser than that of Ce (1.01Å) (Shannon 1976).

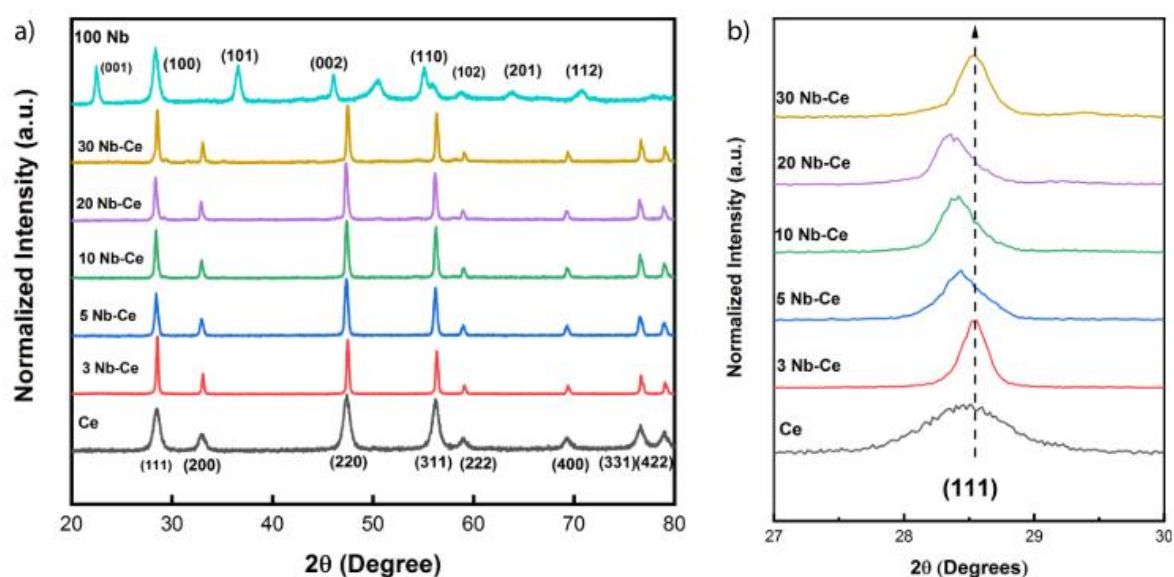


Figure 4.1: (a) XRD patterns (b) Enlarged (111) planes of Ce_{1-x}Nb_xO_{2-δ} (x = 0,0.03,0.05,0.1,0.2, 0.3) samples.

The physicochemical parameters are calculated from the XRD data and tabulated in **Table 4.1**. The average crystallite size obtained for Nb-Ce nanoparticles is calculated using the Debye Scherrer equation and is 24 to 42 nm. The crystallite size for pure Ce and pure Nb samples was 11nm and 16 nm, respectively.

The intensity ratio of reactive planes {110}/{111} was calculated for Ce and Nb-Ce samples and are tabulated in **Table 4.1**, along with lattice strain and BET surface area. The pure Ce sample had the highest facet ratio (1.30) and high lattice strain (~ 0.0108) compared to all Nb-doped samples. The pure Ce sample also attained the highest BET surface area (67m²/g) compared to other samples.

Table 4.1: Physicochemical properties and T₅₀ of Ce_{1-x}Nb_xO_{2-δ} (x = 0,0.03,0.05,0.1,0.2, 0.3 and 1).

Sample code	Crystallite size D_{XRD} (nm)	Lattice strain (ε)	Facet ratio {110/111}	BET Surface area S_A (m²/g)	T₅₀ (°C)
Ce	11	0.0108	1.30	67	388
3Nb-Ce	42	0.003	0.98	51	557
5Nb-Ce	24	0.0052	1.07	45	545
10Nb-Ce	30	0.004	1.02	44	554
20Nb-Ce	32	0.003	1.07	36	552
30Nb-Ce	37	0.003	1.03	40	541
100Nb	16	0.009	-	31	543

4.2. RAMAN SPECTROSCOPY ANALYSIS

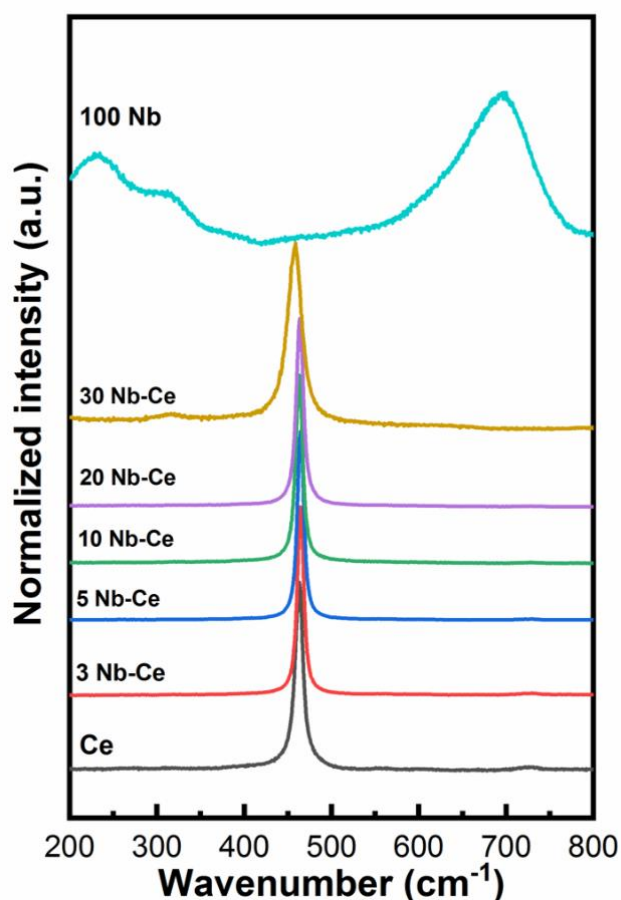


Figure 4.2: Raman Spectra of Ce_{1-x}Nb_xO_{2-δ} (x = 0, 0.03, 0.05, 0.1, 0.2, 0.3 and 1)

Figure 4.2 demonstrates the Raman spectra for Ce and Nb-Ce series. The most intense peak, the F_{2g} peak, is located at about 460 cm⁻¹ and ascribed to the symmetric stretch mode of the O-Ce-O and is a typical characteristic of the fluorite lattice structure of CeO₂ (Durgasri et al. 2014a; Shajahan et al. 2018).

All the Ce samples doped with Nb displayed the presence of the characteristic F_{2g} peak. No additional peaks or peaks corresponding to oxygen vacancies in the samples were noticed (Shajahan et al. 2018). It is challenging to detect O_2 Vacancy peaks when the high-intensity laser wavelength is used. The peak shift is evident towards the lower wavenumber on introducing Nb into the CeO_2 lattice (Bhabu et al. 2016).

The additional peak can be seen between 200 and 400 cm^{-1} for the 30 Nb and pure Nb samples; hence, a solid solution is formed. Cao et al. 2013 (Cao et al. 2013a) reported that NbO does not have any Raman-active modes (Cao et al. 2013a), and NbO bending modes intensities were observed between $600\text{-}700\text{ cm}^{-1}$ (Cao et al. 2013a). Kreissl et al. 2017 (Kreissl et al. 2017) also reported peaks between 200 cm^{-1} and 400 cm^{-1} , 400 cm^{-1} , and 760 cm^{-1} , corresponding to stretching modes of intermediate bonds corresponding to Nb–O.

4.3. SEM ANALYSIS

SEM analysis is performed to recognize the structural morphology of the synthesized samples. The SEM images of pure Ce and Nb-doped models are displayed in **Figure 4.3**. From the SEM images, it can be observed that the particles are agglomerated. The Nb-doped samples' morphology looks similar, slightly different from the pure Ce sample. It can also be witnessed from the SEM micrographs that the particle size of pure Ce and Nb samples is lesser than that of doped samples.

Effect of Niobium-Doped Ceria on Soot Oxidation Activity

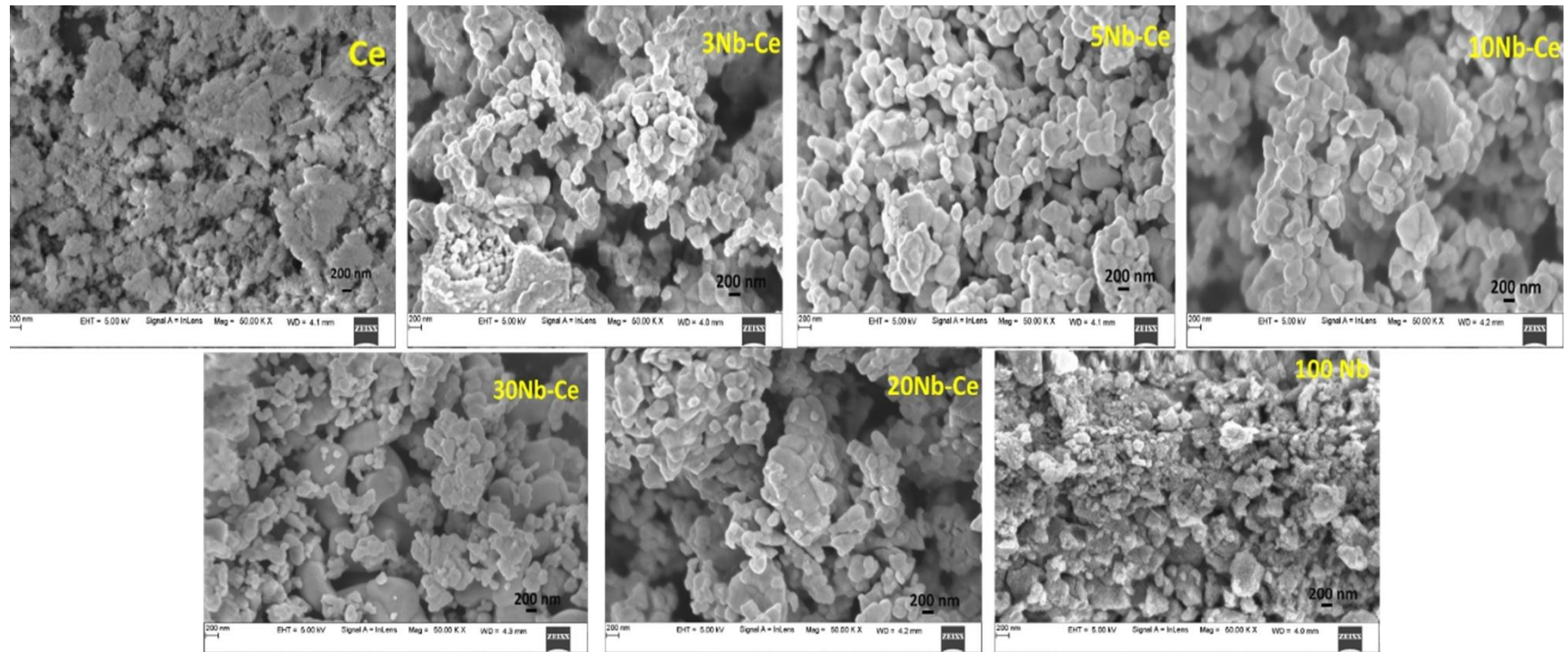


Figure 4.3: SEM micrographs of Ce_{1-x}Nb_xO_{2-δ} (x = 0,0.03,0.05,0.1,0.2, 0.3 and 1)

A Study on the Effect of Transition Metal Dopants in Ceria Praseodymium Catalysts for Soot Oxidation Activity and its Kinetics

4.4. SOOT OXIDATION ACTIVITY

Soot conversion to temperature increase is plotted and presented in **Figure 4.4**. It can be noticed that the addition of Nb did not significantly impact the catalytic activity. A significant drop in T_{50} temperature was observed for the pure Ce sample (388°C), and then there was a difference of 153 °C for the next T_{50} value, which was obtained for 30 Nb (541°C), followed by the pure Nb sample (543°C). 3Nb showed the highest T_{50} of 557°C, which has a ΔT of 30-38°C when compared with uncatalyzed sample /soot (~600°C) (Anantharaman et al. 2017; Rajvanshi et al. 2020; Shenoy et al. 2019).

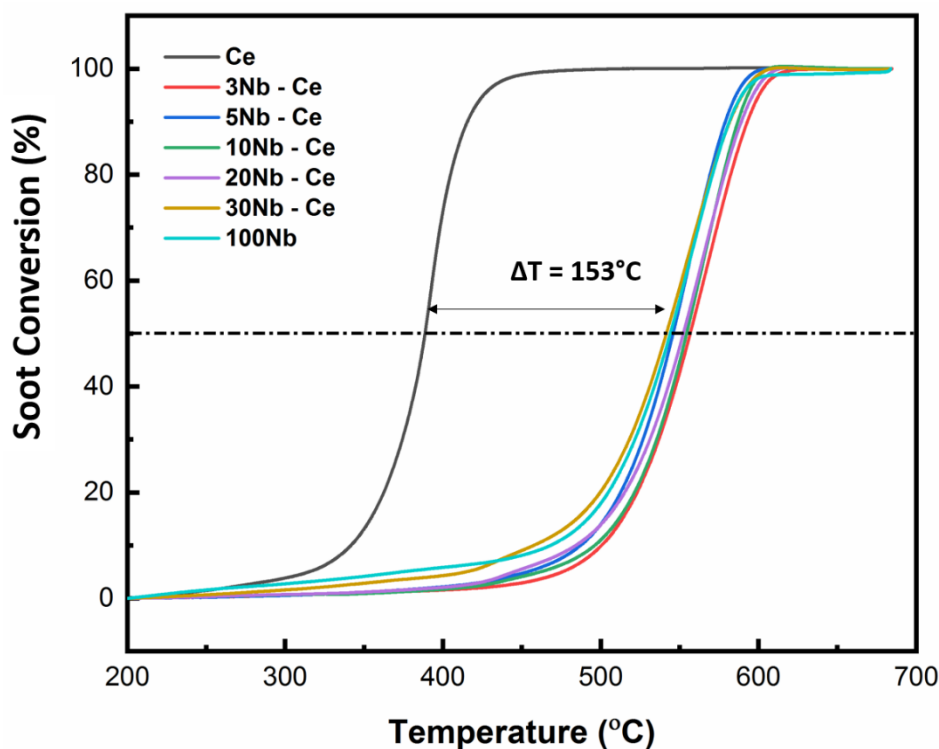


Figure 4.4: Soot Oxidation Activity of $Ce_{1-x}Nb_xO_{2-\delta}$ ($x = 0, 0.03, 0.05, 0.1, 0.2, 0.3$ and 1)

To further obtain the activation energy (E_a) for the synthesized samples, Ozawa and KAS plots were plotted for pure Ce and pure Nb along with 10 and 30 Nb-doped Ceria samples at various soot conversions ($\alpha = 0.1$ to 0.9). The conversion v/s temperature plot of 10 Nb-Ce at different heating rates ($\beta=5,10,15,20$ K min⁻¹) is provided in **Appendix III** for reference. The Ozawa and KAS plots are depicted in **Appendix IV (Figure A4.1 and A4.2)**, respectively. Ozawa and KAS plots demonstrate straight and parallel lines at the same degree of soot conversion, and the E_a is obtained from the slope at each conversion. The mean E_a value is considered for the comparison and tabulated in **Table 4.2**. The E_a values (**Table 4.2**) obtained by both Ozawa and KAS methods were also noted to be low for pure Ce samples, which may be one of the reasons for better catalytic activity.

Table.4.2: Activation energies obtained for (Ce_{1-x}Nb_xO_{2- δ} : x = 0,0.1,0.3,1) by both Ozawa and KAS methods.

Sample Name	T ₅₀ (°C)	Ozawa Method Activation Energy E_a (kJ/mol)	KAS Method Activation Energy E_a (kJ/mol)
Ce	388	125	120
10 Nb-Ce	554	151	145
30 Nb-Ce	543	145	140
100Nb	541	138	130
Soot	595	149-168 (Shenoy et al. 2019)	

The substitution of metal ions with higher valency is generally used as a sintering aid to encourage densification (Keck and Wilcox, 1980). Hence, Nb possessing higher valency than CeO₂ affects its properties and morphology and aids in sintering. SEM analysis shows that the particle size varies when Nb is doped and involves rapid sintering (Keck and Wilcox, 1980).

The sintering process usually supports the deactivation of catalysts as it strongly affects the active sites and surface area. Thus S_A of the doped samples is also decreased compared to undoped samples even though it has a lower ionic radius than Ce. Ramírez-Cabrera et al. 2003 also reported the inhibitory effect of Nb-doped Ce on direct reaction with methane and steam reforming.

Based on their XPS results, it was reported that the segregation of Nb to the CeO_2 surface inhibits the reaction with methane. Catalysts can be altered by lowering crystallite size, high lattice strain, higher S_A values, and less E_a to enhance catalytic activity (Ahn et al. 2012; Reddy et al. 2008b). Here, Nb-doped samples possess a larger crystallite size, lower lattice strain value, lower S_A values, and higher E_a than pure Ce samples. The pure Ce sample exhibits a lower E_a value than all the doped Nb samples. It can be clearly understood from the present study that doping Nb into Ce is not beneficial as the catalyst material for soot oxidation activity.

Further, the conversion v/s temperature plot of $Ce_{0.9}Pr_{0.1}O_{2-\delta}$ synthesized by the EDTA citrate and SCS methods is displayed in **Figure A3.2** in Appendix III. It was noticed that $Ce_{0.9}Pr_{0.1}O_{2-\delta}$ synthesized by the EDTA citrate method showed higher T_{50} of 423 °C than that of $Ce_{0.9}Pr_{0.1}O_{2-\delta}$ synthesized by the SCS method (T_{50} of 408 °C). Hence, the SCS method was adopted for further studies to study the effect of transition metals on the Ce-Pr catalyst system.

4.5. CONCLUSIONS

Pure Ce and Nb-doped Ce series were successfully synthesized and characterized to study soot oxidation activity. From the XRD patterns, the fluorite structure of CeO₂ was retained for all the doped samples, confirming the solid solutions' formation. Nb peaks were noticed only in the pure Nb sample, ensuring no impurities were present. The T₅₀ temperature of the pure Ce sample was 388°C which was 153°C lesser than the T₅₀ temperature of the doped samples. Nb did not help improve catalytic activity compared to the pure Ce sample. Hence, fine-tuning of the catalyst can be altered by descriptors such as lowering crystallite size, high lattice strain, and higher surface area.

It can be observed from the results that the Niobium doped Ceria showed a negative effect on soot oxidation activity, and Praseodymium doped Ceria showed a positive impact on soot oxidation activity. In Nb-doped Ce, Nb acts as sintering aid that increases the crystallite size and decreases the surface area, lattice strain, and facet ratio. Catalysts acquiring a smaller crystallite size, high lattice strain, and high surface area may enhance the soot oxidation activity, as in the Praseodymium-doped Ceria catalyst system. In the following chapters, Praseodymium doped Ceria is taken as the base catalyst system, and transitional metal doping is done using the solution combustion synthesis method.

The next chapter explores Copper doping in Ceria-Praseodymium catalysts obtained by solution combustion synthesis and tested for soot oxidation activity and the kinetics thereof apart from the characterization using X-Ray Diffraction, Raman spectroscopy, BET and BJH analysis, FE-SEM, X-ray Photoelectron Spectroscopy. The results obtained are discussed in detail and are outlined in the next chapter.

CHAPTER 5

EFFECT OF COPPER - DOPED CERIA - PRASEODYMIUM CATALYSTS FOR SOOT OXIDATION ACTIVITY AND ITS KINETICS

Metals with multivalent cations have increased Oxygen Storage Capacity (OSC) and tremendous redox potential due to the high movement of an anion vacancy (Anantharaman et al. 2017; Lykaki et al. 2017; Piumetti et al. 2016). Multivalent cations also have immense potential to lower the temperature required for the combustion of soot (Dulgheru and Sullivan 2013; Patil and Dasari 2019; Wang et al. 2004). It is also known that the transfer of Oxygen (O₂) onto the solid-solid contact plays a vital role in soot oxidation (Deng et al. 2017; Krishna et al. 2007; Shuang et al. 2015).

Rare-earth-dopants such as Lanthanum (La) (Katta et al. 2010a), Praseodymium (Pr) (Andana et al. 2016; Krishna et al. 2007; Reddy et al. 2009), Gadolinium (Gd) (Anantharaman et al. 2018; Durgasri et al. 2014), Samarium (Sm) (Anantharaman et al. 2018; Sudarsanam et al. 2014), Neodymium (Nd) (Patil et al. 2019), have shown excellent performance for soot oxidation activity. The reports show an evident reduction in temperature for soot oxidation compared to uncatalyzed, undoped/pure CeO₂ (Mukherjee et al. 2016).

Ce-Pr has also demonstrated tremendous catalytic activity among the rare-earth materials reported in most works (Andana et al. 2016; Krishna et al. 2007b; Reddy et al. 2009b). The multivalent Pr cation (Pr³⁺/Pr⁴⁺) increases the redox potential of Pr₆O₁₁ due to the high mobility of anion vacancy (Andana et al. 2016; Krishna et al. 2007b). Developing catalysts that enhance the contact between soot and catalyst and possess active O₂ Species becomes necessary. Oxygen vacancies facilitate the diffusion of lattice oxygen from the bulk to the surface by adsorption-desorption reactions (Deng et al. 2017; Katta et al. 2010; Krishna et al. 2007b; Reddy et al. 2008b).

Ternary metal oxides also increase the catalytic activity further. Transition metals /Lanthanides, when doped or loaded onto Ce-based binary metal oxides, successfully reduced the soot combustion temperatures to a greater extent (Lin et al. 2011a; Patil et al. 2019; Reddy and Rao 2009b; Wu et al. 2010). The bimetallic CuO–CoO/CeZr catalyst developed by Reddy and Rao 2009a displayed the best catalytic activity with $T_{50} = 363$ °C. The high activity of the CuO–CoO/CeZr solid solution-catalyst was due to the formation of oxygen vacancies, crystallite size, and specific surface area. Barium (Ba)-Cu-Ce catalysts developed by the impregnation method also displayed better catalytic activity for soot oxidation (Lin et al. 2011b). The CuO-CeO₂ catalysts were also prepared using co-precipitation and citric acid combustion synthesis methods. It was reported that Cu enhanced NO_x consumption by increasing the oxidation ability of CeO₂ (Lin et al. 2011b).

Mathematical description of particulates' combustion focused on describing kinetic triplets. Arrhenius parameters such as Pre-exponential factor (A), Activation energy (E_a), and the reaction models are combinedly known as kinetic triplets (Chrissafis 2009; López-Fonseca et al. 2007). Kinetic evaluations are carried out via Thermo Gravimetric Analysis (TGA) for heterogeneous solid-gas reactions (Chrissafis 2009). Model-free methods such as Flynn-Wall-Ozawa (FWO) approach and Kissinger Akahira Sunose (KAS) method are considered to be the most reliable for calculating E_a values (Li et al. 2019; Vyazovkin 2020). The most appropriate reaction model is estimated by the master plot method (Tighe et al. 2016). This method fits the obtained experimental data to the kinetic theoretic models. The other most popular non-isothermal model-fitting method is the Coats–Redfern (CR) method (Ebrahimi-Kahrizangi and Abbasi 2008; López-Fonseca et al. 2007; Saikia et al. 2017), which gives the best linear fitting to determine Arrhenius Factor (A) and E_a .

The present chapter focuses on studying the effect of Cu on Ce-Pr catalysts synthesized by the SCS method for soot oxidation activity. Solid-state reaction kinetic analysis is performed to obtain the kinetic triplets (E_a , A , and the Reaction model).

5.1. X-RAY DIFFRACTION (XRD) ANALYSIS

Figure.5.1a displays the X-Ray diffractograms for all the samples synthesized by SCS calcined at 600 °C/5h. Ce, Pr, and all other doped samples showed a similar trend for cubic fluorite structure with the presence of the (111), (200), (220), (311), and (222) planes (Patil et al. 2019; Prasad et al. 2008; Shajahan et al. 2018). CuO displayed a monoclinic structure with prominent peaks at $2\theta \sim 35.6$ and 38.8 (Meghana and Kabra 2015). From **Figure.5.1b**, it can also be observed that the minor shift towards the lower 2θ value from the peak position of (111) is probably due to Pr^{3+} (1.12 Å), whose ionic radius is more prominent than that of Ce^{4+} (0.97 Å).

From **Figure. 5.1c**, it can be illustrated that the characteristic Cu peaks were visible only for 15 Cu-CP and 20 Cu-CP samples indicating secondary phase formation as the concentration of Cu increased. **Table 5.1** demonstrates the physicochemical properties obtained by XRD analysis for all the samples. The crystallite size calculated from the Scherer equation is in the range of 12 to 21 nm. Pure Pr displayed a smaller crystallite size, and Pure Ce had the largest. The 20 Cu-CP sample acquired the highest lattice strain (0.0121), whereas Pure Ce showed the strain (0.0071). The interplanar distance and lattice constant were similar for Pure Pr, Pure Ce, and other doped samples. Pure Cu had a lattice constant of 5.05 and an interplanar distance of 2.526 Å.

Facet ratios $\{100\}/\{111\}$ and $\{110\}/\{111\}$ for the reactive planes are calculated for all the samples (except pure Cu) and are tabulated in **Table 5.1**. A higher intensity ratio for reactive planes was obtained for the 5 Cu-CP samples. The reactive planes are primarily responsible for enhancing the energy required for oxygen vacancy formation (Aneggi et al. 2012).

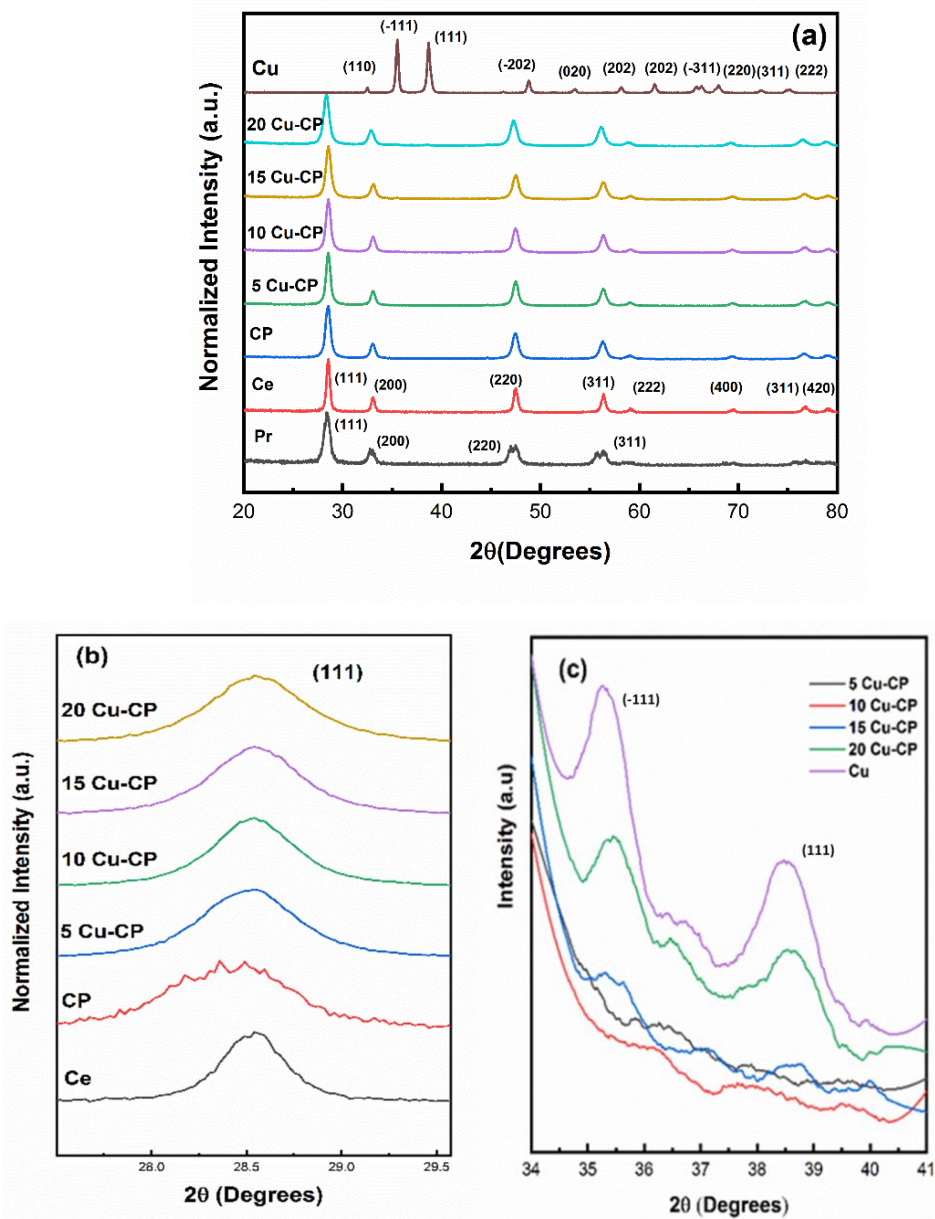


Figure 5.1: (a) XRD spectra (b) Enlarged view of the (111) plane (c) Enlarged view of the (-111) and (111) of CuO planes in Pure Cu, and $\text{Cu}_{x(x=0-0.2)}(\text{Ce}_{0.9}\text{Pr}_{0.1})\text{O}_{2-\delta}$. Catalysts

Table 5.1: Physicochemical properties of Pure Ce, Pr, Cu, and $\text{Cu}_{x(x=0-0.2)}(\text{Ce}_{0.9}\text{Pr}_{0.1})\text{O}_{2-\delta}$ obtained from XRD, Raman spectroscopy, and BET analysis.

Catalyst	Crystallite Size (nm)	Lattice strain (ϵ)	Interplanar distance (\AA)	Lattice Constant	Facet Ratio		I_{F2g}/I_{Ov}	BET S_A m^2/g	Avg. Pore Size (nm)	Pore volume (cc/g)
					{110}/{111}	{100}/{111}				
Ce	21	0.0071	3.146	5.44	0.27	0.48	-	27	07.61	0.102
Pr	12	0.0132	3.139	5.44	-	-	-	61	19.03	0.575
Cu	26	0.0046	2.526	5.05	-	-	-	25	10.00	0.012
CP	14	0.0107	3.128	5.41	0.24	0.38	0.77	31	11.46	0.091
5 Cu-CP	15	0.0094	3.127	5.41	0.30	0.50	0.77	23	05.89	0.067
10 Cu-CP	15	0.0101	3.124	5.41	0.24	0.44	0.75	21	06.05	0.063
15 Cu-CP	13	0.0113	3.123	5.41	0.25	0.40	0.80	17	04.87	0.041
20 Cu-CP	13	0.0121	3.122	5.40	0.24	0.43	0.51	21	05.77	0.064

5.2. RAMAN SPECTROSCOPY ANALYSIS

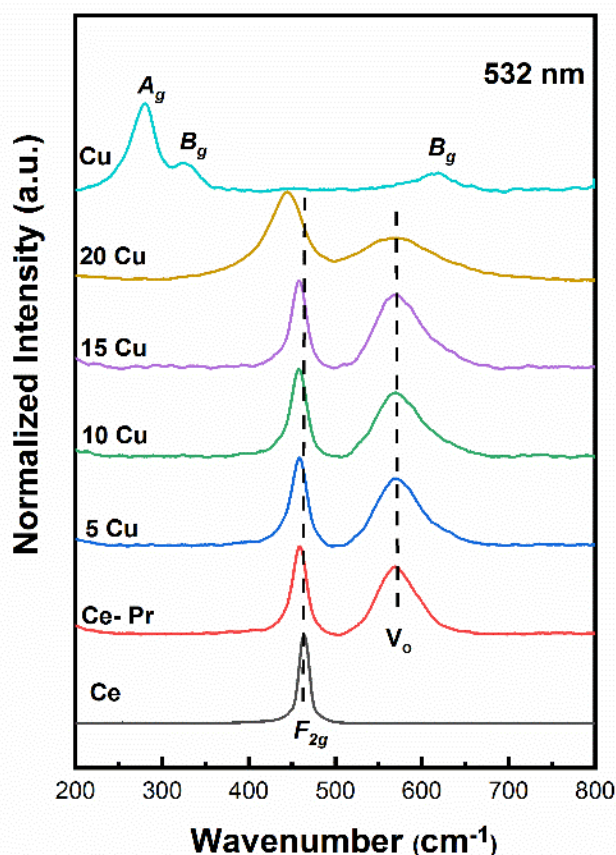


Figure 5.2: Raman Spectra of Pure Ce, Cu, and Cu_{x(x=0-0.2)}(Ce_{0.9}Pr_{0.1})_{1-x}O_{2-δ} Catalysts.

Raman Spectra of Pure Ce, Cu, and Cu_{x(x=0-0.2)}(Ce_{0.9}Pr_{0.1})_{1-x}O_{2-δ} samples are depicted in **Figure 5.2**. The frequency band at ~462 cm⁻¹ is associated with the "F_{2g}" Raman active mode for fluorite type lattice with symmetric breathing mode of O₂ around the Ce ions (O-Ce-O) (Prasad et al. 2008; Shajahan et al. 2018). The characteristic Ce peak position shift can be observed towards a lower wavenumber for doped samples. This may be due to a change in the chemical bond length of molecules with larger dopant sizes than that of the host ion (Vinod Kumar et al. 2018).

The band obtained at 560 cm^{-1} is attributed to the oxygen vacancies (Shajahan et al. 2018) created absent in the pure Ce and Cu. Pure Cu peaked at $\sim 298\text{ cm}^{-1}$, which may be allocated to the "A_g" mode (Chrzanowski et al. 1989). CuO peaks corresponding to the "B_g" modes were observed at ~ 330 and 617 cm^{-1} (Chrzanowski et al. 1989). No additional peaks related to Cu were noticed in the Raman spectra for the doped samples. The ratio of the intensity of Oxygen vacancy to that of the characteristic F_{2g} peak (I_{Ov}/I_{F2g}) was calculated and reported in **Table 5.1**. It was observed that the ratio was almost similar for CP and Cu-doped CP catalysts except for 20 Cu-CP, where the intensity ratio decreased.

5.3. BET-BJH ANALYSIS

Figure 5.3a shows the N₂ adsorption and desorption isotherms (at 77K) of Pure Ce, Cu, and Cu_{x(x=0-0.2)}(Ce_{0.9}Pr_{0.1})_{1-x}O_{2-δ} samples. **Figure. 5.3b** shows the pore size distribution of the respective catalysts. The effect of catalyst modification with the same preparation method on the surface area, the average pore diameter, and total pore volume are shown in **Table 5.1**. From **Figure. 5.3a**, as per the classification of IUPAC, the N₂ adsorption and desorption isotherms in the samples displayed irreversible type IV adsorption isotherms (characteristic of capillary condensation in mesopores (Mandal et al. 2015), indicating the presence of mesopores which might be originated from the inner aggregation of nanoparticles (Venkataswamy et al. 2016a). The non-limiting adsorption at high P/P₀ is the characteristic feature of the H3 hysteresis loop, which implies split-like pore structures of all the samples except in the pure Cu sample (which followed the H4 hysteresis loop).

From **Figure.5.3a**, it can also be noted that the isotherms indicate the presence of interparticle mesopores (Mandal et al. 2015) as adsorption (and hysteresis formation) occurs up to very high P/P₀ (>0.9) and the pore size distribution (**Figure. 5.3b**) reflects the same.

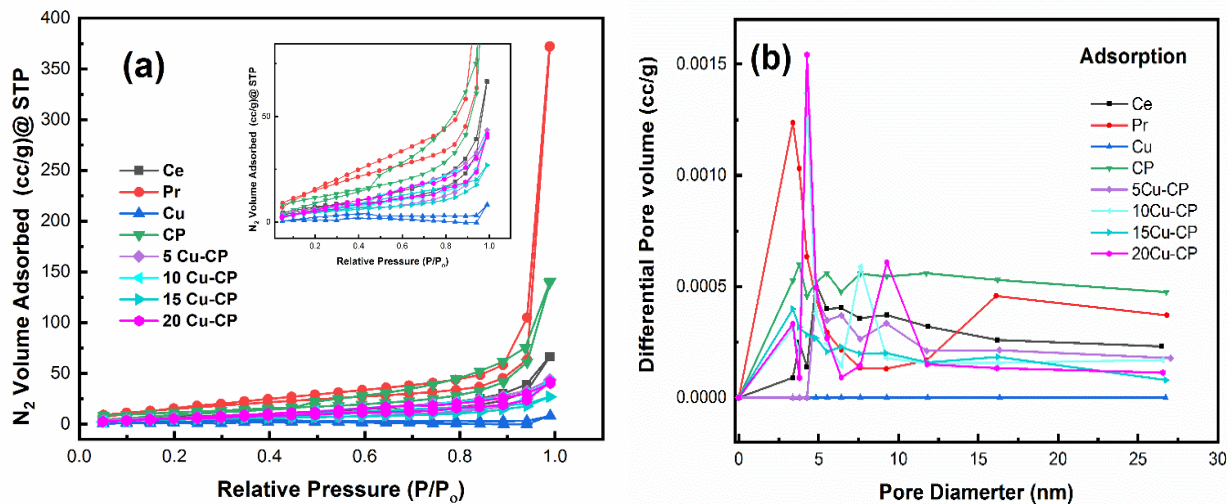


Figure. 5.3: (a) N_2 adsorption-desorption isotherm (b) Pore size distribution of Pure Ce, Pr, Cu, and $Cu_{x(x=0-0.2)}(Ce_{0.9}Pr_{0.1})_{1-x}O_{2-\delta}$ Catalysts

The pore size distribution during adsorption is provided in **Figure. 5.3b**. As can also be seen from **Table 5.1**, the average pore size distribution is in the range of 4 to 19 nm, and total pore volume is in the range of 0.012 to 0.217 cc/g, and the BET surface area is in the range of 17 to 61 m²/g. With the addition of Pr in Ce (CP system), there is an increase in average pore size, total pore volume, and BET surface area. With the further addition of Cu to CP (Cu-CP system), there is a decrease in average pore size, total pore volume, and BET surface area.

5.4. FE-SEM analysis

Figure. 5.4 reveals the FE-SEM images of pure Ce, Pr, Cu, and $\text{Cu}_{x(x=0-0.2)}(\text{Ce}_{0.9}\text{Pr}_{0.1})_{(1-x)}\text{O}_{2-\delta}$. From the images, it can be noticed that the samples are porous. Nanomaterials synthesized using SCS generally result in the formation of nanopowder with porous nature. It may be due to the evolution of gases during combustion synthesis (Varma and Mukasyan 2004). It can also be seen that the samples tend to sinter when Cu concentration increases in the doped samples as Cu aids as a sintering agent (Vu et al. 2013).

According to the studies reported by Vu et al., Cu promoted the reduction of step-free energy leading to abnormal grain growth (Vu et al. 2013). The sintering mechanism is generally not beneficial as its essential for the loss of catalyst activity, especially in high-temperature catalytic processes (Hansen et al. 2013).

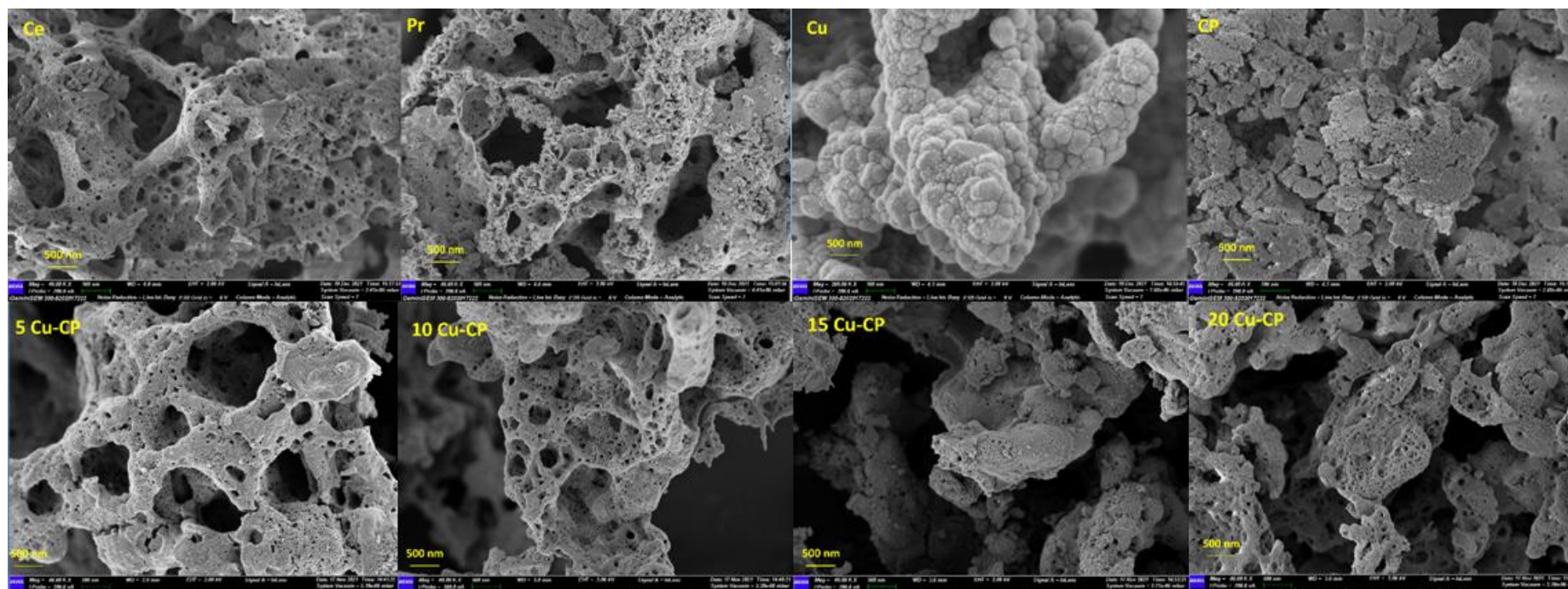


Fig. 5.4: FE-SEM images of Pure Ce, Pr, Cu, and $\text{Cu}_x(x=0-0.2) (\text{Ce}_{0.9}\text{Pr}_{0.1})_{1-x} \text{O}_{2-\delta}$ Catalysts

5.5. XPS ANALYSIS

The XPS analysis is carried out for $\text{Cu}_{x(x=0-0.2)}(\text{Ce}_{0.9}\text{Pr}_{0.1})_{(1-x)}\text{O}_{2-\delta}$ samples to obtain information about the multiple oxidation states of the elements present on the surface. The presence of Oxygen species, Ce, Pr, and Cu peaks confirms the presence of Cu in all the Ce-Pr doped samples. The relative peaks corresponding to oxidation states for Ce, Pr, Cu, and Oxygen were compared from the literature reported (Anantharaman et al. 2017; Holgado et al. 2000; Marbán et al. 2009; Poggio-Fraccari et al. 2018; Shenoy et al. 2019). Based on the earlier literature reported, the Ce 3d spectrum is assigned into two sets (Holgado et al. 2000; Poggio-Fraccari et al. 2018), corresponding to $3d_{3/2}$ and $3d_{5/2}$ orbitals.

The peaks assigned to Ce^{4+} and Ce^{3+} states are noted (Anantharaman et al. 2017; Holgado et al. 2000; Marbán et al. 2009), and the area under the curve is utilized to calculate the reducibility and species ratios. Similarly, $3d_{3/2}$ and $3d_{5/2}$ spin orbitals for Pr at ~935 and 945, 950, 969 eV represent the Pr^{4+} , and the peaks at ~930, 933, 955, eV represent the Pr^{3+} species (Govardhan et al. 2022; Poggio-Fraccari et al. 2018). The peak at ~975 eV corresponds to the oxygen Auger peak (OKLL) (Govardhan et al. 2022; Poggio-Fraccari et al. 2018).

For Cu $2p_{3/2}$ region, peaks at ~929 - 933 eV are associated with Cu^+ species and peaks at 933.6–934.3 eV are attributed to Cu^{2+} oxidation states (Marbán et al. 2009). The peaks ~952 eV were credited to the $2p_{1/2}$ region (Poulose et al. 2016) and are assigned mainly to Cu^{2+} .

Figure 5.5 depicts deconvoluted peaks for Ce, Pr, Cu, and Oxygen species. The reducibility ratio [$\text{Ce}^{3+}/(\text{Ce}^{3+}+\text{Ce}^{4+})$, $\text{Pr}^{3+}/(\text{Pr}^{3+}+\text{Pr}^{4+})$ and $\text{Cu}^+/(\text{Cu}^++\text{Cu}^{2+})$] for all the elements and oxygen vacancy ratios are calculated and depicted in **Table 5.2**. The area under the curve is used to detect the reducibility ratios. The table shows that the Ce^{3+} concentration is slightly high for the 15 Cu-CP sample, whereas 20 Cu-CP had high Pr^{3+} , and 15 Cu-CP had better Cu^+ concentrations than all doped samples.

The O1s spectra reveal the information corresponding to the lattice oxygen species (O^{2-}) and the chemisorbed oxygen species (O^- and O_2^{2-}).

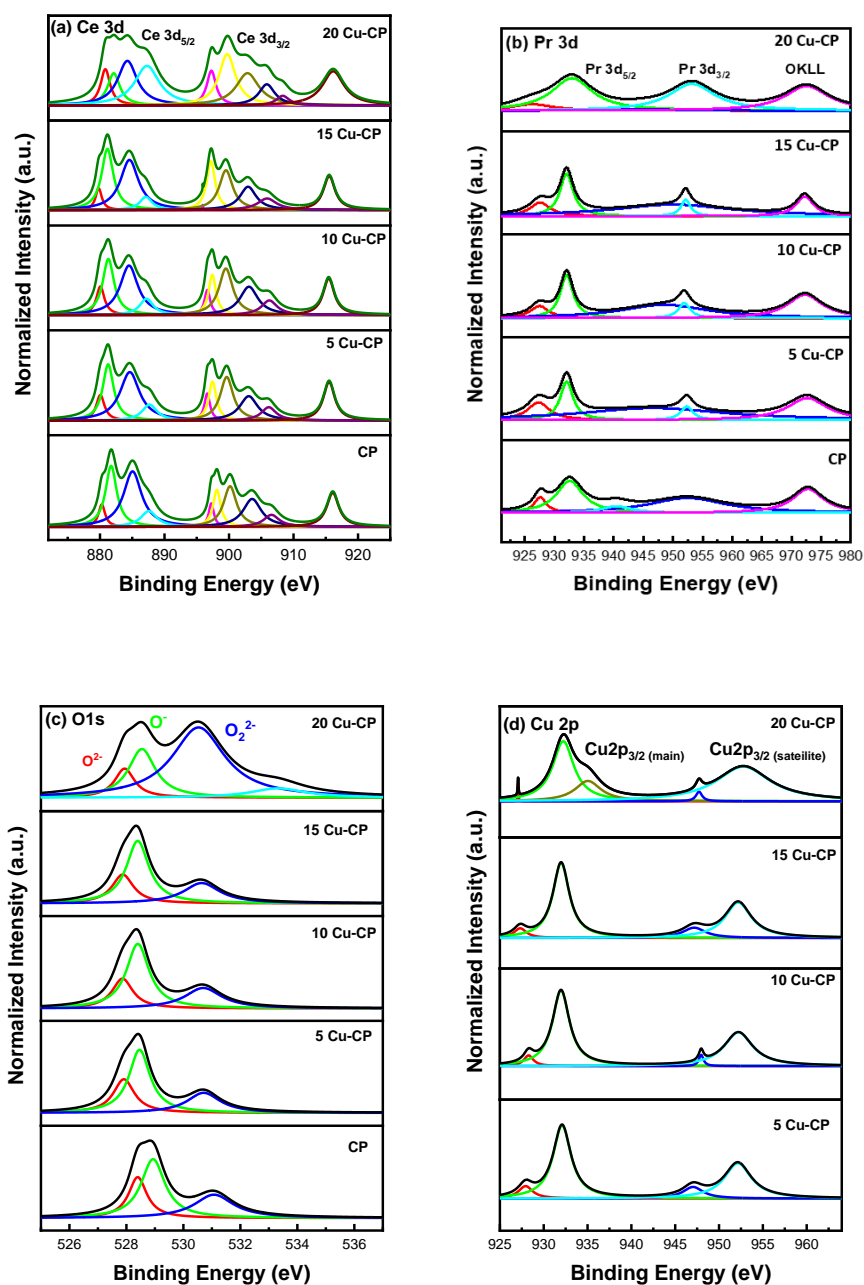


Figure. 5.5: (a) Ce 3d (b) Pr 3d (c) O 1s (d) Cu 2p XPS spectra for $\text{Cu}_x(x=0-0.2) (\text{Ce}_{0.9}\text{Pr}_{0.1})_{1-x} \text{O}_{2-\delta}$ Catalysts.

Table 5.2: Reducibility ratio and Surface Oxygen species of $\text{Cu}_{x(x=0-0.2)}(\text{Ce}_{0.9}\text{Pr}_{0.1})_{(1-x)}\text{O}_{2-\delta}$

Catalyst	Reducibility Ratio				Lattice Oxygen ratio $\frac{O^{2-}}{O^{2-} + O^{-} + O_2^{2-}}$	Adsorbed Oxygen ratio	
	$\frac{Ce^{3+}}{Ce^{3+} + Ce^{4+}}$	$\frac{Pr^{3+}}{Pr^{3+} + Pr^{4+}}$	$\frac{Cu^{+}}{Cu^{3+} + Cu^{2+}}$	$\frac{Cu^{2+}}{Cu^{3+} + Cu^{2+}}$		$\frac{O^{-}}{O^{2-} + O^{-} + O_2^{2-}}$	$\frac{O_2^{2-}}{O^{2-} + O^{-} + O_2^{2-}}$
CP	0.42	0.15	-	-	0.26	0.49	0.24
5 Cu-CP	0.48	0.25	0.42	0.85	0.22	0.54	0.26
10 Cu-CP	0.48	0.27	0.44	0.93	0.22	0.51	0.27
15 Cu-CP	0.50	0.31	0.42	0.86	0.09	0.22	0.61
20 Cu-CP	0.28	0.40	0.16	0.43	0.72	0.49	0.25

It can be noticed from **Table 5.2** that the presence of lattice oxygen species (O^{2-}) was high for 20 Cu-CP, whereas 15 Cu-CP had the highest Ce^{3+} and O_2^{2-} species. The surface chemisorbed oxygen species (O^-) presence was high for the 5 Cu-CP samples, which may favor better catalytic activity. It can also be deduced that incorporating 5 mol % Cu into the Ce-Pr catalyst enhanced surface oxygen formation compared to other samples and, hence, took part in the oxidation reaction efficiently. Surface-active oxygen species (O^-) are also critical in improving catalytic activity at high temperatures (Wei et al. 2011). Hence it is evident that 5 Cu-CP has a better capability to enhance the creation of O_v .

5.6. SOOT OXIDATION ACTIVITY

Figure 5.6 demonstrates the soot conversion plots for pure Ce, Pr, Cu, and $Cu_{x(x=0-0.2)}(Ce_{0.9}Pr_{0.1})_{1-x}O_{2-\delta}$ samples, and the corresponding T_{50} temperatures are given in **Table 5.3**. The obtained results from TGA show that the catalytic activity is in the order of 5Cu-CP (402 °C) > CP (408 °C) > Pr (410 °C) > Ce (413 °C) = 10Cu-CP (413 °C) = 15Cu-CP (413 °C) = 20Cu-CP (413 °C) > Cu (440 °C). 5 Cu-CP displayed better catalytic activity with $T_{50} = 402$ °C. The pure Cu sample showed a higher $T_{50} = 440$ °C. Catalytic activity tests were carried out thrice to ensure reproducibility, and the T_{50} obtained from the three trials is nearly similar, with an error range of less than \pm four-degree Celsius (**Table 5.3**).

The enhanced catalytic activity of the 5 Cu-CP sample can be credited due to the presence of high reactive planes and high chemisorbed oxygen species (O^-). The oxygen vacancies formation energy at the {111} facet is more significant than {110} and {100}. Hence, there may be an additional number of oxygen vacancies on the {110} and {100} reactive facets than the {111} facet.

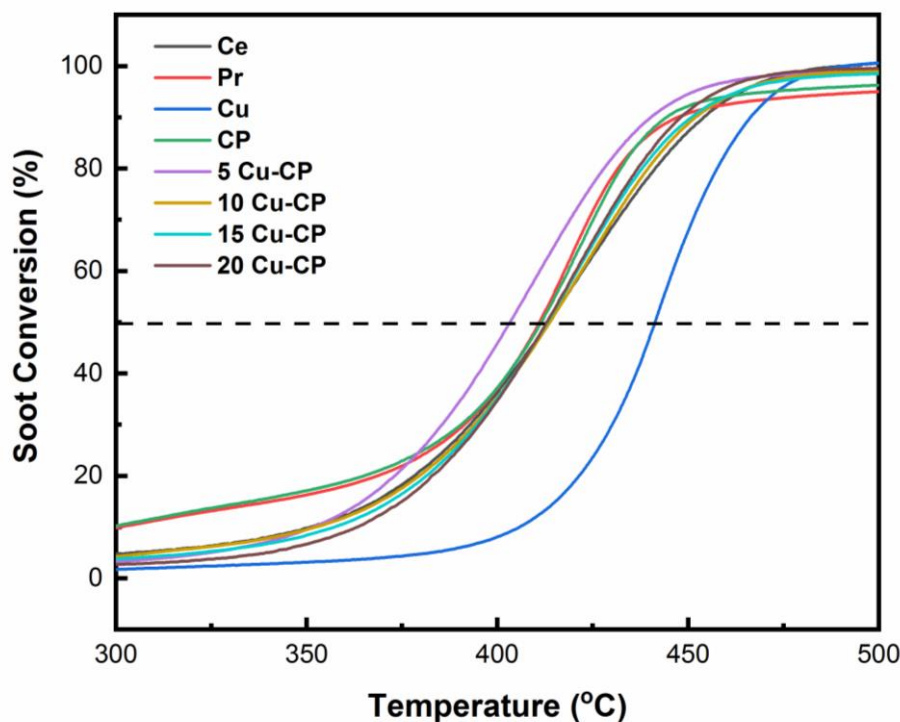


Figure. 5.6: Soot Oxidation Plot of Pure Ce, Pr, Cu, and $\text{Cu}_x(x=0-0.2)$ $(\text{Ce}_{0.9}\text{Pr}_{0.1})_{1-x} \text{O}_{2-\delta}$ Catalysts.

The nanoparticles generally comprise octahedral sites exposed to mainly the {111} facet to retain minimum surface energy (Younis et al. 2016). High oxygen vacancies and the transfer of oxygen atoms favor redox reactions on the surface, improving the catalytic activity (Younis et al. 2016). From the literature (Chi et al. 2023 and Wei et al. 2020), it is noticed that the facet ratios ($\{110\}/\{111\}$ and $\{100\}/\{111\}$) of Ceria plays a critical role in the catalytic activity of oxidation reactions. Wei et al. 2020 improvised the soot oxidation activity controlling the optimally exposed facets ($\{110\}$, $\{100\}$, and $\{111\}$) of Ceria in Au/CeO₂ catalysts. The order of the optimally exposed facets which control the soot oxidation activity is $\{110\} > \{100\} > \{111\}$, and the addition of Au to Ceria further enhanced the soot oxidation activity.

Similarly, Chi et al. 2023, studied facet-dependent soot oxidation activity over single-crystalline MnO₂. They demonstrated that {310} facet exhibited higher catalytic activity than low-indexed facets. As per the DFT calculations of Chi et al. 2023, {310}, the facet of MnO₂ induces the formation of coordinative unsaturated atoms and surface defect sites, enhancing the adsorption-activation ability of oxygen, which further enhances the soot oxidation activity.

Similarly, in the present study, the addition of 5Cu in the CP system increased the facet ratios ($\{110\}/\{111\}$ and $\{100\}/\{111\}$) from 0.24 to 0.30 and from 0.38 to 0.50 (**Table 5.1**). With the further addition of Cu (10, 15, 20) in the CP system, there is a decrease in the facet ratio. The facet ratio is one of the factors influencing the soot oxidation activity, and the 5 Cu-CP catalyst showed slightly better performance than the other Cu-CP catalysts.

As per the literature (**Table 2.3**) on incorporating Cu / Pr into Ce-based catalysts, the soot oxidation catalytic performance was significantly enhanced. Reddy and Rao 2009b reported CuO-Ceria-Zirconia (Cu-Ce-Zr) prepared via co-precipitation and impregnation methods for catalytic soot oxidation activity. The better T₅₀ (363 °C) of Cu-Ce-Zr was attributed to the catalyst's high oxygen vacancies, smaller crystallite size, and high specific surface area (Reddy and Rao 2009a). Doping Pr into Ce improves OSC and enhances catalytic activity at high temperatures (Andana et al. 2016; Reddy et al. 2009b).

5.7. SOOT OXIDATION KINETIC ANALYSIS:

5.7.1. Ozawa and KAS method to evaluate activation energy

Ozawa and KAS iso-conversational methods determined all catalysts' activation energy E_a value. It involves measuring “T” at a constant conversion (α) and varying heating rates (β). The " α " values 0.2 to 0.8 were considered as there may be deviance of experimental data from theoretical values at the extremes (López-Fonseca et al. 2007). Graph of $\log \beta$ vs $\frac{1}{T}$ for the same degree of conversion plotted for the Ozawa method and exhibited in **Figure. A 5.1** (Appendix I).

Graph of $\ln \left(\frac{\beta}{T^2}\right)$ vs $\frac{1}{T}$ for the same degree of conversion has been plotted for the KAS method and is depicted in **Figure. A 5.2**. The slope of the graph ($-\frac{E_a}{R}$) is used to find the E_a value; nearly a series of parallel lines were obtained. The average activation energy is calculated from the graph's slope and tabulated in **Table 5.3**. The table shows that the pure Ce sample displayed the lowest E_a value of 77 and 70 kJ mol^{-1} , while pure Cu showed the highest E_a value of 225 and 238 kJ mol^{-1} by Ozawa and KAS methods.

The Cu-Ce-Pr catalysts in the present work displayed an E_a value ranging from 150-160 kJ mol^{-1} in both methods. **Table 5.4** demonstrates T_{50} temperature, E_a , and A values for various Ceria-based Catalysts from earlier pieces of literature reported. Among the Ce-Pr-based catalysts, Ni-loaded Ce-Pr catalysts displayed E_a values ranging from 133 - 137 kJ mol^{-1} (Rajvanshi et al. 2020), whereas Ag-loaded Ce-Pr catalysts showed E_a values ranging from 140 - 150 kJ mol^{-1} (Govardhan et al. 2022) obtained by Ozawa method.

The Average E_a value of $\sim 130 \text{ kJ mol}^{-1}$ to 200 kJ mol^{-1} was reported for uncatalyzed soot oxidation (Christensen et al. 2016; Nascimento et al. 2015; Neeft et al. 1997; Suárez-Vázquez et al. 2018); on the other hand, Suárez-Vázquez et al. 2018 reported an E_a value of 133 kJ mol^{-1} for uncatalyzed soot oxidation. Christensen et al. 2016 said that the non-catalytic oxidation of soot occurs with an E_a value of $198.5 \text{ kJ mol}^{-1}$. It can be perceived that even if the T_{50} of bare soot or uncatalyzed is way higher than that of catalysts, the E_a values of soot and catalysts don't vary considerably. Hence, the other kinetic parameters, such as the pre-exponential factor (A), which may influence the catalytic activity, must be assessed further.

5.7.2. Determination of Pre-Exponential Factor (A)

The A_m function with non-integer kinetic exponent (m) was the most suitable conversion model (López-Fonseca et al. 2007). The lines corresponding to $[\ln(\beta R/E) - \ln(p(x))]$ versus $[\ln(-\ln(1 - \alpha))]$ for different heating rates nearly superimposed each other, as seen in **Figure. A 5.3**. Obtained “ A ” and m values are listed in **Table 5.3**. It was observed that the values of A and “ m ” did not change significantly when the heating rate was changed, which showed consistency. As a result, it was possible to infer that random nucleation and subsequent growth were possible mechanisms for the chosen material. The obtained “ A ” value ($1.59 \times 10^{16} \text{ min}^{-1}$) was high for the pure Cu sample and low for the pure Ce sample ($1.40 \times 10^5 \text{ min}^{-1}$). The significant pre-exponential factor corresponds to an effective reactive collision between soot and O_2 . In the present study, 5 Cu-CP showed better catalytic activity, with an “ A ” value of $5.23 \times 10^{11} \text{ min}^{-1}$. “ A ” value, along with T_{50} and activation energy for various Ce-based catalysts reported from the literature, is listed in **Table 2.5** and compared with the obtained values in the present study.

From the literature (**Table 2.5**), it can be observed that the pre-exponential factor “A” value is in the range of 1×10^{02} to $4.5 \times 10^{14} \text{ min}^{-1}$ for soot oxidation activity with and without the presence of a catalyst. It can be noticed that there is no direct correlation or tendency between the pre-exponential factor, the activation energy, and the T_{50} temperature.

Zouaoui et al. 2012, noticed that with the addition of NO apart from oxygen, the pre-exponential factor has been increased from 3.24×10^{02} to $4.92 \times 10^{02} \text{ min}^{-1}$, and the activation energy is decreased from 135 to 59 kJ mol^{-1} . In studies conducted by Nascimento et al. 2015, pure Printex-U soot oxidation activity showed a pre-exponential factor of 4.5×10^{14} with an activation energy of 175 kJ mol^{-1} , and T_{50} temperature is around 610 °C. Catalysts like $\text{CeO}_2\text{-ZnO}$ displayed lower pre-exponential factor (up to $1.14 \times 10^{08} \text{ min}^{-1}$), and T_{50} temperature decreased from 610 to 420 °C. There is no direct correlation between the pre-exponential factor, activation energy, and T_{50} temperature. Similarly, in the present study, for Cu-CP catalysts, the pre-exponential factor ranges from 1.40×10^{05} to 1.59×10^{16} with an activation energy of 140~160 kJ mol^{-1} and T_{50} temperature in the range of 400~415 °C.

5.7.3. Coats-Redfern (CR) Method

The CR plots were plotted using the model-free approach to compare the obtained E_a and A values (Ganiger et al., 2022). The CR plot for all the synthesized samples is generated and shown in **Figure A 5.4**. The best linear fit, reaction models, and E_a values calculated from the other models were utilized to predict the exact reaction model. The A and E_a values attained via the CR method are also tabulated in **Table 5.3**. The E_a and A values reported from the CR method were, to a certain extent, in the range of previously obtained model-free and A_m methods.

5.7.4. Master plot method to evaluate the conversion models

Figure. A5.5 reveals the master plots of the samples with $g(\alpha)$ values calculated for different reaction models(**Table 2.4**) by varying conversion (α). The plots coordinated each other irrespective of the β values. The $p(x)$ values are also calculated for different temperatures for different β values. The reaction models coinciding for each catalyst were noted and are provided in **Table 5.3**. Comparing the theoretical and experimental data revealed that the kinetic process for the combustion of carbon was defined by the A_m (Nucleation and Growth / Avrami-Erofeev) model. In such a case, the $g(\alpha) = [-\ln(1-\alpha)]^{1/m}$ value is close to the unity.

The occurrence of a conversion model for each catalyst sample was different. Ce and CP samples followed the Nucleation and growth model ($A_{1.5}$) along with phase boundary-controlled reaction (contracting linear) (P_1). CP followed a Phase boundary-controlled reaction (contracting area) (P_2). All other Cu-doped samples followed the Nucleation and growth model ($A_{1.5}$), a second-order chemical reaction (R_2), and Power-law IV (L_4) in common except 20 Cu-CP and pure Cu samples. Apart from that, 5 Cu-CP followed a phase boundary-controlled reaction (contracting - linear, area, and volume - P_{1-3}) for lower conversion, and 1–3-Dimensional Diffusion (D_{1-3}) was followed at a higher conversion value. The results for solid-state reaction models show a linear trend, and the E_a value obtained from the CR method can also be used to compare the reaction model; hence, the coinciding models from the master plots were selected.

Table 5.3: Kinetic triplets and “m” value for Pure Ce, Pr, Cu, and $\text{Cu}_{x(x=0-0.2)}(\text{Ce}_{0.9}\text{Pr}_{0.1})_{1-x}\text{O}_{2-\delta}$ Catalysts

Catalysts	T_{50} °C	E_a (kJ mol ⁻¹)			Reaction Model	A (min ⁻¹)		m
		Ozawa method	KAS method	CR method		A _m method	CR method	
Ce	413±3	77	70	76	A _{1.5} , P ₁	1.40×10 ⁰⁵	2.43×10 ⁰⁵	1.43
Pr	410±2	166	173	207	A ₁ ,A _{1.5} , L ₄ , R ₂	3.70×10 ¹²	5.27×10 ¹²	0.45
Cu	440±3	225	238	251	L ₄ , R ₂	1.59×10 ¹⁶	4.66×10 ¹⁶	1.01
CP	408±4	96	111	94	A _{1.5} , P ₁ ,P ₂	5.42×10 ⁰⁶	3.83×10 ⁰⁶	1.35
5 Cu-CP	402±2	158	156	159	A ₁ ,A _{1.5} , P ₁ ,P ₂ ,P ₃ ,L ₄ ,R ₂ , D ₁₋₄	5.23×10 ¹¹	4.26×10 ¹¹	0.77
10 Cu-CP	413±3	152	160	168	A ₁ , L ₄ , R ₂	1.04×10 ¹¹	1.50×10 ¹¹	0.70
15 Cu-CP	413±3	156	145	155	A ₁ , L ₄ , R ₂	2.03×10 ¹¹	1.59×10 ¹¹	0.76
20 Cu-CP	413±4	162	159	160	L ₄ , R ₂	5.96×10 ¹¹	4.40×10 ¹¹	0.80

For solid-state reaction kinetics, the probable reaction models are listed by (López-Fonseca et al. 2007). Suppose the reaction follows first-order kinetics (A_1). In that case, the nucleation and growth ($A_{1.5}$, A_{2-4}) process is the rate-determining step, and there may be a probability of nucleation occurring at every active site (Diefallah et al. 1987). In phase-boundary reactions, the nucleation step may occur instantly, and the surface of each particle is enclosed with a product layer. In solid-state reactions, diffusion is critical and occurs between the crystal lattices. A thick product layer formation may be observed, wherein the reactants' movement to or products from the interface controls the reaction rate. The D_1 diffusion model is based on the rate equation for an infinite flat plate that does not involve a shape factor. D_2 assumes cylindrical solid particles; here, diffusion occurs radially, and D_3 assumes solid particles are spherical. $L_1 - L_4$ are power law models, in which the nucleation rate is assumed to follow a power law and nuclei growth is assumed constant (Hofman and Bayon 2019).

5.7.5. Experimental and theoretical kinetic curves construction and comparison

Thermo-analytical curves were constructed again to verify that each heating rate's composite kinetic analysis method selected the most accurate kinetic triplet parameter (A , E_a , and kinetic model). The experimental data was extracted directly from the TGA data, and α was plotted against temperature. For theoretical data, the $g(\alpha) = (AE_a/R\beta) \times p(x)$ equation was used to calculate $g(\alpha)$. For varying temperatures, $p(x)$ was calculated and then used to calculate $g(\alpha)$. So using $g(\alpha) = [-\ln(1-\alpha)]^{1/m}$, α values can be calculated, and these α values were plotted against temperatures for the calculated plot. From **Figure. 5.7**, it can be noticed that most of the catalysts had a relatively good consistency compared to all other samples. It also indicates that the proposed kinetic analysis was appropriate for modeling soot combustion.

Effect of Copper-Doped Ceria-Praseodymium Catalysts for Soot Oxidation Activity and its Kinetics

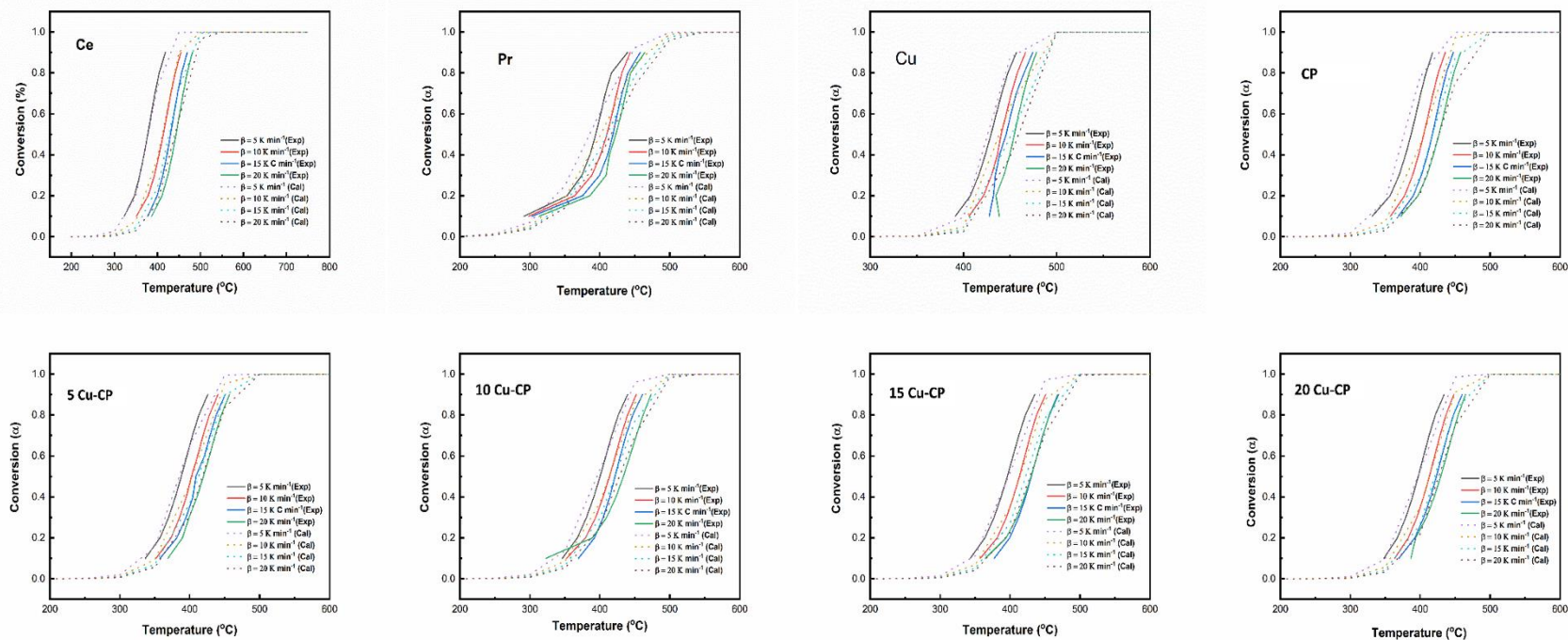


Figure 5.7: Conversion v/s Temperature plots of pure Ce, Pr, Cu, and $\text{Cu}_x(x=0-0.2) (\text{Ce}_{0.9}\text{Pr}_{0.1})_{1-x} \text{O}_{2-\delta}$ Catalysts.

It also signifies that the nucleation and growth model plays a significant role in describing the reaction mechanism. The plots obtained show that the pure Pr and Cu showed minor variation. Substantial deviation in the plots indicates that it does not follow the Nucleation and Growth model for all α values.

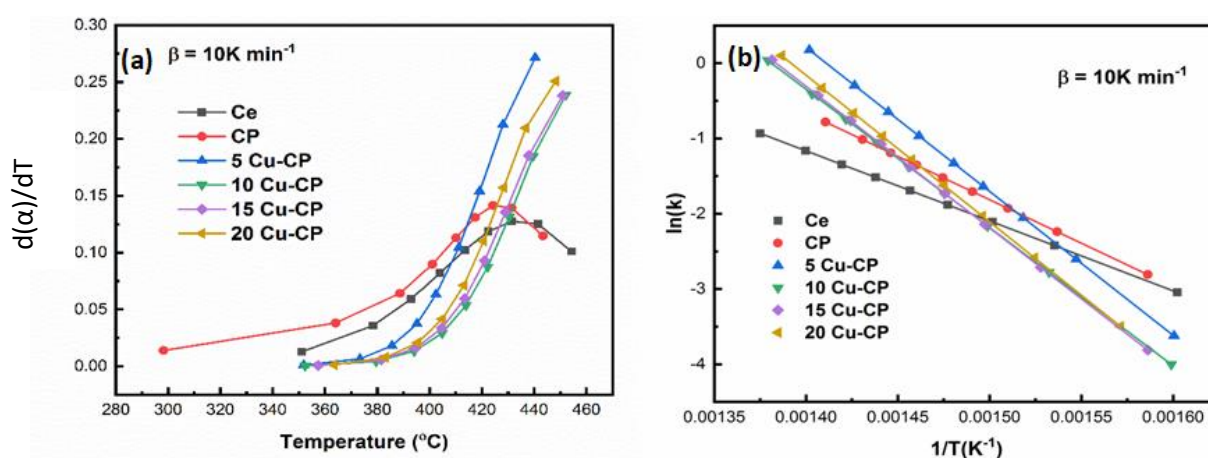


Figure. 5.8. (a) Rate vs. Temperature plot (b) Arrhenius plot for pure Ce and $\text{Cu}_{x(x=0-0.2)}(\text{Ce}_{0.9}\text{Pr}_{0.1})_{1-x}\text{O}_{2-\delta}$ Catalysts.

The $d\alpha/dT$ v/s $1/T$ is plotted and is shown in **Figure. 5.8 (a)** for Ce, CP, and $\text{Cu}_{x(x=0-0.2)}(\text{Ce}_{0.9}\text{Pr}_{0.1})$ doped samples. It can be noticed that the temperature where the maximum rate is attained is high for the 5 Cu-CP samples. It can also be perceived that the rate increases with an increase in α value. Hence, 5 Cu-CP has a higher rate compared to all the samples. The kinetic activity is deduced via the Arrhenius plot ($\ln(k)$ v/s. $1/T$) and plotted in **Figure. 5.8 (b)**. It can be seen that the activity of 5 Cu-CP is higher compared to other doped samples where Cu is present.

5.8. CONCLUSIONS

Pure Ce, Pr, Cu, and $\text{Cu}_{x(x=0-0.2)}(\text{Ce}_{0.9}\text{Pr}_{0.1})_{1-x}\text{O}_{2-\delta}$ doped samples were synthesized using the SCS method calcined at 600/5h. Ce, Pr, and the doped samples showed a cubic fluorite structure, and Cu displayed a monoclinic structure. Raman spectra analysis confirmed the presence of peaks related to Oxygen vacancies for the doped samples. The T_{50} temperature obtained for the soot oxidation activity is in the order of 5Cu-CP (402 °C) > CP (408 °C) > Pr (410 °C) > Ce (413 °C) = 10Cu-CP (413 °C) = 15Cu-CP (413 °C) = 20Cu-CP (413 °C) > Cu (440 °C). The better catalytic activity of 5 Cu-CP (T_{50} =402 °C) may be attributed to high reactive planes and the presence of high chemisorbed oxygen species (O^-) than all other catalysts. Even though the obtained T_{50} value would be too high to allow the complete passive regeneration of a DPF, the developed catalyst would help to improve the fuel efficiency and CO_2 emissions of the vehicle by reducing the quantity of fuel injection into the exhaust during active regeneration. The kinetic triplets (activation energy, pre-exponential factor, and reaction model) were evaluated for all the samples. Pure Ce and Cu displayed the lowest and highest E_a and A values, respectively, with all the methods employed. Most doped catalysts followed the nucleation and growth model except Pure Pr and Cu catalysts. 5 Cu-CP also followed the phase boundary-controlled reaction (P_{1-3}) for lower conversion, and 1-3 dimensional diffusion (D_{1-3}) was observed at a higher conversion value. 5 Cu-CP also had a higher rate of reaction compared to other catalysts.

It can be noted that the 5Cu-CP catalyst system showed better soot oxidation activity which is attributed to the better reactive planes and chemisorbed oxygen species than compared to other Cu-CP and CP catalyst systems. In the next chapter, Cobalt-doped Ceria-Praseodymium catalysts were synthesized, characterized, and obtained soot oxidation activity and kinetic behavior. The descriptors controlling the soot oxidation activity of the Cobalt-doped Ceria-Praseodymium catalysts system are further explored in the next chapter.

CHAPTER 6

INVESTIGATION OF COBALT - DOPED CERIA - PRASEODYMIUM CATALYSTS FOR SOOT OXIDATION ACTIVITY AND ITS KINETICS

CeO₂ doped with cobalt oxides influences the distribution of active oxygen species in CeO₂-based catalysts and effectively promotes soot oxidation activity (Mahofa et al. 2018). The interfaces between high-redox ability materials such as Co₃O₄ and CeO₂ show enhanced active sites for catalytic soot oxidation (Xing et al. 2020). The selectivity, activity, and reactivity of Ce-Co catalysts reported were related to the strong redox ability of cobalt oxide (Bratan et al. 2022).

Song et al. 2021 reported that Co-La catalysts possessed weak Co-O bonds, abundant Co³⁺ species, and active O₂ species on the surface, and hence better reducibility, which improves oxygen mobility and redox ability. Therefore, The present chapter investigates the catalytic effect of Cobalt-doped Ce-Pr for soot oxidation activity and its kinetics.

6.1. X-RAY DIFFRACTION (XRD) ANALYSIS:

The XRD spectra for Co_{x(x=0 - 0.2)}(Ce_{0.9}Pr_{0.1})_{1-x}O_{2-δ} and Pure Co catalysts developed by the SCS method are displayed in **Figure. 6.1**. It can be noticed in **Figure. 6.1** that all the catalysts ensured the fluorite structure of CeO₂. The planes (111), (200), (220), (311), (222), (400), (331), (422) correspond to characteristic fluorite CeO₂ (Reddy et al. 2011; Shajahan et al. 2018). The slight shift in peaks towards lower 2θ was observed in all Co- CP catalysts compared to CP, which may be due to variation in the ionic size of Co (0.75 Å) from Ce (0.97 Å) and Pr (1.101 Å).

The planes ((111), (220), (311), (222), (400), (511), (440)) of pure Co matched well with the Co_3O_4 nanoparticles belonging to the typical cubic spinel structure (Garces et al. 2015; Prabakaran et al. 2017). Co_3O_4 generally possesses a spinel structure where Co^{3+} and Co^{2+} are located on tetrahedral and octahedral sites (Xing et al. 2020). Further, no secondary diffraction peaks attributed to pure Co were noticed in Co_x ($x=0-0.20$) $(\text{Ce}_{0.9}\text{Pr}_{0.1})_{(1-x)}\text{O}_{2-\delta}$ catalysts.

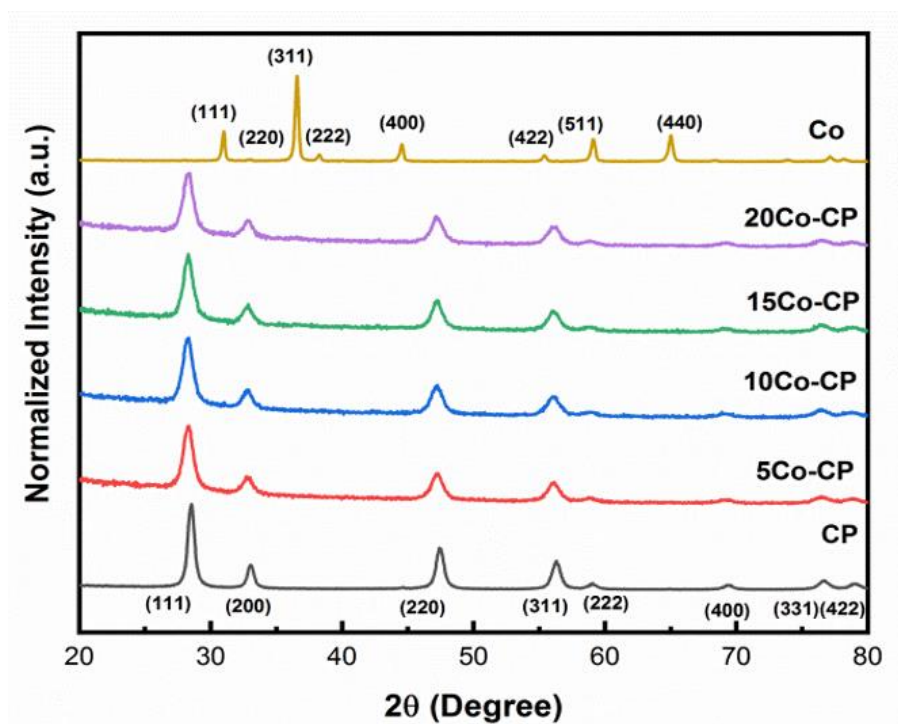


Figure. 6.1. XRD spectra of Co_x ($x=0-0.20$) $(\text{Ce}_{0.9}\text{Pr}_{0.1})_{(1-x)}\text{O}_{2-\delta}$ Catalysts.

The crystallite size, lattice strain, and facet ratios [$\{100\}/\{111\}$ and $\{110\}/\{111\}$] were calculated for all the catalysts and are provided in **Table 6.1**. It can be seen that the crystallite size reduced from 14nm to ~9 nm on the introduction of Co to the CP catalyst system. A substantial increase in lattice strain was observed can also be noticed from CP to all Co-CP catalysts. The crystallite size and lattice strain were more or less the same for all the catalysts, whereas pure Co had a high crystallite size (28.11 nm) and lowest lattice strain (0.0041). There was also an improvement in facet ratios from CP to other Co-CP catalysts. It can be observed that 20 Co-CP had a high facet ratio (0.41) for $\{110\}/\{111\}$ and 15 Co-CP had a high facet ratio (0.44) for $\{100\}/\{111\}$. Reactive facets are one of the most critical parameters to determine the ability to enhance catalytic activity. Hence, loading Co into CP may significantly impact the catalytic activity.

6.2. RAMAN SPECTROSCOPY ANALYSIS

Figure 6.2. portrays Raman spectra for $\text{Co}_x (x=0-0.2) (\text{Ce}_{0.9}\text{Pr}_{0.1})_{1-x} \text{O}_{2-\delta}$ and pure Co. The characteristic peak observed at $\sim 465 \text{ cm}^{-1}$ in all the catalysts can be allotted to the active F_{2g} Raman modes of CeO_2 (Mukherjee et al. 2016; Patil et al. 2019; Shajahan et al. 2018). This peak demonstrates the bending modes of symmetric breathing of O_2 around Ce atoms (O-Ce-O). Another significant peak present at $\sim 560 \text{ cm}^{-1}$ in all the catalysts is assigned to oxygen vacancies (Mukherjee et al. 2016a; Shajahan et al. 2018).

No significant shift in the F_{2g} peak was detected in all the catalysts in the Raman spectra. Pure Co showed two F_{2g} , A_{1g} , and E_g Raman modes comprising pure crystalline Co_3O_4 (Farhadi et al. 2016). The strong band at $\sim 675\text{ cm}^{-1}$ (A_{1g}) is ascribed to the characteristic peak of the octahedral sites for Co_3O_4 . The band at $\sim 467\text{ cm}^{-1}$ is attributed to E_g modes, whereas the band at 508 cm^{-1} and the weak band at $\sim 610\text{ cm}^{-1}$ correspond to $\sim F_{2g}$ symmetry. 15 Co-CP and 20 Co-CP catalysts exhibited secondary peaks of A_{1g} Raman mode at $\sim 675\text{ cm}^{-1}$ and F_{2g} Raman mode at $\sim 508\text{ cm}^{-1}$.

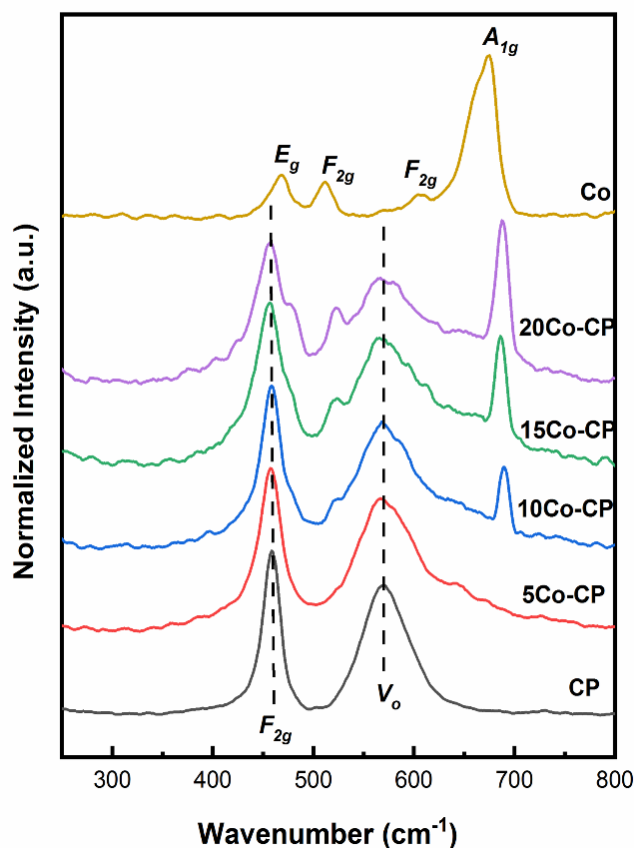


Figure. 6.2. Raman Spectra of Co_x ($x=0-0.2$) $(\text{Ce}_{0.9}\text{Pr}_{0.1})_{(1-x)}\text{O}_{2-\delta}$ Catalysts

Investigation of Cobalt-Doped Ceria-Praseodymium Catalysts for Soot Oxidation Activity and its Kinetics

The intensity ratios (I_{Ov}/I_{F2g}) of oxygen vacancy peaks to characteristic F_{2g} mode of Ce were calculated for all the catalysts and tabulated in Table 6.1. The presence of Ov tends to improve the catalytic performance of soot oxidation. The table shows that I_{Ov}/I_{F2g} of 5 Co-CP was the highest (0.83) compared to all the catalysts. The increase in the intensity of the ratio has been assigned to the creation of extrinsic oxygen vacancies in CeO₂ to retain charge neutrality (Ming et al. 2011). Paunovi et al. 2012 also reported the intensity ratio of vacancy to F_{2g} mode. It was concluded that the concentrations of intrinsic and extrinsic defects created by Pr doping increase and, at a definite point, exceed the Ce³⁺-V_o complexes (Paunovi et al. 2012). Liu et al. 2016 reported that catalyst stability is closely related to the concentration of surface oxygen vacancies created after doping.

Table 6.1. Physicochemical properties of Co_{x(x=0-0.2)} (Ce_{0.9}Pr_{0.1})_(1-x) O_{2-δ} Catalysts from XRD and Raman spectroscopy Analysis

Catalyst	Crystallite Size (nm)	Lattice strain (ε)	Facet Ratio		I_{Ov}/I_{F2g}	Secondary Phase (Raman Spectroscopy Analysis)
			{110}/{111}	{100}/{111}		
CP	14	0.0107	0.24	0.38	0.77	-
5 Co-CP	09	0.0162	0.36	0.41	0.83	-
10-Co-CP	09	0.0166	0.37	0.43	0.77	-
15 Co-CP	09	0.0165	0.40	0.44	0.78	Co ₃ O ₄
20 Co-CP	09	0.0166	0.38	0.43	0.73	Co ₃ O ₄
Co	28	0.0041	-	-	-	-

6.3. FE-SEM ANALYSIS

FE-SEM Micrographs of Co_x ($x=0-0.2$) $(\text{Ce}_{0.9}\text{Pr}_{0.1})_{1-x}\text{O}_{2-\delta}$ and Pure Co catalysts at 500 nm scale are displayed in **Figure. 6.3**. All the catalysts revealed a highly porous nature as the SCS synthesized them. method (Aruna and Mukasyan 2008). Catalysts synthesized using SCS show porous agglomerates, possibly due to increased contained temperature during combustion (Valechha et al. 2011). From the FE-SEM images, CP revealed minimum pores than all other Co-doped catalysts. It can also be observed from the images that the agglomerate size tends to increase as the concentration of Co increases and the porosity decreases. To further understand the porous nature of the developed catalysts, BET- BJH analysis was performed.

6.4. BET AND BJH PORE SIZE ANALYSIS

BET Surface area analysis and BJH Pore volume analysis were performed for all the catalysts to determine the influence of the surface area and pore size on the catalytic activity. The parameters obtained from the analysis are summarized in **Table 6.2**. The table demonstrates that the surface area varied mainly from 13 to 34 m^2/g , where 5 Co-CP had the highest surface area of 34 m^2/g with a high average pore size diameter of ~20.64 nm. Pure Co had the smallest surface area of 13 m^2/g and a minimum average pore size diameter of ~07.10 nm. It was noticed that there was only a slight increase in the surface area upon adding Co to CP (Chapter 5). Additionally, the surface area tended to decrease due to the sintering behavior of Co (Fagg et al. 2003), which was also noticed with the pore volume of the catalysts.

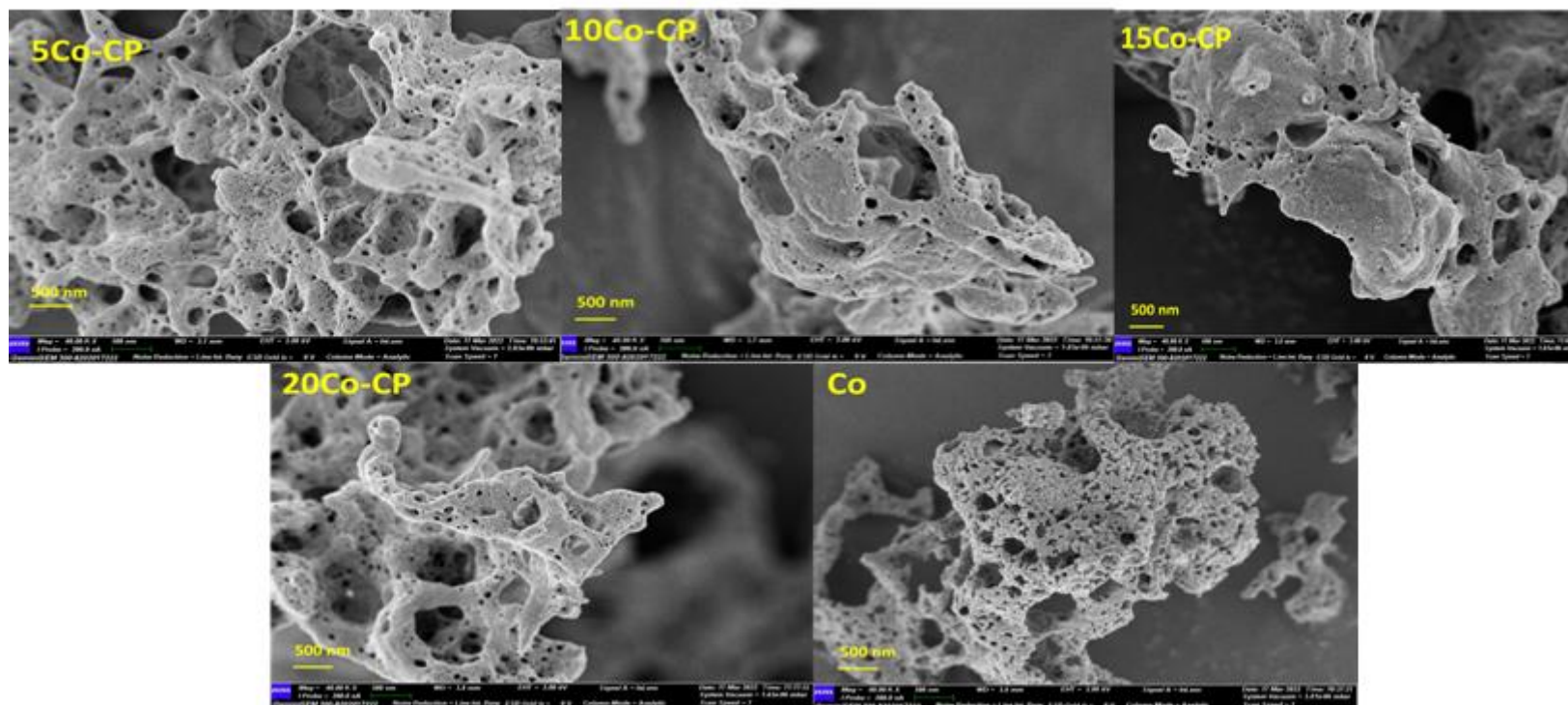


Figure. 6.3. FE-SEM images of Co_x ($x=0-0.20$) $(\text{Ce}_{0.9}\text{Pr}_{0.1})_{1-x}\text{O}_{2-\delta}$ Catalysts

The N₂ adsorption-desorption isotherm and the pore size distribution of all the catalysts are represented in **Figure. 6.5 (a) and (b)**, respectively. It can be seen that most of the Co-CP catalysts showed Type IV isotherms with an H3 hysteresis loop, confirming the presence of mesopores. Mesopores in such type of isotherm are filled by capillary condensation, which opens up and continues to higher relative pressure (Thommes et al. 2015). 20 Co CP and pure Co catalysts showed minimum adsorbance with Type IV with an H4 hysteresis loop (**Figure. 6.5 (a)**). In this case, the N₂ uptake at low P/P₀ is generally associated with micropore filling (Thommes et al. 2015).

The pore size distributions of the catalysts from the BJH method are shown in **Figure. 6.5(b)**. The catalysts expressed pore diameters ranging from ~5 to 30 nm for all the developed catalysts with narrow pore size distribution around 2 to 10 nm. The porous nature improves the soot to catalyst contact points which helps to improvise the catalytic activity. According to Liu et al. 2016, the number of contact points plays a more vital role in enhancing the catalytic activity.

Table 6.2: BET Analysis of Co_{x(x=0-0.2)} (Ce_{0.9}Pr_{0.1})_(1-x) O_{2-δ} Catalysts

Catalyst	BET S _A (m ² /g)	Pore Volume (cc/g)	Avg. Pore Size (dia) (nm)
CP	31	0.217	11.46
5 Co-CP	34	0.083	20.64
10 Co-CP	28	0.049	06.47
15 Co-CP	31	0.080	10.58
20 Co-CP	22	0.030	07.40
Co	13	0.023	07.10

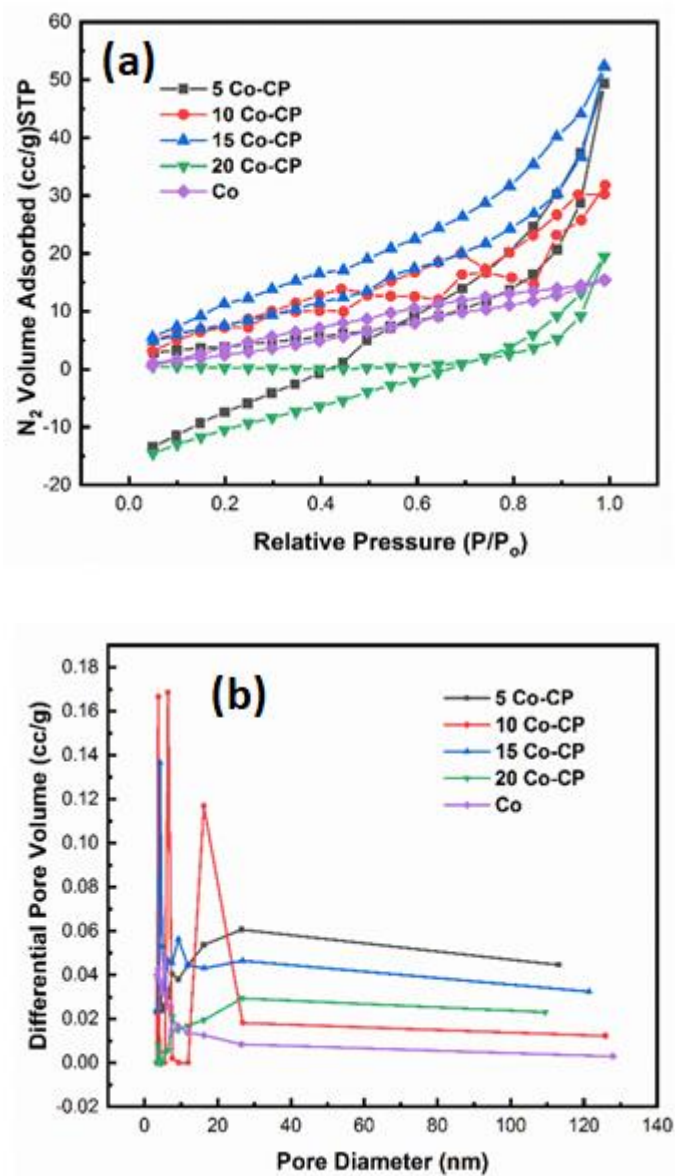


Figure 6.4. (a) N₂ adsorption-desorption Isotherm (b) BJH pore size analysis of Co_x (x=0-0.20) (Ce_{0.9}Pr_{0.1})_(1-x) O_{2-δ} Catalysts

6.5. XPS ANALYSIS

XPS analyses are performed to study the effect of the catalysts' redox ability and surface properties on the soot oxidation. **Figure. 6.5 (a)** denotes XPS spectra for Ce 3d, and based on the literature reported, the Ce 3d spectrum is assigned into two sets corresponding to 3d_{3/2} and 3d_{5/2} orbitals (Fu et al. 2014; Mittal et al. 2018). After deconvolution, the peaks are split according to the valence states and assigned based on the binding energies (Fu et al. 2014; Holgado et al. 2000; Mittal et al. 2018).

According to Li et al. 2015 the peaks ~ 882.9 eV, 888.6 eV, 898.4 eV, 901.2 eV, 907.2 eV, and 917.0eV can be assigned to Ce⁴⁺, and peaks ~880.7 eV, 885.7 eV, 899.3 eV, and 904.3eV can be assigned to that of Ce³⁺ (Li et al. 2015). The area under the curves is noted for further calculating the redox ability concerning Ce³⁺; hence $Ce^{3+} / (Ce^{3+} + Ce^{4+})$ is calculated and tabulated in **Table 6.3**.

It was observed that incorporating 5 mol% of Co in the CP concentration of Ce³⁺ ions improved. For CeO₂-based catalysts, the oxygen vacancies are significant for catalytic performance (Yang et al. 2010). The presence of high Ce³⁺ is related to creating more oxygen vacancies. For soot oxidation, creating more vacancies indicates gaining active oxygen species during the reaction, which is vital for redox ability (Qin et al. 2019).

Figure. 6.5b demonstrates the XPS spectra for Pr 3d spectrum; the three-fold envelopes are noticed. The envelope, ~ 930 to 950eV and ~ 950 to 970eV, corresponds to Pr 3d_{5/2} and Pr 3d_{3/2} orbitals, respectively. The last envelope of Pr 3d is observed at ~ 975eV, and the Auger peak corresponds to the OKLL oxygen (Paunovi et al. 2012). The deconvoluted peaks corresponding to Pr³⁺ and Pr⁴⁺ oxidation states confirm that Pr exists in multi-oxidation states in the developed catalysts. The peak positions ~ 927.6 eV and 932.9 eV are assigned to Pr³⁺, and the remaining corresponding to Pr⁴⁺ oxidation states (Krishna et al. 2007; Paunovi et al. 2012).

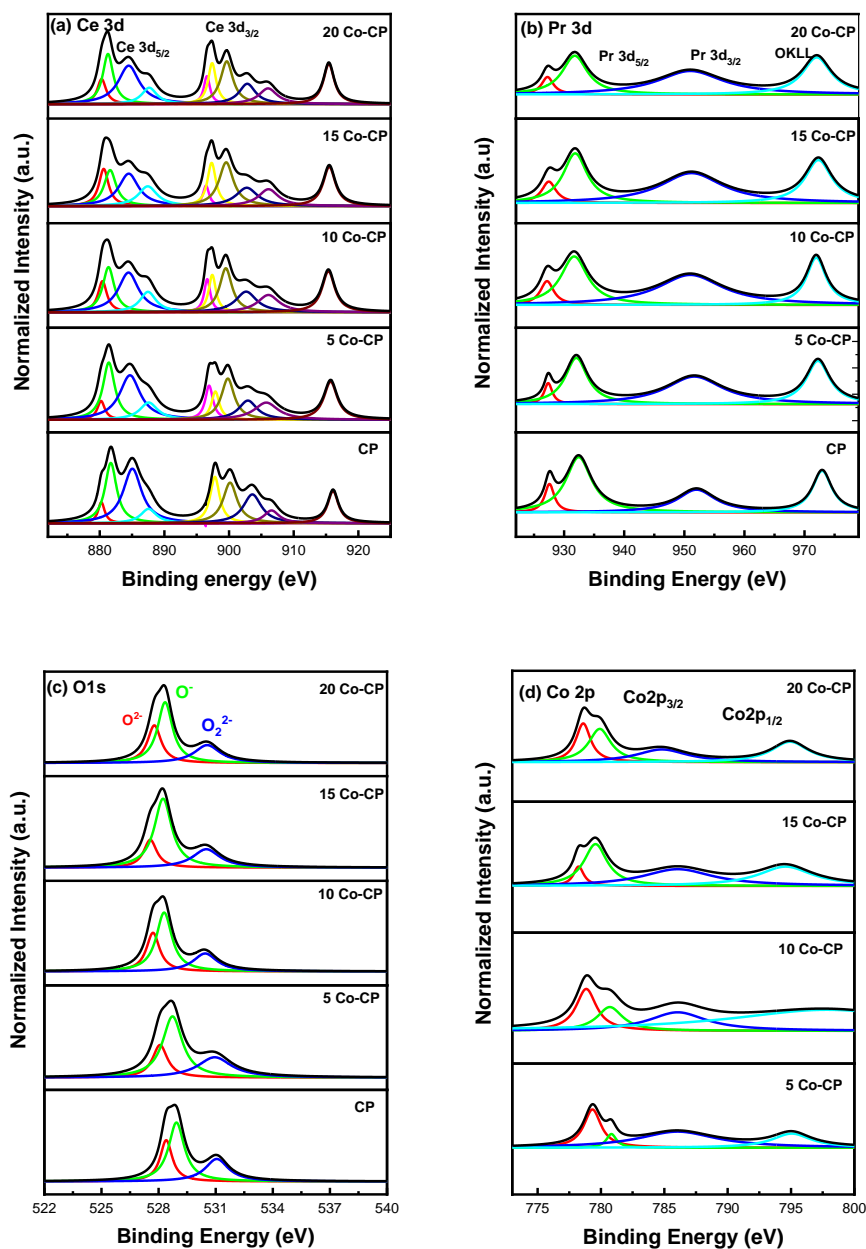


Figure. 6.5 (a)Ce 3d (b)Pr 3d (c)Co 2p (d) O 1s XPS spectra for of Co_x ($x=0-0.20$) $(\text{Ce}_{0.9}\text{Pr}_{0.1})_{1-x}\text{O}_{2-\delta}$ Catalysts

The characteristic oxygen Auger peak-OKLL ~ 973.3 eV was noticed in all the catalysts. Pr^{3+} redox ratio ($\text{Pr}^{3+}/(\text{Pr}^{3+} + \text{Pr}^{4+})$) was calculated and tabulated in **Table 3**. It can be seen that Pr^{3+} concentration was higher on 5 Co-CP catalysts than the other CP and other Co-doped CP catalysts.

Figure. 6.5c shows the Co2p spectra, which have two envelopes at ~ 780 eV and 795 eV, attributed to $\text{Co}2p_{3/2}$ and $\text{Co}2p_{1/2}$, respectively (Xie et al. 2009; Guangjun et al. 2019; Stegmayer et al. 2022). The peak at ~ 785 eV is referred to as a satellite peak. The peaks corresponding to two valence states, Co^{3+} and Co^{2+} , were noticed as the deconvolution of Co2p spectra revealed the peak split at ~ 779 eV (Co^{3+}) and 781eV (Co^{2+}) and 796 eV (Co^{3+}) (Guangjun et al. 2019; Stegmayer et al. 2022). The concentration ratio of Co^{3+} and Co^{2+} was calculated and tabulated in **Table 6.3**. It can be seen that 5 Co-CP showed a high concentration (~ 0.89) of Co^{3+} ions, and 15 Co-CP had a high concentration of Co^{2+} ions. The literature study reported that Co^{3+} plays a more vital role than Co^{2+} in an oxidation reaction (Xie et al. 2009; Guangjun et al. 2019). Co^{3+} is also known as the reactive site, and in most cases, Co^{2+} cations remain inactive (Guangjun et al. 2019).

The O1s spectra (**Figure. 6.5d**) reveal the information corresponding to the lattice oxygen species (O^{2-}) and the chemisorbed surface oxygen species (O^- and O_2^{2-}) present. It can also be noticed from **Table 6.3** that CP had the highest surface chemisorbed oxygen species O^- and O_2^{2-} (~ 0.82), and 20 Co-CP possessed high lattice oxygen species (O^{2-}); both the species may contribute to enhancing the catalytic activity (Liang et al. 2007a). Surface-active oxygen species (O^-) are also critical in improving catalytic activity at high temperatures (Wei et al. 2011). The active oxygen species obtained near binding energies ~ 530 eV play a crucial role in oxidation reactions (Jones et al. 2015), which are generally assigned to O^- species.

Table 6.3: Reducibility ratio and Surface Oxygen species ratio of $\text{Co}_{x(x=0-0.2)}(\text{Ce}_{0.9}\text{Pr}_{0.1})_{(1-x)}\text{O}_{2-\delta}$ Catalysts

Catalyst	Reducibility Ratio				Lattice Oxygen ratio	Adsorbed Oxygen ratio	
	$\frac{\text{Ce}^{3+}}{\text{Ce}^{3+} + \text{Ce}^{4+}}$	$\frac{\text{Pr}^{3+}}{\text{Pr}^{3+} + \text{Pr}^{4+}}$	$\frac{\text{Co}^{3+}}{\text{Co}^{3+} + \text{Co}^{2+}}$	$\frac{\text{Co}^{2+}}{\text{Co}^{3+} + \text{Co}^{2+}}$		$\frac{\text{O}^-}{\text{O}^{2-} + \text{O}^- + \text{O}_2^{2-}}$	$\frac{\text{O}_2^{2-}}{\text{O}^{2-} + \text{O}^- + \text{O}_2^{2-}}$
CP	0.42	0.15	-	-	0.26	0.49	0.24
5 Co-CP	0.46	0.66	0.90	0.10	0.25	0.48	0.26
10 Co-CP	0.27	0.26	0.43	0.56	0.21	0.47	0.23
15 Co-CP	0.42	0.39	0.56	0.44	0.20	0.48	0.28
20 Co-CP	0.42	0.46	0.59	0.43	0.26	0.48	0.25

The presence of lattice Oxygen species also plays a significant role in catalytic soot oxidation if the surface area is low (Liang et al. 2007b). The lattice oxygen species ratio presented in the table revealed that 20 Co-CP had the highest (~0.80) O^{2-} species than other Co-doped CP catalysts. But the effect of secondary phases in 20 Co-CP may also demonstrate the catalytic behavior. 5 Co-CP confirmed solid solution formation with better reducible surface ions than all other catalysts with a high Ce^{3+} , Pr^{3+} , and Co^{3+} surface ions concentration ratio. Reddy et al. 2009a and Krishna et al. 2007a demonstrated that surface enrichment of Ce^{3+} and Pr^{3+} ions improves soot oxidation activity.

6.6. SOOT OXIDATION ACTIVITY

Figure.6.6 depicts soot conversion curves with an increase in temperature. The soot oxidation is carried out in triplicates to ensure the repeatability of the catalyst. The T_{50} temperature is noted for all the catalysts and is listed in **Table 6.4**. From the table, it can be noticed that there was a significant reduction in T_{50} on loading Co to CP. CP showed a T_{50} of 408 ± 4 °C, whereas the lowest T_{50} at 349 ± 1 °C was obtained by 5Co-CP catalyst.

Further, no change was noticed in T_{50} for 15 Co-CP and 20 Co-CP. Pure Co also showed a low T_{50} of 402 ± 2 °C, and loading Co to the CP catalyst system influenced catalytic activity significantly. From XRD and Raman spectroscopy studies, the solid solution was formed by 5 Co-CP without evidence of an impurity phase. The secondary phases of Co_3O_4 were detected by Raman spectroscopy for 15 Co-CP and 20 Co-CP. Hence, adding small amounts (5 mol %) of Co into the CP catalyst system improves catalytic activity.

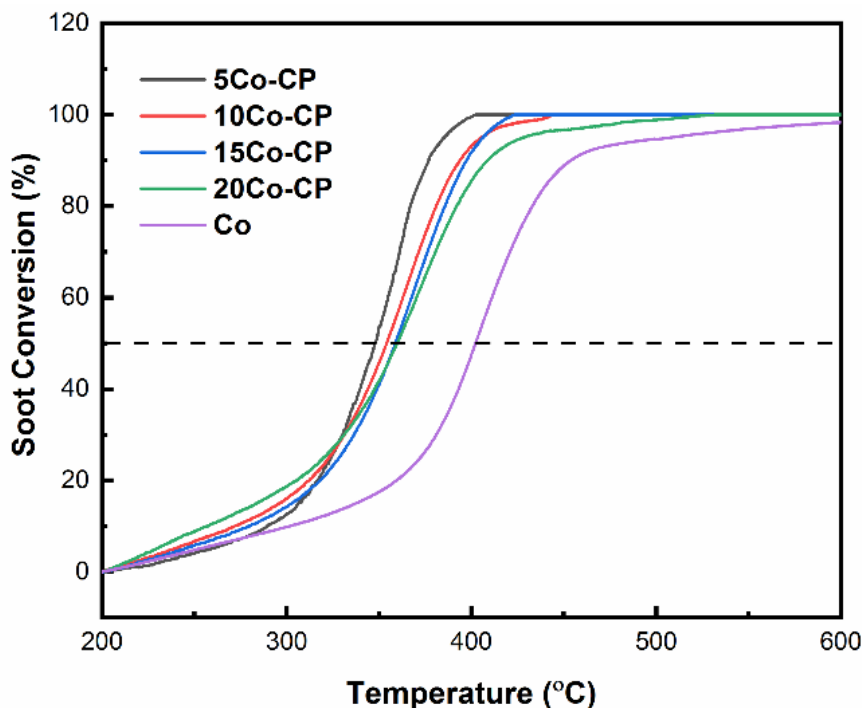


Figure. 6.6. Soot Oxidation curves for Co_x ($x=0-0.20$) $(\text{Ce}_{0.9}\text{Pr}_{0.1})_{(1-x)}\text{O}_{2-\delta}$ Catalysts

The parameters and descriptors that may enhance catalytic activity were analyzed from the characterization studies of the developed catalysts. The XRD studies showed that the crystallite size for Co_x ($x=0.05-0.20$) $(\text{Ce}_{0.9}\text{Pr}_{0.1})_{(1-x)}\text{O}_{2-\delta}$ catalysts were below 10 nm. Raman analysis confirmed the presence of Oxygen vacancy peaks for all the catalysts. 5 Co-CP had the highest Oxygen vacancy ratio ($I_{\text{Ov}}/I_{\text{F}2g}$) of ~ 0.82 . The S_A of $34 \text{ m}^2/\text{g}$ was highest for 5 Co-CP, and the surface area decreased on further Co addition to CP. From BJH analysis, the catalysts showed mesopores with average pore size diameters ranging from 1.50 nm (20 Co-CP) to 9.8 nm (5Co-CP).

The porous nature of the catalysts also helps improve contact points between soot and catalyst, and FE-SEM analysis also revealed the catalysts prepared are porous. The XPS analysis showed that the surface ion concentration did not vary significantly for Ce^{3+} concentration. 5 Co-CP had better reducibility than all other catalysts with a high Ce^{3+} , Pr^{3+} , and Co^{3+} surface ions concentration ratio. On the other hand, CP had better active surface adsorbed species of ~ 0.82 . 20 Cr-CP had a better-lattice oxygen species ratio ($\text{O}^{2-} = 0.28$).

Reddy et al. 2009a observations revealed an increase of Ce^{3+} species and enrichment of Pr^{3+} , indicating enhanced reducibility of the CeO_2 upon Pr doping. Krishna et al. 2007a reported improvement of $\text{Pr}^{3+/4+}$ reducible ions on the surface on doping with CeO_2 improves soot oxidation activity. The XPS results of Zhang et al. 2016 demonstrated that Co is present as Co^{3+} on the surface of the catalysts, and more surface oxygen species were observed, which provided more catalytic active species for soot combustion. It was also revealed that adding Co_3O_4 improved the interaction between Co and Ce. Hence, in the present study, 5 Co-CP showed better T_{50} of $348 \pm 1^\circ\text{C}$ mainly due to better reducible Ce^{3+} , Pr^{3+} , and Co^{3+} ions on the surface.

6.7. SOOT OXIDATION KINETICS

For kinetic studies, the soot oxidation reaction on the catalysts was performed in TGA at different heating rates (5,10,15,20 $^\circ\text{C}/\text{min}$). The current study determines the E_a value using model-free methods such as FWO, KAS, and CR methods (Chen et al. 1993; Ebrahimi-Kahrizsangi and Abbasi 2008; Ganiger et al. 2022; López-Fonseca et al. 2007; Ozawa 1992; Starink 2003). FWO plots (**Figure A6.1**), KAS plots (**Figure A6.2**), CR plots (**Figure A6.3**), and Am plots (**Figure A6.4**) are plotted for all the catalysts and are provided in the appendix section. The E_a and A values obtained are represented in **Table 6.4**, along with the Avrami integer (m) values.

The table shows that the E_a values obtained from all the methods show a slight difference, and the E_a values obtained from the FWO method varied from 92 to 127 kJ mol⁻¹. Pure Co obtained the highest E_a and A values by all reported methods, and the change in E_a values wasn't significant when Co was introduced to the CP system. The E_a value reported from literature for soot combustion without a catalyst ranges from 130 to 160 kJ mol⁻¹ (Neeft et al. 1997; Shenoy et al. 2019).

The A values (**Table 6.4**) from A_m method ranged from 23.25 min⁻¹ (Co) to 15.50 min⁻¹ (CP). It was noticed that the A values increased on the incorporation of Co into the CP catalyst system. The computations of E_a and pre-exponential factor A were reported by Fonseca et al. (López-Fonseca et al. 2007) and Sbirrazzuoli et al. 2013 for the soot combustion reaction. The E_a and A values by CR method were reported to be 79.76 kJmol⁻¹ and 18.84 min⁻¹, respectively, for bare soot without any catalyst at 10 °C min⁻¹ (Sbirrazzuoli 2013). When "m" is close to unity or "1" in the A_m model, it agrees with the first-order chemical reaction, and $1.5 < m < 4$ corresponds to the Avrami- Erofeev model (Ganiger et al. 2022). In the present study, "m" values reported in **Table 6.4** for the catalysts ranged from 0.70 to 1.35; hence the possibility of various reaction models can be predicted. The m value decreased below unity when Co was incorporated into CP, which might indicate the deviation in the catalyst's reaction models (Ganiger et al. 2022).

The master plots with $g(\alpha)$ values calculated for different reaction models by varying conversion (α) are plotted and are shown in **Figure S5**. The reaction models coinciding for all the catalysts were noted and are provided in **Table 6.4**. CP followed the nucleation and growth model ($A_{1.5}$) and phase boundary-controlled reaction (P_1 and P_2). In contrast, the Co-CP catalyst followed the Power law (L_4), 2 and 4-dimensional diffusion model (D_2 and D_4), and First (A_1) and second-order reactions (R_2). The reaction models followed may vary at lower and higher " α " values and can be observed in the master plots (**Figure S5**). The Arrhenius parameters obtained depend mainly on the kinetic model and heating rates to some extent (López-Fonseca et al. 2007).

Investigation of Cobalt-Doped Ceria-Praseodymium Catalysts for Soot Oxidation Activity and its Kinetics

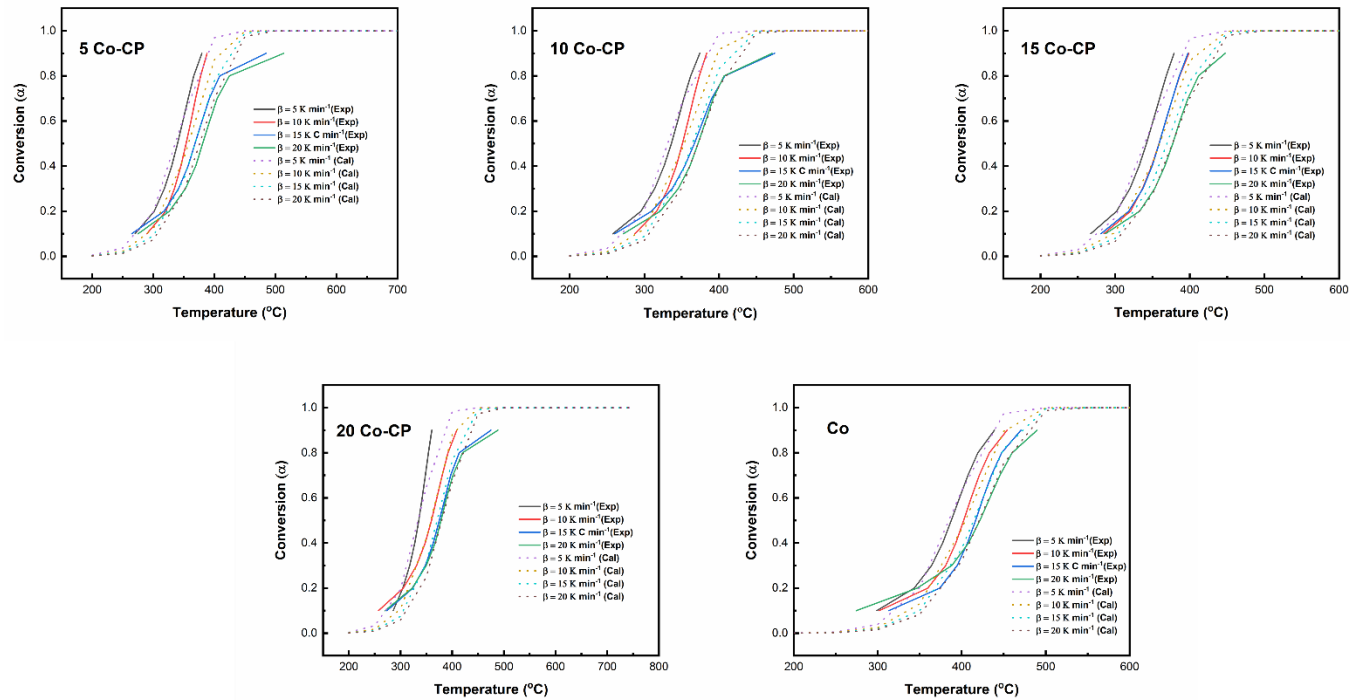


Figure 6.7. Experimental and calculated Curves for $\text{Co}_x(x=0.05-0.2) (\text{Ce}_{0.9}\text{Pr}_{0.1})_{(1-x)} \text{O}_{2-\delta}$ Catalysts

Figure 6.7 illustrates the thermo-analytical curves constructed using the kinetic triplets obtained for experimental and calculated data. It can be noticed from the figure that catalysts had good consistency for the α value between 0.2 to 0.8. Hence, the nucleation and Growth model play a crucial role in the reaction for Co-doped CP catalysts.

Figure 6.8 (a) and (b) demonstrate $d\alpha/dT$ vs. temperature and $\ln(k)$ vs. $1/T$ plots, respectively, for $\text{Co}_{(x=0.05-0.2)}(\text{Ce}_{0.9}\text{Pr}_{0.1})_{1-x}\text{O}_{2-\delta}$ samples. From **Figure 6.8 (a)**, it can be noticed that the 5 Co-CP catalyst showed a better reaction rate than compared to other catalysts. From **Figure 6.8 (b)**, the kinetic activity is high for 5 Co-CP and the least for the Pure Co sample.

Hence it can be concluded that on the incorporation of Co to CP catalyst system, there's a slight variation in E_a value, A values increased, and the "m" value decreased. Co-CP catalysts followed A_1 , D_2 , D_4 , L_4 , and R_2 irrespective of CP concentration, whereas CP followed $A_{1.5}$, P_1 , and P_2 reaction models. 5 Co-CP performed as a better soot oxidation catalyst mainly due to the presence of redox surface ions and high oxygen vacancy ratio.

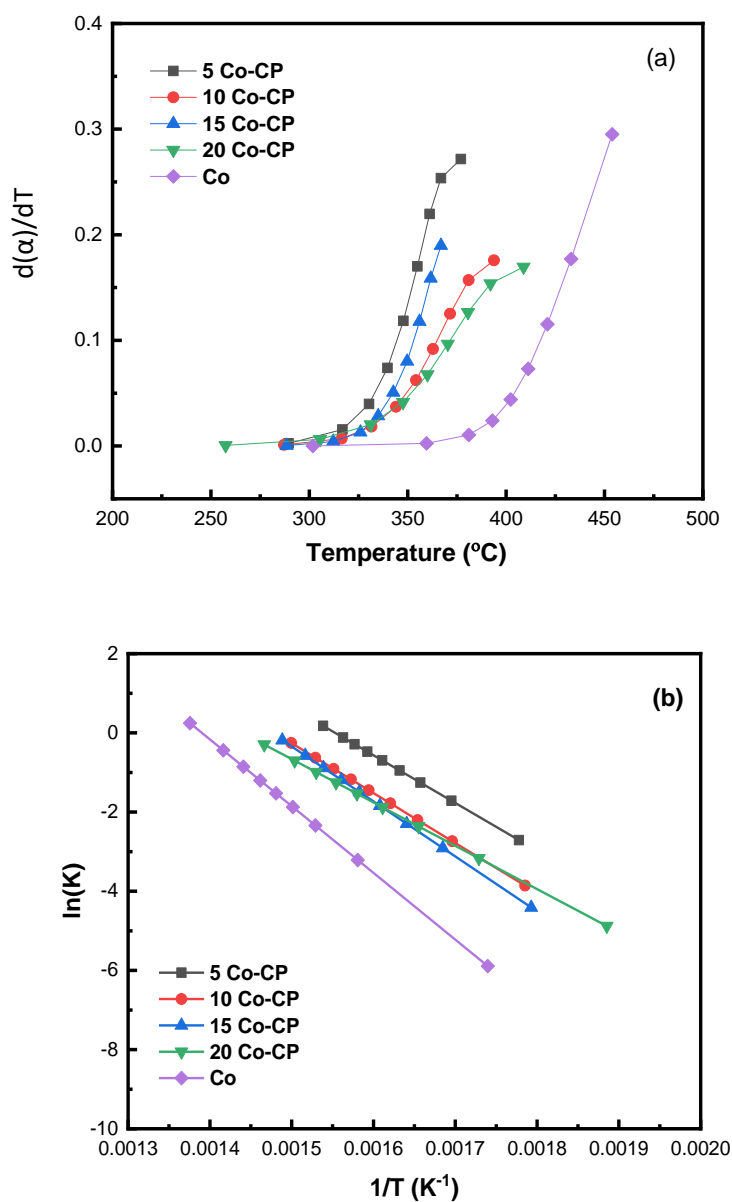


Figure 6.8. (a) Rate vs. Temperature plot (b) Arrhenius plot for $Co_x(x=0.05-0.2)$ $(Ce_{0.9}Pr_{0.1})_{1-x}O_{2-\delta}$ Catalysts

Table 6.4: T₅₀ and Kinetic parameters of Co_{x(x=0-0.2)} (Ce_{0.9}Pr_{0.1})_(1-x)O_{2-δ} Catalysts

Catalysts	T ₅₀ (°C)	E _a (kJ mol ⁻¹)			Reaction Model	A × 10 ¹⁰ (min ⁻¹)		m
		Ozawa method	KAS method	CR method		Am method	CR method	
CP	408±4	111	96	94	A _{1.5} ,P ₁ ,P ₂	0.13	0.11	1.35
5 Co-CP	349±1	104	101	105	A ₁ ,L ₄ ,D ₂ ,D ₄ ,R ₂	0.12	0.05	0.76
10 Co-CP	351±2	105	103	104	A ₁ ,L ₄ ,D ₂ ,D ₄ ,R ₂	0.07	0.06	0.82
15 Co-CP	358±2	115	110	116	A ₁ ,L ₄ ,D ₂ ,D ₄ ,R ₂	0.008	0.006	0.81
20 Co-CP	359±3	92	97	101	A ₁ ,L ₄ ,D ₂ ,D ₄ ,R ₂	1.51	1.25	0.70
Co	402±2	127	125	123	A ₁ ,L ₄ ,D ₂ ,D ₄ ,R ₂	0.13	0.11	0.68

6.8. CONCLUSION

Co_x ($x=0 - 0.20$) $(\text{Ce}_{0.9}\text{Pr}_{0.1})_{(1-x)}\text{O}_{2-\delta}$ and Pure Co catalysts were successfully synthesized by solution combustion synthesis. From XRD studies, catalysts revealed the fluorite structure of CeO_2 , and the crystallite size was in the range of ~ 9 nm. Pure Co and CP had a crystallite size of ~ 28 nm and 14 nm, respectively. Facet ratios for $\{110\}/\{111\}$ and $\{100\}/\{111\}$ was obtained high (~ 0.40 and 0.44 respectively) for 15 Co-CP. The Raman analysis of increasing Co-loading concentration (15 Co-CP and 20 Co-CP) showed the presence of a secondary phase of Co_3O_4 . 5 Co-CP had the highest Oxygen vacancy ratio ($I_{\text{Ov}}/I_{\text{F2g}}$) of 0.83. FE-SEM micrographs showed the porous nature of the catalyst. Further, BET surface area and BJH pore size analysis determined that all the catalysts were micro and mesoporous. The S_A of the catalysts was 34 to 13 m^2/g , with 5 Co-CP possessing the highest S_A of 34 m^2/g . 5 Co-CP had better reducibility than all other Co-CP catalysts with high concentrations of Ce^{3+} , Pr^{3+} , and Co^{3+} ions. On the other hand, CP and 20 Co-CP, respectively, had better active surface adsorbed species (O^- & O_2^{2-}) and the lattice oxygen species (O^{2-}). From TGA analysis for soot oxidation, a better T_{50} of 349 ± 1 °C was achieved by 5 Co-CP catalysts. From the descriptors controlling oxidation reaction, the better T_{50} may be attributed to solid solution formation and better redox properties of 5 Co-CP.

It can be noted that the 5Co-CP catalyst system showed better soot oxidation activity, and the descriptors controlling the catalytic activity are phase cooperation (solid-solution formation) and better redox properties compared to Co-CP and CP catalyst systems. In the next chapter, Iron-doped Ceria-Praseodymium catalysts were synthesized, characterized, and obtained soot oxidation activity and kinetic behavior. The descriptors controlling the soot oxidation activity of the Iron-doped Ceria-Praseodymium catalysts system are further explored in the next chapter.

CHAPTER 7

EFFECT OF IRON-DOPED CERIA-PRASEODYMIUM CATALYST ON SOOT OXIDATION ACTIVITY

Several catalytic materials consisting of transition metals such as Mn, Fe, Co, Ni, and Cu were developed in the past decade. The redox ability of such transition metals can efficiently enhance soot oxidation activity as the mechanism mainly depends on forming active oxygen species, which aids soot oxidation. Fe-oxide is one of the essential transition metal oxides, exhibiting different phases such as FeO, Fe₂O₃, and Fe₃O₄. Fe-oxide is also cost-effective and environment-friendly (Mallick and Dash 2013). Fe oxide is a mixture of Fe and O ions, where the ionic size of oxygen is more prominent than Fe, and Fe exists in Fe²⁺ or Fe³⁺ states, providing tetrahedral or octahedral linkages. Hence, the spatial displacement of O completes the crystal structure (Maggi et al. 2017).

Zhang et al. 2010 investigated Fe-doped Ce catalysts and reported that the redox cycle of Fe plays a vital role in catalytic reactions. Fe³⁺ provides active oxygen species to oxidize soot and reduce it to Fe²⁺. Fe²⁺ can then convert back to Fe³⁺ on interaction with Ce (Zhang et al. 2010). Based on different ratios of Fe-doping, the number of active sites can vary, as Fe-doping can alter the fluorite structure and create more oxygen vacancies. Hence, the doping ratio also affects the catalyst activity and needs to be optimized with reaction conditions (Li et al. 2019).

7.1. X-RAY DIFFRACTION (XRD) ANALYSIS

The XRD spectra for $\text{Fe}_{x(x=0-0.2)} (\text{Ce}_{0.9}\text{Pr}_{0.1})_{1-x} \text{O}_{2-\delta}$ catalysts developed by the SCS method are displayed in **Figure 7.1**. From the figure, it can be noticed that all the doped samples ensured the fluorite structure of Ce. The planes (111), (200), (220), (311), (222), (400), (331), (422) correspond to the characteristic fluorite CeO_2 (Reddy et al. 2011; Shajahan et al. 2018). The slight shift in peaks towards lower 2θ was observed due to variation in the ionic size of Fe from Ce and Pr ions. The planes of pure Fe viz. (220), (311), (222), (400), (511), and (440) were relevant to the crystalline structure of Fe_2O_3 (Aliahmad and Nasiri Moghaddam 2013; Arumugam et al. 2020).

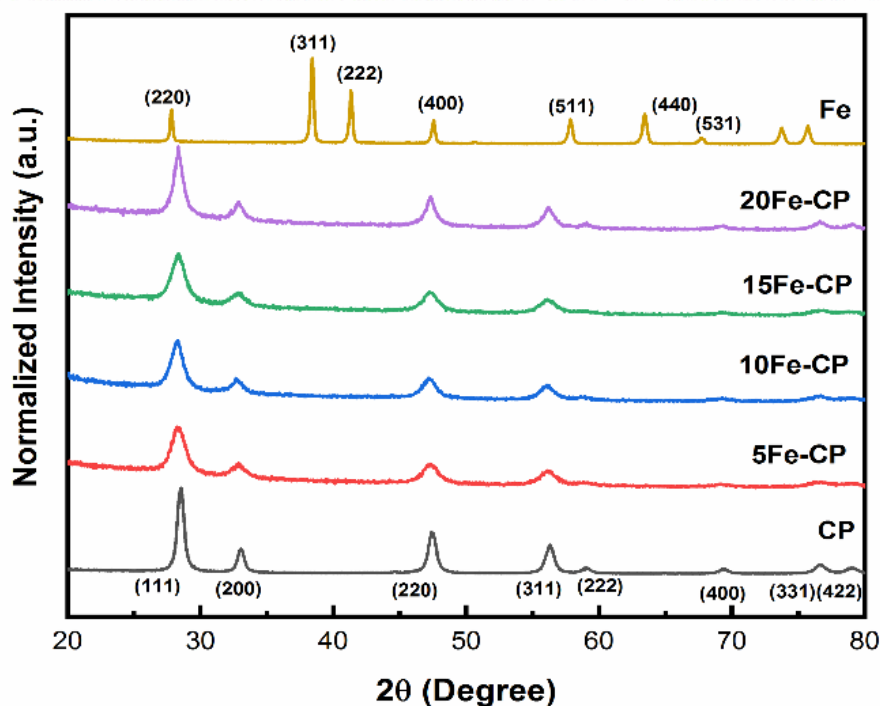


Figure 7.1: XRD Spectra of $\text{Fe}_{x(x=0-0.2)} (\text{Ce}_{0.9}\text{Pr}_{0.1})_{1-x} \text{O}_{2-\delta}$ Catalysts.

The physicochemical properties obtained from the XRD analysis are displayed in **Table 7.1**. The crystallite size calculated ranges from 6-31 nm. It can be seen that the crystallite size decreased for Fe-doped CP catalysts than for pure CP catalyst systems. 5 Fe-CP displayed the smallest crystallite size and highest lattice strain of 6 nm and 0.0222, respectively. In contrast, Pure Fe had a large crystallite size of 31.36 nm and a lower lattice strain of 0.0035. It can be observed from the Table that after the incorporation of Fe into the CP catalyst system, there was an increase in {110}/{111} facet ratio when compared to CP but no significant variation in {100}/{111} facet ratio. The physicochemical parameters deduced from XRD analysis, such as smaller crystallite size, increased lattice stain, and improved facets, significantly enhance the catalytic soot oxidation activity. It was noticed that there was a significant variation in physicochemical properties after the incorporation of Fe into the CP catalyst system, which may further influence catalytic performance.

7.2. RAMAN SPECTROSCOPY ANALYSIS

Figure 7.2. portrays Raman spectra for $\text{Fe}_{x(x=0-0.2)}(\text{Ce}_{0.9}\text{Pr}_{0.1})_{(1-x)}\text{O}_{2-\delta}$ catalysts. The characteristic peak observed in the spectra at $\sim 465\text{ cm}^{-1}$ for all Fe-doped samples can be allotted to the active F_{2g} Raman modes of CeO_2 (Mukherjee et al. 2016; Patil et al. 2019; Shajahan et al. 2018). This peak demonstrates the bending modes of symmetric breathing of O_2 around Ce atoms (Mukherjee et al. 2016; Patil et al. 2019; Shajahan et al. 2018).

Another significant peak at $\sim 560\text{ cm}^{-1}$ in all the doped samples is assigned to Oxygen Vacancies (O_v). No significant shift in the F_{2g} peak was detected in all the doped samples. For pure Fe, the Raman modes corresponding to Fe_2O_3 were observed with " A_{1g} " and " E_g " modes. A_{1g} modes were noticed at ~ 225 and 498 cm^{-1} , whereas E_g modes were present at ~ 247 , 293, 299, 412, and 613 cm^{-1} (Qayoom et al. 2020; Santillán et al. 2017).

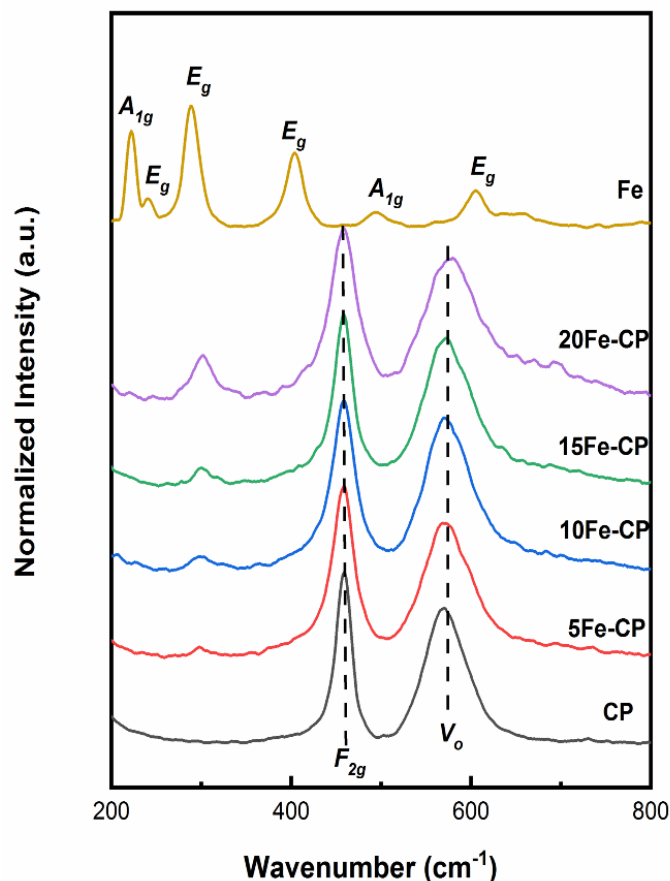


Figure 7.2: Raman spectra of $\text{Fe}_{x(x=0-0.2)}(\text{Ce}_{0.9}\text{Pr}_{0.1})_{1-x}\text{O}_{2-\delta}$ catalysts.

All Fe-doped CP displayed E_g mode at ~ 247 , indicating the presence of a secondary phase. The intensity ratios ($I_{O_v}/I_{F_{2g}}$) of Oxygen vacancy peaks to characteristic F_{2g} of Ce were calculated for all the doped samples and tabulated in **Table 7.1**. The $I_{O_v}/I_{F_{2g}}$ of 10 Fe-CP was the highest (0.89) compared to all other samples. O_v and secondary phase (Fe_2O_3) existence may benefit the soot oxidation (Shenoy et al. 2019).

Table 7.1. Physicochemical properties of $\text{Fe}_{x(x=0-0.2)}(\text{Ce}_{0.9}\text{Pr}_{0.1})_{(1-x)}\text{O}_{2-\delta}$ from XRD and Raman spectroscopy Analysis.

Sample	Crystallite Size (nm)	Lattice strain (ϵ)	Facet Ratio		I_{Ov}/I_{F2g}	Secondary Phase
			{110}/{111}	{100}/{111}		
CP	14	0.0107	0.24	0.38	0.77	-
5 Fe-CP	06	0.0222	0.38	0.35	0.77	Fe_2O_3
10 Fe-CP	07	0.0205	0.34	0.28	0.89	Fe_2O_3
15 Fe-CP	07	0.0222	0.34	0.40	0.85	Fe_2O_3
20 Fe-CP	09	0.0162	0.41	0.42	0.81	Fe_2O_3
Fe	31	0.0035	-	-	-	-

7.3. FE-SEM ANALYSIS

FE-SEM images (**500 nm scale**) for $\text{Fe}_{x(x=0-0.2)}(\text{Ce}_{0.9}\text{Pr}_{0.1})_{(1-x)}\text{O}_{2-\delta}$ catalysts are displayed in **Figure 7.3**. The images reveal the porous nature of the catalysts. It can be observed that the Fe-doped CP catalyst is highly porous, and as the concentration increases, the porous nature of the catalysts tends to decrease. It can also be observed that the pure Fe catalysts showed a network of rod-like structures. Porous catalysts generally improve the contact points of soot and catalysts, improving the catalytic behavior. BET-BJH analysis further confirms the porous nature of all the samples.

Effect of Iron-Doped Ceria-Praseodymium Catalysts for Soot Oxidation Activity and its Kinetics

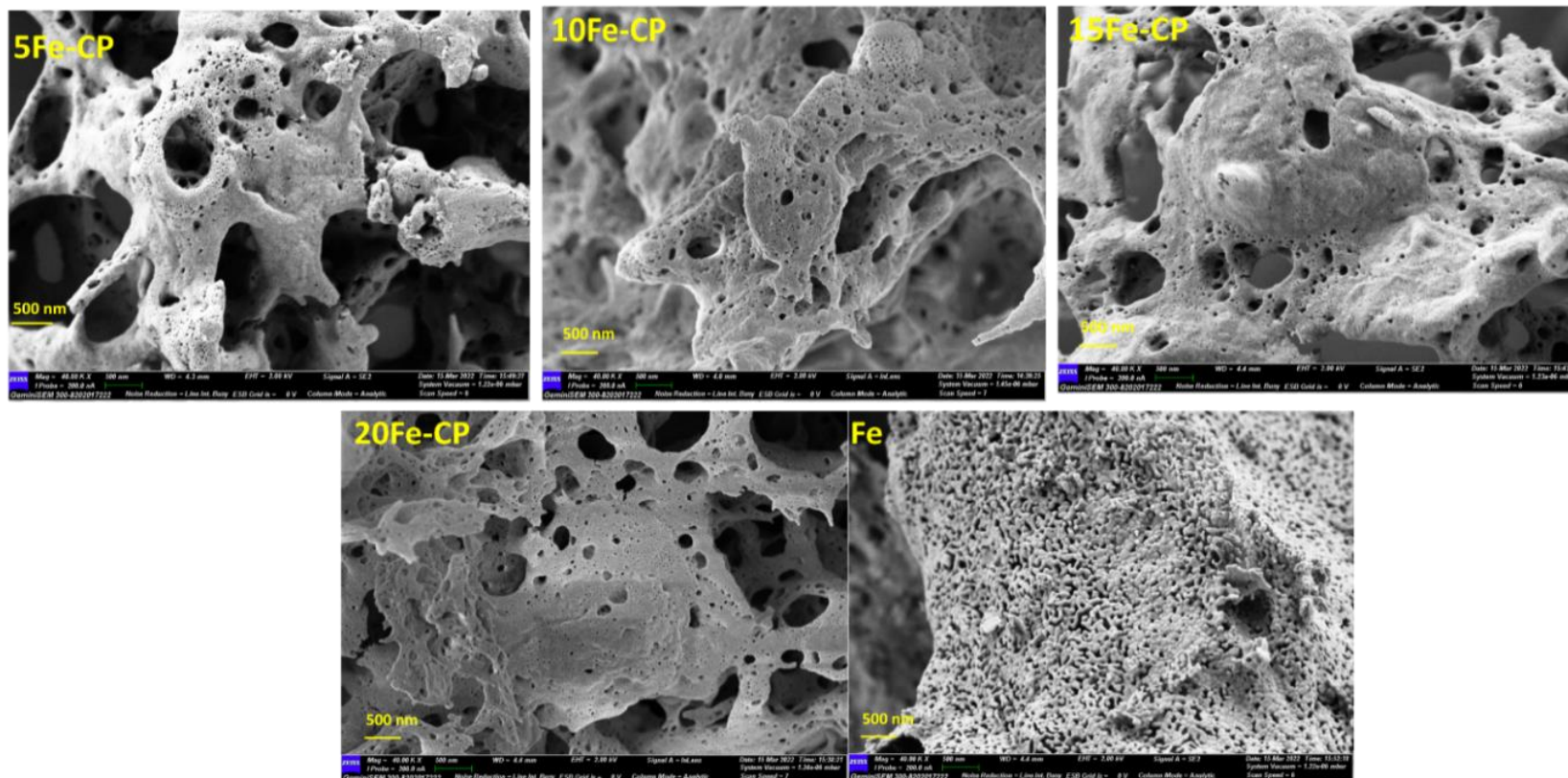


Figure 7.3. FE-SEM analysis of $\text{Fe}_x(x=0-0.2) (\text{Ce}_{0.9}\text{Pr}_{0.1})(1-x)\text{O}_{2-\delta}$ Catalysts (500nm)

A Study on the Effect of Transition Metal Dopants in Ceria Praseodymium Catalysts for Soot Oxidation Activity and its Kinetics

7.4. BET AND BJH PORE SIZE ANALYSIS

BET Surface area analysis and BJH Pore volume analysis were performed for all the catalysts to determine their influence on the catalytic activity summarized in **Table 7.2**. From the Table, it can be noticed that the surface area ranged from 15 -43 m²/g. CP catalyst had the highest surface area of 43 m²/g, while 20 Fe-CP and Pure Fe had the smallest surface area of 15 m²/g. CP catalyst also possessed a higher pore volume (0.217 cc/g), while 20 Fe-CP gained a high avg—pore size diameter of 5.33 nm.

Figure 7.4 (a) reveals the N₂ adsorption-desorption isotherms for all Fe-doped CP catalysts. All Fe-doped CP catalysts illustrated Type IV isotherms with an H3 hysteresis loop. Pure Fe showed minimum adsorbance with Type IV with an H4 hysteresis loop. The pore size distributions of the catalysts were calculated by the BJH method from the adsorption isotherm curves and are shown in **Figure 7.4 (b)**. The samples expressed narrow pore size distribution ranging from ~5 to 25 nm for all the developed catalysts confirming their mesoporous nature.

Table 7.2 BET-BJH Analysis of Fe_{x(x=0-0.2)} (Ce_{0.9}Pr_{0.1})_(1-x)O_{2-δ} Catalysts

Sample	BET S_A (m²/g)	Pore Volume (cc/g)	Avg. Pore Size (nm)
CP	31	0.217	11.46
5 Fe-CP	33	0.082	4.95
10 Fe-CP	32	0.074	4.70
15 Fe-CP	33	0.074	4.54
20 Fe-CP	15	0.071	5.33
Fe	15	0.023	3.00

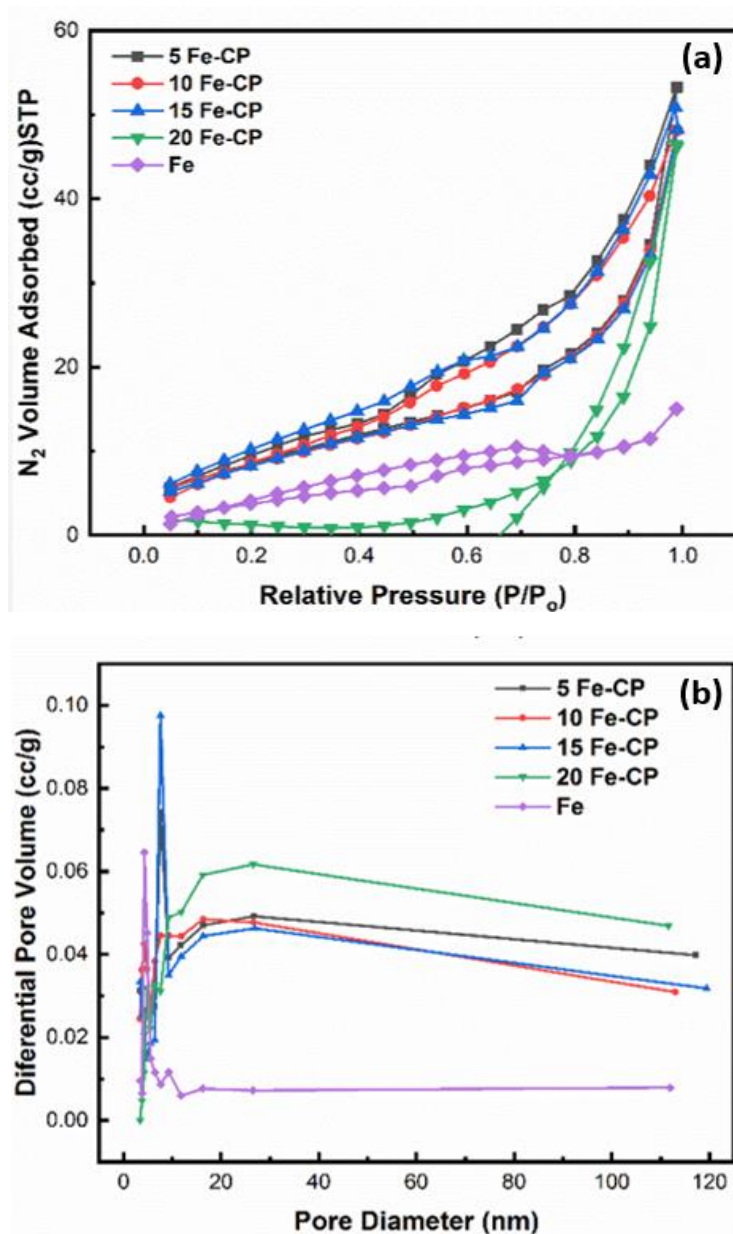


Figure 7.4 (a): Adsorption-Desorption isotherm (b): BJH Pore Size Distribution of $Fe_{x(x=0.05-0.2)}(Ce_{0.9}Pr_{0.1}(1-x)O_{2-\delta})$ Catalysts

7.5. XPS ANALYSIS

XPS analysis is performed to study the effect of the catalysts' redox ability and surface properties. **Figure 7.5** denotes XPS spectra for Ce 3d, Pr 3d, O1s and Fe 2p of $\text{Fe}_{x(x=0.05-0.2)}(\text{Ce}_{0.9}\text{Pr}_{0.1})_{1-x}$ catalysts. Based on the earlier works of literature reported, the Ce 3d spectrum is assigned into two sets corresponding to $3d_{3/2}$ and $3d_{5/2}$ orbitals (Fu et al. 2014; Mittal et al. 2018). The peak position assigned to the oxidation states Ce^{4+} and Ce^{3+} was noted in the literature reported (Fu et al. 2014; Holgado et al. 2000; Mittal et al. 2018).

The area under the curve was utilized to compute the reducibility ratio, $\text{Ce}^{3+}/(\text{Ce}^{3+}+\text{Ce}^{4+})$ ratio, and surface oxygen species ratio listed in **Table 7.3**. Similarly, the peaks for Pr^{3+} , Fe^{2+} , and Fe^{3+} were also assigned (Govardhan et al. 2022; Shenoy et al. 2019), and the reducibility ratio was calculated to check the presence of reducible ions in the catalysts presented in **Table 7.3**. From the Table, it can be seen that CP showed a slightly high reducibility ratio (0.42) for Ce^{3+} . 5 Fe-CP catalyst had higher Pr^{3+} ions (0.37) than all Fe-doped catalysts. 5 Fe-CP and 15 Fe-CP showed higher Fe^{3+} and Fe^{2+} ions concentrations, respectively. The presence of Fe^{2+} ions promotes catalytic activity by lowering soot oxidation temperatures (Shenoy et al. 2019).

The O1s spectra reveal the information corresponding to the lattice oxygen species (O^{2-}) and the chemisorbed oxygen species (O^- and O_2^{2-}). It was noticed that 5 Fe-CP and CP had a high concentration of O^{2-} (0.26) and O^- (0.46), respectively, whereas 20 Fe-CP had a high concentration of O_2^{2-} ions (0.58). 5 Fe-CP showed high Pr^{3+} , O^{2-} , and O^- ions and may improve catalytic performance better than other Fe-doped CP catalysts. Zhang et al. 2016 reported that a higher Ce^{3+} reducibility ratio infers the reduction of the metal oxide catalysts and, thus, higher oxygen vacancy. Similarly, Anantharaman et al. 2018 also reported that GDC samples synthesized by the EDTA Citrate method showed superior soot oxidation activity due to high Ce^{3+} and surface oxygen species.

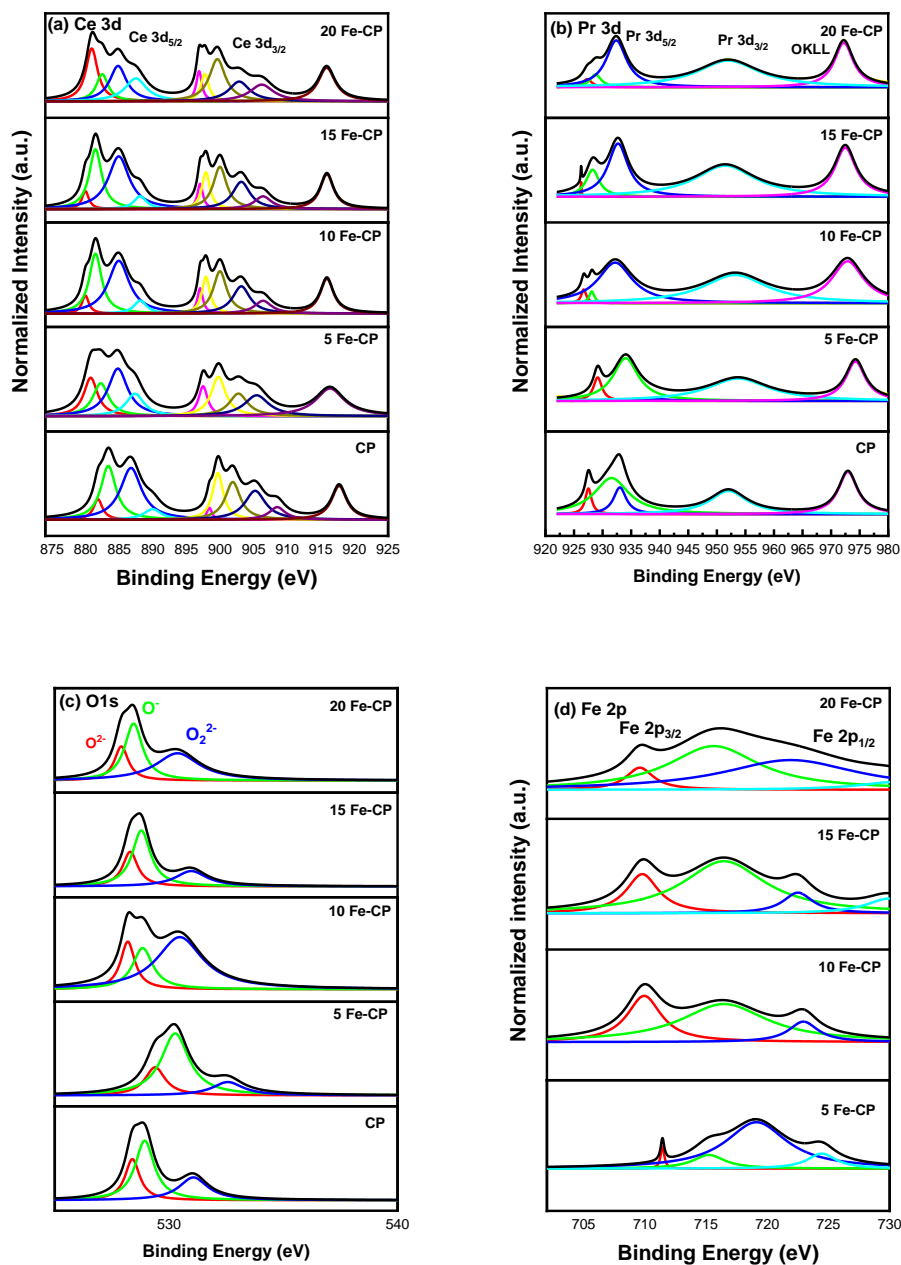


Figure 7.5 XPS (a) Ce3d (b) Pr3d (c) Co 2p (d) O1s spectra of Fe_x ($x=0-0.20$) ($\text{Ce}_{0.9}\text{Pr}_{0.1}$) $_{1-x}$ $\text{O}_{2-\delta}$ Catalysts.

Table 7.3: Reducibility ratio and Surface Oxygen species of $\text{Fe}_{x(x=0-0.2)x}(\text{Ce}_{0.9}\text{Pr}_{0.1})_{(1-x)}\text{O}_{2-\delta}$ Catalysts.

Catalyst	Reducibility Ratio				Lattice Oxygen ratio $\frac{\text{O}^{2-}}{\text{O}^{2-} + \text{O}^- + \text{O}_2^{2-}}$	Adsorbed Oxygen ratio	
	$\frac{\text{Ce}^{3+}}{\text{Ce}^{3+} + \text{Ce}^{4+}}$	$\frac{\text{Pr}^{3+}}{\text{Pr}^{3+} + \text{Pr}^{4+}}$	$\frac{\text{Fe}^{3+}}{\text{Fe}^{3+} + \text{Fe}^{2+}}$	$\frac{\text{Fe}^{2+}}{\text{Fe}^{3+} + \text{Fe}^{2+}}$		$\frac{\text{O}^-}{\text{O}^{2-} + \text{O}^- + \text{O}_2^{2-}}$	$\frac{\text{O}_2^{2-}}{\text{O}^{2-} + \text{O}^- + \text{O}_2^{2-}}$
CP	0.42	0.15	-	-	0.17	0.46	0.24
5 Fe-CP	0.35	0.37	0.77	0.23	0.26	0.35	0.39
10 Fe-CP	0.32	0.08	0.39	0.60	0.17	0.25	0.57
15 Fe-CP	0.32	0.09	0.27	0.72	0.23	0.28	0.48
20 Fe-CP	0.32	0.06	0.50	0.49	0.18	0.23	0.58

7.6. SOOT OXIDATION ACTIVITY

Figure 7.6 depicts soot conversion curves to increase in temperature. The soot oxidation is carried out in triplicates to ensure the repeatability of the catalyst. The T_{50} temperature is noted for all the catalysts and is listed in **Table 7.4**. From the Table, it can be noticed that there was a significant reduction in T_{50} on loading TM 5 Fe-CP displayed better T_{50} at $367\pm 2^\circ\text{C}$, and Pure Fe showed high T_{50} among all the pure TM at $498\pm 1^\circ\text{C}$. The parameters which may enhance catalytic activity were analyzed from the characterization of the developed catalysts. The XRD studies showed that the crystallite size for all the Fe-CP catalysts was below 10nm. $\{110\}/\{111\}$ facet ratio was found to be high (0.41) for 20 Fe-CP; also, 10 Fe-CP had the highest Oxygen vacancy ratio (I_{Ov}/I_{F2g}) of 0.89.

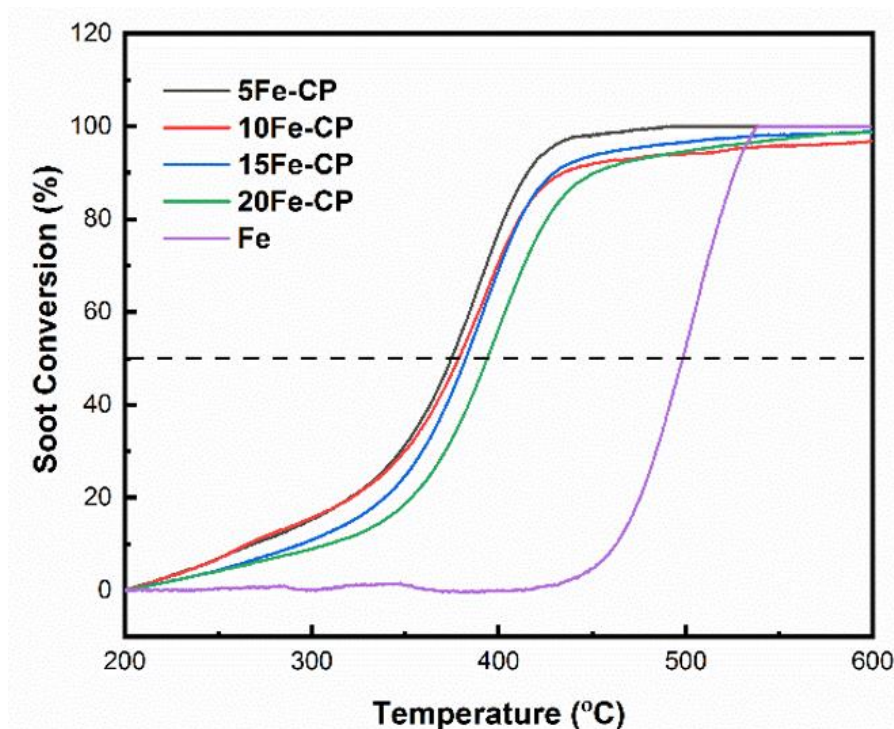


Figure 7.6. Soot Oxidation activity of Fe_x ($x=0-0.2$) $(\text{Ce}_{0.9}\text{Pr}_{0.1})_{1-x}\text{O}_{2-\delta}$ Catalysts.

The secondary phase (Fe_3O_4) formation in the BSCF sample positively affected soot oxidation activity due to lattice/bulk oxygen vacancy (Shenoy et al. 2019). Also, high surface oxygen species and reducible ions greatly influence catalytic activity, as discussed previously in Chapter 6.

7.7. KINETIC ANALYSIS

7.7.1. Determination of Activation Energy (E_a) and Pre-Exponential Factor (A)

The soot oxidation activity was performed using TGA at different heating rates, namely 5,10,15,20 °C/min, and is employed to perform kinetic studies on the developed catalysts. The current chapter also determines the E_a value by model-free methods such as Ozawa, KAS, and CR (Ganiger et al. 2022; Gotor et al. 2000; Landa et al. 2007). The "Am" method is employed to obtain the A value and exponential integer "m" value which is further utilized in the CR method to obtain both E_a and A values for the catalysts.

Ozawa, KAS, CR, and Am plots are plotted for all the samples and are provided in the Appendix section from **Figure A7.1 (a-d) to A7.4 (a-d)**, respectively. The E_a value by all three methods was low for the 5 Fe-CP catalyst, whereas the pure Fe Catalyst displayed a higher E_a value; pure Fe catalyst obtained a high pre-exponential factor. The discussion on the ranges of both E_a and A values for catalytic soot oxidation activity was provided in Chapter 5. The master plots with $g(\alpha)$ values calculated for different reaction models by varying conversion (α) are plotted and are shown in **Figure A7.5 (a-d)**. The reaction models coinciding for all the catalysts were noted and are provided in **Table 7.4**.

Table 7.4. Kinetic triplets and "m" value for Fe_x (x=0-0.20) (Ce_{0.9}Pr_{0.1})_(1-x) O_{2-δ} Catalysts.

Catalyst	T ₅₀ (°C)	E _a (kJ mol ⁻¹)			Reaction Model	A × 10 ¹⁰ (min ⁻¹)		m
		Ozawa method	KAS method	CR method		Am method	CR method	
5 Fe-CP	367±2	102	98	103	A1,L4,D2,D3,D4,P3,R2	0.048	0.0012	0.87
10 Fe-CP	376±2	118	113	118	A1,L4,D2,D3,D4,P3,R2	0.8	0.9	0.93
15 Fe-CP	381±1	122	117	121	A1,L4,P2,P3,R2	0.14	0.12	0.90
20 Fe-CP	390±2	116	111	123	A1,L4,D2,D3,D4,P3,R2	0.04	0.13	0.81
Fe	498±1	160	156	160	A1,A1.5,L4,D2,P1,P2,P3,R2	2.13	1.85	1.02

Effect of Iron-Doped Ceria-Praseodymium Catalysts for Soot Oxidation Activity and its Kinetics

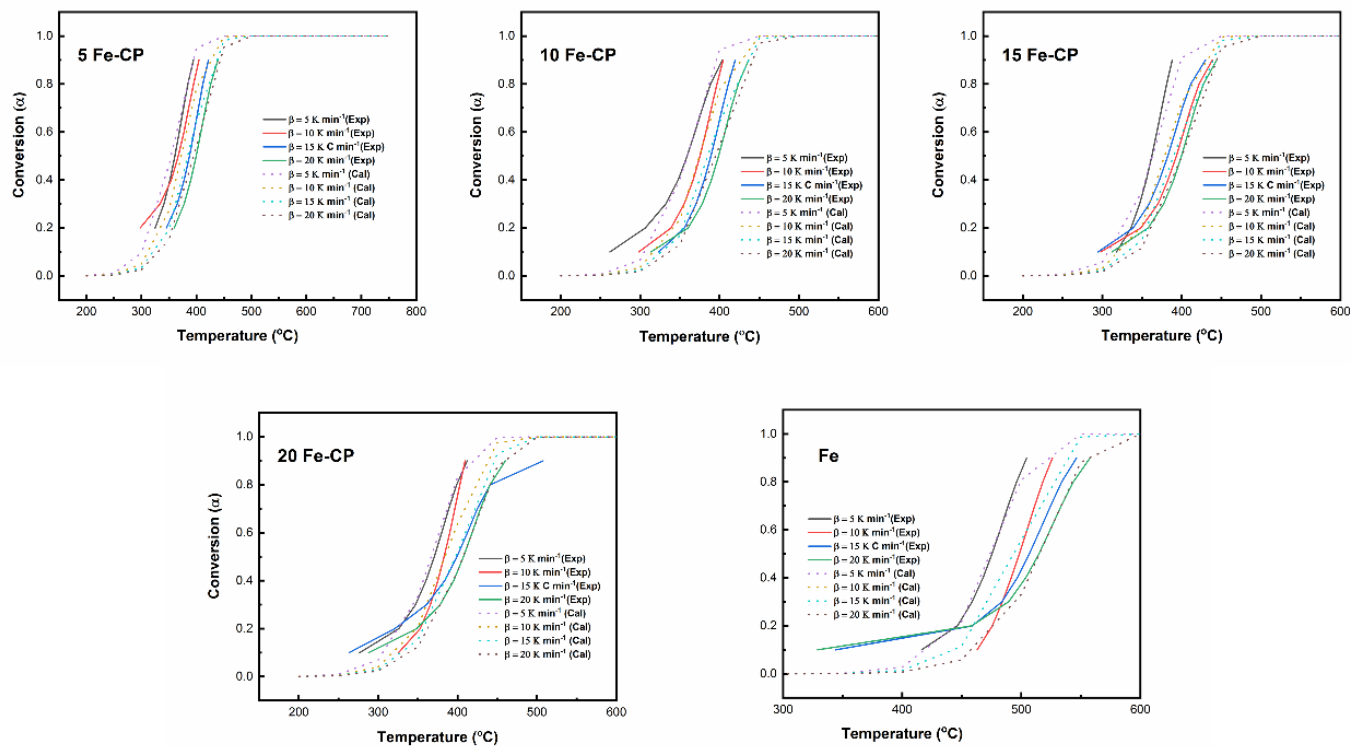


Figure 7.7. Experimental and calculated Curves for $Fe_x(x=0.5-0.2) (Ce_{0.9}Pr_{0.1})_{1-x} O_{2-\delta}$ Catalysts

A Study on the Effect of Transition Metal Dopants in Ceria Praseodymium Catalysts for Soot Oxidation Activity and its Kinetics

It can be seen that most of the Fe-doped CP catalysts followed the nucleation and growth model, power law, phase boundary-controlled reaction, 2-4D diffusion model, and first and second-order reaction. A catalyst's reaction model follows as the reaction proceeds may vary at lower conversion and higher conversion values.

7.7.2. Experimental and Calculated Data Comparison

The thermoanalytical curves were reconstructed, the experimental data obtained from TGA, and α was plotted against temperature. Comparing the experimental and calculated thermoanalytical curves (**Figure 7.7**) at a constant heating rate measures the adequate consistency of the kinetic triplets evaluated. From the plots obtained in **Figure 7.7**, it can also be noticed 20 Fe-CP and pure Fe showed minor variation in the experimental and calculated curves. A certain deviation of theoretical values from experimental data at the extremities of reaction at both low and high conversion values can be noticed due to the oxidation of adsorbed hydrocarbons (Lopez-Fonseca et al. 2007). The excellent consistency of theoretical and experimental curves confirms that the nucleation and growth model with a non-integer “ m ” value was more suitable to define the actual soot combustion.

Figure 7.8 (a) and (b) display $d\alpha/dT$ vs. Temperature and $\ln(k)$ vs. $1/T$ plots, respectively, for $\text{Fe}_{x(x=0.05-0.2)}(\text{Ce}_{0.9}\text{Pr}_{0.1})_{1-x}\text{O}_{2-\delta}$ samples. From **Figure 7.8 (a)**, it can be noticed that the 5 Fe-CP catalyst showed a better reaction rate than compared to other catalysts. The temperature at which the maximum reaction rate is achieved was low for 5 Fe-doped CP catalysts. **Figure 7.8 (b)** also reflects that the 5 Fe-CP catalyst showed better kinetic activity than the other catalysts.

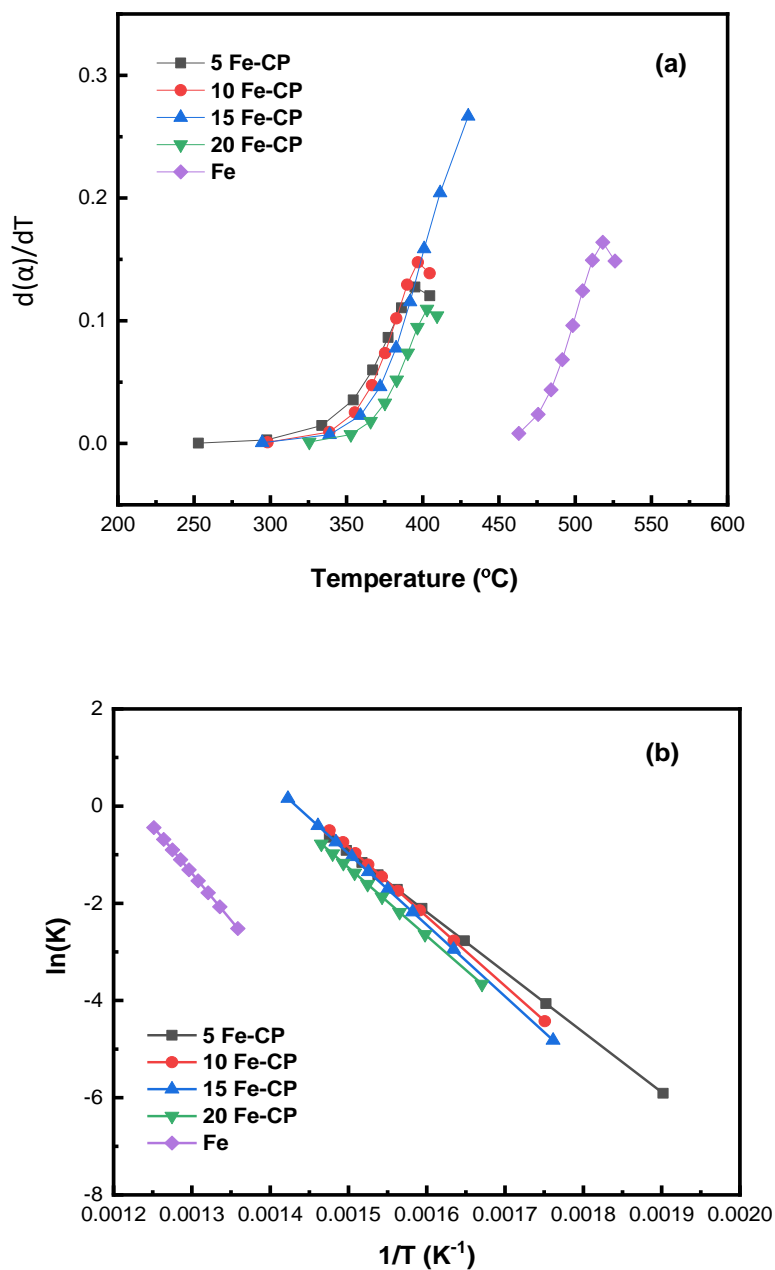


Figure. 7.8. (a) Rate vs. Temperature plot (b) Arrhenius plot for $\text{Fe}_{x(x=0-0.2)}$ $(\text{Ce}_{0.9}\text{Pr}_{0.1})_{1-x}\text{O}_{2-\delta}$ Catalysts.

7.8. CONCLUSION

$\text{Fe}_{x(x=0-0.2)}(\text{Ce}_{0.9}\text{Pr}_{0.1})_{1-x}\text{O}_{2-\delta}$ catalysts were synthesized using solution combustion synthesis and further characterized and tested for soot oxidation activity using TGA. From XRD analysis, all the doped samples ensured the fluorite structure of CeO_2 , whereas pure Fe displayed the crystalline structure of Fe_2O_3 . 5 Fe-CP had the smallest Crystallite size and highest lattice strain of 6 nm and 0.0222, respectively. Raman spectroscopy revealed that all the doped samples possessed F_{2g} Raman modes of CeO_2 and the presence of oxygen vacancy peaks. The secondary phase for E_g Raman modes corresponding to Fe_2O_3 $\sim 300\text{ cm}^{-1}$ was noticed for all the Fe-doped samples.

10 Fe-CP had the highest Oxygen vacancy ratio (I_{Ov}/I_{F2g}) of 0.89. FE-SEM analysis revealed the porous nature of the catalysts, and pure Fe also resembles a network of rods. 5 Fe-CP showed high Ce^{3+} , O^{2-} , and O^- ions and may improve catalytic performance better than other Fe-doped CP catalysts. 5 Fe-CP displayed better catalytic activity with the lowest T_{50} of 367 ± 2 °C, and it can be attributed to smaller crystallite size, higher lattice strain and lower activation energy (102 kJ mol^{-1}).

The descriptors controlling the soot oxidation activity of the Fe-CP catalyst system are (secondary phase formation and redox properties). The 5Fe-CP catalyst system showed better soot oxidation activity, and as the Fe content increased in the Fe-CP system, the catalytic activity decreased. In the next chapter, Manganese-doped Ceria-Praseodymium catalysts were synthesized, characterized, and obtained soot oxidation activity and kinetic behavior. The descriptors controlling the soot oxidation activity of the Manganese-doped Ceria-Praseodymium catalysts system are further explored in the next chapter.

CHAPTER 8

EFFECT OF MANGANESE - DOPED CERIA - PRASEODYMIUM CATALYST ON SOOT OXIDATION ACTIVITY AND ITS KINETICS

Manganese is one of the most abundant transition metals widely used in various applications (Khaskheli et al. 2022). Manganese gains its popularity in the field of catalysis mainly due to its multi-oxidation states (Ghosh 2020). Manganese oxide-based catalysts were reported by various researchers for soot oxidation activity (Fu et al. 2014; Ghosh 2020; Khaskheli et al. 2022; Kuwahara et al. 2020; Neelapala et al. 2018). Catalytic soot oxidation relies on contact efficiency between the active sites and soot (Gao et al. 2022). Mn possesses a much smaller ionic size than Ce. It is easily reducible as it exists in multiple valance states, thereby passing on the extrinsic and intrinsic oxygen vacancies (Venkataswamy et al. 2016b). Pr exhibits higher ionic radii than Ce and is also easily reducible. Pr also exhibits a multi-oxidation state, which may further enhance the properties and help lower the temperature required for soot combustion (Mukherjee et al. 2016). The current chapter describes the effect of Mn-doped CP on catalytic soot oxidation and its kinetics.

8.1. X-RAY DIFFRACTION (XRD) ANALYSIS:

The XRD spectra for $Mn_{x(x=0-0.2)}(Ce_{0.9}Pr_{0.1})_{1-x}O_{2-\delta}$ and pure Mn catalysts (**Figure 8.1**) reveal that the planes observed correspond to characteristic fluorite CeO_2 (Reddy et al. 2011; Shajahan et al. 2018). No secondary diffraction peaks attributed to pure Mn_2O_3 were noticed in any doped catalyst samples.

The planes (200), (211), (222), (321) (400), (332), (431), (440), and (622) observed for pure Mn corresponded well with the bixbyite crystal structure of Mn_2O_3 . The crystallite size was calculated by the Scherrer equation for all the samples and is provided in **Table 8.1**, along with the lattice strain and facet ratios $\{100\}/\{111\}$ and $\{110\}/\{111\}$. It was noticed that 20 Mn-CP had the smallest crystallite size and highest lattice strain of 5.67 nm and 0.0262, respectively. Pure Mn had a larger crystallite size and low lattice strain of 30.04 nm and 0.0043, respectively. Reactive facets are one of the most critical parameters to determine the ability to enhance catalytic activity.

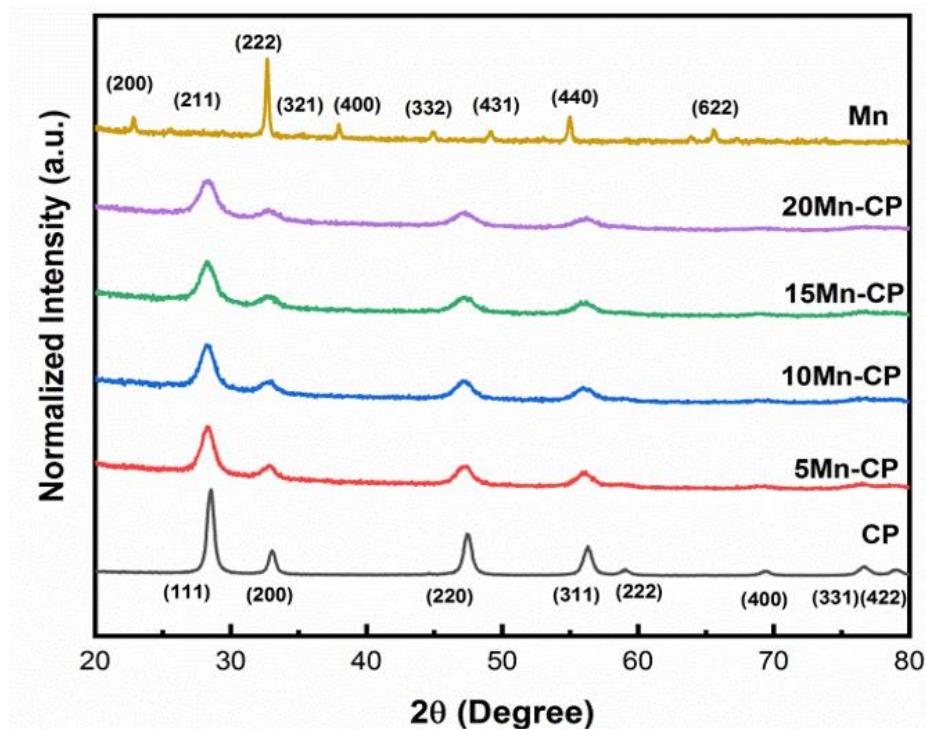


Figure 8.1: XRD spectra of $Mn_x(x=0-0.2) (Ce_{0.9}Pr_{0.1})_{1-x} O_{2-\delta}$ Catalysts

It can be seen that the crystallite size reduced from 14.25 nm to below ~10 nm when Mn is added to the CP catalyst system. A substantial increase in lattice strain and facet ratios ($\{110/111\}$) can also be noticed from CP to Mn-CP catalysts. From the descriptors discussed in previous chapters, smaller crystallite sizes, high lattice strain, and high reactive facets may improve catalytic activity (Anantharaman et al., 2018). However, a single descriptor cannot be termed for catalytic activity of ceria-based materials; the multiple descriptors exist depending upon various reaction conditions (Capdevila et al. 2016).

8.2. RAMAN SPECTROSCOPY ANALYSIS

Figure 8.2 portrays Raman spectra for $Mn_{x(x=0-0.2)}(Ce_{0.9}Pr_{0.1})_{1-x}O_{2-\delta}$ catalysts. The characteristic peak observed at $\sim 465\text{ cm}^{-1}$ in all the doped samples can be allotted to the active F_{2g} Raman modes of CeO_2 which indicate a symmetric arrangement of O-Ce-O (Mukherjee et al. 2016; Patil et al. 2019; Shajahan et al. 2018). The significant peak of $\sim 560\text{ cm}^{-1}$ is attributed to Oxygen Vacancies (O_v) (Patil et al. 2019; Shajahan et al. 2018). Similar to XRD analysis, no significant shift in the F_{2g} peak was detected in all the Mn-doped samples.

In the case of pure Mn, the two intense peaks were noticed at 306 cm^{-1} (ν_5 mode) and 643 cm^{-1} (ν_1 mode) attributed to Mn_2O_3 , which corresponds to the modes of Mn-O-Mn asymmetric and symmetric stretching (Naeem et al. 2016; Xin et al. 2022). The secondary phase was evident as the concentration of Mn-doping increased. Mn-CP catalysts showed secondary peaks of ν_1 mode merged with the existing O_v peaks for 15 and 20 Mn-CP catalysts, and it is difficult to differentiate for 5 and 10 Mn-CP catalysts.

The intensity ratios ($I_{O_v}/I_{F_{2g}}$) of Oxygen vacancy peaks to characteristic F_{2g} of Ce were calculated for all the doped samples and tabulated in **Table 8.1**. It was noticed that 10 Mn-CP displayed the highest $I_{O_v}/I_{F_{2g}}$ of 0.78.

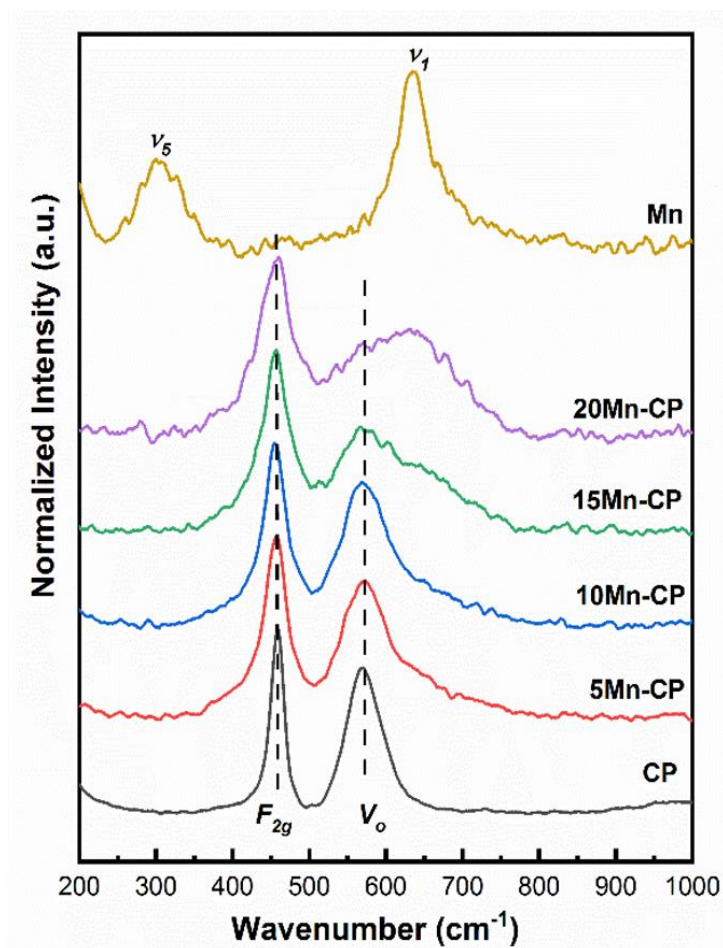


Figure 8.2: Raman spectra of $Mn_{x(x=0-0.2)}(Ce_{0.9}Pr_{0.1})_{1-x}O_{2-\delta}$ Catalysts

Table 8.1. Physicochemical properties of $Mn_{x(x=0-0.2)}(Ce_{0.9}Pr_{0.1})_{1-x}O_{2-\delta}$ Catalysts from XRD and Raman spectroscopy Analysis.

Sample	Crystallite Size (nm)	Lattice strain (ϵ)	Facet Ratio		I_{Ov}/I_{F2g}
			{110}/{111}	{100}/{111}	
CP	14	0.0107	0.24	0.38	0.77
5 Mn-CP	7	0.0218	0.35	0.37	0.75
10 Mn-CP	7	0.0220	0.37	0.38	0.78
15 Mn-CP	6	0.0234	0.39	0.36	0.57
20 Mn-CP	6	0.0262	0.40	0.38	0.60
Mn	30	0.0043	-	-	-

8.3. FE-SEM ANALYSIS

FE-SEM images of $Mn_{x(x=0-0.2)}(Ce_{0.9}Pr_{0.1})_{1-x}O_{2-\delta}$ and Pure Mn metal oxides at 500 nm magnification scale are displayed in **Figure 8.3 (a)**. Similarly to all other transition metals doped CP catalysts discussed in the previous chapters, Mn-doped CP catalysts revealed porous nature as they were synthesized by the SCS method (Aruna and Mukasyan 2008). The particle size tends to increase as the concentration of Mn doping and the porosity decreases. It can be observed that pure Mn resembles a network of particles which is seen in the images provided at a 200 nm scale (**Figure 8.3 (b)**). The porous nature of the sample improves the active contact points for soot and the catalyst (Drake et al. 2018).

Effect of Manganese-doped Ceria-Praseodymium Catalysts for Soot Oxidation Activity and its Kinetics

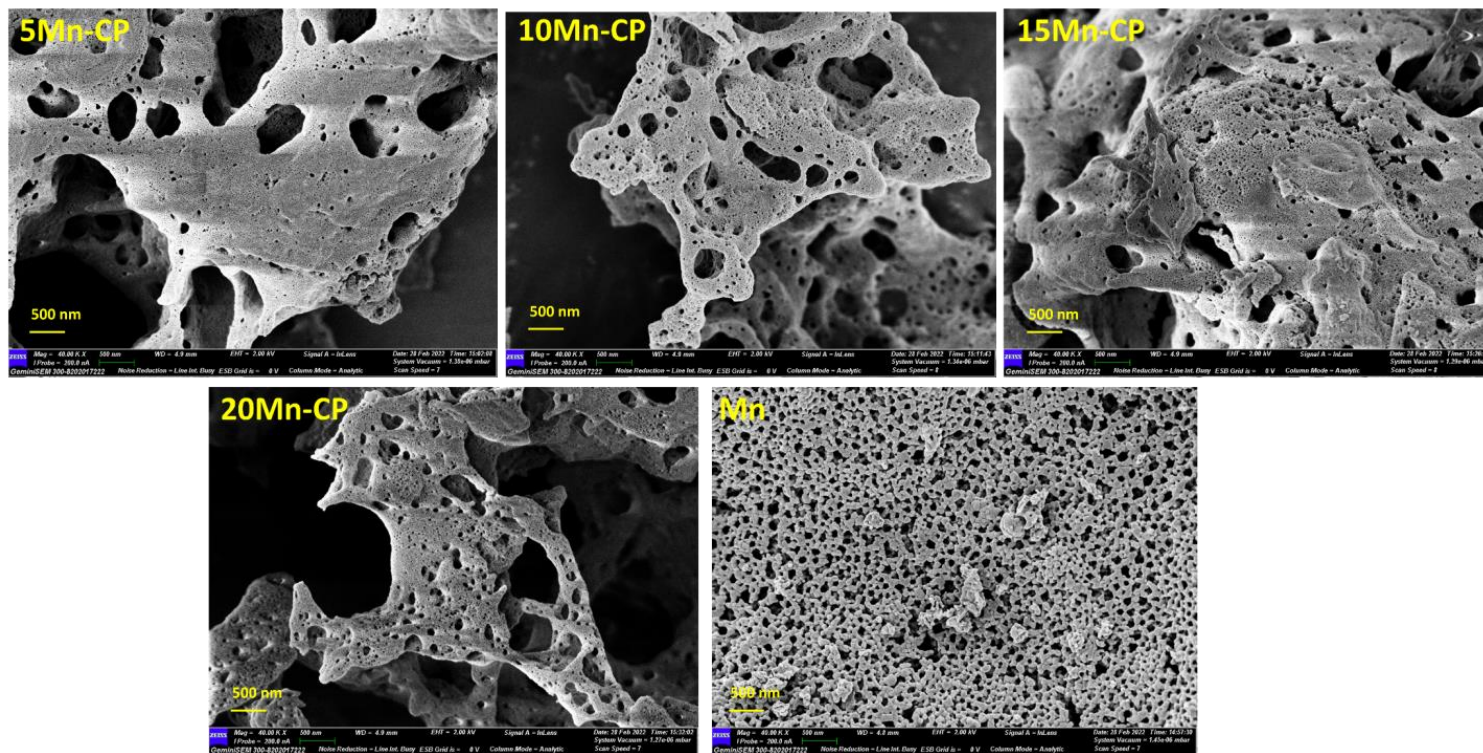


Figure 8.3 (a). FE-SEM images of $Mn_x(x=0-0.2)$ $(Ce_{0.9}Pr_{0.1})_{1-x} O_{2-\delta}$ Catalysts (500nm)

A Study on the Effect of Transition Metal Dopants in Ceria Praseodymium Catalysts for Soot Oxidation Activity and its Kinetics

Effect of Manganese-doped Ceria-Praseodymium Catalysts for Soot Oxidation Activity and its Kinetics

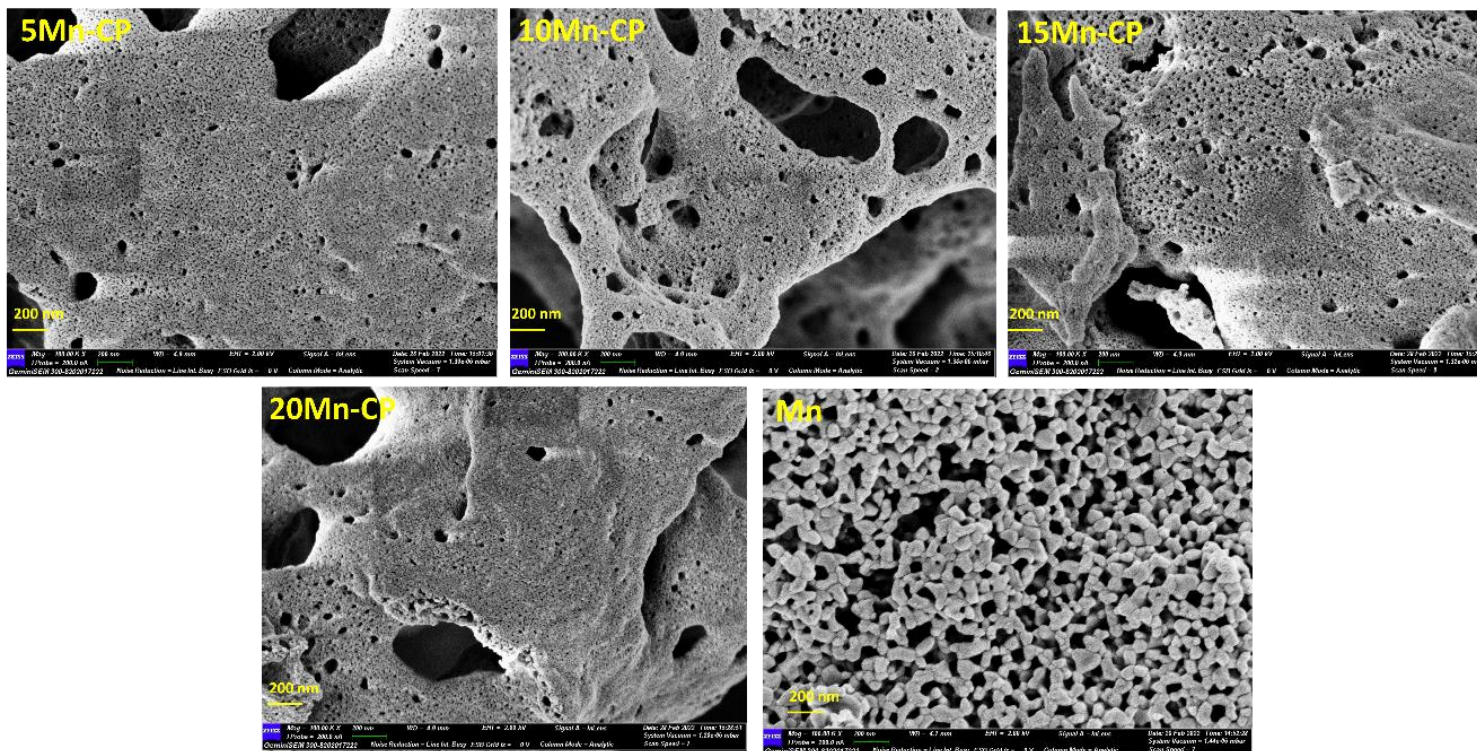


Figure 8.3 (b). FE-SEM images of $Mn_{x(x=0-0.2)}(Ce_{0.9}Pr_{0.1})_{1-x}O_{2-\delta}$ Catalysts (200nm)

A Study on the Effect of Transition Metal Dopants in Ceria Praseodymium Catalysts for Soot Oxidation Activity and its Kinetics

8.4. BET AND BJH ANALYSIS

BET Surface area analysis and BJH Pore volume analysis were performed for all the Mn-doped Ce catalysts. The BET surface area, average Pore size distribution, and pore volume are summarized in **Table 8.2**. From the table, it can be noticed that the surface area varied mainly from 20 to 45 m²/g. 5 Mn-CP showed the highest S_A of 45 m²/g among Mn-CP catalysts. 20 Mn-CP had the highest average pore size of 6.94 nm, and 15 Mn-CP had a high total pore volume of 0.333 cc/g. The N₂ adsorption-desorption isotherm and the pore size distribution of all the catalysts are represented in **Figures 8.4(a) and (b)**, respectively.

Figure 8.4(a) shows that 5 Mn-CP and 20 Mn-CP showed similar Type IV isotherms with H4 hysteresis with minimum adsorption for Mn-doped CP catalysts. Pure Mn and 10 Mn-CP also expressed Type IV isotherms with H3 hysteresis with high N₂ adsorption. 15 Mn CP Type IV isotherms showed multiple loops leading to a step-wise isotherm related to non-existing pores filled by sub-step to actual pores (Groen et al.2003). The pore size distributions of the Mn-doped catalysts were calculated by the BJH method from the adsorption isotherm curves and are shown in **Figure 8.4 (b)**. The samples expressed narrow pore size distribution ranging from ~5 to 20nm for all the developed catalysts. In their studies, Yang et al. 2019 reported that the developed Mn₂O₃ resembled spongy nature and was highly porous, with a high surface area, giving better catalytic performances.

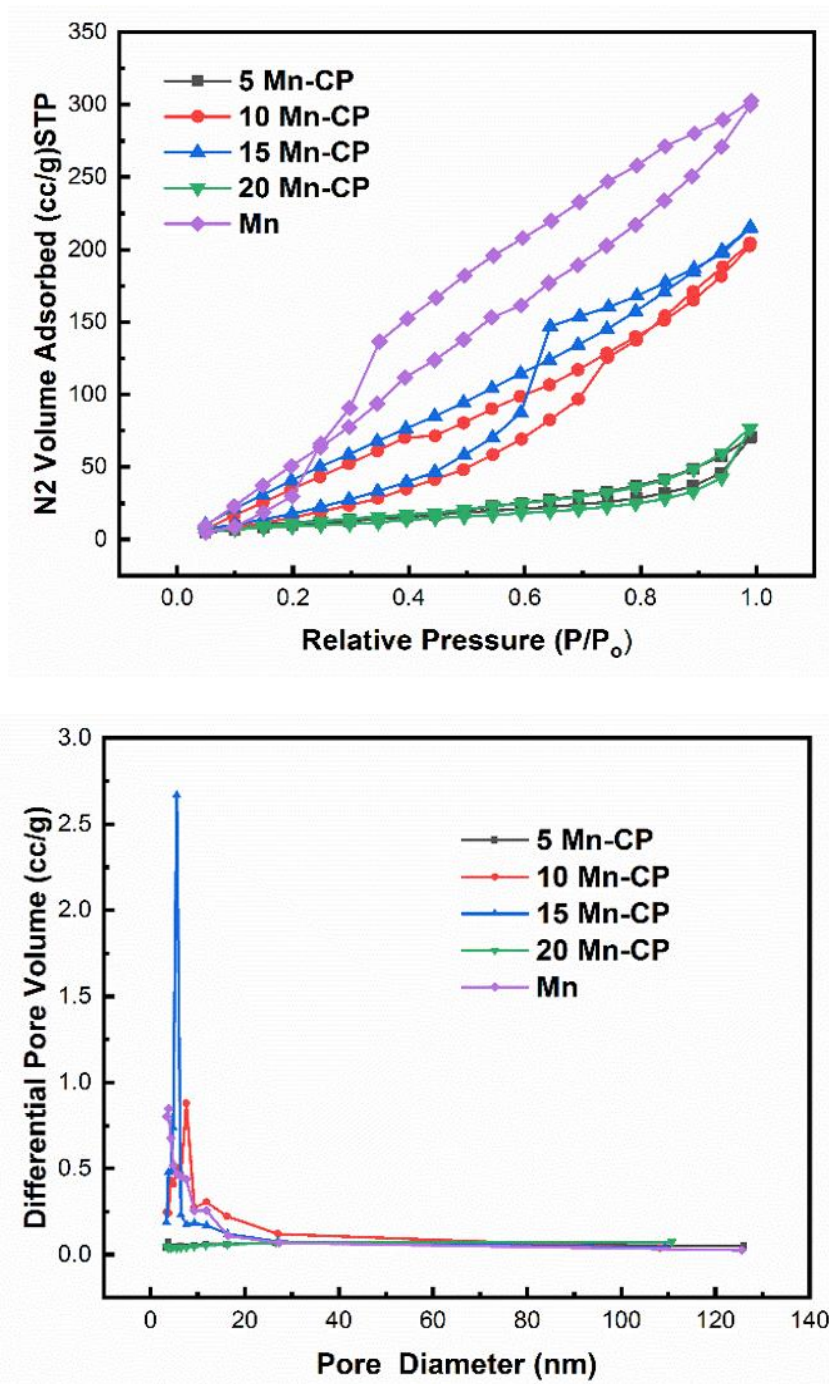


Figure 8.4 (a) : N₂ Adsorption-Desorption isotherm (b) : BJH Pore Size Distribution of Mn_{x(x=0-0.2)} (Ce_{0.9}Pr_{0.1})_{1-x} O_{2-δ} Catalysts

Table 8.2 BET and BJH Analysis for $Mn_{x(x=0-0.2)}(Ce_{0.9}Pr_{0.1})_{1-x}O_{2-\delta}$ Catalysts

Sample	BET S_A (m^2/g)	Pore Volume (cc/g)	Avg. Pore Size (nm)
CP	31	0.217	11.46
5 Mn-CP	45	0.110	4.92
10 Mn-CP	36	0.109	6.39
15 Mn-CP	33	0.333	5.92
20 Mn-CP	35	0.118	6.94
Mn	20	0.039	4.08

8.5. XPS ANALYSIS

Figure 8.5 (a-d) denotes Ce 3d, Pr 3d, O1s, and Mn 2p XPS spectra for $Mn_{x(x=0-0.2)}(Ce_{0.9}Pr_{0.1})_{1-x}O_{2-\delta}$ catalysts. The Ce 3d spectrum is assigned into two sets corresponding to $3d_{3/2}$ and $3d_{5/2}$ orbitals (Fu et al. 2014; Mittal et al. 2018). The peak position assigned to the oxidation states Ce^{4+} and Ce^{3+} was noted in the literature reported (Fu et al. 2014; Holgado et al. 2000; Mittal et al. 2018). Similarly, based on the literature reported, the deconvoluted XPS peaks for Pr (Pr^{3+} and Pr^{2+}) and Mn (Mn^{2+} , Mn^{3+} , and Mn^{4+}) were also assigned (Govardhan et al. 2022; Naeem et al. 2016; Niu et al. 2016; Poggio-Fraccari et al. 2018). The area under the curve was utilized to compute the reducibility ratio, $Ce^{3+}/(Ce^{3+}+Ce^{4+})$ ratio, and surface oxygen species ratio listed in **Table 8.3**.

The table shows that CP showed a high reducibility ratio for Ce^{3+} (0.42) and Pr^{3+} (0.55) compared to all the Mn-doped catalysts. The O1s spectra reveal the information corresponding to the lattice oxygen species (O^{2-}) and the chemisorbed oxygen species (O^- , O_2^- and H-O-H) (Jones et al. 2015). From **Figure 8.5**, it can be seen that 5 Mn-CP and 10 Mn-CP showed additional Oxygen species at ~ 534 eV, and the binding energy at 534 eV is assigned to the adsorbed H_2O or adsorbed molecular water (Yafarova et al. 2021).

It can also be noticed from **Table 8.3** that the presence of surface chemisorbed oxygen species O_2^- was found to be highest for the 5 Mn-CP catalysts, which may favor better catalytic activity. It can also be deduced that incorporating 5 mol % Mn into the CP catalyst system enhanced surface oxygen formation compared to other samples. Hence, it took part in the oxidation reaction efficiently. Surface-active oxygen species (O^-) are also critical in improving catalytic activity at high temperatures (Wei et al. 2011). CP had a high O^- species of 0.58.

This peak observed ~529 eV to 530 eV generally assigned to O^- species. and it was seen that O^- was absent in 5 Mn-CP. Generally, Ce-based catalysts express more than a single form of oxygen ion species (Sudarsanam et al. 2014a), and the active oxygen species obtained near binding energies near 530 eV play a critical role in oxidation reactions (Jones et al. 2015), which are generally assigned to O^- species. The presence of lattice Oxygen species also plays a significant role in catalytic soot oxidation if the surface area is low (Liang et al. 2007b). Hence, the lattice oxygen species ratio presented in the table revealed that CP had the highest (0.49) O^{2-} species, whereas chemisorbed oxygen species (O^-) and (O_2^-) species were high for 15 Mn-CP and 5 Mn-CP, respectively. Additional H-O-H peak was observed in the case of 5 Mn-CP and 10 Mn-CP.

Mn consists of peaks assigned to Mn^{2+} , Mn^{3+} , and Mn^{4+} (Naeem et al. 2016; Niu et al. 2016). Table 8.3 shows that 15 Mn-CP had high concentrations of Mn^{2+} ions (0.64). Mn^{3+} ion concentrations were high (0.55) in 5 Mn-CP and 15 Mn-CP, while Mn^{4+} ions were high (0.32) in 5 Mn-CP. According to Wu et al. 2011, it has been reported that Mn is mainly in the Mn^{3+} state due to its better size compatibility with Ce^{4+} compared to Mn^{4+} (Murugan and Ramaswamy 2005). Mn^{3+} . The presence of an Mn^{4+} ion on the surface of a Ce-based catalyst is considered due to better oxygen mobility in Ce (Casapu et al. 2010).

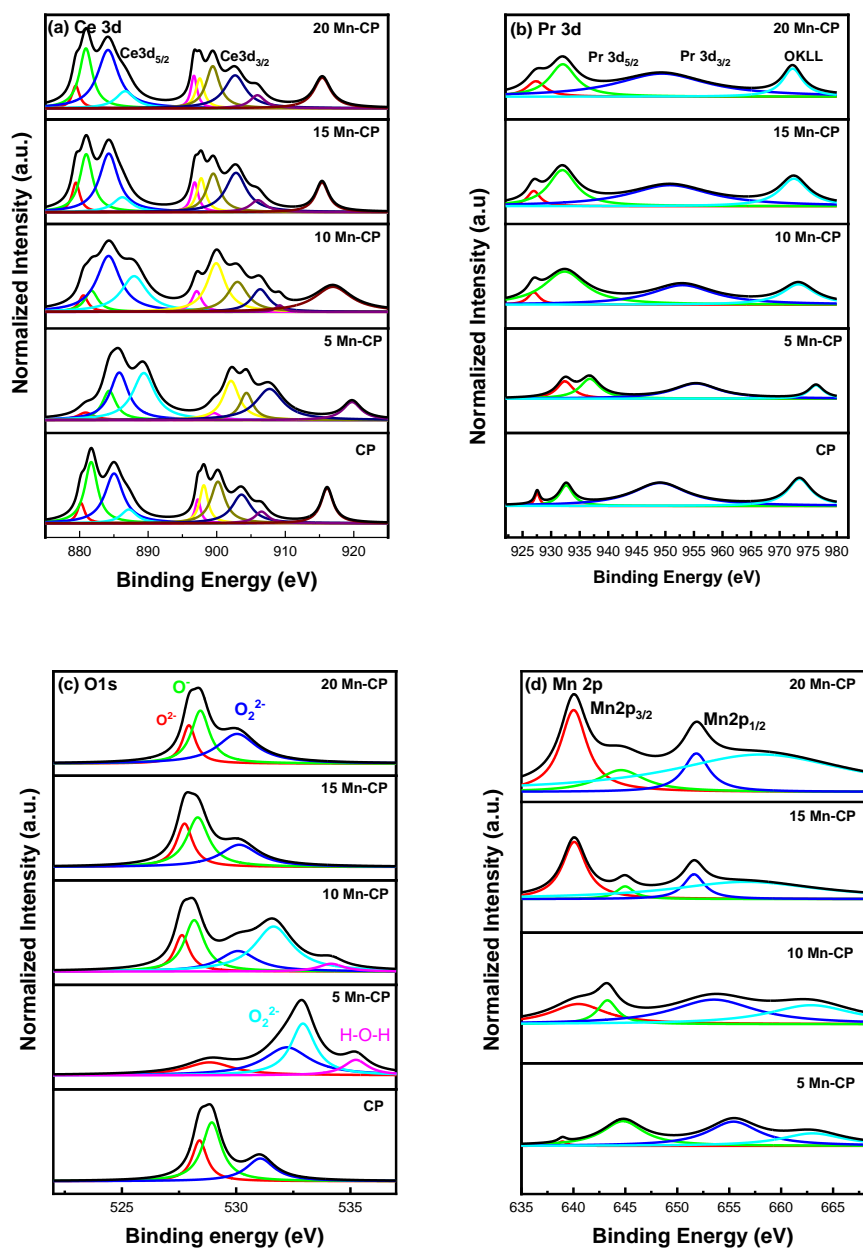


Figure 8.5 (a) : (a) Ce 3d (b)Pr 3d (c) O1s (d) Mn 2p XPS spectra for Mn_x(x=0-0.2)(Ce_{0.9}Pr_{0.1})_{1-x}O_{2-δ} Catalysts

Table 8.3: Reducibility ratio and Surface Oxygen species ratio of $Mn_{x(x=0-0.2)}(Ce_{0.9}Pr_{0.1})_{1-x}O_{2-\delta}$ Catalysts

Catalyst	Reducibility Ratio					Lattice Oxygen	Adsorbed Oxygen species		
	$\frac{Ce^{3+}}{Ce^{3+} + Ce^{4+}}$	$\frac{Pr^{3+}}{Pr^{3+} + Pr^{4+}}$	$\frac{Mn^{2+}}{Mn^{3+} + Mn^{2+}}$	$\frac{Mn^{3+}}{Mn^{3+} + Mn^{2+}}$	$\frac{Mn^{4+}}{Mn^{4+} + Mn^{3+}}$	$\frac{O^{2-}}{O^{2-} + O^- + O_2^{2-}}$	$\frac{O^-}{O^{2-} + O^- + O_2^{2-}}$	$\frac{O_2^{2-}}{O^{2-} + O^- + O_2^{2-}}$	<i>H - O - H</i>
CP	0.42	0.15	-	-	0.26	0.49	0.24	0.42	-
5 Mn-CP	0.25	0.43	0.01	0.55	0.32	0.17	-	0.72	0.10
10 Mn-CP	0.39	0.43	0.30	0.55	0.09	0.37	0.17	0.4	0.04
15 Mn-CP	0.33	0.32	0.64	0.24	0.04	0.27	0.42	0.31	-
20 Mn-CP	0.32	0.30	0.52	0.23	0.09	0.20	0.36	0.44	-

8.6. SOOT OXIDATION ACTIVITY

Figure 8.6 depicts soot conversion curves with the increase in temperature. The T_{50} temperature is noted for all the catalysts and is listed in **Table 8.4**. From the table, it can be noticed that there was a significant reduction in T_{50} on loading Mn to the CP catalyst system. Mn-CP catalysts showed a comparatively high surface area and better T_{50} ranging from 365 to 395 °C. Bare CP catalyst showed T_{50} of 408 ± 4 °C, whereas the lowest T_{50} at 365 ± 1 °C was obtained by 5Mn-CP catalyst; Mn displayed 433 ± 1 °C. The secondary phases were detected by Raman spectroscopy on increasing Mn-doped CP concentration, which may also influence the catalytic activity.

5-Mn CP possessed the highest S_A of $45 \text{ m}^2/\text{g}$. The replacement of higher ionic radii "Ce" by a smaller ionic radius "Mn" in the fluorite structure would decrease the lattice constant owing to improving catalytic activity (Wu et al. 2011). 5 Mn-CP had high concentrations of Mn^{3+} and Mn^{4+} ions along with high O_2^{2-} ions which may be the probable reason for better catalytic activity due to the redox stability of Mn and the presence of surface-adsorbed oxygen species.

8.7. KINETIC ANALYSIS

8.7.1. Determination of Activation Energy (E_a) and Pre-Exponential Factor (A)

Ozawa, KAS, CR, and Am plots are plotted for all the samples and are provided in the Appendix section from **Figure A8.1(a-d) to A8.4(a-d)**, respectively. The E_a and A values obtained from all three methods are represented in **Table 8.4**, along with the "m" values. The table shows that the E_a values obtained from all the methods show a slight difference, and the activation energy varied from 94 to 151 kJ mol^{-1} for the Mn-doped Ce catalysts.

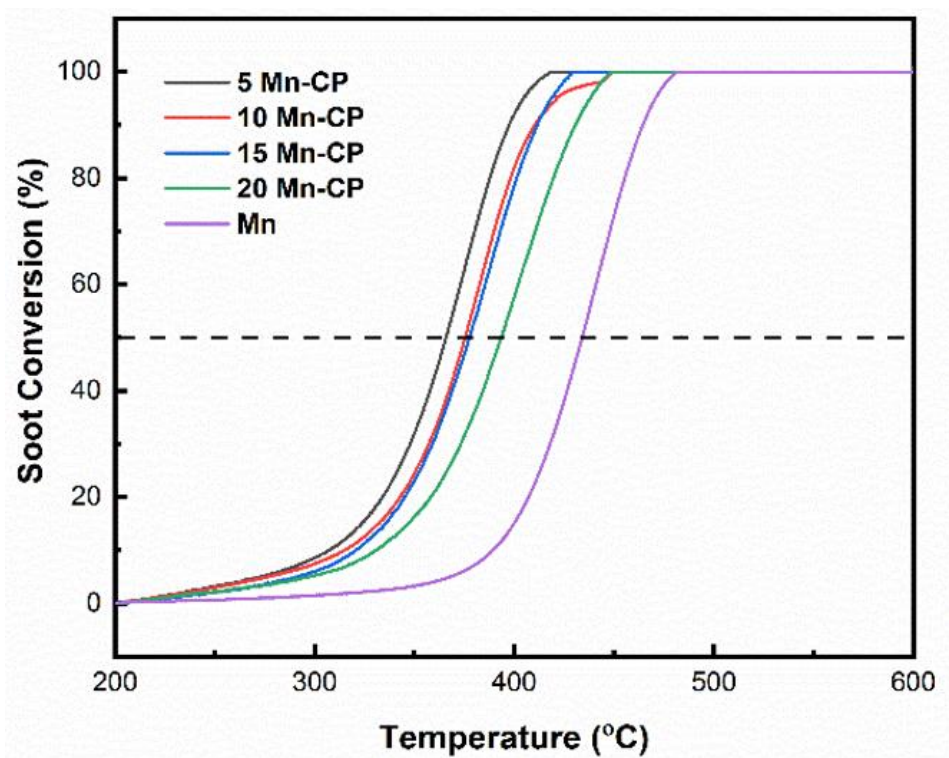


Figure 8.6. Soot Oxidation activity of $Mn_{x(x=0.05-0.2)}(Ce_{0.9}Pr_{0.1})_{(1-x)}O_{2-\delta}$ Catalysts

Pure Mn ($151 \pm 3 \text{ kJmol}^{-1}$) displayed an E_a value slightly higher than that of Mn-doped catalysts. 5 Mn-CP showed the lowest E_a value of $94 \pm 1 \text{ kJ mol}^{-1}$ among all the Mn-doped catalysts. The "m" values for the catalysts ranged from 0.78 to 1.35, almost close to unity. The present study also observed that the E_a is directly proportional to the A value. The highest A value (Am method) of $9.57 \times 10^{10} \text{ min}^{-1}$ was obtained by 15 Mn-CP.

The master plots with $g(\alpha)$ values calculated for different reaction models by varying conversion (α) are plotted and are shown in **Figure A 8.5 (a-d)**. The reaction models coinciding for all the catalysts were noted and are provided in **Table 8.4**. Mn-doped CP catalyst followed the nucleation and growth model, power law, phase boundary-controlled reaction, 2-4D diffusion model, and first and second-order reaction. A catalyst's reaction model follows as the reaction proceeds may vary at lower conversion and higher conversion values. The discussions on literature and ranges of kinetic triplets are discussed previously in Chapter 5.

8.7.2. Experimental and Calculated Data Comparison

Figure 8.7 shows the experimental and theoretical curves, and it can be seen that most of the catalysts had relatively good consistency in experimental and theoretical curves. As discussed earlier in the chapters, it also indicates that the acquired kinetic parameters had adequate consistency.

Figure 8.8 (a) and (b) portray the Rate vs. Temperature and Arrhenius plot for pure $Mn_{x(x=0-0.2)}(Ce_{0.9}Pr_{0.1})_{1-x}O_{2-\delta}$ catalysts, respectively. It can be observed from **Figure 8.8 (a)** that 5 Mn-CP had a maximum reaction rate, and **Figure 8.8 (b)** reveals that the kinetic activity is high for 5 Mn-CP.

Table 8.4. Kinetic triplets and "m" value for $Mn_{x(x=0-0.2)}(Ce_{0.9}Pr_{0.1})_{(1-x)}O_{2-\delta}$ Catalysts

Catalysts	T_{50} (°C)	Ea (kJ mol ⁻¹)			Reaction Model	A ×10 ¹⁰ (min ⁻¹)		m
		Ozawa method	KAS method	CR method		Am method	CR. method	
CP	408±4	111	96	94	A1.5 ,P1,P2	0.000055	0.000039	1.35
5 Mn-CP	365±1	94	89	91	A1,A1.5,P1,P2,P3,L4	0.0013	0.0021	1.03
10 Mn-CP	372±2	138	135	138	A1, L4, R2	4.40	1.80	0.81
15 Mn-CP	377±2	143	140	143	A1,L4,D2,R2	9.57	7.68	0.78
20 Mn-CP	395±3	139	148	138	A1,L4,D2,R2	2.10	2.36	0.83
Mn	433±1	151	155	141	A1,L4,D2,D3,D4,R2	8.22	9.8	0.91

Effect of Manganese-Doped Ceria-Praseodymium Catalysts for Soot Oxidation Activity and its Kinetics

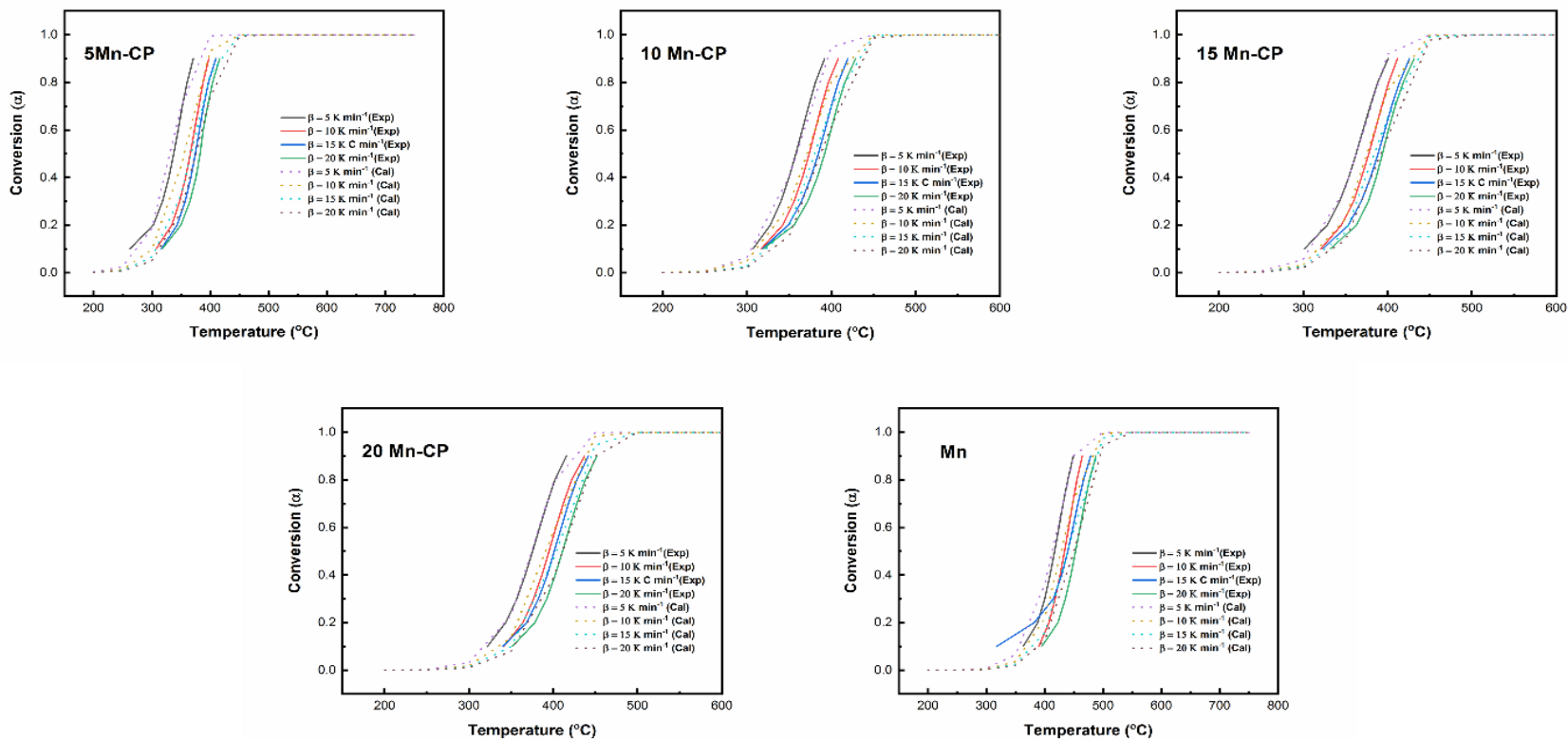


Figure 8.7. Experimental and calculated Curves for $Mn_x(x=0.05-0.2)$ $(Ce_{0.9}Pr_{0.1})_{(1-x)} O_{2-\delta}$ Catalysts.

A Study on the Effect of Transition Metal Dopants in Ceria Praseodymium Catalysts for Soot Oxidation Activity and its Kinetics

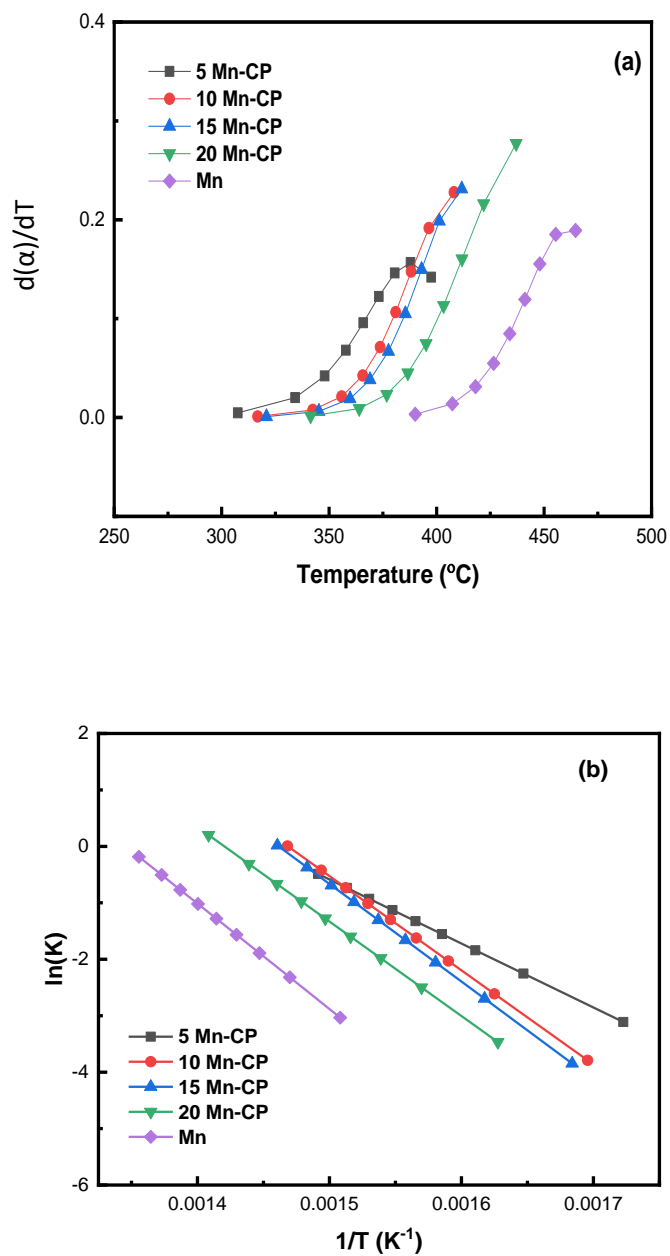


Figure 8.8: (a) Rate vs. Temperature plot (b) Arrhenius plot for $Mn_{x(x=0,05-0.2)}$ $(Ce_{0.9}Pr_{0.1})_{1-x}O_{2-\delta}$ Catalysts.

8.8. CONCLUSION

From XRD and Raman studies, the Mn-doped CP catalysts revealed the fluorite structure of Ceria, and the crystallite size was in the range of ~5 to 10 nm. 10 Mn-CP had the highest Oxygen vacancy ratio (I_{Ov}/I_{F2g}) of 0.78. The S_A was 45 to 15 m²/g. 5 Mn CP possessed the highest S_A of 45 m²/g. CP had better reducibility compared to all Mn-doped CP catalysts. On the other hand, 5 Mn-CP had better active surface adsorbed O_2^- species. A better T_{50} (349±1 °C) may be attributed to active surface adsorbed O_2^- species and Mn^{3+} and Mn^{4+} ions. Kinetic analysis was conducted for all the Mn-CP catalysts and pure Mn oxides. Kinetic triplets, namely Activation energy, Pre-Exponential Factor, and Reaction model, were obtained by model-free methods and the master plot method. The Pre-Exponential factor was high for 15 Mn-CP (9.6×10^{10}) and Pure Mn (9.8×10^{10}) by Am and CR methods, respectively. Mn-doped CP catalyst followed the nucleation and growth model, power law, phase boundary-controlled reaction, 2-4D diffusion model, and first and second-order reaction. Experimental and calculated curve consistency confirmed that the developed catalysts followed the Avrami-Erofeev equation (Am) or the Nucleation and Growth model.

In Mn-CP catalytic system, the 5Mn-CP catalyst showed better catalytic activity for the soot oxidation reaction. The descriptors controlling the soot oxidation activity are surface area, crystallite size, active surface adsorbed oxygen species, and Mn^{3+}/Mn^{4+} surface concentration. With the increase of Mn content in the Mn-CP catalytic system, a secondary phase is formed, resulting in a decrease in soot oxidation activity. In the next chapter, Chromium-doped Ceria-Praseodymium catalysts were synthesized, characterized, and obtained soot oxidation activity and kinetic behavior. The descriptors controlling the soot oxidation activity of the Chromium-doped Ceria-Praseodymium catalysts system are further explored in the next chapter.

CHAPTER 9

THE CATALYTIC EFFECT OF CHROMIUM - DOPED CERIA - PRASEODYMIUM ON SOOT OXIDATION ACTIVITY AND ITS KINETICS

Chromium (Cr) is reported to be an efficient catalyst for oxidation reactions (Pradier et al. 2000; Stein et al. 1960). The most prominent property of Cr is it exists in multi-oxidation (+2 to +6) (Shupack 1991). It was also reported that Cr-based perovskites exhibit the best catalytic activity toward soot oxidation, mainly due to the high concentration of chemisorbed oxygen (Stein et al. 1960). The interaction of Cr with Ce improved the catalytic soot oxidation activity (Li et al. 2011). On the other hand, pure CeO₂ performed better than Cr-Ce mixed oxides prepared by the sol-gel method via glucose and fructose additives (Neelapala and Dasari 2018b). In the studies conducted by Neelapala and Dasari 2018, the Cr incorporation into the Ce lattice reduced crystal size and lattice parameter; the surface area was lesser than that of pure Ce (Neelapala and Dasari 2018b). The present chapter deals with the catalytic investigation of Cr-doped Ce-Pr catalysts for soot oxidation activity and its kinetics.

9.1. X-RAY DIFFRACTION (XRD) ANALYSIS

The XRD spectra for Cr_{x(x=0-0.2)}(Ce_{0.9}Pr_{0.1})_{1-x}O_{2-δ} catalysts are displayed in **Figure 9.1**. The XRD peaks obtained in the spectra corresponded well to the characteristic fluorite CeO₂ (Reddy et al. 2011; Vinodkumar et al. 2013). A slight shift in peaks towards lower 2θ was observed as the concentration of Cr increased due to variation in the ionic size of Cr from Ce and Pr. The shift returns to the standard 2θ value; hence, it can be understood that the Cr is well settled in the CP system and is saturated.

No secondary diffraction peaks attributed to pure Cr were noticed in doped catalyst samples. Pure Cr obtained the planes [(012), (104), (110), (113), (023), (116), (212), and (300)], which correspond to rhombohedra Cr₂O₃ (Awadiet al. 2020).

The physicochemical properties obtained from XRD analysis are provided in **Table 9.1**. The crystallite size obtained for all the samples ranged from 5 nm to 25 nm. Among the Cr- CP catalysts, 20 Cr-CP had the smallest crystallite size of 5 nm, and Pure Cr had the largest crystallite size of 25nm. The lattice strain was also significantly considerable (0.0268) for 20 Cr-CP. The facet ratios [{100}/{111} and {110}/{111}] were also estimated and tabulated in **Table 9.1**. A substantial increase in lattice strain and facet ratios can also be noticed from CP to Cr-CP catalysts. Hence, doping Cr into CP may significantly impact the catalytic activity.

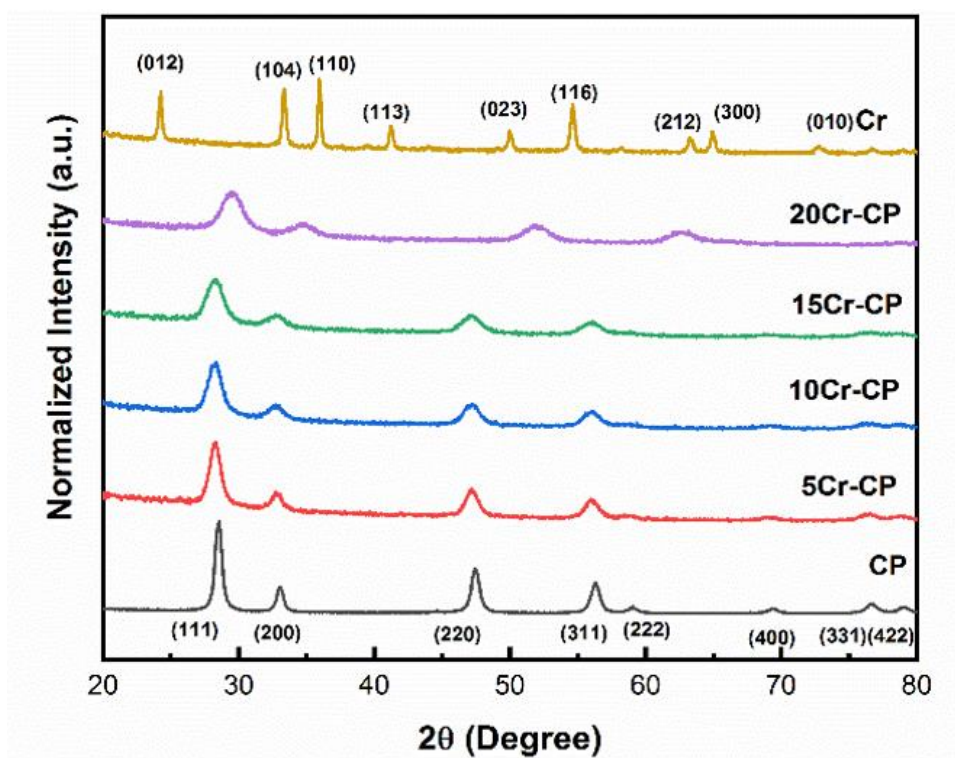


Figure 9.1: XRD spectra of Cr_x(x=0-0.2) (Ce_{0.9}Pr_{0.1})_{1-x} O_{2-δ} Catalysts

9.2. RAMAN SPECTROSCOPY ANALYSIS

Figure 9.2 portrays Raman spectra for $\text{Cr}_{x(x=0-0.2)} (\text{Ce}_{0.9}\text{Pr}_{0.1})_{1-x} \text{O}_{2-\delta}$. The peak observed at $\sim 465 \text{ cm}^{-1}$ is allotted to the active F_{2g} Raman modes of CeO_2 (Mukherjee et al. 2016; Patil et al. 2019; Shajahan et al. 2018). Another significant peak at $\sim 560 \text{ cm}^{-1}$ obtained is assigned to Oxygen Vacancies (O_v) peak. It was also noticed that as the concentration of Cr increases, the intensity of O_v decreases.

No significant shift in the F_{2g} peak was detected in all the doped samples. The peaks obtained from both " A_{1g} " and " E_g " modes observed at $\sim 303 \text{ cm}^{-1}$, 348 cm^{-1} , 548 cm^{-1} , 607 cm^{-1} , and 648 cm^{-1} assigned to the Raman modes of Cr_2O_3 (Bhardwaj et al. 2022; Guillén and Herrero 2021). No secondary peaks were observed for Cr-doped CP catalysts. The intensity ratios ($I_{\text{Ov}}/I_{F_{2g}}$) of the O_v F_{2g} peak are calculated and tabulated in **Table 9.1**. 10 Cr-CP displayed the highest $I_{\text{Ov}}/I_{F_{2g}}$ of 0.78.

Table 9.1. Physicochemical properties of $\text{Cr}_{x(x=0-0.2)} (\text{Ce}_{0.9}\text{Pr}_{0.1})_{1-x} \text{O}_{2-\delta}$ Catalysts from XRD and Raman spectroscopy Analysis

Sample	Crystallite Size (nm)	Lattice strain (ϵ)	Facet Ratio		$I_{\text{Ov}}/I_{F_{2g}}$
			{110}/{111}	{100}/{111}	
CP	14	0.0107	0.24	0.38	0.77
5 Cr-CP	8	0.0183	0.34	0.40	0.75
10 Cr-CP	7	0.0226	0.35	0.36	0.78
15 Cr-CP	6	0.0261	0.40	0.39	0.68
20 Cr-CP	5	0.0268	0.36	0.34	0.57
Cr	25	0.0050	-	-	-

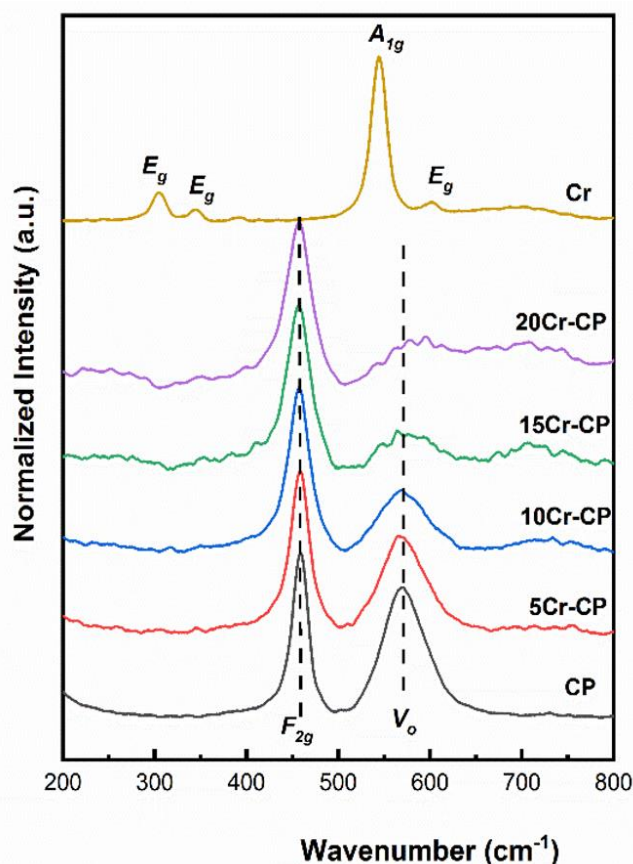


Figure 9.2: Raman spectra of Cr_{x(x=0-0.2)} (Ce_{0.9}Pr_{0.1})_{1-x} O_{2-δ} Catalysts

9.3. FE-SEM ANALYSIS

FE-SEM Micrographs of Cr_{x(x=0-0.2)} (Ce_{0.9}Pr_{0.1})_{1-x} O_{2-δ} catalysts at 500 nm and 200 nm magnification are displayed in **Figure 9.3 (a) and (b)**, respectively. Similar to all the catalysts discussed in the previous chapters, the Cr-doped CP catalysts also revealed porous nature mainly due to the evolution of gases during the synthesis process (Aruna and Mukasyan 2008). It was also noticed that the particle size tends to increase as the concentration of Cr increases and the porosity decreases. Cr-CP catalysts displayed porous agglomerates, whereas Cr₂O₃ displayed a rod-like structure which can be observed in **Figure 9.3 (b)**.

The catalytic effect of Chromium-Doped Ceria-Praseodymium on Soot Oxidation Activity and its Kinetics

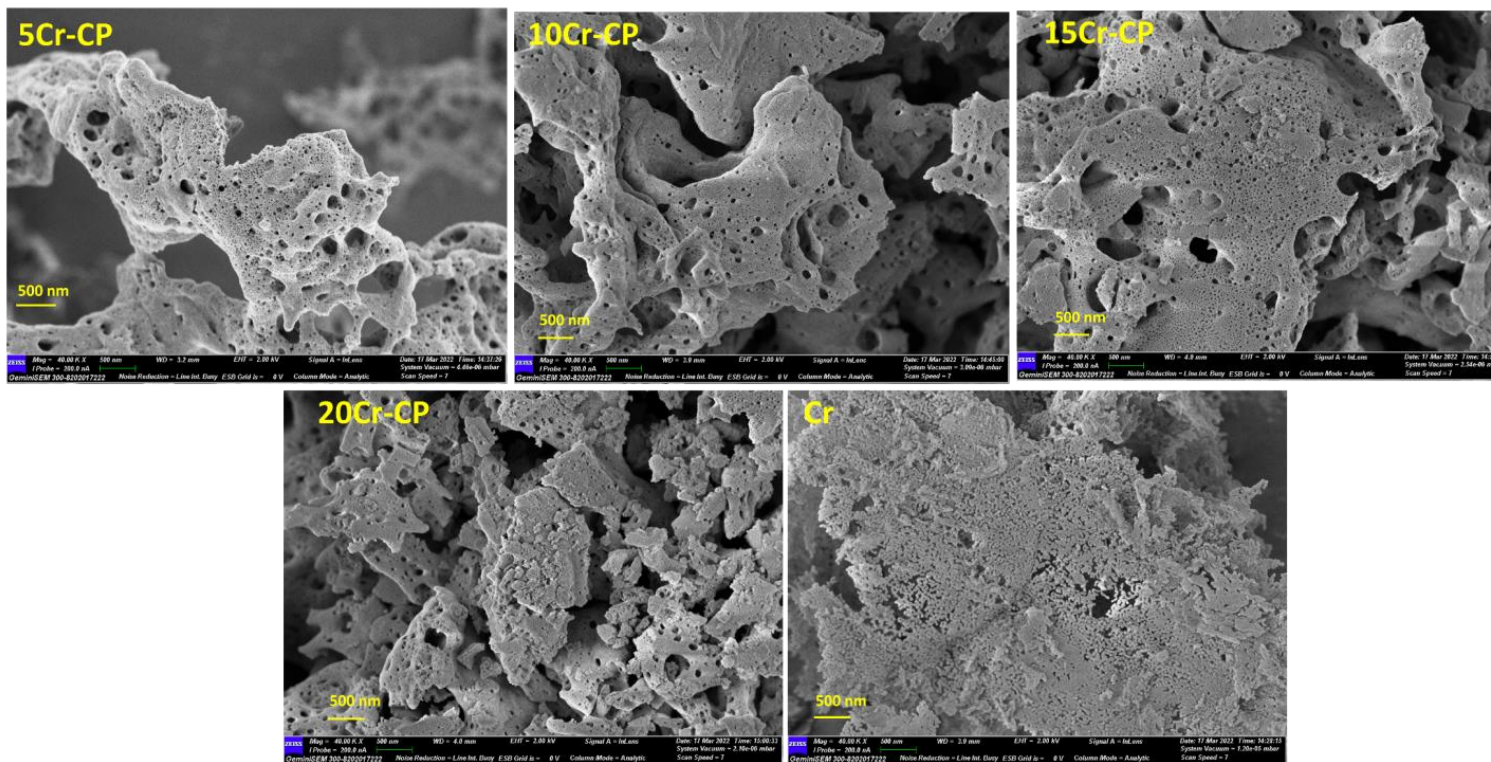


Figure 9.3 (a). FE-SEM analysis of $\text{Cr}_x(x=0-0.2)$ $(\text{Ce}_{0.9}\text{Pr}_{0.1})_{1-x} \text{O}_{2-\delta}$ catalysts (500nm)

A Study on the Effect of Transition Metal Dopants in Ceria Praseodymium Catalysts for Soot Oxidation Activity and its Kinetics

The catalytic effect of Chromium-Doped Ceria-Praseodymium on Soot Oxidation Activity and its Kinetics

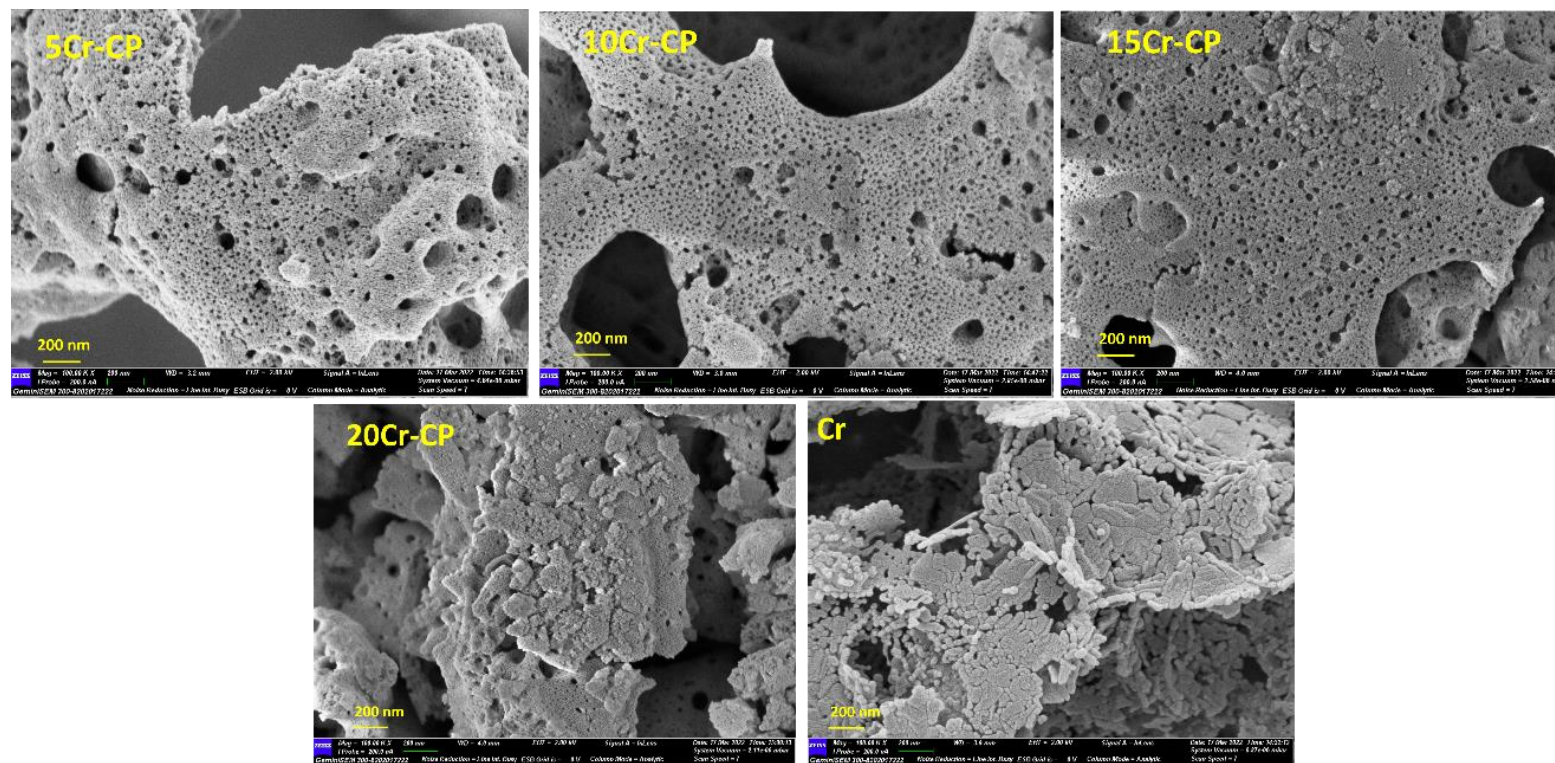


Figure 9.3 (b). FE-SEM analysis of $\text{Cr}_x(x=0-0.2)$ $(\text{Ce}_{0.9}\text{Pr}_{0.1})_{1-x}\text{O}_{2-\delta}$ Catalysts (200nm)

A Study on the Effect of Transition Metal Dopants in Ceria Praseodymium Catalysts for Soot Oxidation Activity and its Kinetics

9.4. BET AND BJH PORE SIZE ANALYSIS

BET Surface area analysis and BJH Pore volume analysis were performed for all the catalysts to determine their influence on the catalytic activity summarized in **Table 9.2**. From the table, it can be noticed that the surface area varied mainly from 36 to 96 m²/g. Among the Cr-CP catalysts, 20 Cr-CP showed a high S_A of 96 m²/g with Avg. pore size and volume of 5.10 nm and 0.11 cc/g, respectively. The adsorption-desorption isotherm and the pore size distribution of all the catalysts are represented in **Figures 9.4 (a) and (b)**, respectively.

From Figure 9.4(a), for Cr-CP catalysts, it can be noticed that the catalysts followed Type IV isotherms with H3 hysteresis. 20 Cr-CP catalysts showed maximum N₂ adsorbed. Hence, mesoporous agglomerates can be confirmed for all the samples (Fu et al. 2021). The pore size distributions of the catalysts were calculated by the BJH method from the adsorption isotherm curves and are shown in **Figure 9.4 (b)**. The samples expressed pore diameters ranging from ~ 5 to 25 nm for all the developed catalysts.

Table 9.2. BET Analysis of Cr_{x(x=0-0.2)} (Ce_{0.9}Pr_{0.1})_{1-x} O_{2-δ} Catalysts

Sample	BET S_A (m²/g)	Pore Volume (cc/g)	Avg. Pore Size (nm)
CP	31	0.217	11.46
5 Cr-CP	36	0.076	4.33
10 Cr-CP	42	0.109	5.28
15 Cr-CP	44	0.111	5.12
20 Cr-CP	96	0.245	5.10
Cr	43	0.165	3.53

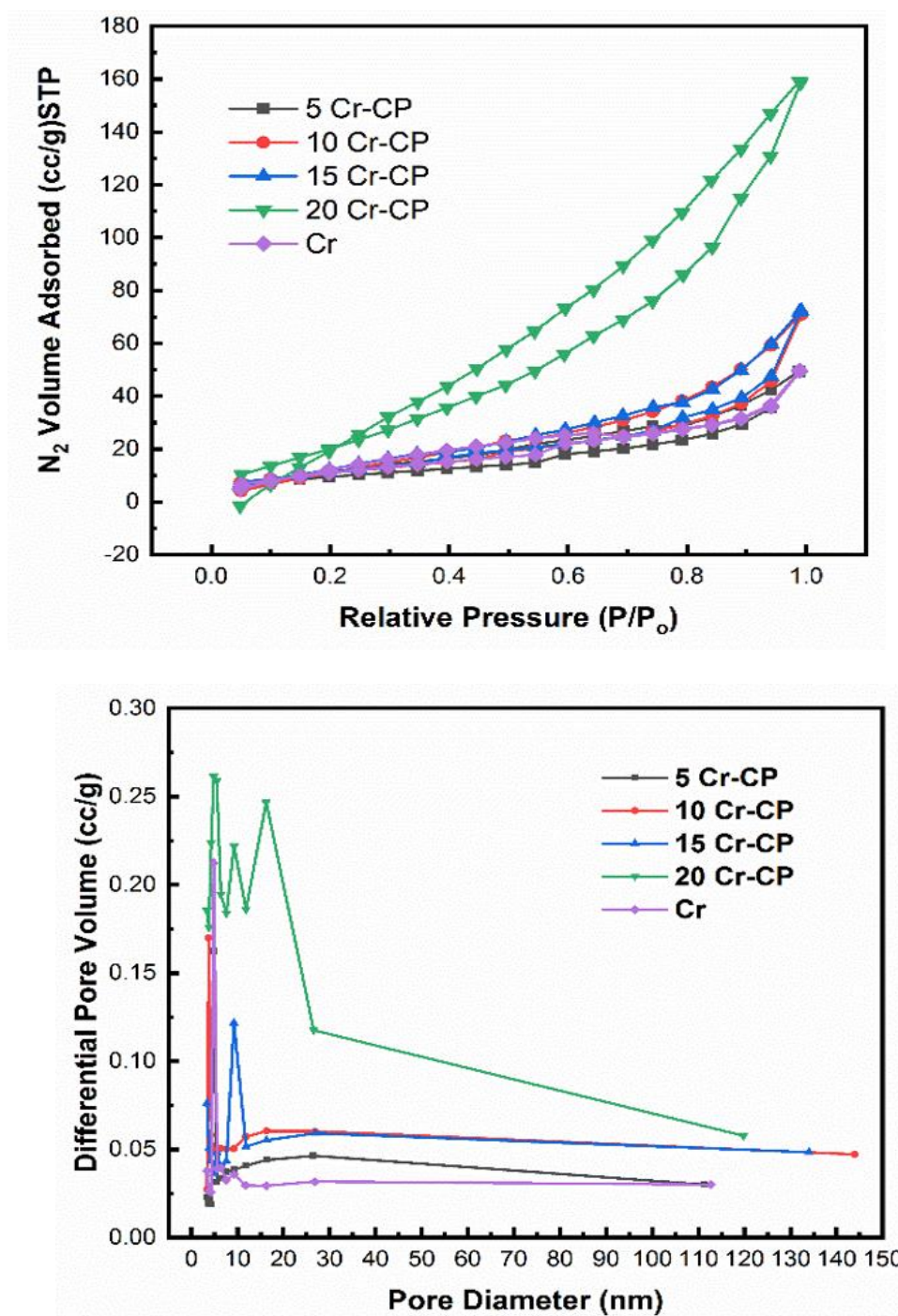


Figure 9.4 (a) Adsorption-Desorption isotherm (b) BJH Pore Size Distribution of $\text{Cr}_x(x=0-0.2) (\text{Ce}_{0.9}\text{Pr}_{0.1})_{1-x} \text{O}_{2-\delta}$ Catalysts

9.5. XPS ANALYSIS

XPS spectra of Ce 3d, Pr 3d, O1s, and Cr 2p were depicted in **Figure 9.5 (a-d)**, respectively. The peak positions assigned to Ce (Ce^{4+} and Ce^{3+}), Pr (Pr^{4+} and Pr^{3+}) were noted in the literature reported (Fu et al. 2014; Holgado et al. 2000; Mittal et al. 2018; Poggio-Fraccari et al. 2018). The O1s spectra consist of lattice oxygen species (O^{2-}) and the chemisorbed oxygen species (O^- , O_2^{2-} and H-O-H) (Jones et al. 2015; Patil et al. 2019). The Cr 2p spectra provide information on surface Cr ions and show that Cr generally has a multi-oxidation state (Cr^{2+} to Cr^{6+}) (Shupack 1991). It was noticed in **Figure 9.5c** that the spectra consist of Cr^{3+} and Cr^{4+} ions on the surface. **Table 9.3** reveals the information on the reducibility ratio of reducible ions (Ce^{3+} , Pr^{4+} , Cr^{3+} , and Cr^{4+}) and surface oxygen ion ratio for $\text{Cr}_{x(x=0-0.2)}(\text{Ce}_{0.9}\text{Pr}_{0.1})_{1-x}\text{O}_{2-\delta}$ catalysts. It can be seen from the table that the CP showed a high reducibility ratio of 0.43 for Ce^{3+} and 5 Cr-CP had high Pr^{3+} ions (0.40) compared to all the $\text{Cr}_{x(x=0-0.2)}(\text{Ce}_{0.9}\text{Pr}_{0.1})_{1-x}\text{O}_{2-\delta}$ catalysts.

It can also be noticed from **Table 9.3** that the presence of surface chemisorbed oxygen species O^- and O_2^{2-} was found to be highest for the 15 Cr-CP and 10 Cr-CP catalysts, respectively. 5 Cr-CP catalysts comprised additional oxygen species at ~534 eV, assigned to adsorbed molecular water (Yafarova et al. 2021). Generally, Ceria-based catalysts express more than a single form of oxygen ion species (Sudarsanam et al. 2014a), which may influence catalytic activity. The presence of O^{2-} species also plays a significant role in catalytic soot oxidation if the surface area is low (Liang et al. 2007b). Hence, the O^{2-} species ratio presented in the table revealed that 20 Cr-CP had the highest (0.79) O^{2-} species than other $\text{Cr}_{x(x=0-0.2)}(\text{Ce}_{0.9}\text{Pr}_{0.1})_{1-x}\text{O}_{2-\delta}$ catalysts. When considering Cr 2p spectra, Cr^{3+} surface ions were high (0.40) for 5 Cr-CP ions, and Cr^{4+} concentration was high (0.53) for 10 Cr-CP ions. Cr^{3+} is the most stable oxidation state than Cr^{2+} , Cr^{4+} , Cr^{5+} , and Cr^{6+} (Mangaiyarkarasi et al. 2011). The surface ionic species' concentration and interactions may boost the adsorption capacity (Cai et al. 2015).

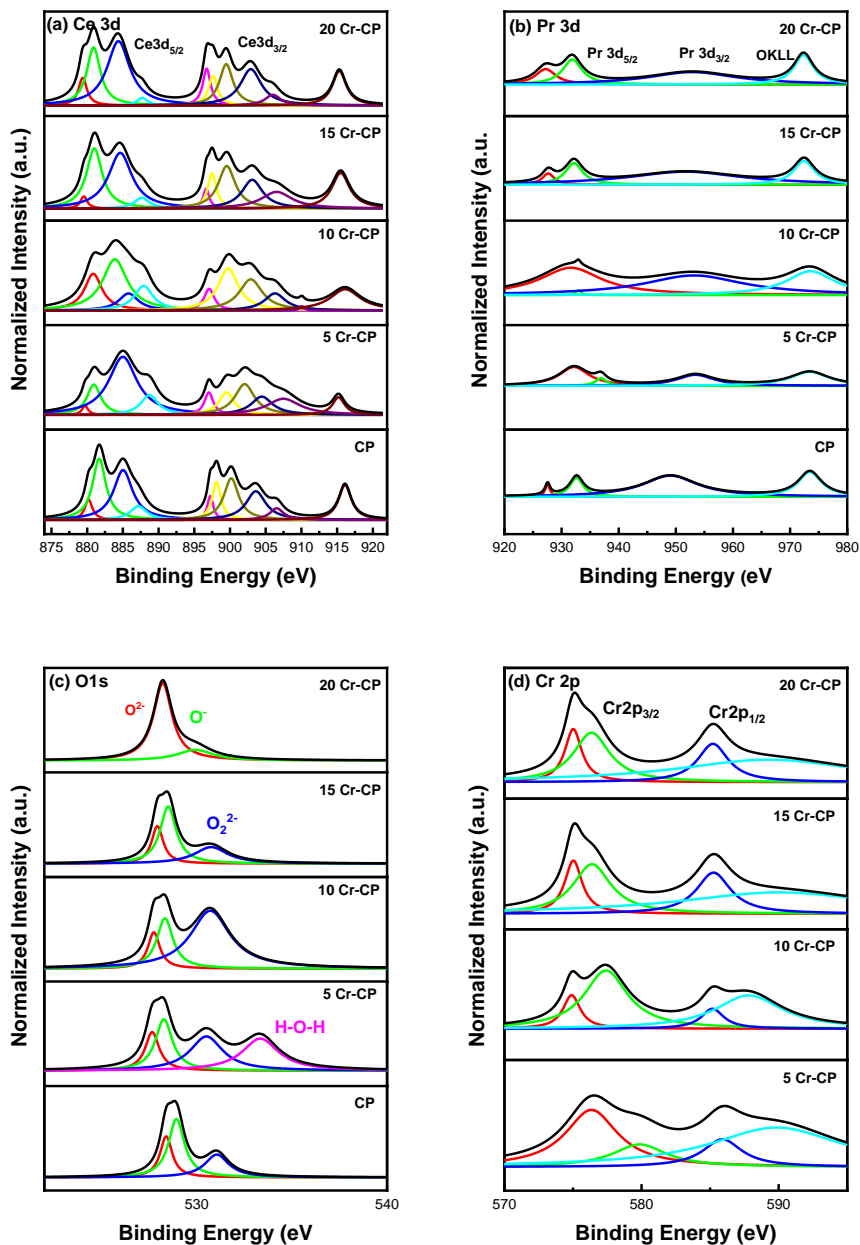


Figure 9.5 (a) Ce 3d (b)Pr 3d (c) O1s (d) Cr 2p XPS spectra for $\text{Cr}_x(x=0-0.2)$ ($\text{Ce}_{0.9}\text{Pr}_{0.1}$) $_{1-x}\text{O}_{2-\delta}$ Catalysts

Table 9.3: Reducibility ratio and Surface Oxygen species ratio of $\text{Cr}_{x(x=0-0.2)} (\text{Ce}_{0.9}\text{Pr}_{0.1})_{1-x} \text{O}_{2-\delta}$ Catalysts

Catalyst	Reducibility Ratio				Lattice Oxygen	Adsorbed Oxygen species		
	$\frac{\text{Ce}^{3+}}{\text{Ce}^{3+} + \text{Ce}^{4+}}$	$\frac{\text{Pr}^{3+}}{\text{Pr}^{3+} + \text{Pr}^{4+}}$	$\frac{\text{Cr}^{3+}}{\text{Cr}^{3+} + \text{Cr}^{4+}}$	$\frac{\text{Cr}^{4+}}{\text{Cr}^{3+} + \text{Cr}^{4+}}$	$\frac{\text{O}^{2-}}{\text{O}^{2-} + \text{O}^- + \text{O}_2^{2-}}$	$\frac{\text{O}^-}{\text{O}^{2-} + \text{O}^- + \text{O}_2^{2-}}$	$\frac{\text{O}_2^{2-}}{\text{O}^{2-} + \text{O}^- + \text{O}_2^{2-}}$	H - O - H
CP	0.42	0.15	-	-	0.17	0.46	0.24	-
5 Cr-CP	0.18	0.40	0.40	0.40	0.14	0.23	0.30	0.31
10 Cr-CP	0.18	0.35	0.18	0.53	0.12	0.23	0.64	-
15 Cr-CP	0.31	0.20	0.27	0.33	0.22	0.48	0.28	-
20 Cr-CP	0.31	0.30	0.25	0.33	0.79	0.20	-	-

9.6. SOOT OXIDATION ACTIVITY

Figure 9.6 depicts soot conversion curves with an increase in temperature. The T_{50} temperature is noted for all the catalysts and is listed in **Table 9.4**. From the table, it can be noticed that there was a significant reduction in T_{50} on loading Cr and the CP system. CP showed T_{50} of 408 ± 4 °C. 5 Cr-CP exhibited T_{50} of 393 ± 2 °C, and T_{50} remained constant ~ 413 °C on further addition of Cr; Pure Cr displayed T_{50} of 422 ± 1 °C.

The descriptors and catalyst properties, which may probably enhance catalytic activity, were analyzed from the characterization of the developed catalysts. The XRD studies showed that the crystallite size for all the Cr-doped CP was reduced and increased in lattice strain and Facet ratios. Raman analysis confirmed the presence of O_v peaks for all Cr-doped CP catalysts. 20 Cr CP possessed the highest SA of $96 \text{ m}^2/\text{g}$. CP had a better reducibility ratio for Ce^{3+} and Pr^{3+} ions. On the other hand, 5 Cr-CP had high concentrations of Cr^{3+} ions. 20 Cr-CP had better lattice oxygen species (O^{2-}), whereas the surface chemisorbed oxygen species O^- and O_2^{2-} was found to be highest for the 15 Cr-CP and 10 Cr-CP catalysts, respectively. Additionally, adsorbed H_2O or adsorbed molecular water peak in O1s spectra was observed for 5 Cr-CP catalyst alone. Hence, 5 Cr-CP showed better T_{50} of 393 ± 2 °C mainly due to the presence of Cr^{3+} ions species from XPS analysis.

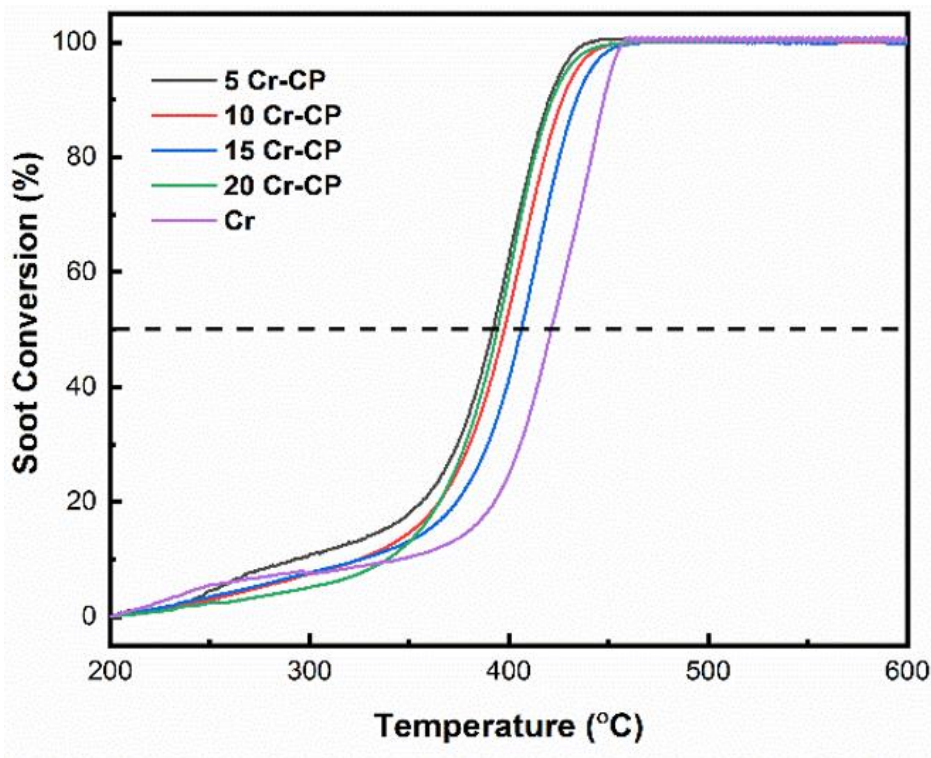


Figure 4.7. Soot Oxidation activity of $\text{Cr}_{x(x=0,05-0.2)}(\text{Ce}_{0.9}\text{Pr}_{0.1})_{1-x}\text{O}_{2-\delta}$ Catalysts

9.7. KINETIC ANALYSIS

9.7.1. Determination of Kinetic Triplets (Activation Energy (E_a) and Pre-Exponential Factor (A) and Reaction Model).

As described in previous chapters, the E_a value was determined by model-free methods such as Ozawa, KAS, and CR (Ganiger et al. 2022; Gotor et al. 2000; Landa et al. 2007). The "Am" method is employed to obtain the A value and exponential integer "m" value which is further utilized in the CR method to obtain both E_a and A values for the catalysts.

Ozawa, KAS, CR, and Am plots are plotted for all the samples and are provided in the Appendix section from **Figure A9.1(a-d) to A9.4(a-d)**, respectively. The E_a and A values obtained from all three methods are represented in **Table 9.4**, along with the "m" values. The activation energy varied from 87 to 143 kJmol⁻¹ for the Cr-doped CP catalysts. 15 Cr-CP displayed lower E_a values of 87 kJmol⁻¹, while 5 Cr-CP showed a higher E_a value of 143 kJmol⁻¹ among all the Cr-doped CP catalysts. In the present study, "m" values for the catalysts ranged from 0.5 to 1.5; hence the possibility of various reaction models can be predicted. The highest A value (Am method) of $7.39 \times 10^{10} \text{ min}^{-1}$ was obtained by 5 Cr-CP, and the lowest 15 Cr-CP obtained a value of $0.00014 \times 10^{10} \text{ min}^{-1}$ among the Cr-doped CP catalysts.

The master plots with $g(\alpha)$ values calculated for different reaction models by varying conversion (α) are plotted and are shown in **Figure A9.5 (a-d)**. The reaction models coinciding for all the catalysts were noted and are provided in **Table 9.4**. It can be seen that most of the catalysts followed the nucleation and growth model. Cr-doped CP catalyst followed a power law; phase boundary controlled reaction, nucleation, and growth model.

9.7.2. Experimental and Calculated Data Comparison

Figure 9.8 shows thermoanalytical curves for experimental and calculated data for Cr_{x(x=0.05-0.2)} (Ce_{0.9}Pr_{0.1})_{1-x} O_{2- δ} catalysts. It revealed that most catalysts had a relatively good consistency compared to all other samples. It also indicates that the proposed kinetic analysis was suitable for modeling soot combustion. It also signifies that the nucleation and growth model plays a significant role in describing the reaction mechanism. Substantial deviation in the plots indicates that it does not follow the Nucleation and Growth model for all α values. It can be seen that as the concentration of Cr increased, the deviation was evident.

Table 9.4. Kinetic triplets and "m" value for $\text{Cr}_{x(x=0-0.2)} (\text{Ce}_{0.9}\text{Pr}_{0.1})_{1-x} \text{O}_{2-\delta}$ Catalysts.

Catalyst	T_{50} (°C)	E_a (kJ mol ⁻¹)			Reaction Model	$A \times 10^{10}$ (min ⁻¹)		m
		Ozawa method	KAS method	CR method		Am method	CR method	
CP	408±4	111	96	94	A1.5 ,P1,P2	0.000055	0.000039	1.35
5 Cr-CP	393±2	143	145	144	A1, P3, L4	7.39	5.36	0.93
10 Cr-CP	413±1	138	141	138	A1, L4	3.44	2.39	0.79
15 Cr-CP	413±2	87	90	85	A1,A1.5,A2,P1,P2,P3,L4	0.00014	0.00016	1.36
20 Cr-CP	413±3	103	108	105	A1,A1.5, P1,P2, L4,R2	0.0050	0.012	1.08
Cr	422±1	106	103	105	A1.5, P1	0.0017	0.0013	1.43

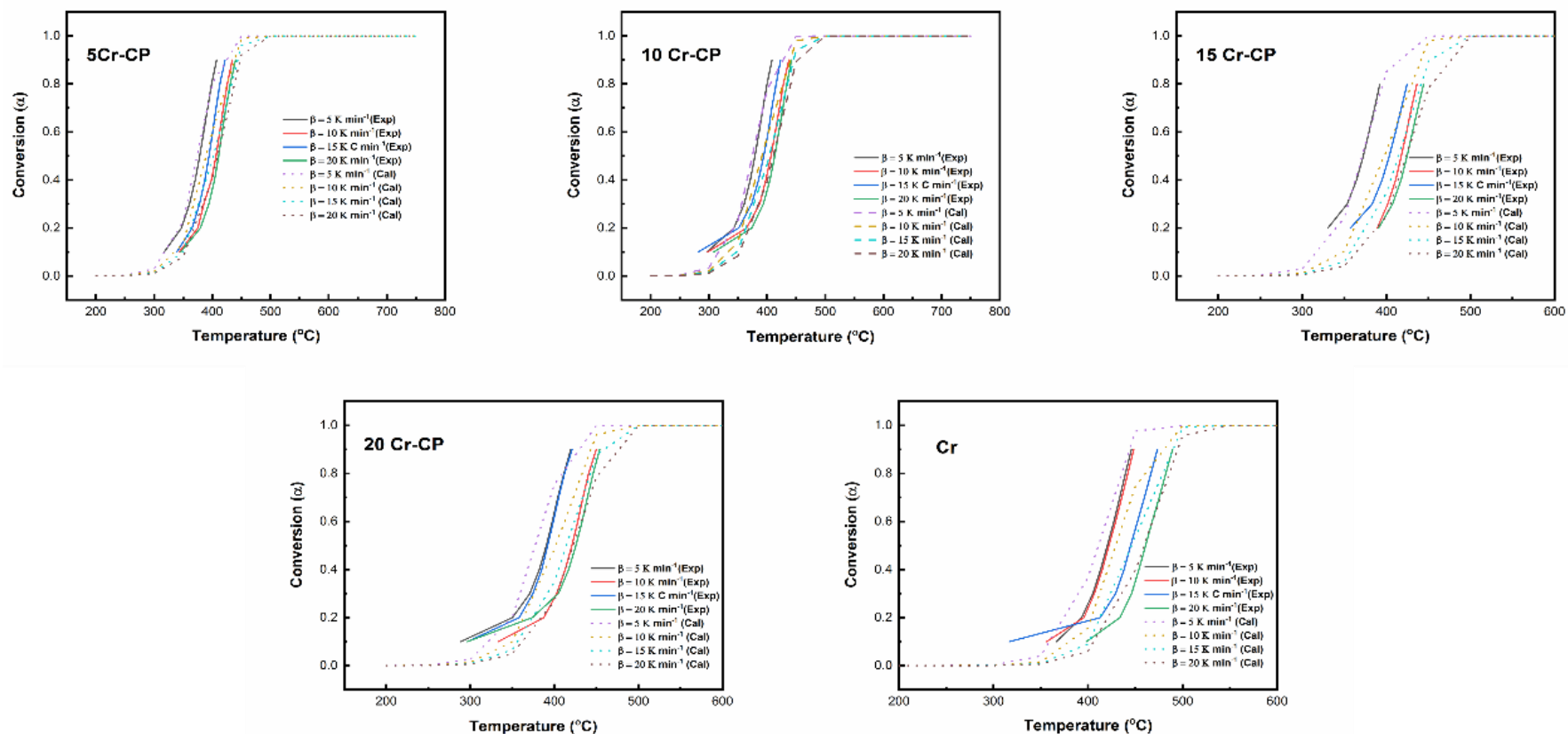


Figure 9.8. Experimental and calculated curves for $\text{Cr}_x(x=0.05-0.2) (\text{Ce}_{0.9}\text{Pr}_{0.1})_{1-x} \text{O}_{2-\delta}$ Catalysts

The catalytic effect of Chromium-Doped Ceria-Praseodymium on Soot Oxidation Activity and its Kinetics

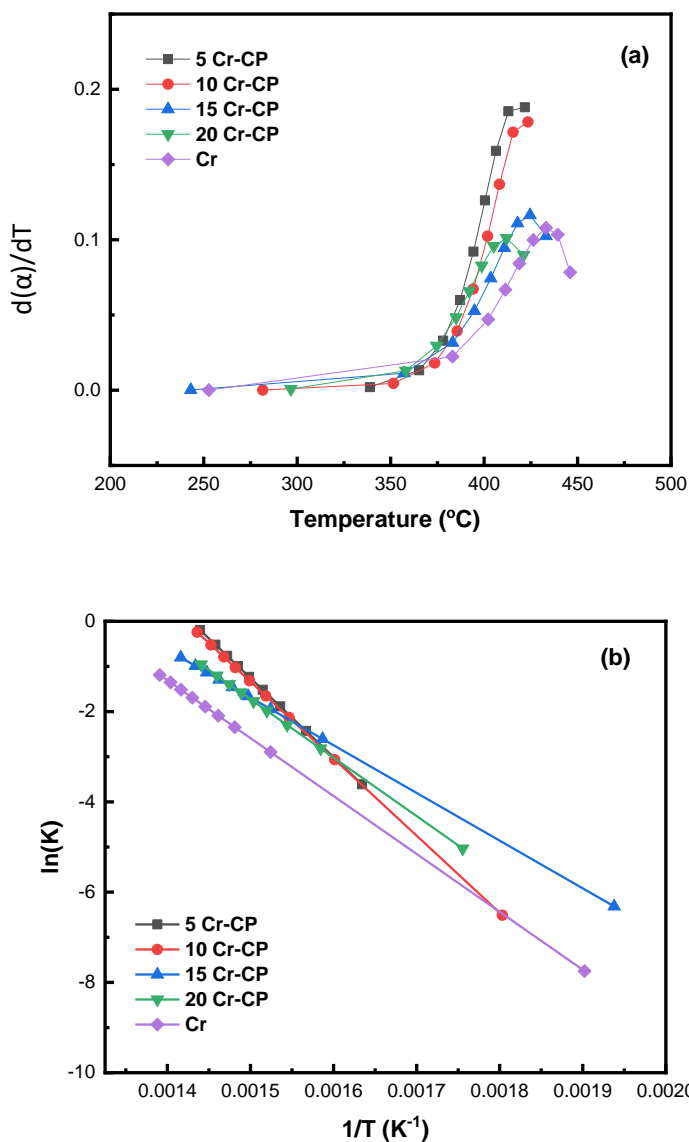


Figure 9.7. (a) Rate vs. Temperature plot (b) Arrhenius plot for $\text{Cr}_x(x=0.05-0.2)$ $(\text{Ce}_{0.9}\text{Pr}_{0.1})_{1-x}\text{O}_{2-\delta}$ Catalysts

Figure 9.9 (a) and (b) demonstrate $d\alpha/dT$ vs. temperature and $\ln(k)$ vs. $1/T$ plots, respectively, for $\text{Cr}_{x(x=0.05-0.2)}(\text{Ce}_{0.9}\text{Pr}_{0.1})_{1-x}\text{O}_{2-\delta}$ catalysts. From **Figure 9.9 (a)**, it can be noticed that 5 Cr-CP had a higher rate compared to the other catalyst. From **Figure 9.9 (b)**, the kinetic activity is high for 5 Cr-CP and the least for the Pure Cr catalyst.

9.8. CONCLUSION

$\text{Cr}_{x(x=0-0.2)}(\text{Ce}_{0.9}\text{Pr}_{0.1})_{1-x}\text{O}_{2-\delta}$ catalysts were successfully developed by the SCS method. The XRD studies showed reduced crystallite size for all the Cr-doped CP and increased lattice strain and Facet ratios. Raman analysis confirmed the presence of O_v peaks for all Cr-doped CP catalysts. 20 Cr CP possessed the highest SA of $96\text{ m}^2/\text{g}$. CP had a better reducibility ratio for Ce^{3+} and Pr^{3+} ions. On the other hand, 5 Cr-CP had high concentrations of Cr^{3+} ions. 20 Cr-CP had better lattice oxygen species (O^{2-}), whereas the surface chemisorbed oxygen species O^- and O_2^{2-} was found to be highest for the 15 Cr-CP and 10 Cr-CP catalysts, respectively. Additionally, adsorbed H_2O or adsorbed molecular water peak in O1s spectra was observed for 5 Cr-CP catalyst alone. From TGA analysis for soot oxidation, 5 Cr-CP showed better T_{50} of $393\pm 2^\circ\text{C}$ mainly due to the presence of Cr^{3+} ions species from XPS analysis.

Kinetic analysis was conducted for all the Cr-doped CP catalysts to evaluate kinetic triplets, namely the Activation energy, Pre-Exponential Factor, and Reaction model. The activation energy was lowest (87 kJmol^{-1} , Ozawa method) for 15 Cr-CP, and the Pre-Exponential factor was high for 5-Cr-CP ($7.39 \times 10^{10}\text{ min}^{-1}$).

The catalysts followed a power law; phase boundary controlled reaction, nucleation, and growth model. Experimental and calculated curve consistency confirmed that the developed catalysts followed the Avrami-Erofeev equation (Am) or the Nucleation and Growth model.

The surface concentration of Cr^{3+} and Pr^{3+} played a significant descriptor role, and 5Cr-CP catalytic system showed better soot oxidation activity than other Cr-CP catalytic systems. As the Cr concentration increased, there was a decrease in the Cr^{3+} and Pr^{3+} concentrations in the Cr-CP catalyst system. Compared to other transitional metal-doped CP catalytic systems with increased Cr content, there is only a slight decrease in soot oxidation activity. From Chapters 5 to 9, it is observed that irrespective of the transitional metal, 5 mol% transitional metal doping in the Ceria- Praseodymium catalytic system showed better soot oxidation activity even though various descriptors controlled the activity. In the next chapter, 5 mol% transitional metal doped Ceria-Praseodymium catalyst nanofibers were obtained using an electrospinning technique, characterized, and tested for soot oxidation activity.

CHAPTER 10

ELECTROSPUN TRANSITION METAL ($T.M_{(x=0.05)} = Cr, Mn, Fe, Co, Cu$) - DOPED $Ce_{0.9}Pr_{0.1}O_{2-\delta}$ (CP) NANOFIBERS AND ITS SOOT OXIDATION ACTIVITY

10.1. BACKGROUND

Electrospinning is a widely used technology for nanofiber fabrication with controllable diameter and structure (Bhardwaj and Kundu 2010). The electrospinning technique gained significant attention as it can fabricate nanofibers on a nanometer scale with high quality (CUI et al. 2008; Stegmayer et al. 2022). Unique electrospinning methods can produce nanofibers with porous core-shell or hollow nanofiber structures (Thavasi et al. 2008). Nanofibers are used in several catalytic applications, such as photocatalysis and oxidation reactions (Stegmayer et al. 2022). Nanofibers in the past decade indicated a favorable impact and represented a key technology for environmental applications (Thavasi et al. 2008).

Nanofibers as soot oxidation catalysts are preferred due to increased surface area, eventually leading to enhanced soot and nanofiber contact points (Stegmayer et al. 2022). Ce-based nanofibres for soot oxidation have been studied and are reported to improve the catalytic performance (Bensaid et al. 2013b; Stegmayer et al. 2022; Zhu et al. 2022). Miceli et al. 2014 reported that Ce-based nanofibers enhance soot-catalyst contact and contact morphology. The number of soot-catalyst contact points plays a significant role in solid-solid catalysis (Stegmayer et al. 2022; Zhu et al. 2022).

Similarly, Lee et al. (Lee et al. 2015) studied Ag-supported electrospun CeO_2 nanofibers for diesel soot oxidation with nanofibers ranging from ~241–253 nm dia. The temperature at which 50% of soot converted (T_{50}) was reported to be ~530-495°C under tight contact mode. Bensaïd et al. (Bensaïd et al. 2013a) worked on fibrous CeO_2 catalysts for soot oxidation. It was reported that the morphology affects the nature of soot–catalyst contact. It was also concluded that the nanofibers are one of the perfect morphologies for soot combustion due to soot particles being entrapped in a network of fibers, augmenting the sum of contact points. Aneggi et al. (Aneggi et al. 2014b) reported that morphologically controlled catalysts could enhance catalytic performance due to increased active or contact points.

Kumar et al. (Kumar et al. 2012a) produced CeO_2 nanofibers and deposited them on a SiC lab scale and real DPFs to promote soot combustion. It was reported that the soot oxidation was better inside the DPF when coated with nanofibers than other morphologies. Kumar et al. (Kumar et al. 2012b) also performed studies on CeO_2 and Co- CeO_2 nanofibres for diesel soot oxidation activity; it was determined that the mobility of the oxygen species was enhanced due to cobalt loading. It was also inferred that the fibrous morphology could trap and convert soot to non-detrimental form at low temperatures. Stegmeyer et al. (Stegmeyer et al. 2022) reported that the differences in surface area and crystallite sizes might only not influence the catalytic behavior as the soot oxidation reaction takes place on the external surface of the fibers. From the previous chapters, it was noticed that doping 5 mol % in the Ceria- Praseodymium catalytic system showed better soot oxidation activity even though various descriptors controlled the activity.

The present work is directed to develop efficient Transition Metal ($T.M_{(X=0.05)} = Cr, Mn, Fe, Co, Cu$) doped $(Ce_{0.9}Pr_{0.1})_{0.95} O_{2-\delta}$ nanofibres using the electrospinning technique for catalytic soot oxidation.

10.2. XRD AND RAMAN SPECTROSCOPY ANALYSIS

Fig. 10.1 (a) displays the XRD spectra of electrospun nanofibers. From the Figure, it can be seen that all the nanofibers show evidence of planes corresponding to the cubic fluorite structure of CeO_2 (Mukherjee et al. 2016; Prasad et al. 2012b). No impurity phase was noticed in the nanofiber's spectra, indicating that all the transition metals were incorporated well into the CP catalyst system. Hence solid solution formation can be confirmed from the XRD analysis.

The physicochemical parameters obtained from XRD and Raman spectroscopy analysis are tabulated in **Table 10.1**. The crystallite size obtained for all the nanofibers is in the range of 8 to 14 nm. The crystallite size decreased from 14 nm with the addition of transition metals. 5 Fe-CP and 5 Mn-CP obtained a smaller crystallite size of ~8 nm. In contrast, CP had a crystallite size of ~14 nm, which indicates a slight decrease in crystallite size with the addition of transition metals into the CP catalyst system due to solid solution formation. It can be noticed that the lattice strain increased to some extent from 0.0107 to 0.0193 with the addition of T.M. into CP. The facet ratios for exposed reactive planes (200) and (220) were calculated and reported in **Table 10.1**. Remarkably there was no significant change in the facet ratio $\{100\}/\{111\}$, and the ratio ranged with a narrow range from 0.32 to 0.35. Whereas the facet ratio of $\{110\}/\{111\}$ ranged from 0.30 to 0.43. The above analysis indicates that the physicochemical properties of the nanofibers showed no significant difference with the transition metals doping. The facets for the reactive planes (200) and (220) are generally where the oxygen vacancy formation is less than that on the (111) plane (Cordatos et al. 1996). Hence the increase in the ratio signifies the improved oxygen vacancies, which may play a vital role in influencing catalytic soot oxidation activity.

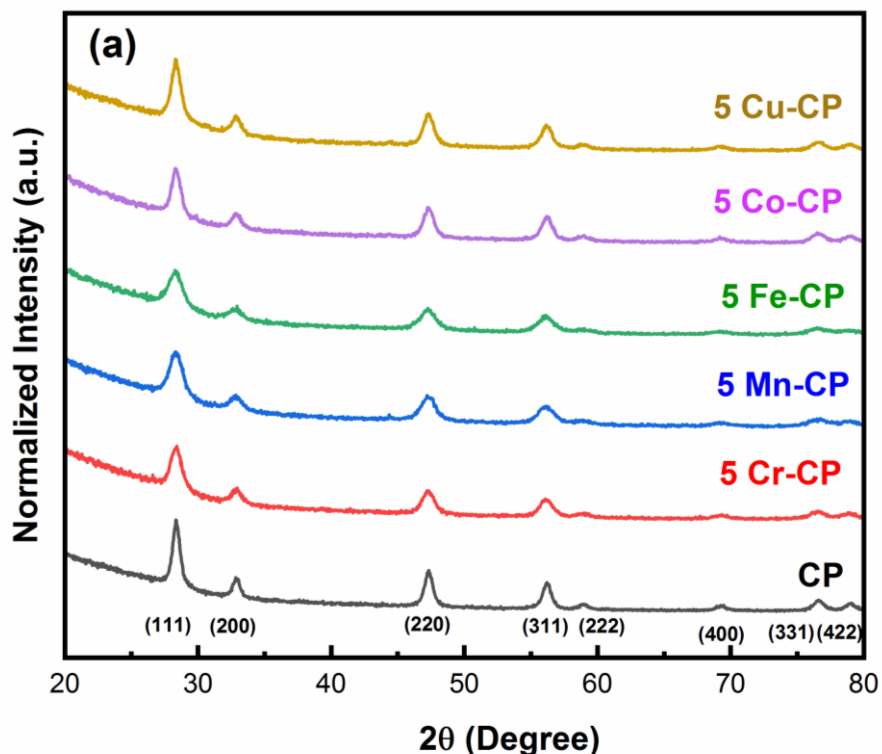


Figure 10.1: XRD analysis for T.M_(x=0.05) doped (Ce_{0.9}Pr_{0.1}) O_{2-δ} nanofibers

Figure 10.2 represents the Raman spectra of electrospun nanofibers. It can be observed from the figure that all the nanofibers exhibited the F_{2g} mode of CeO₂, which is attributed to the symmetric breathing of O-Ce-O atoms (Anantharaman et al. 2018d; Shajahan et al. 2018). All the nanofibers also exhibited a peak of $\sim 560\text{ cm}^{-1}$, corresponding to oxygen vacancies. As observed from XRD analysis, Raman spectra show no evidence of impurity or secondary phases.

The intensity ratio ($I_{O_v}/I_{F_{2g}}$) was calculated to evaluate the O_v concentration in the nanofibers and is shown in **Table 10.1**. From the intensity ratios calculated, it can be seen that the values ranged from 0.26 to 0.40, where 5 Cr-CP had the lowest $I_{O_v}/I_{F_{2g}}$ of 0.26.

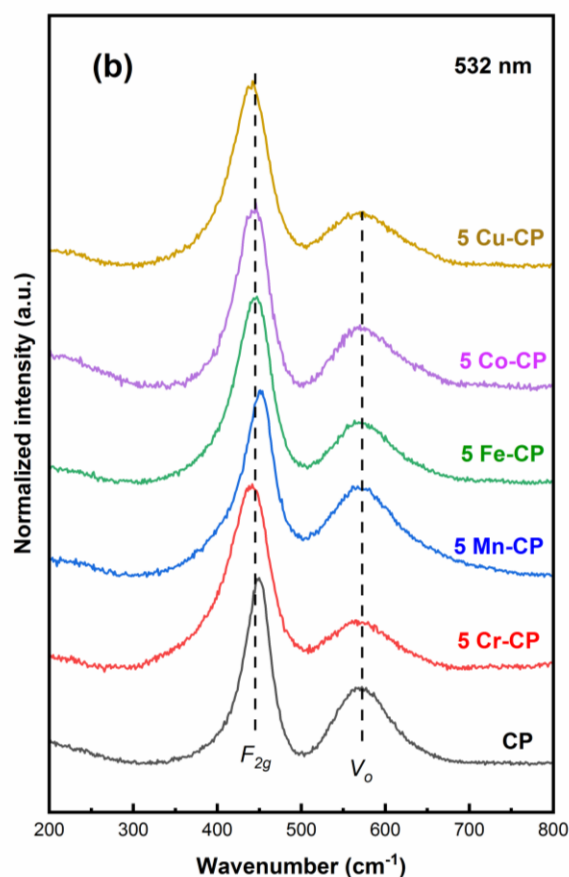


Figure 10.2: Raman spectroscopy analysis for $T.M_{(x=0.05)}$ doped $(Ce_{0.9}Pr_{0.1})O_{2-\delta}$ nanofibers

10.3. BET-BJH ANALYSIS

BET and BJH analysis was performed for all the electrospun nanofibers. The surface area of the nanofibers varied from 59 to 128 m²/g. **Figure 10.3(a)** demonstrates the N₂ adsorption-desorption isotherm, which indicates that all the catalysts followed Type IV adsorption with H4 hysteresis, indicating the presence of mesoporous and microporous nature (Thommes et al. 2015).

The obtained nanofibers' average pore size diameter and pore volume ranged from 05.42 to 15.16 nm and 0.09 to 0.35 cc/g, respectively. 5 Cr-CP and 5 Cu-CP gained the largest and smallest pore size and volume, respectively. **Figure 10.3(b)** displays the pore size distribution of the obtained nanofibres. It can be noticed that the pore size was distributed between 5 to 15 nm, confirming the presence of mesopores (Thommes et al. 2015).

10.4. FE-SEM ANALYSIS

Figure 10.4 shows the FE-SEM images of T.M doped CP nanofiber catalysts obtained by electrospinning technique and calcined at 600°C / 5 h in the air at atmospheric pressure. It can be observed in **Figure 10.4a** shows some morphological changes in the nanofiber structures by adding transitional metals (T.M= Cr, Mn, Fe, Co, and Cu) as dopants in the CP-based catalyst system. The cross-linked nanofiber webs are thin in CP catalyst, and adding transitional metals increases the number of cross-linked nanofiber webs. 5 Cr-CP and 5 Cu-CP nanofiber catalysts displayed similar nanofiber morphology with irregular cross-linked nano-finer webs. 5 Mn-CP and 5 Fe-CP catalysts showed similar cross-linked nanofiber webs.

Electrospun Transition Metal ($T.M_{(x=0.05)} = Cr, Mn, Fe, Co, Cu$) - Doped $Ce_{0.9}Pr_{0.1}O_{2-\delta}$ (CP) Nanofibers and its Soot Oxidation Activity

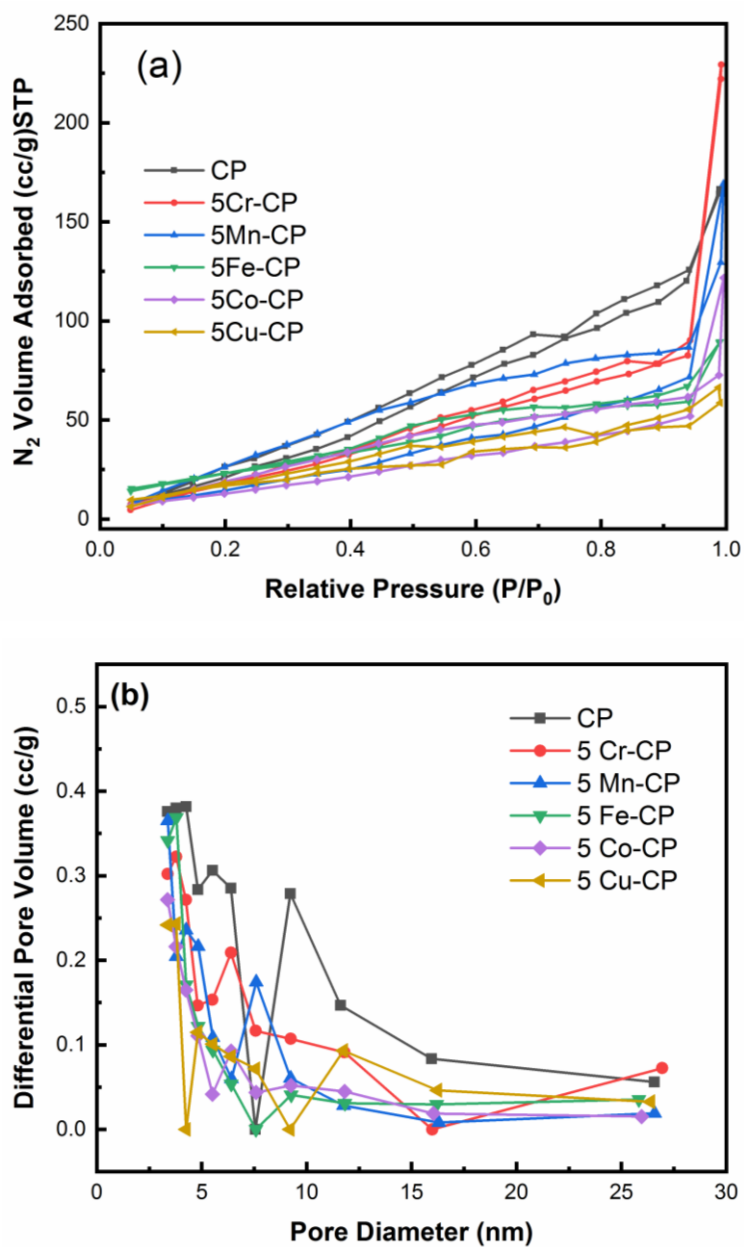


Figure 10.3: (a) N_2 -adsorption-desorption isotherm (b) Pore size distribution curves for $T.M_{(x=0.05)}$ doped $(Ce_{0.9}Pr_{0.1})O_{2-\delta}$ nanofibers

Figure 10.4b shows that the diameter of a single nanofiber string of CP catalyst is around ~246 nm. With the addition of transitional metals (Cr, Mn, Fe, Co, and Cu) as dopants in the CP-based catalyst system, the diameter of the single nanofiber string is decreased, and it is in the range of 100 ~ 170 nm.

Lee et al.2015, fabricated the three-dimensional arrangements of LSCF perovskite-based oxide nanofibers and the 3D nanofiber web (with a thickness of ~ 55 μ m and nanofiber diameter of ~ 240 nm) the high-contact area by soot in the unique pore structure which enhanced the soot oxidation activity. The macropores developed in YSZ nanofiber were of bimodal distribution with a size range of 50 and 180 nm. Compared with the literature (Stegmayer et al. 2022, Lee et al. 2015 and Liang et al. 2021) in the present study, the addition of transitional metals (Cr, Mn, Fe, Co, and Cu) as dopants in the CP-based catalyst system, the diameter of the single nanofiber string is decreased, and it is in the range of 100~170nm. The Cobalt incorporated into Ceria fibrous structure displayed a diameter in the range of 120~200 nm. The improvement in performance in solid-solid-gas reaction, i.e., soot oxidation, is owed to the Co-Ce mixed oxide nanofiber diameter (Stegmayer et al. 2022).

Table 10.1: Physicochemical properties of $T.M_{(x=0.05)}(Ce_{0.9}Pr_{0.1})_{1-x}O_{2-\delta}$ nanofibers obtained from XRD, Raman Spectroscopy, and BET-BJH analysis along with String diameter and T_{50} temperature.

Sample	Crystallite Size (nm)	Lattice strain (ϵ)	Facet Ratio		I_{0v}/I_{F2g}	BET S_A m^2/g	Avg. Pore Size (nm)	Pore volume (cc/g)	String diameter (nm)	T_{50} ($^{\circ}C$)
			{100}/ {111}	{110}/ {111}						
CP	14	0.0107	0.35	0.42	0.40	128	08.06	0.25	246-256	412
5 Cr-CP	10	0.0151	0.34	0.32	0.26	094	15.16	0.35	103-146	379
5 Mn-CP	08	0.0182	0.35	0.35	0.40	071	14.74	0.26	130-336	394
5 Fe-CP	08	0.0193	0.32	0.30	0.32	089	06.22	0.13	187-210	391
5 Co-CP	10	0.0145	0.35	0.43	0.34	059	12.80	0.18	157-290	415
5 Cu-CP	10	0.0147	0.35	0.43	0.28	067	05.42	0.09	141-365	388

Electrospun Transition Metal ($T.M_{(x=0.05)} = Cr, Mn, Fe, Co, Cu$) - Doped $Ce_{0.9}Pr_{0.1}O_{2-\delta}$ (CP) Nanofibers and its Soot Oxidation Activity

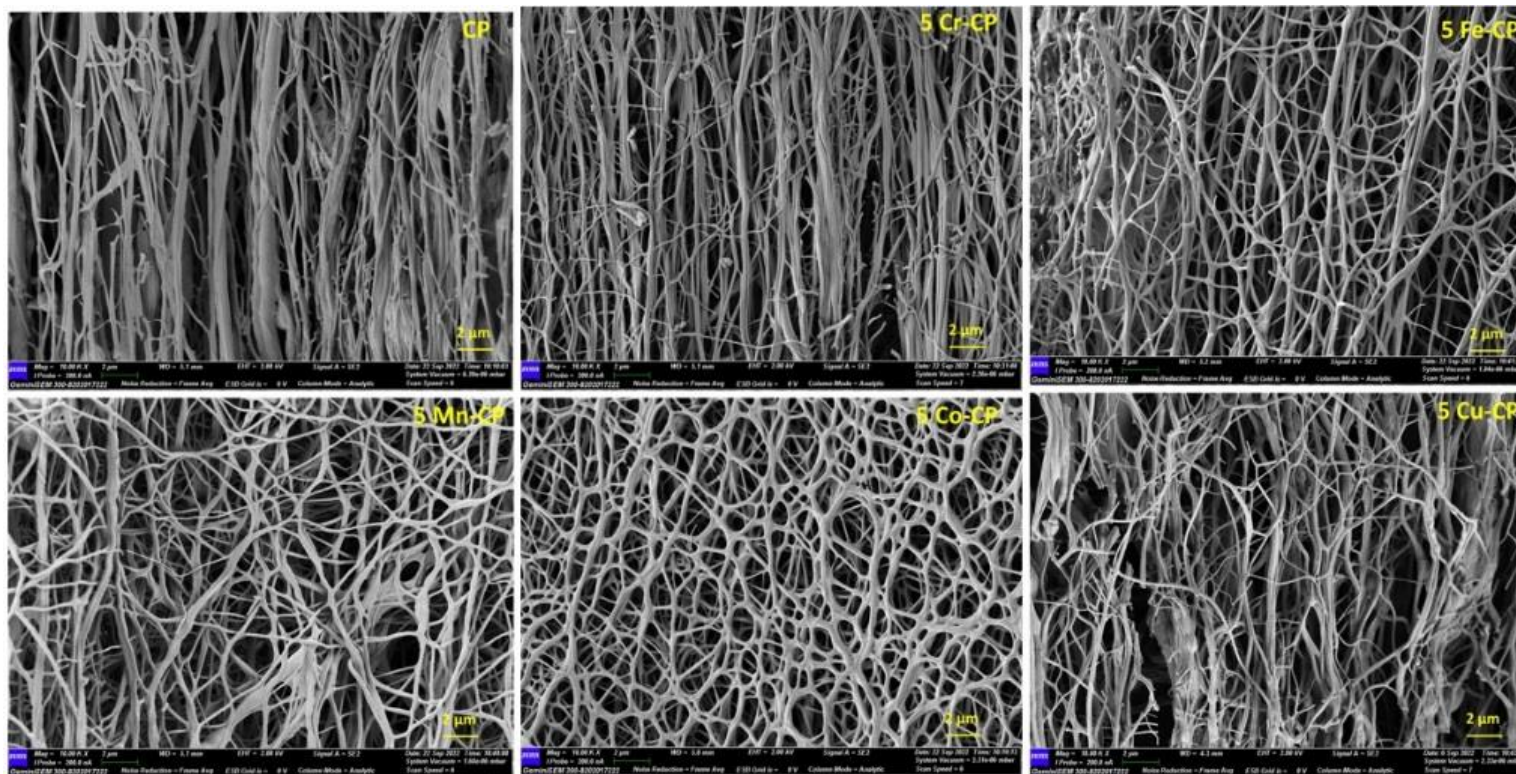


Figure 10.4(a): FE-SEM images of $T.M_{(x=0.05)}$ ($Ce_{0.9}Pr_{0.1}O_{2-\delta}$) nanofibers (2 μ m)

Electrospun Transition Metal ($T.M_{(x=0.05)} = Cr, Mn, Fe, Co, Cu$) - Doped $Ce_{0.9}Pr_{0.1}O_{2-\delta}$ (CP) Nanofibers and its Soot Oxidation Activity

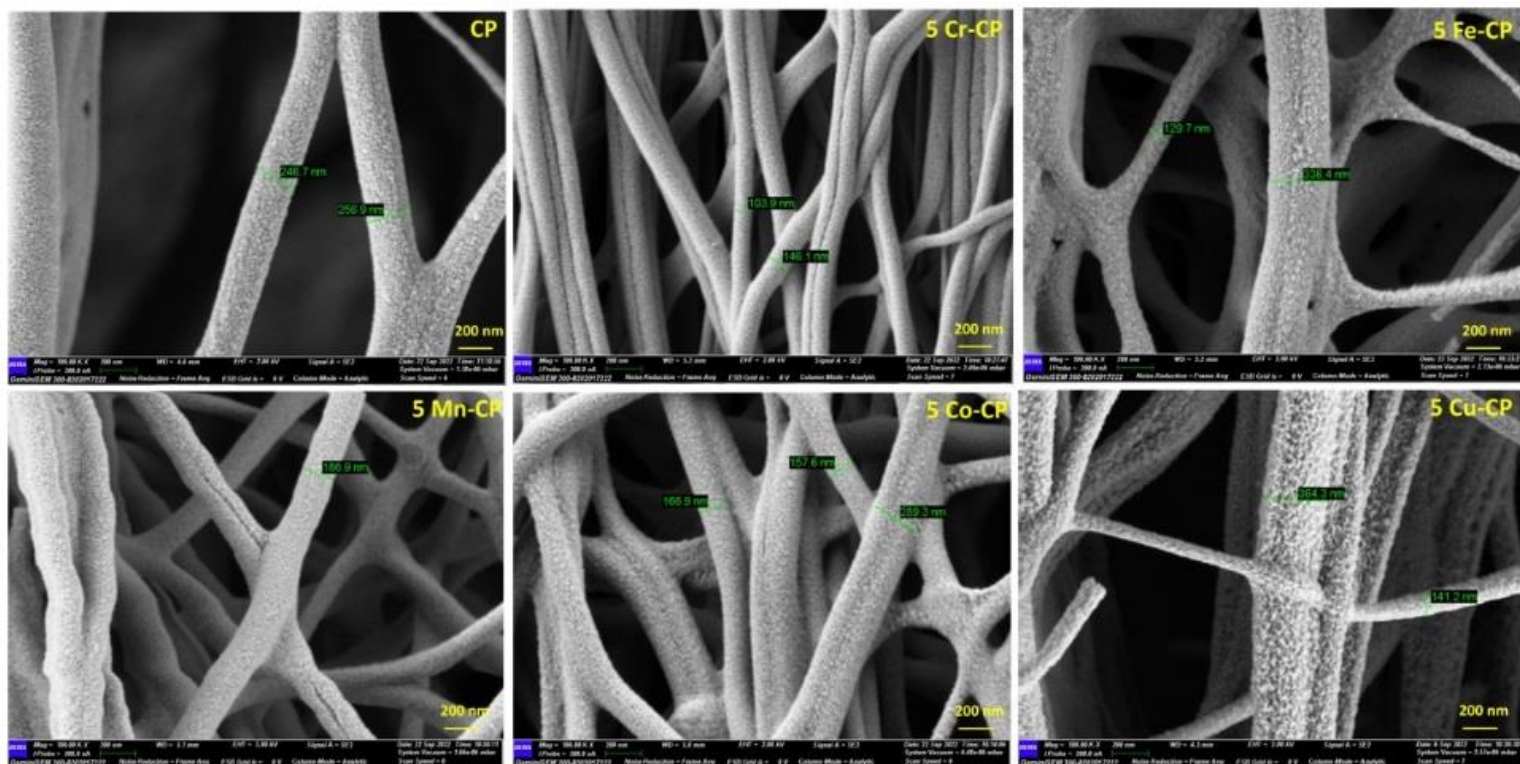


Figure 10.4(b): FE-SEM images of $T.M_{(x=0.05)} (Ce_{0.9}Pr_{0.1})_{1-x} O_{2-\delta}$ nanofibers (200 nm)

10.5. SOOT OXIDATION ACTIVITY

The soot oxidation activity of T.M doped CP nanofiber catalysts is depicted in **Figure 10.5**. The T_{50} temperature (**Table 10.1**) is in the order of 5Cr-CP ($379^{\circ}C$) < 5Cu-CP ($388^{\circ}C$) < 5Fe-CP ($391^{\circ}C$) < 5Mn-CP ($394^{\circ}C$) < CP ($412^{\circ}C$) < 5Co-CP ($415^{\circ}C$). 5Cr-CP displayed better catalytic activity, possibly due to the high average pore size diameter (15.16 nm) and pore volume (0.35 cc/g) compared to other developed nanofibers. 5 Cr-CP nanofiber catalysts also possessed the lowest diameter of ~103 to 146 nm, whereas the diameter of nanofiber catalysts ranged from ~103 to 365 nm. It was also noticed that the descriptors influencing nanopowder's catalytic activity showed no significant influence on the catalytic activity of nanofibers. Here, the morphology of the nanofibers played a critical role in influencing catalytic performance.

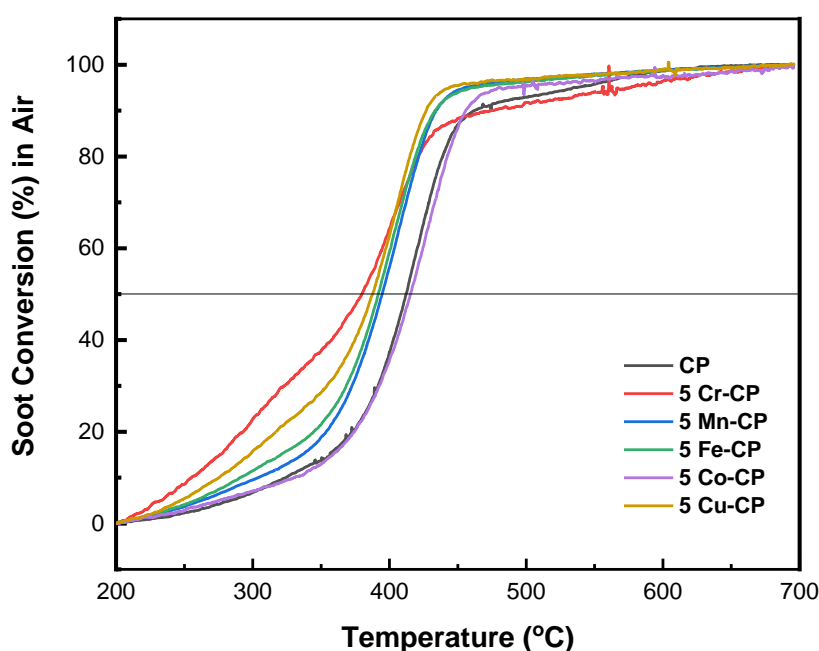


Figure 10.5: Soot conversion curves of $T.M_{(x=0.05)} (Ce_{0.9}Pr_{0.1})_{1-x} O_{2-\delta}$ nanofibers

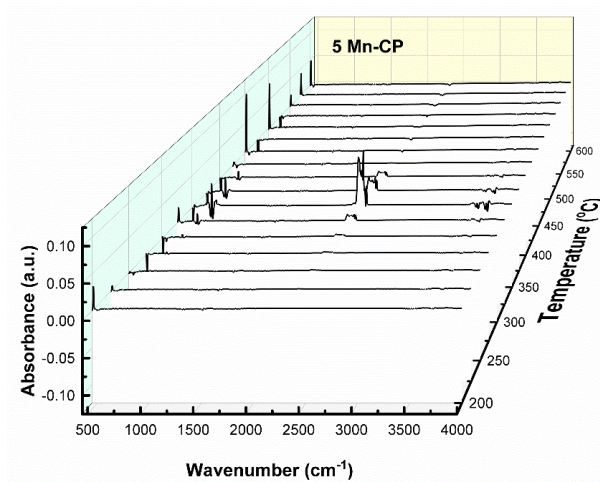
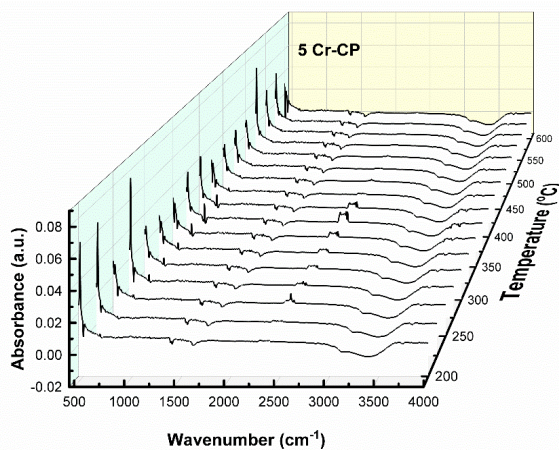
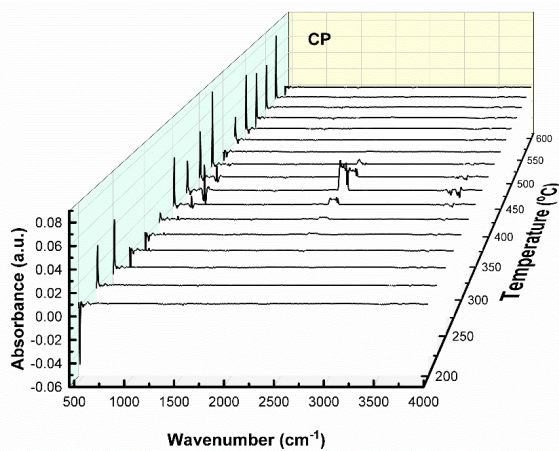
Stegmayer et al. (Stegmayer et al. 2022) fabricated Co-Ce mixed oxides nanofibers using an electrospinning technique and tested them for diesel soot reaction and reported that the contact points between the catalyst and soot particles were enhanced due to the nanofiber diameter. Hanying Liang et al. (Liang et al. 2021) developed highly reactive and thermally stable silver-loaded yttria (Ag/YSZ) macroporous fiber-like catalysts for soot oxidation activity and abundant defect sites on the surface of Ag-loaded macroporous YSZ resulted in silver re-dispersion further resulting in enhancement of the reactive oxygen species and thus improved the activity.

10.6. TGA-FTIR OF SOOT OXIDATION ACTIVITY

When TGA is hyphenated with FTIR, information regarding evolved gas composition can be deduced. The absorbance bands provide information on the typical compounds present during the oxidation reaction. **Figure 10.6** demonstrates three-dimensional (3D) TGA-FTIR plots for electrospun nanofibers mixed with soot.

The carrier gas carries the gases evolved to the IR, and the absorbance bands and vibrational modes acquired in the IR region ($450\text{-}4000\text{ cm}^{-1}$) are identified. The vibrational modes of functional groups present in the gases obtained at different temperatures are represented in the 3D spectra. The stretching bands below 500 cm^{-1} are related to Ce-O stretching vibration of the catalyst. The temperature range of the TG furnace is provided from $200\text{ to }600\text{ }^{\circ}\text{C}$ at $10\text{ }^{\circ}\text{C min}^{-1}$. From **Figure 10.6**, it can be observed that as the temperature increases, the intensity at a particular wavenumber also increases due to a rise in the gas evolved and wasn't observed at lower temperatures ($<300\text{ }^{\circ}\text{C}$) and higher temperatures ($>550\text{ }^{\circ}\text{C}$). The sharp, intense peaks observed below 500 cm^{-1} are assigned to the cubic fluorite structure of CeO_2 (Anantharaman et al. 2017).

Electrospun Transition Metal ($T.M_{(X=0.05)} = Cr, Mn, Fe, Co, Cu$) - Doped $Ce_{0.9}Pr_{0.1}O_{2-\delta}$ (CP) Nanofibers and its Soot Oxidation Activity



(Contd.)

A Study on the Effect of Transition Metal Dopants in Ceria Praseodymium Catalysts for Soot Oxidation Activity and its Kinetics

Electrospun Transition Metal ($T.M_{(x=0.05)} = Cr, Mn, Fe, Co, Cu$) - Doped $Ce_{0.9}Pr_{0.1}O_{2-\delta}$ (CP) Nanofibers and its Soot Oxidation Activity

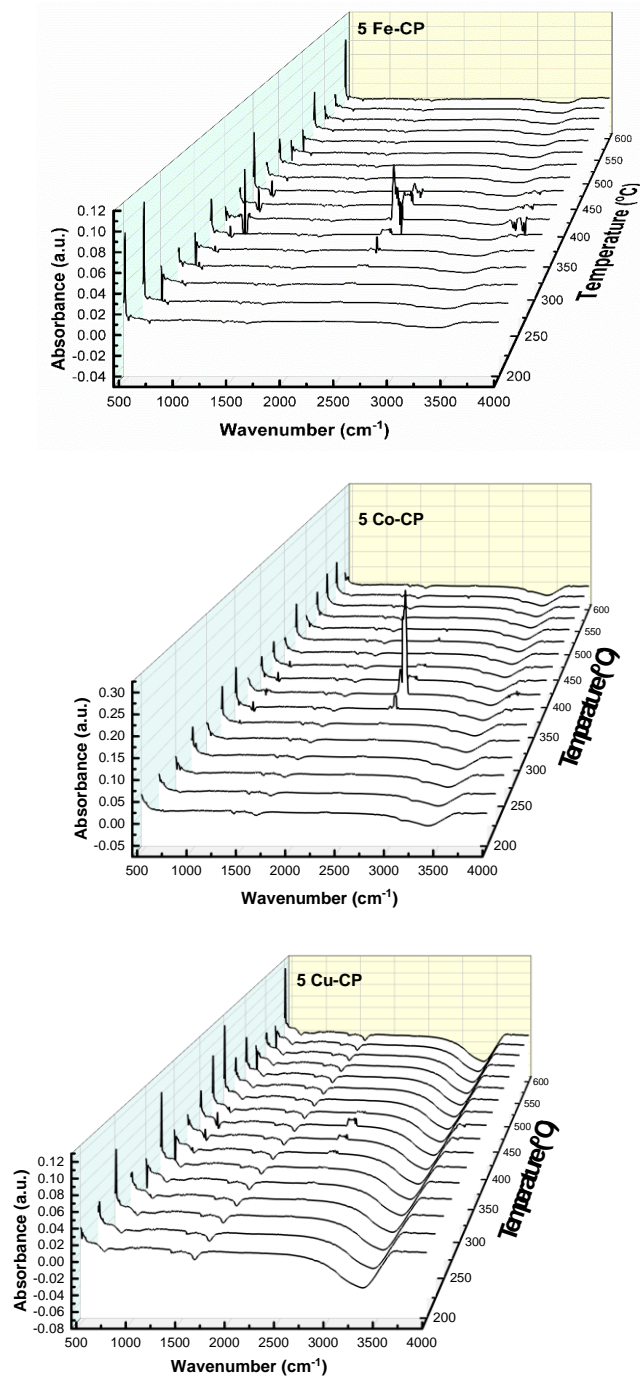


Figure 10.6: TGA-FTIR Plots for $T.M_{(x=0.05)} (Ce_{0.9}Pr_{0.1})_{1-x} O_{2-\delta}$ nanofibers

A Study on the Effect of Transition Metal Dopants in Ceria Praseodymium Catalysts for Soot Oxidation Activity and its Kinetics

It was noticed that the peaks reach a maximum at a temperature of around 400- 450 °C due to the evolution of CO₂. As per Tan and Lebron 2012, the IR modes for CO are observed around ~2144 cm⁻¹, whereas bands for CO₂ were obtained at ~ 669 and 2349 cm⁻¹. Abdul Jameel et al. 2017 also reported the IR bands ~ 2400–2224 and 2180–2108 for CO₂ and CO, respectively. In the present study the peaks ~ 670-672 cm⁻¹ and in the range of 2300-2360 cm⁻¹, which may be assigned to CO₂. The peaks observed at ~500 cm⁻¹, which is generally assigned to CeO₂ in FTIR spectra which represents Ce-O stretching vibration.

5 Co-CP showed an intense peak at ~ 425 °C, whereas the intensity was low for 5 Cr-CP. From soot oxidation curves observed in **Figure 10.5**, 5 Co-CP had the highest T₅₀ of 415 °C compared to other T.M doped nanofibers, and 5 Cr-CP had the lowest T₅₀ of 379 °C. From the present chapter, it can be concluded that, for catalytic soot oxidation activity, 5Cr-CP performed better mainly due to low nanofiber diameter, high average pore size diameter, and high pore volume, improving the contact points.

It was understood in the previous chapters that each transition metal had various properties responsible for better performance for catalytic activity. 5Co-CP, in nano-powder form performed better with lower T₅₀ of 350 °C due to better reducibility and high oxygen vacancy ratio whereas T₅₀ was high (415 °C) for 5 Co-CP in nanofibers form. Hence it can be said that the nanostructured catalysts may not be the factor influencing catalytic activity but depend on various parameters, such as smaller crystallite size, high facet ratios, surface area, pore volume and diameter, presence of oxygen vacancies, ionic active oxygen species, morphology or structure, and reducible ions which ultimately improves the contact points between soot and the catalyst.

10.7. CONCLUSIONS

The transition metal (TM (5 mol%) = Cr, Mn, Fe, Co, and Cu) -doped Ceria-Praseodymium catalysts nanofibers are synthesized using an electrospinning technique, characterized and tested for soot oxidation activity. Some of the key points are noted below:

- XRD analysis revealed the solid-solution formation in all transitional metal-doped Ceria-Praseodymium catalysts nanofibers, and the crystallite size decreased, and lattice strain increased with the transition metal doping.
- Raman spectroscopy analysis also showed the F_{2g} mode of Ceria and the presence of oxygen vacancies, and no secondary phase peaks were identified, confirming the formation of solid-solution.
- There is a decrease in surface area with the addition of transitional metal, and 5Cr-CP nanofibers showed larger average pore size and pore volume. The nano string diameter is smaller than all other nanofiber catalysts resulting in better soot oxidation activity.

CHAPTER 11

CONCLUSIONS

11.1. SUMMARY

The summary drawn from the research with respect to the transition metal-doped Ceria-Praseodymium catalyst system for soot oxidation activity is discussed in this section.

Transition metal-doped Ceria-Praseodymium catalysts were successfully synthesized, characterized by various characterization tools, and tested for soot oxidation activity, and their kinetic studies were explored.

Copper-doped Ceria-Praseodymium catalysts system is synthesized, characterized, and tested for soot oxidation activity, and some of the key points are noted below:

- Pure Ce, Pr, Cu, and $\text{Cu}_{(x=0-0.2)}(\text{Ce}_{0.9}\text{Pr}_{0.1})_{1-x}\text{O}_{2-\delta}$ doped samples were synthesized using the SCS method calcined at 600/5h. Ce, Pr, and the doped samples showed a cubic fluorite structure, and Cu displayed a monoclinic structure.
- The T_{50} temperature obtained for the soot oxidation activity is in the order of 5Cu-CP (402 °C) > CP (408 °C) > Pr (410 °C) > Ce (413 °C) = 10Cu-CP (413 °C) = 15Cu-CP (413 °C) = 20Cu-CP (413 °C) > Cu (440 °C).
- The better catalytic activity of 5 Cu-CP ($T_{50}=402$ °C) may be attributed to high reactive planes and the presence of high chemisorbed oxygen species (O^-) than all other catalysts.

Conclusions

- The kinetic triplets (activation energy, pre-exponential factor, and reaction model) were evaluated for all the samples. Pure Ce and Cu displayed the lowest and highest E_a and A values, respectively, with all the methods employed. Most doped catalysts followed the nucleation and growth model except Pure Pr and Cu catalysts.
- 5 Cu-CP followed the phase boundary controlled reaction (P_{1-3}) for lower conversion, and 1-3 dimensional diffusion (D_{1-3}) was observed at a higher conversion value. 5 Cu-CP also had a higher rate of reaction compared to other catalysts.

Cobalt-doped Ceria-Praseodymium catalysts system is synthesized, characterized, and tested for soot oxidation activity, and some of the key points are noted below:

- From XRD studies, Co_x ($x=0-0.20$) $(Ce_{0.9}Pr_{0.1})_{(1-x)} O_{2-\delta}$ catalysts revealed the fluorite structure of CeO_2 , and the crystallite size was in the range of ~ 9 nm. Pure Co and CP had a crystallite size of ~ 28 nm and 14 nm, respectively.
- Facet ratios for $\{110\}/\{111\}$ and $\{100\}/\{111\}$ was obtained high (~ 0.40 and 0.44 , respectively) for 15 Co-CP catalyst system.
- F_{2g} Raman active mode of fluorite structured Ce was visible in all Co_x ($x=0-0.20$) $(Ce_{0.9}Pr_{0.1})_{(1-x)} O_{2-\delta}$ catalysts. Bands ~ 560 cm^{-1} to 580 cm^{-1} are attributed to the oxygen vacancies added by Co and Pr. The Raman spectra analysis of increasing Co-loading concentration (15 Co-CP and 20 Co-CP) showed the presence of a secondary phase of Co_3O_4 .
- 5 Co-CP had better reducibility than all other Co-CP catalysts with high Ce^{3+} , Pr^{3+} , and Co^{3+} ions concentrations. On the other hand, CP and 20 Co-CP, respectively, had better active surface adsorbed species (O^- & O_2^{2-}) and the lattice oxygen species (O^{2-}).
- From TGA analysis for soot oxidation, a better T_{50} of 349 ± 1 °C was achieved by 5 Co-CP catalysts. From the descriptors controlling oxidation reaction, the better T_{50} may be attributed to solid solution formation and better redox properties of 5Co-CP.

Conclusions

Iron-doped Ceria-Praseodymium catalysts system is synthesized, characterized, and tested for soot oxidation activity, and some of the key points are noted below:

- From XRD analysis, all the doped samples ensured the fluorite structure of CeO₂, whereas pure Fe displayed the crystalline structure of Fe₂O₃. 5 Fe-CP had the smallest Crystallite size and highest lattice strain of 6 nm and 0.0222, respectively.
- Raman spectroscopy revealed that all the doped samples possessed F_{2g} Raman modes of CeO₂ and the presence of oxygen vacancy peaks. The secondary phase for E_g Raman modes corresponding to Fe₂O₃ ~300 cm⁻¹ was noticed for all the Fe-doped samples.
- 5 Fe-CP showed high Ce³⁺, O²⁻, and O⁻ ions and may improve catalytic performance better than other Fe-doped CP catalysts. 5 Fe-CP displayed better catalytic activity with the lowest T₅₀ of 367 ± 2 °C, and it can be attributed to smaller crystallite size, higher lattice strain and lower activation energy (102 kJ mol⁻¹).

The Manganese-doped Ceria-Praseodymium catalysts system is synthesized, characterized, and tested for soot oxidation activity, and some of the key points are noted below:

- From XRD and Raman studies, the Mn-doped CP catalysts revealed the fluorite structure of Ceria, and the crystallite size was in the range of ~5 to 10 nm. F_{2g} Raman active mode of fluorite structured Ce was visible in all Mn-doped CP catalysts. Bands ~560 cm⁻¹ to 580 cm⁻¹ are attributed to the oxygen vacancies created by adding Mn and Pr.
- Further, BET surface area and BJH pore size analysis determined that the Mn-doped CP catalysts were micro and mesoporous.
- A better T₅₀ (349 ± 1 °C) for 5Mn-CP catalytic system may be attributed to active surface adsorbed O₂²⁻ species and Mn³⁺ and Mn⁴⁺ ions.

Conclusions

- Mn-doped CP catalyst followed nucleation and growth model, power law, phase boundary controlled reaction, 2-4D diffusion model, and first and second order reaction. Experimental and calculated curve consistency confirmed that the developed catalysts followed the Avrami-Erofeev equation (Am) or the Nucleation and Growth model.

The Chromium-doped Ceria-Praseodymium catalysts system is synthesized, characterized, and tested for soot oxidation activity, and some of the key points are noted below:

- The XRD studies showed reduced crystallite size for all the Cr-doped CP and increased lattice strain and Facet ratios. Raman analysis confirmed the presence of O_v peaks for all Cr-doped CP catalysts.
- Additionally, adsorbed H_2O or adsorbed molecular water peak in O1s spectra was observed for 5 Cr-CP catalyst alone. From TGA analysis for soot oxidation, 5 Cr-CP showed better T_{50} of $393\pm 2^\circ C$ mainly due to the presence of Cr^{3+} ions species from XPS analysis.
- The Cr-CP catalyst system followed a power law; phase boundary controlled reaction, nucleation, and growth model. Experimental and calculated curve consistency confirmed that the developed catalysts followed the Avrami-Erofeev equation (Am) or the Nucleation and Growth model.

Conclusions

The transition metal (TM (5 mol%) = Cr, Mn, Fe, Co, and Cu) -doped Ceria-Praseodymium catalysts nanofibers are synthesized using an electrospinning technique, characterized and tested for soot oxidation activity. Some of the key points are noted below:

- XRD analysis revealed the solid-solution formation in all transitional metal-doped Ceria-Praseodymium catalysts nanofibers, and the crystallite size decreased, and lattice strain increased with the transition metal doping.
- Raman spectroscopy analysis also showed the F_{2g} mode of Ceria and the presence of oxygen vacancies, and no secondary phase peaks were identified, confirming the formation of solid-solution.
- There is a decrease in surface area with the addition of transitional metal, and 5Cr-CP nanofibers showed larger average pore size and pore volume. The nano string diameter is smaller than all other nanofiber catalysts resulting in better soot oxidation activity.

11.2. CONCLUSIONS

The thesis mainly explores the Transition metal doping in the Ceria-Praseodymium catalyst system synthesis, characterization, and testing for soot oxidation activity and its kinetics. It is noticed that the descriptors (lattice oxygen, metal-oxygen bond strength, host structure, redox capability, multi-functionality of active sites, site isolation, and phase cooperation) govern the soot oxidation catalysis and each transitional metal doping in Ceria-Praseodymium catalysts system followed one or more descriptors and differed from one transition metal to the other. It can be noted that the 5 mol% Copper doped Ceria-Praseodymium catalyst system showed better soot oxidation activity which is attributed to the better reactive planes and chemisorbed oxygen species compared to other Copper doped Ceria-Praseodymium catalyst system and Ceria-Praseodymium catalyst systems.

Conclusions

Further, the 5 mol % Cobalt doped Ceria-Praseodymium catalyst system showed better soot oxidation activity, and the descriptors controlling the catalytic activity are phase cooperation (solid-solution formation) and better redox properties compared to Cobalt doped Ceria-Praseodymium catalyst system and Ceria-Praseodymium catalyst system.

The descriptors controlling the soot oxidation activity of the Iron doped Ceria-Praseodymium catalyst system are (secondary phase formation and redox properties). 5 mol % Iron doped Ceria-Praseodymium catalyst system showed better soot oxidation activity, and as the Fe content increased in the Iron doped Ceria-Praseodymium catalyst system, the catalytic activity decreased.

In Manganese doped Ceria-Praseodymium catalyst system, the 5 mol% Manganese-doped Ceria-Praseodymium catalyst system showed better catalytic activity for the soot oxidation reaction. The descriptors controlling the soot oxidation activity are surface area, crystallite size, active surface adsorbed O⁻ species, and Mn³⁺/Mn⁴⁺ surface concentration. The increase of Mn content in the Manganese-doped Ceria-Praseodymium catalyst system forms a secondary phase, decreasing soot oxidation activity.

The surface concentration of Cr³⁺ and Pr³⁺ played a significant descriptor role, and Chromium doped Ceria-Praseodymium catalyst system showed better soot oxidation activity than other Ceria-Praseodymium catalyst systems. As the Cr concentration increased, there was a decrease in the Cr³⁺ and Pr³⁺ concentrations in the Chromium-doped Ceria-Praseodymium catalyst system. Compared to other transitional metal-doped Ceria-Praseodymium catalyst systems with increased Cr content, there is only a slight decrease in soot oxidation activity.

Compared to all the transition metals doped Ceria-Praseodymium catalysts in the present study 5 mol % Cobalt doped Ceria-Praseodymium catalyst system showed better catalytic activity with lowest T₅₀ of 349±1°C.

In the transition metal (TM (5 mol%) = Cr, Mn, Fe, Co, and Cu) -doped Ceria-Praseodymium nanofiber catalysts 5 mol% Chromium doped Ceria-Praseodymium nanofiber showed better soot oxidation activity and is attributed to larger average pore size and pore volume and also, the nano string diameter is smaller than all other nanofiber catalysts.

11.3. FUTURE SCOPE OF THE WORK

- Transitional metal-doped Ceria-Praseodymium catalysts with better soot oxidation activity can be further tested for real-time Diesel Particulate Filters and analyze the activity and understand the role of descriptors in controlling the activity.
- Further, transitional metal-doped Ceria-Praseodymium catalysts can be explored for CO oxidation reactions.
- Additionally, transitional metal-doped Ceria-Praseodymium catalysts can be explored for NO_x and SO_x reactions.

APPENDIX – I

A 1.1 PRINTEX-U Carbon-Soot Characteristics (Ganiger, Patil et al. 2022)

Printex U Soot [Orion Engineered Carbons, (Particle size ~25 nm; $S_A \sim 100 \text{ m}^2/\text{g}$)] was used for soot oxidation and kinetic studies. The commercial soot obtained was characterized by XRD, Raman Spectroscopy, and SEM analysis.

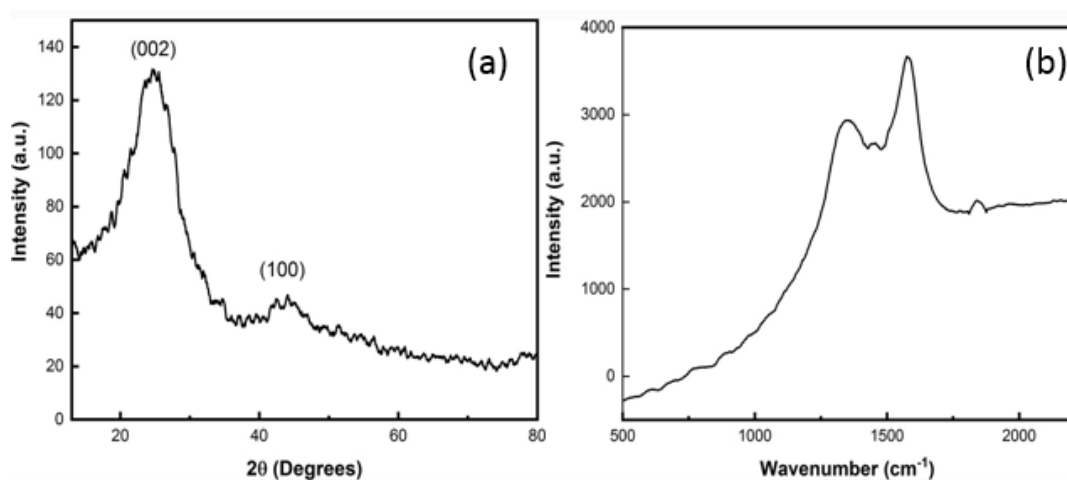


Figure. A1.1. (a) XRD and Raman spectroscopy analysis of a Printex-U sample.

The XRD pattern contains two peaks which are about $2\theta = 25-26^\circ$ and at $2\theta = 44^\circ$. The peak around $2\theta = 25-26^\circ$ in **Figure. A1.1 (a)** has occurred due to the reflection of carbon and corresponds to the (002) plane. Amorphous carbon concentrations are indicated by the background intensity in the peak (Arnal et al., 2012). The crystallite size obtained was 0.3399 nm, and the Lattice strain was 1.3773. The band (100), at $2\theta = 44^\circ$, indicates graphite-like atomic order (Arnal et al., 2012). As a result of the comparison to chars of rice husk and eucalyptus and their diffraction patterns, Printex-U can be considered to have a less amorphous structure and less aliphatic carbon side chains due to lower background intensity (Guerrero et al., 2008).

The Raman spectra in **Figure. A1.1(b)** show two sharp peaks at 1350 cm^{-1} and 1585 cm^{-1} with maximum intensity. The peak at 1585 cm^{-1} is called the *G* mode and is attributed to an ideal graphitic lattice vibration mode with E_{2g} symmetry. The peak at 1350 cm^{-1} , called *D* mode, corresponds to disordered graphitic lattice vibration mode with A_{1g} symmetry (Liu et al., 2008) (Sadezky et al., 2005). The other bands at around 1800 cm^{-1} (*DI*) are assigned to non-zero-center phonons. The *G* band is arising around 1585 cm^{-1} instead of 1582 cm^{-1} ; this is because of the influence of the *D'* on the *G* band confirming the disordered structure of Printex-U Soot.

A 1.2. SEM Analysis

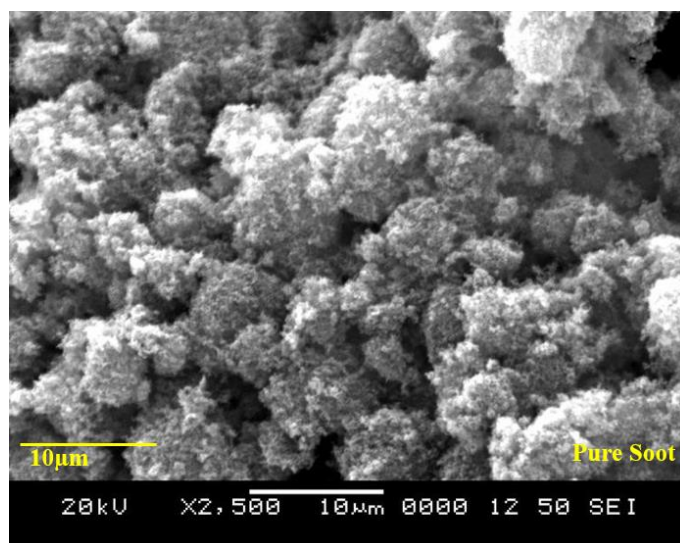


Fig. A1.2. SEM Images (10 μm) of Pure Soot sample

Figure A1.2. reveals the SEM images of pure soot sample, and it can be noticed from the image that the particles are porous agglomerates.

APPENDIX – II**Table A2.1: Sample codes for the catalysts synthesized**

Catalyst	Sample Code
CeO ₂	Ce/Pure Ce
Ce _{0.97} Nb _{0.03} O _{2-δ}	3 Nb-Ce
Ce _{0.95} Nb _{0.05} O _{2-δ}	5 Nb-Ce
Ce _{0.9} Nb _{0.1} O _{2-δ}	10 Nb-Ce
Ce _{0.8} Nb _{0.2} O _{2-δ}	20 Nb-Ce
Ce _{0.7} Nb _{0.3} O _{2-δ}	30 Nb-Ce
NbO	100 Nb/ Pure Nb
Pr ₆ O ₁₁	Pr/Pure Pr
CuO	Cu/ Pure Cu
Ce _{0.9} Pr _{0.1} O _{2-δ}	CP
Cu _(x=0.05) (Ce _{0.9} Pr _{0.1}) _{1-x} O _{2-δ}	5 Cu-CP
Cu _(x=0.1) (Ce _{0.9} Pr _{0.1}) _{1-x} O _{2-δ}	10 Cu-CP
Cu _(x=0.15) (Ce _{0.9} Pr _{0.1}) _{1-x} O _{2-δ}	15 Cu-CP
Cu _(x=0.2) (Ce _{0.9} Pr _{0.1}) _{1-x} O _{2-δ}	20 Cu-CP
Co ₃ O ₄	Co/ Pure Co
Co _(x=0.05) (Ce _{0.9} Pr _{0.1}) _{1-x} O _{2-δ}	5 Co-CP
Co _(x=0.1) (Ce _{0.9} Pr _{0.1}) _{1-x} O _{2-δ}	10 Co-CP
Co _(x=0.15) (Ce _{0.9} Pr _{0.1}) _{1-x} O _{2-δ}	15 Co-CP
Co _(x=0.2) (Ce _{0.9} Pr _{0.1}) _{1-x} O _{2-δ}	20 Co-CP
Fe ₂ O ₃	Fe/ Pure Fe
Fe _(x=0.05) (Ce _{0.9} Pr _{0.1}) _{1-x} O _{2-δ}	5 Fe-CP
Fe _(x=0.1) (Ce _{0.9} Pr _{0.1}) _{1-x} O _{2-δ}	10 Fe-CP
Fe _(x=0.15) (Ce _{0.9} Pr _{0.1}) _{1-x} O _{2-δ}	15 Fe-CP
Fe _(x=0.2) (Ce _{0.9} Pr _{0.1}) _{1-x} O _{2-δ}	20 Fe-CP
Mn ₂ O ₃	Mn/ Pure Mn
Mn _(x=0.05) (Ce _{0.9} Pr _{0.1}) _{1-x} O _{2-δ}	5 Mn-CP
Mn _(x=0.1) (Ce _{0.9} Pr _{0.1}) _{1-x} O _{2-δ}	10 Mn-CP
Mn _(x=0.15) (Ce _{0.9} Pr _{0.1}) _{1-x} O _{2-δ}	15 Mn-CP
Mn _(x=0.2) (Ce _{0.9} Pr _{0.1}) _{1-x} O _{2-δ}	20 Mn-CP
Cr ₂ O ₃	Cr/ Pure Cr
Cr _(x=0.05) (Ce _{0.9} Pr _{0.1}) _{1-x} O _{2-δ}	5 Cr-CP
Cr _(x=0.1) (Ce _{0.9} Pr _{0.1}) _{1-x} O _{2-δ}	10 Cr-CP
Cr _(x=0.15) (Ce _{0.9} Pr _{0.1}) _{1-x} O _{2-δ}	15 Cr-CP
Cr _(x=0.2) (Ce _{0.9} Pr _{0.1}) _{1-x} O _{2-δ}	20 Cr-CP

A Study on the Effect of Transition Metal Dopants in Ceria Praseodymium Catalysts for Soot Oxidation Activity and its Kinetics

APPENDIX – III

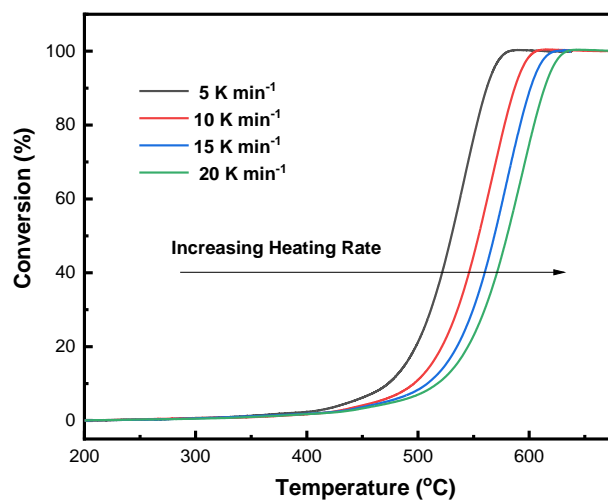


Figure A 3.1: Conversion v/s temperature plot of 10 Nb-Ce Sample at different heating rates.

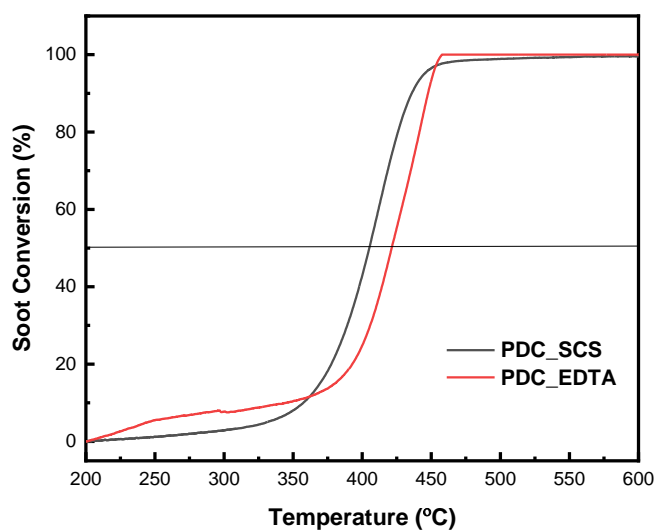


Figure A 3.2: Conversion v/s temperature plot of Ce_{0.9}Pr_{0.1}O_{2-δ} synthesised by EDTA citrate method and SCS method

APPENDIX – IV

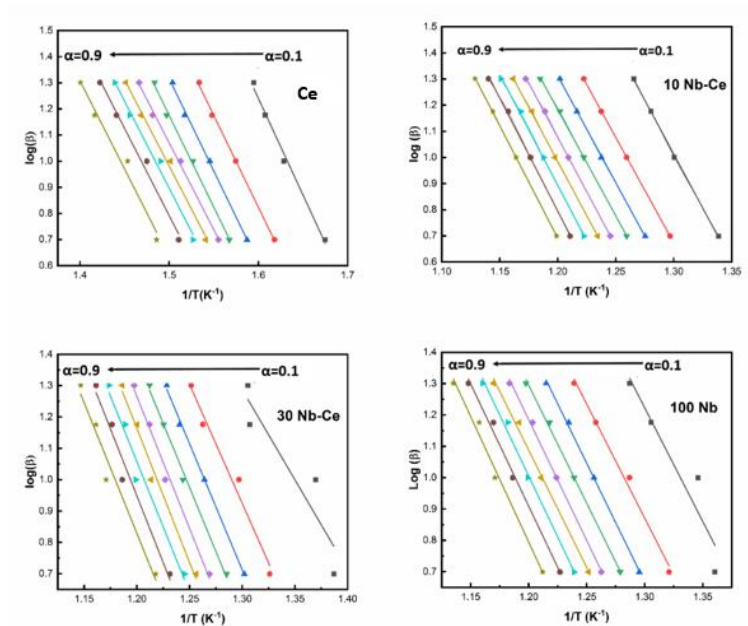


Figure A 4.1: Ozawa Plots of Ce, 10 Nb-Ce,30 Nb-Ce, and 100Nb samples.

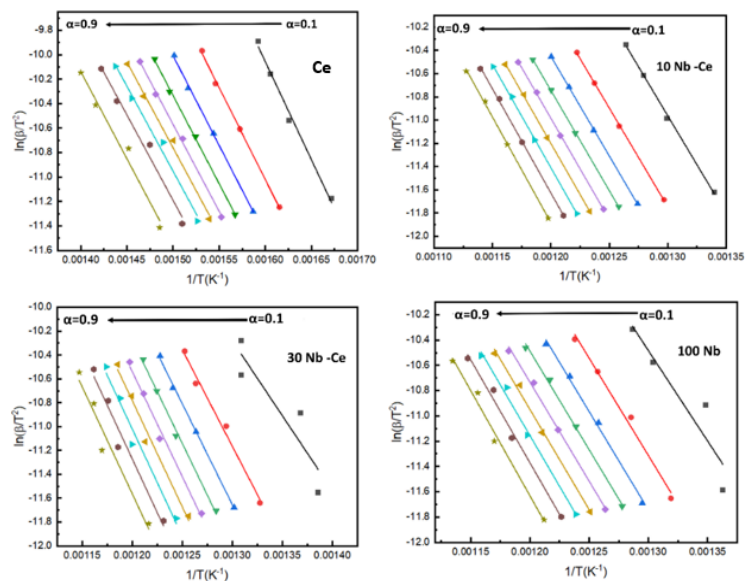


Figure A 4.2: KAS Plots of Ce, 10 Nb-Ce,30 Nb-Ce, and 100Nb samples.

APPENDIX - V

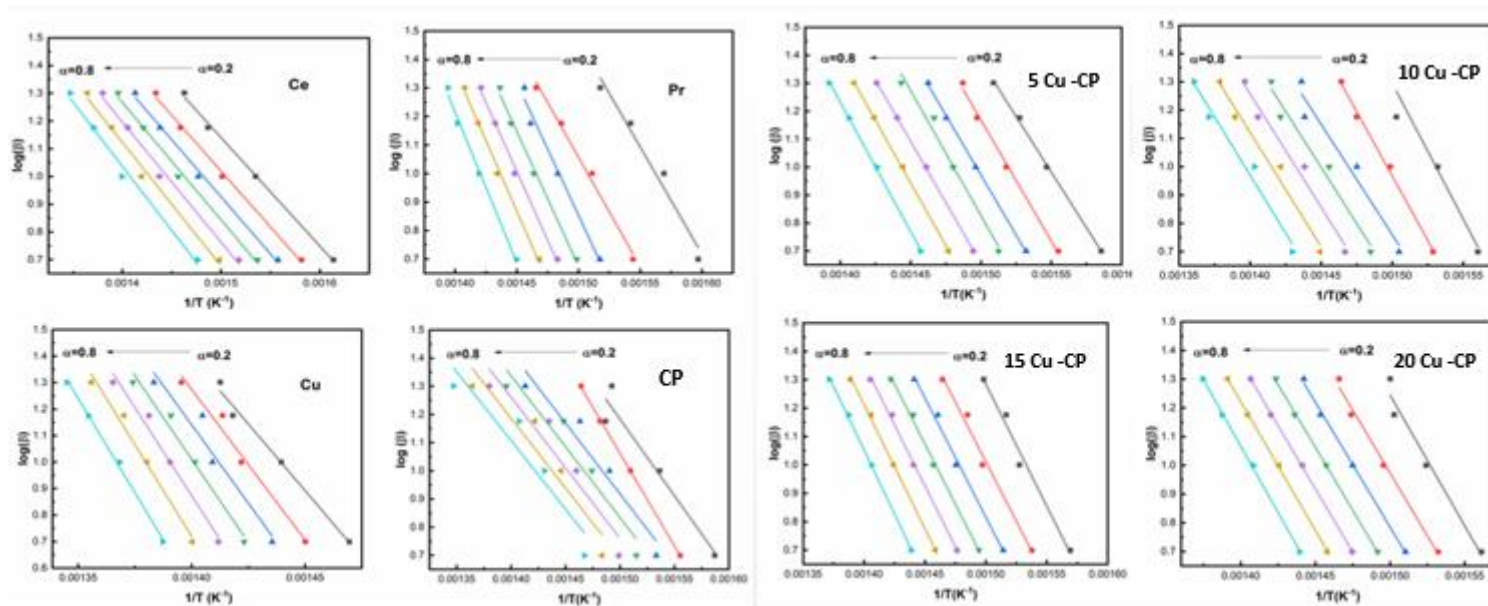


Figure A5.1: Ozawa Plots of Pure Ce, Pr, Cu, and $Cu_x(x=0-0.2)$ $(Ce_{0.9}Pr_{0.1})_{1-x} O_{2-\delta}$ catalysts

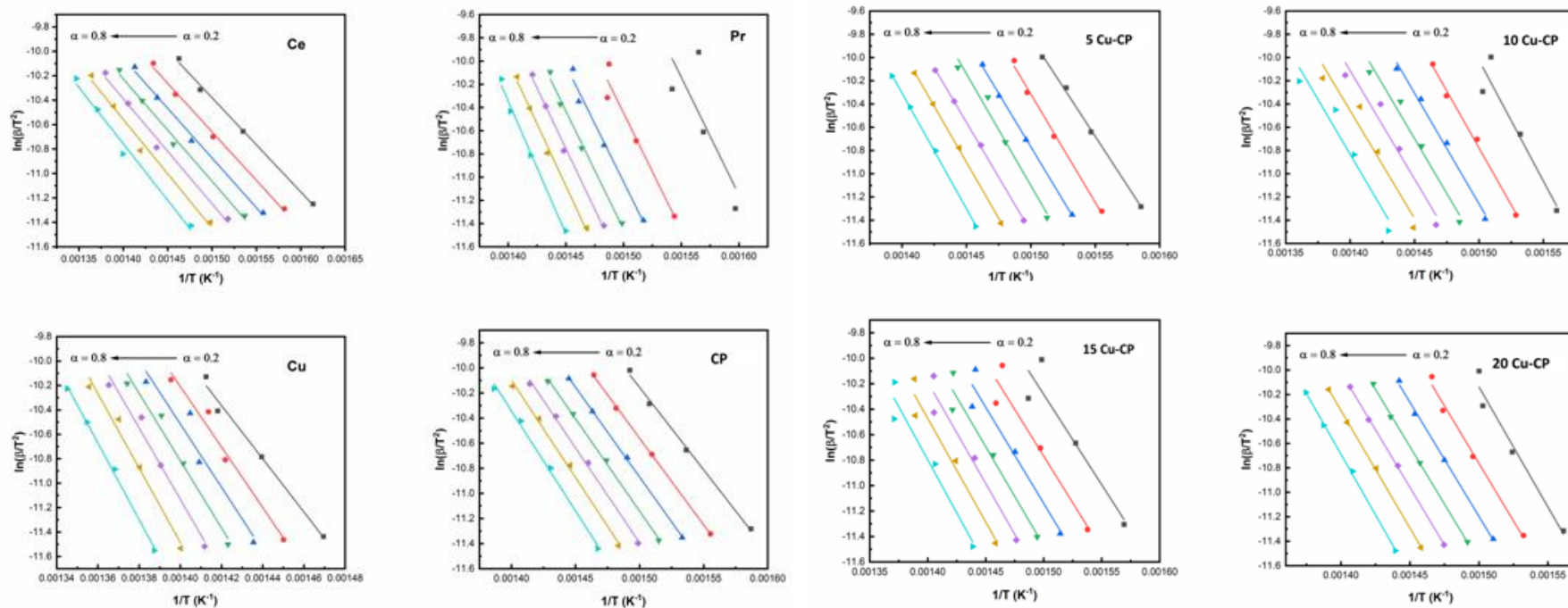


Figure A5.2: KAS Plots of Pure Ce, Pr, Cu, and $\text{Cu}_x(x=0.2)$ $(\text{Ce}_{0.9}\text{Pr}_{0.1})_{1-x}\text{O}_{2-\delta}$ catalysts

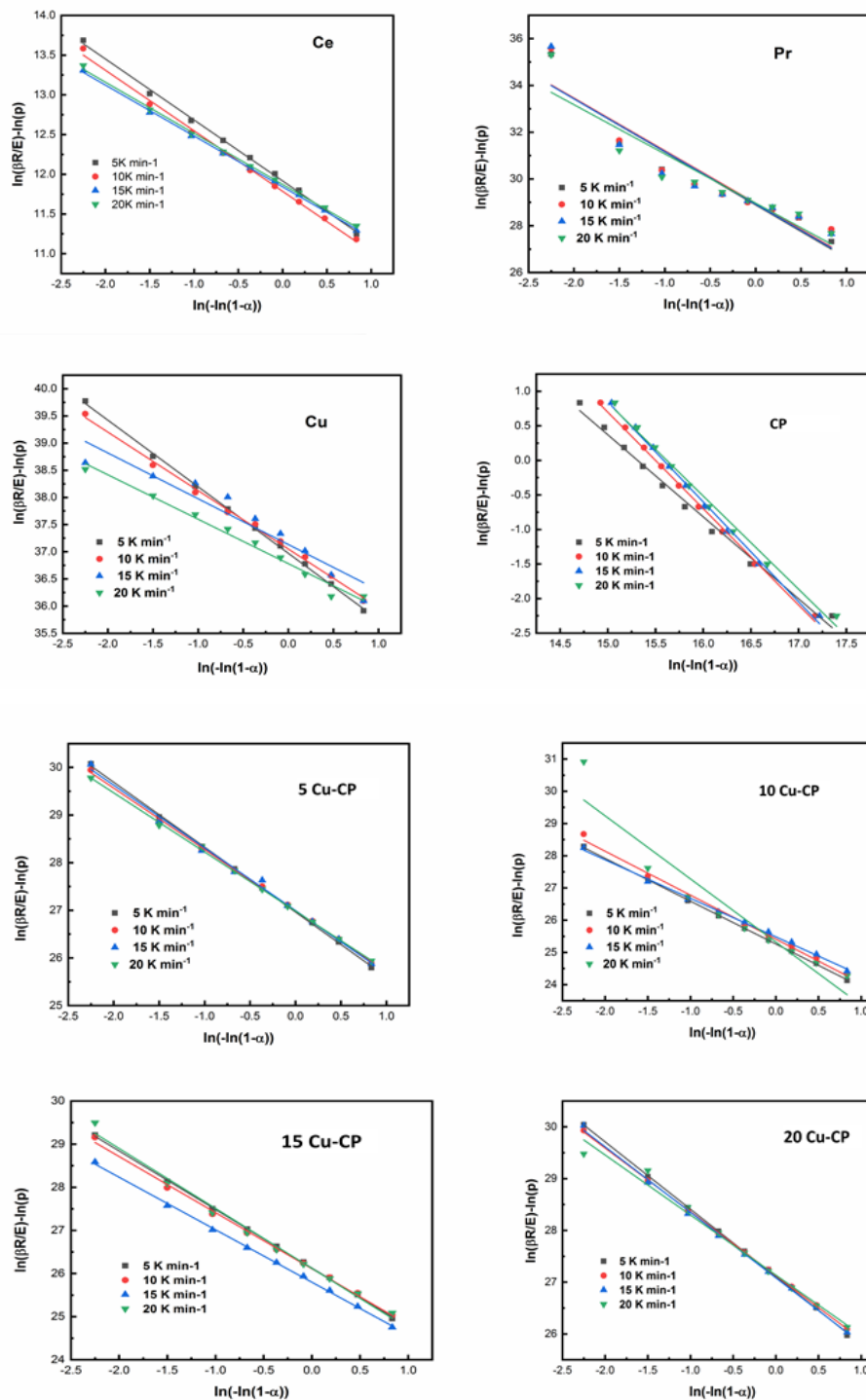


Figure A 5.3: Am Plots of Pure Ce, Pr, Cu, and $\text{Cu}_x(x=0-0.2) (\text{Ce}_{0.9}\text{Pr}_{0.1})_{1-x} \text{O}_{2-\delta}$ catalysts.

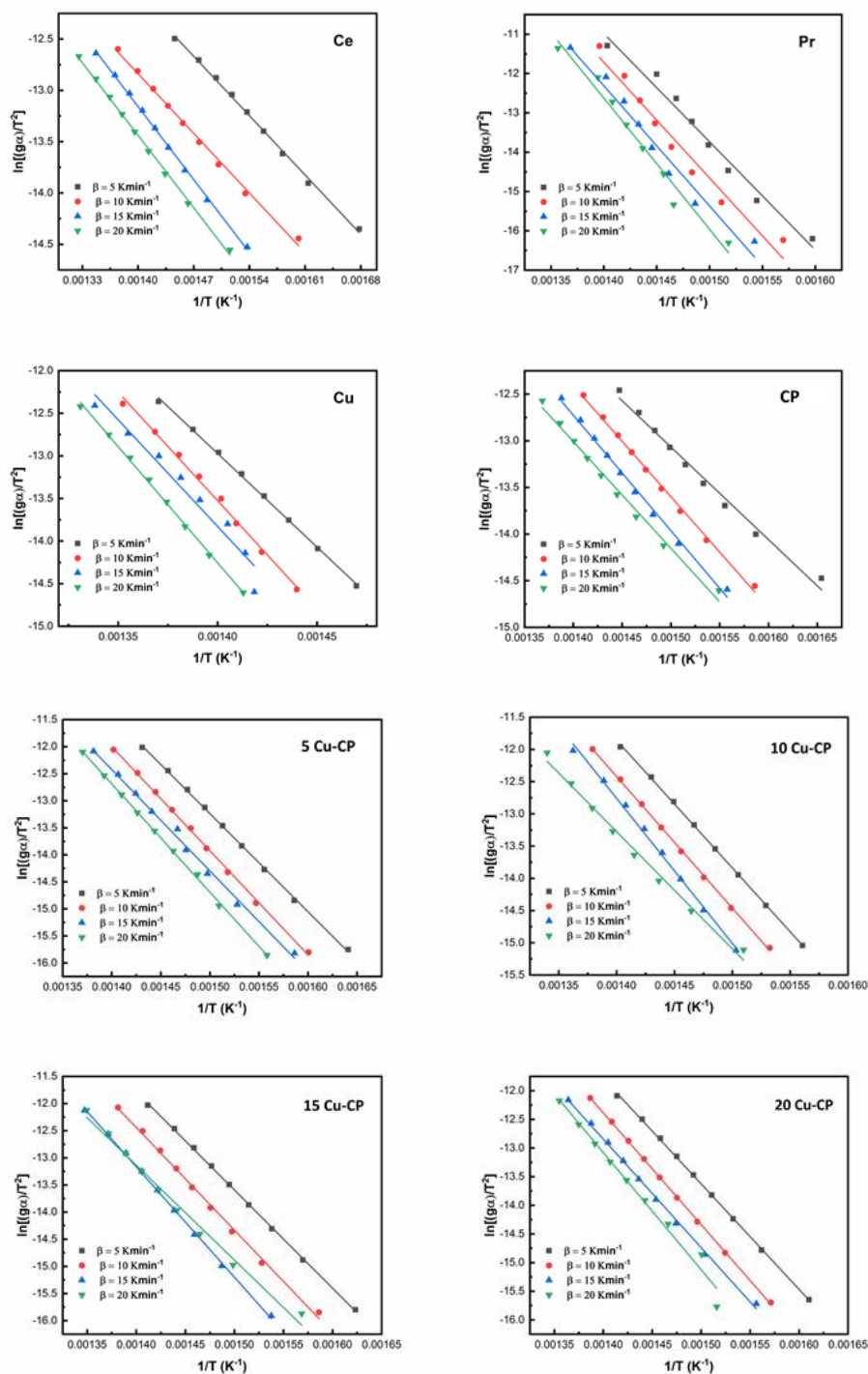


Figure A 5.4: CR Plots of Pure Ce, Pr, Cu, and $\text{Cu}_x(x=0-0.2) (\text{Ce}_{0.9}\text{Pr}_{0.1})_{1-x} \text{O}_{2-\delta}$ catalysts.

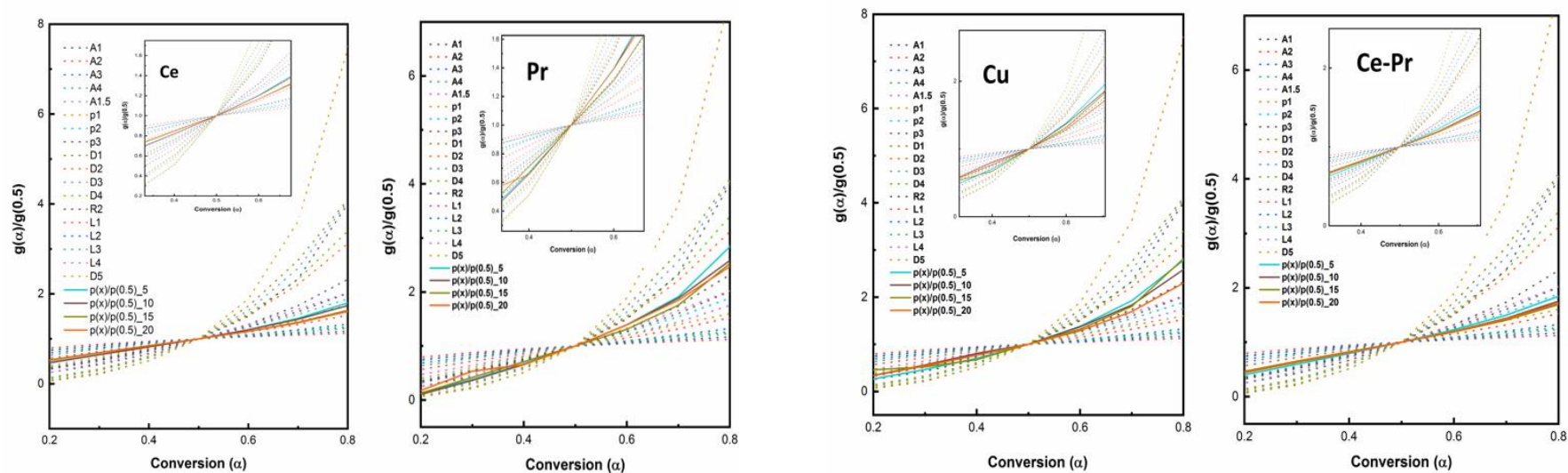


Figure A 5.5: Master Plots Pure Ce, Pr, Cu, and $\text{Cu}_{x(x=0.2)}(\text{Ce}_{0.9}\text{Pr}_{0.1})_{1-x}\text{O}_{2-\delta}$ catalysts.

(contd.)

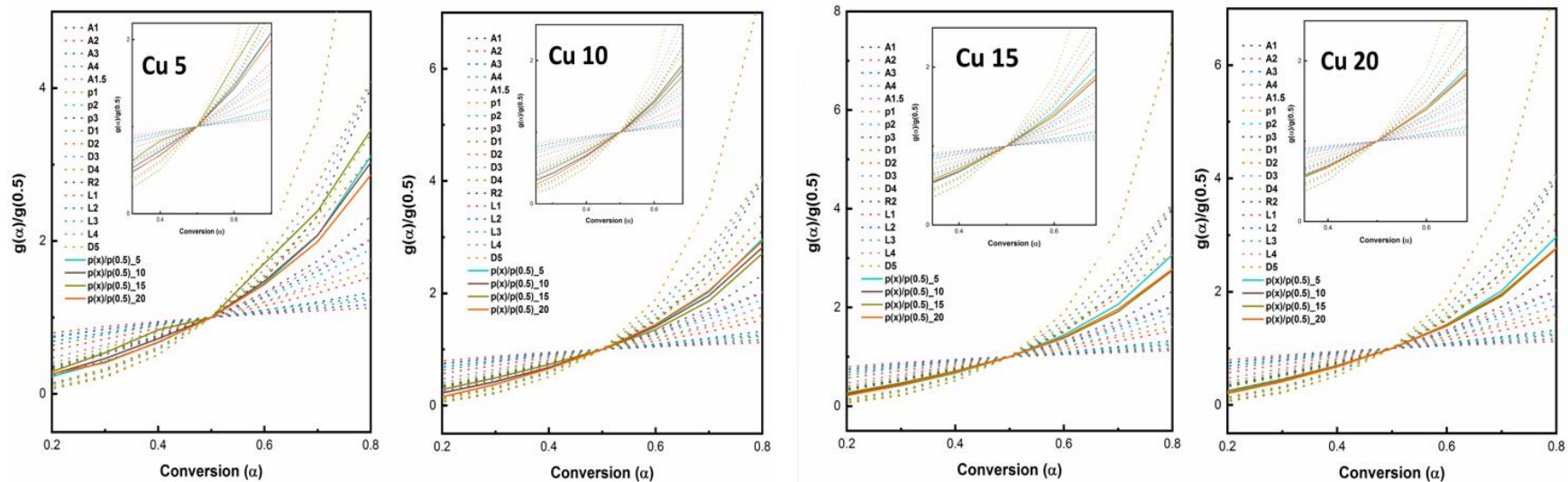


Figure A 5.5: Master Plots Pure Ce, Pr, Cu, and Cu_{x(x=0-0.2)} (Ce_{0.9}Pr_{0.1})_{1-x} O_{2-δ} catalysts.

APPENDIX - VI

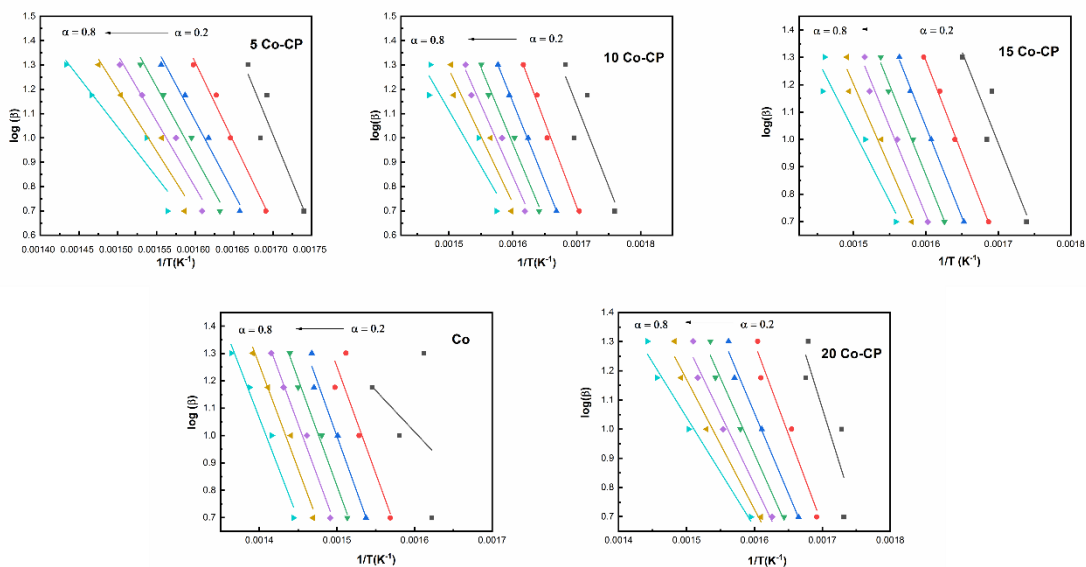


Figure A 6.1: Ozawa Plots of $\text{Co}_x(x=0.05-0.2)$ $(\text{Ce}_{0.9}\text{Pr}_{0.1})_{1-x}\text{O}_{2-\delta}$ catalysts.

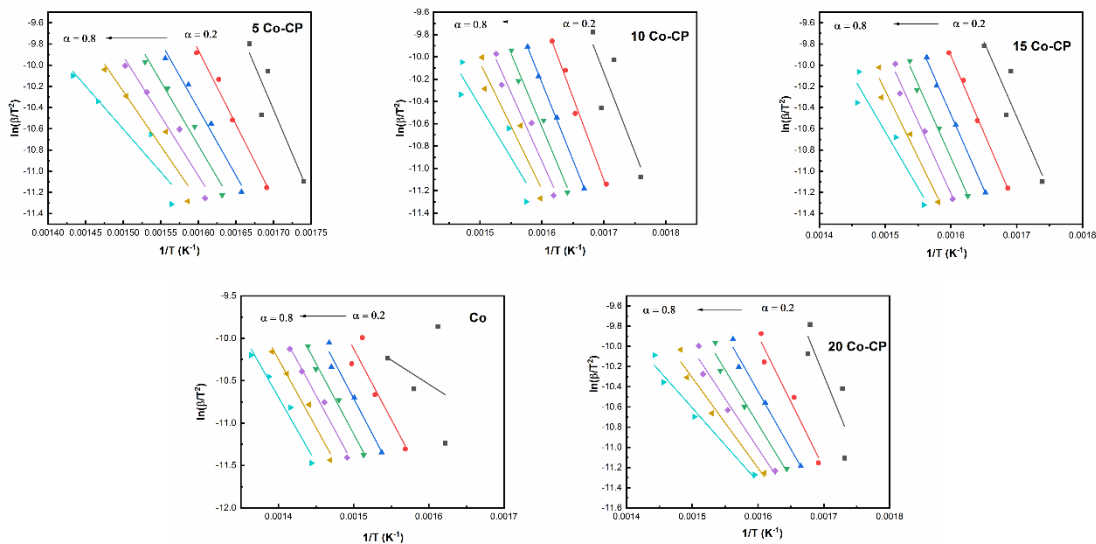


Figure A 6.2: KAS Plots of $\text{Co}_x(x=0.05-0.2)$ $(\text{Ce}_{0.9}\text{Pr}_{0.1})_{1-x}\text{O}_{2-\delta}$ catalysts.

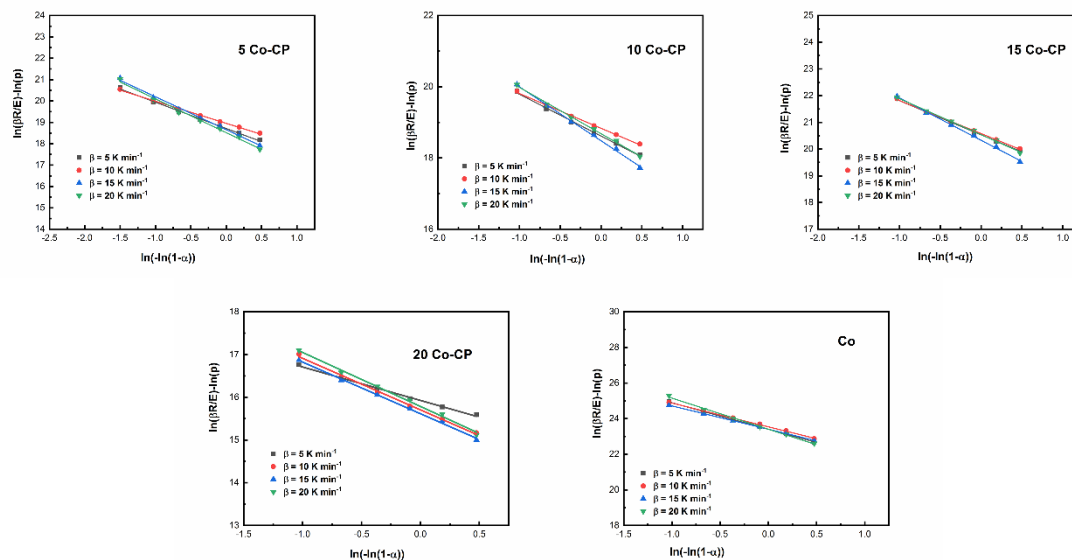


Figure A 6.3: Am Plots of $\text{Co}_x(x=0.05-0.2) (\text{Ce}_{0.9}\text{Pr}_{0.1})_{1-x} \text{O}_{2-\delta}$ catalysts.

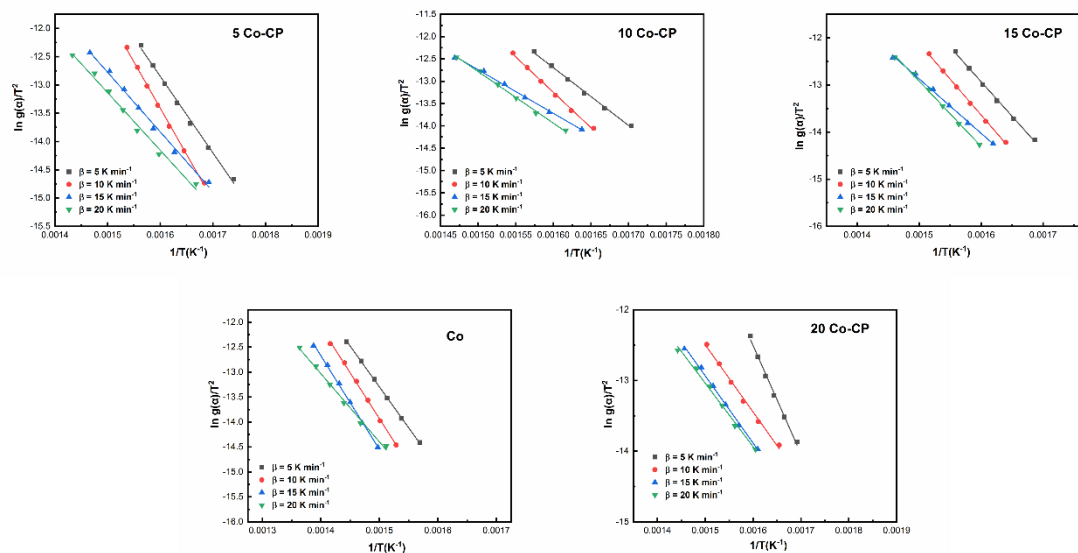


Figure A 6.4: CR Plots of $\text{Co}_x(x=0.05-0.2) (\text{Ce}_{0.9}\text{Pr}_{0.1})_{1-x} \text{O}_{2-\delta}$ catalysts.

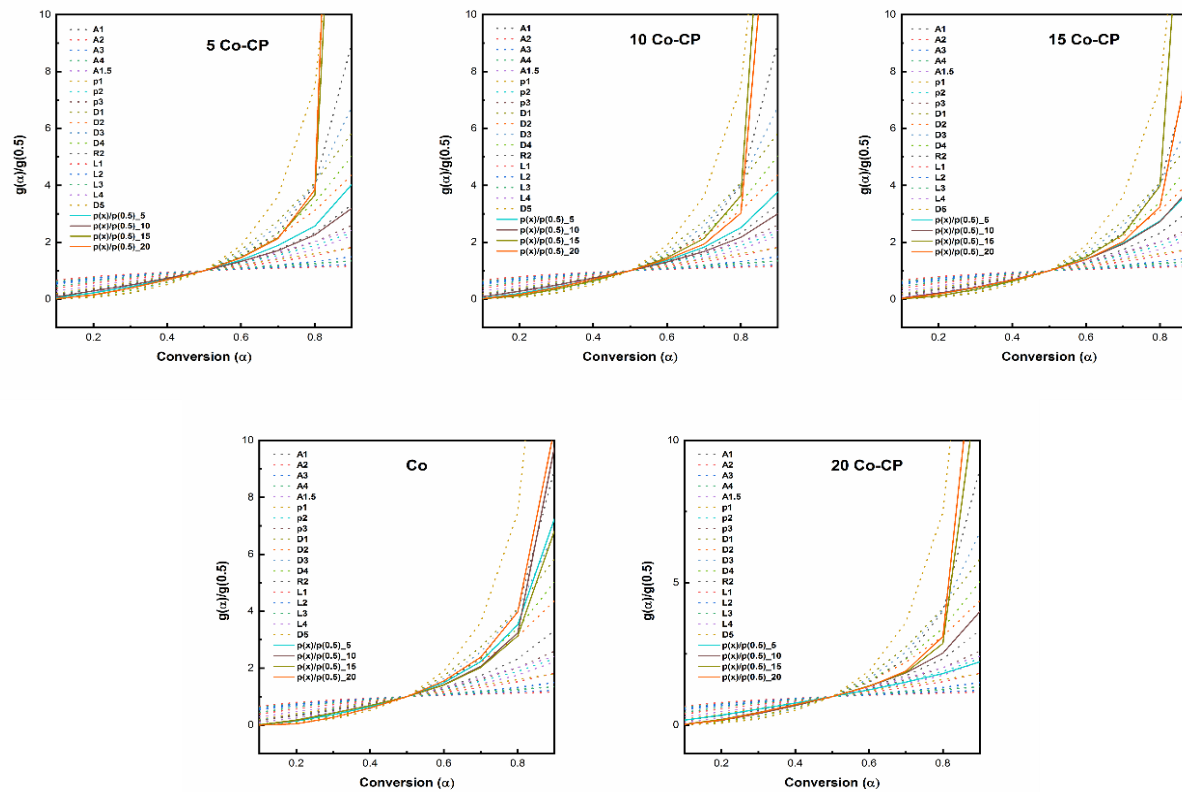


Figure A6.5 (d) Master Plots of $\text{Co}_{x(x=0.05-0.2)}(\text{Ce}_{0.9}\text{Pr}_{0.1})_{1-x}\text{O}_{2-\delta}$ catalysts.

APPENDIX - VII

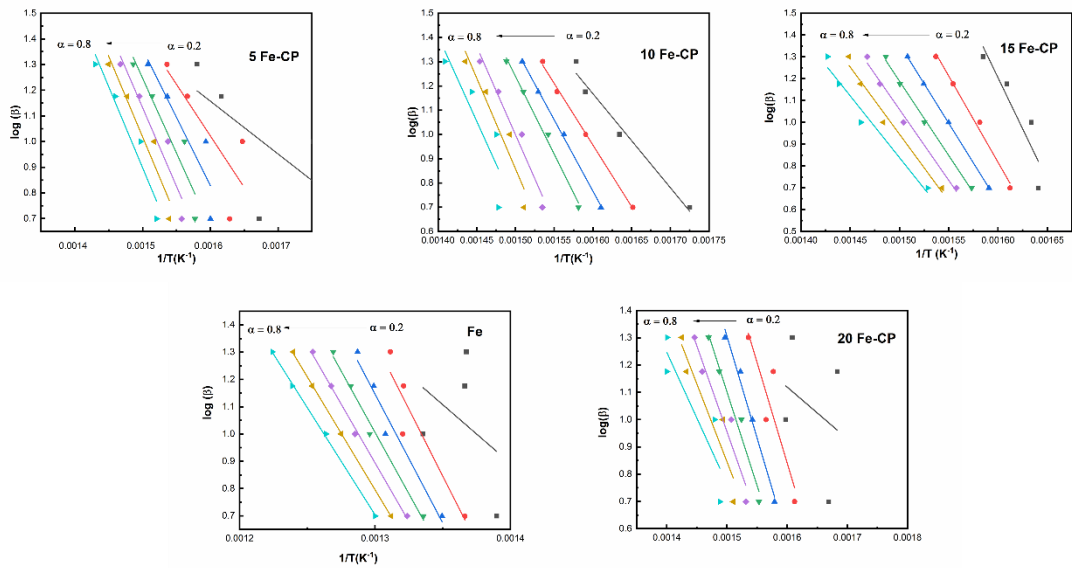


Figure A 7.1: Ozawa Plots of $Fe_x(x=0.05-0.2) (Ce_{0.9}Pr_{0.1})_{1-x} O_{2-\delta}$ catalysts.

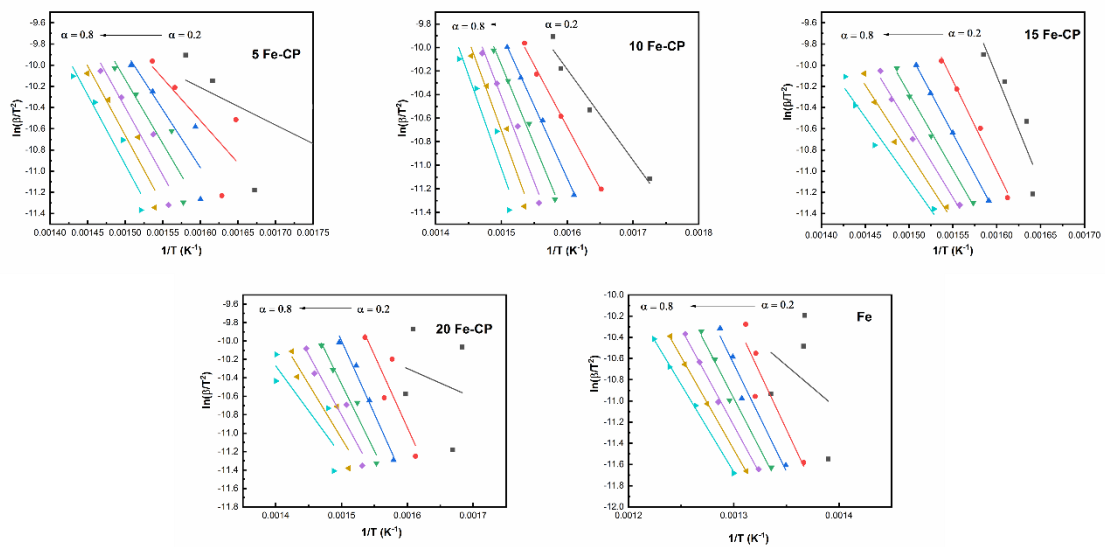


Figure A 7.2: KAS Plots of $Fe_x(x=0.05-0.2) (Ce_{0.9}Pr_{0.1})_{1-x} O_{2-\delta}$ catalysts.

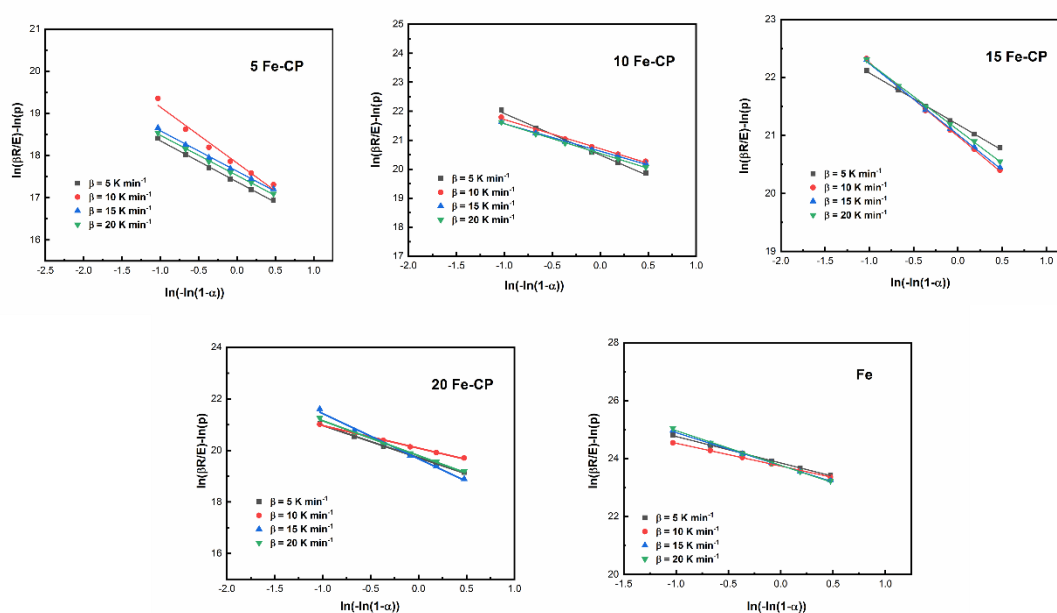


Figure A 7.3: Am Plots of $\text{Fe}_x(x=0.05-0.2) (\text{Ce}_{0.9}\text{Pr}_{0.1})_{1-x} \text{O}_{2-\delta}$ catalysts.

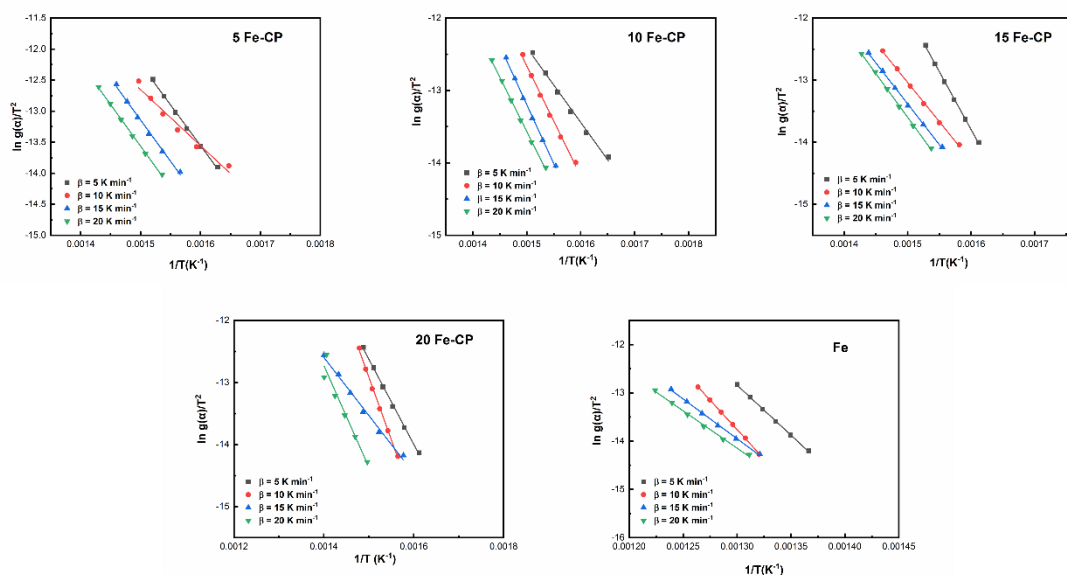


Figure A 7.4: CR Plots of $\text{Fe}_x(x=0.05-0.2) (\text{Ce}_{0.9}\text{Pr}_{0.1})_{1-x} \text{O}_{2-\delta}$ catalysts.

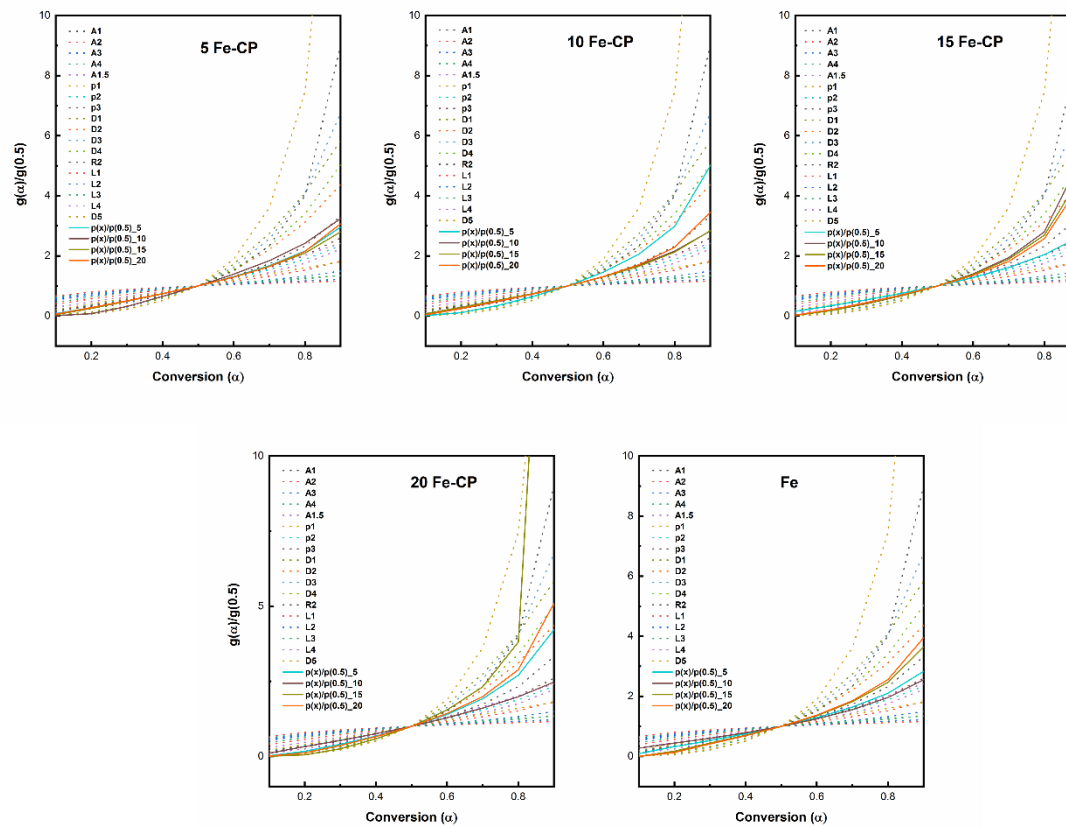


Figure A 7.5. Master Plots of $\text{Fe}_{x(x=0.05-0.2)}(\text{Ce}_{0.9}\text{Pr}_{0.1})_{1-x}\text{O}_{2-\delta}$ catalysts.

APPENDIX - VIII

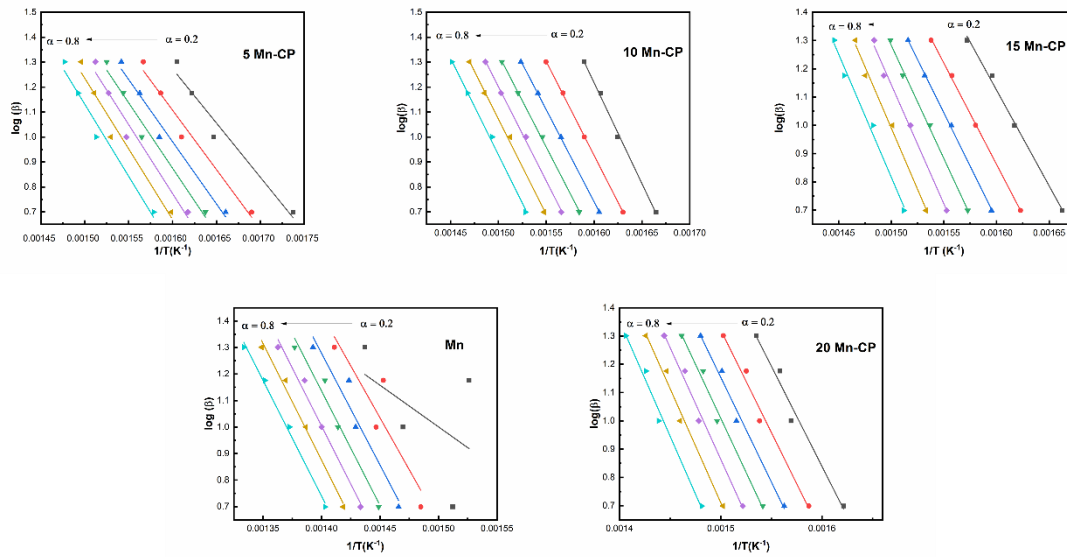


Figure A 8.1: Ozawa Plots of $Mn_x(x=0.05-0.2)$ $(Ce_{0.9}Pr_{0.1})_{1-x} O_{2-\delta}$ catalysts.

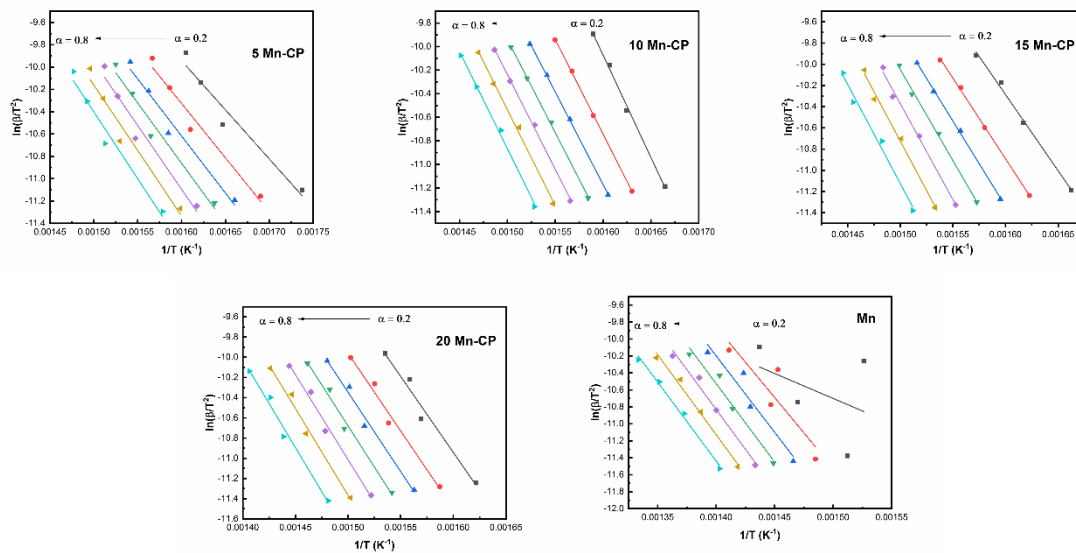


Figure A 8.2: KAS Plots of $Mn_x(x=0.05-0.2)$ $(Ce_{0.9}Pr_{0.1})_{1-x} O_{2-\delta}$ catalysts.

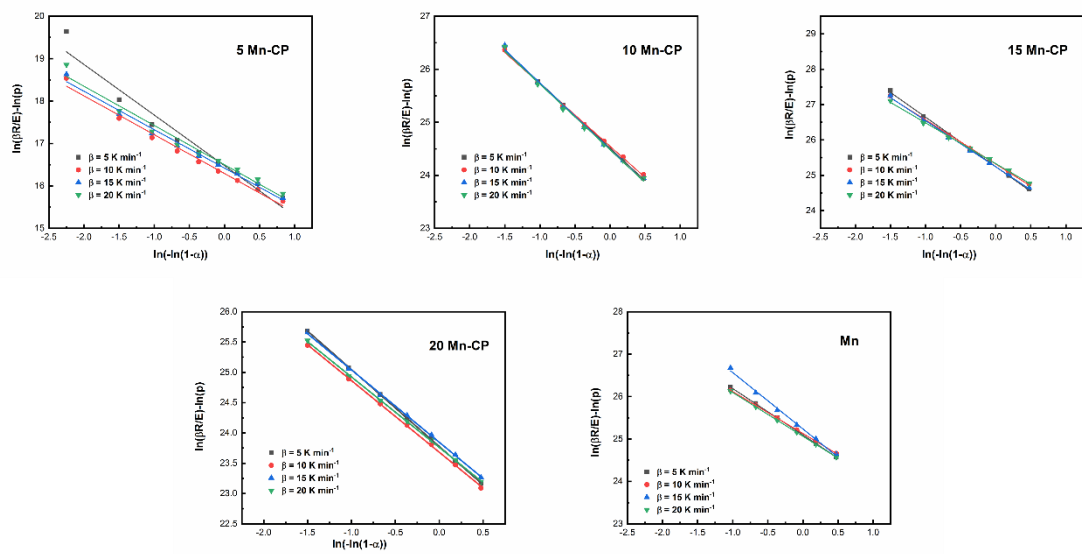


Figure A 8.3: Am Plots of $Mn_x(x=0.05-0.2)$ $(Ce_{0.9}Pr_{0.1})_{1-x} O_{2-\delta}$ catalysts.

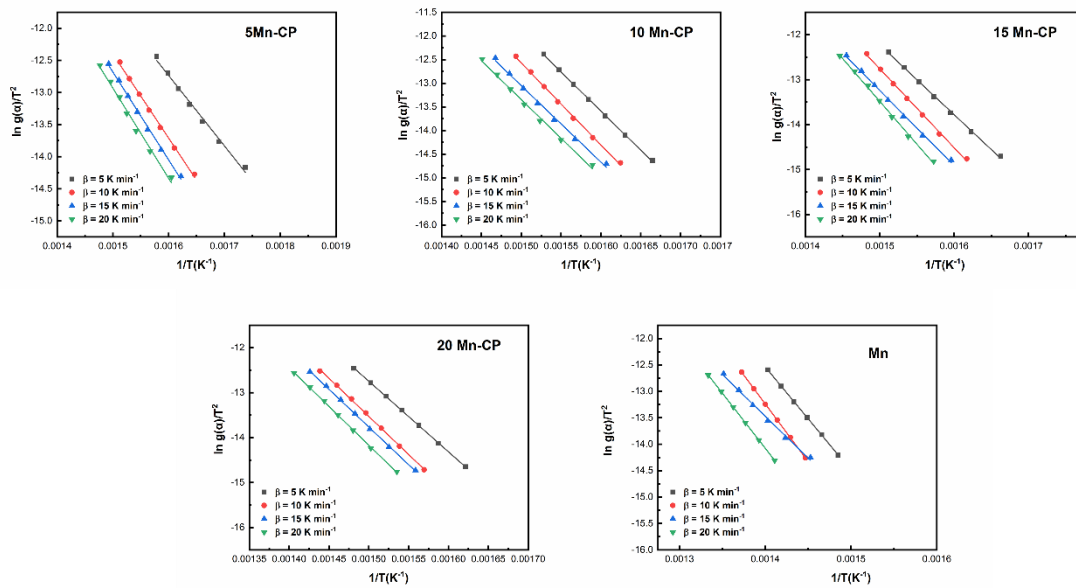


Figure A 8.4: CR Plots of $Mn_x(x=0.05-0.2)$ $(Ce_{0.9}Pr_{0.1})_{1-x} O_{2-\delta}$ catalysts.

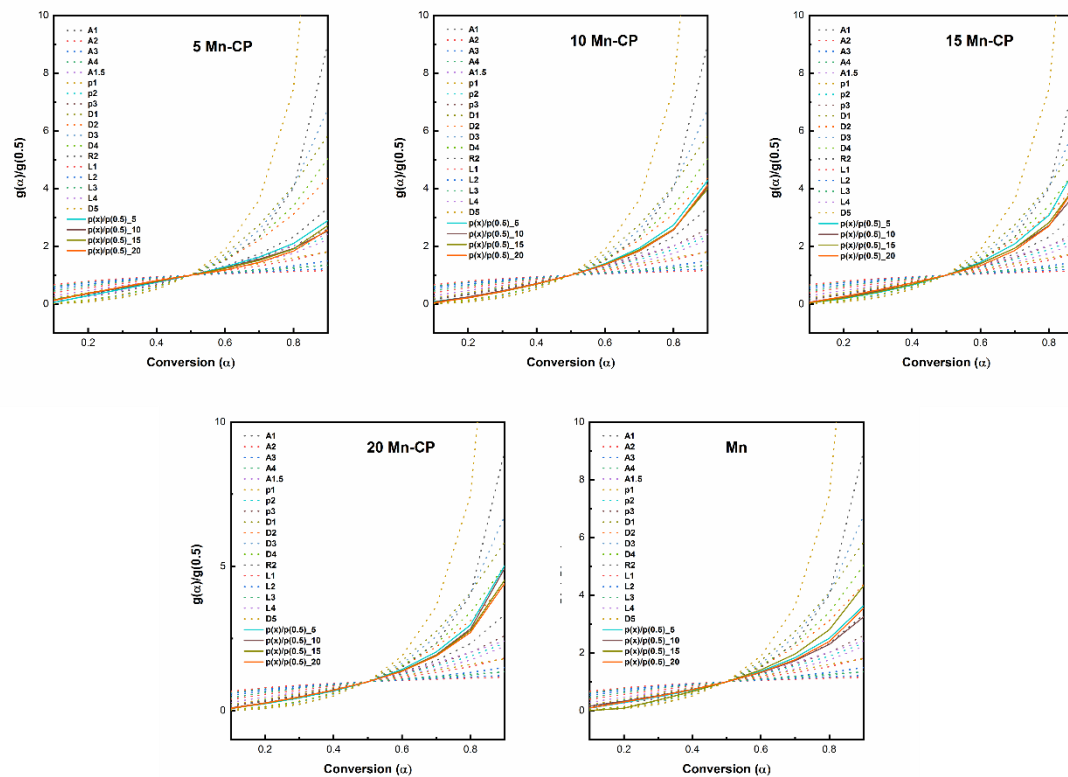


Figure A 8.5. Master Plots of $Mn_x(x=0.05-0.2) (Ce_{0.9}Pr_{0.1})_{1-x} O_{2-\delta}$ catalysts.

APPENDIX - IX

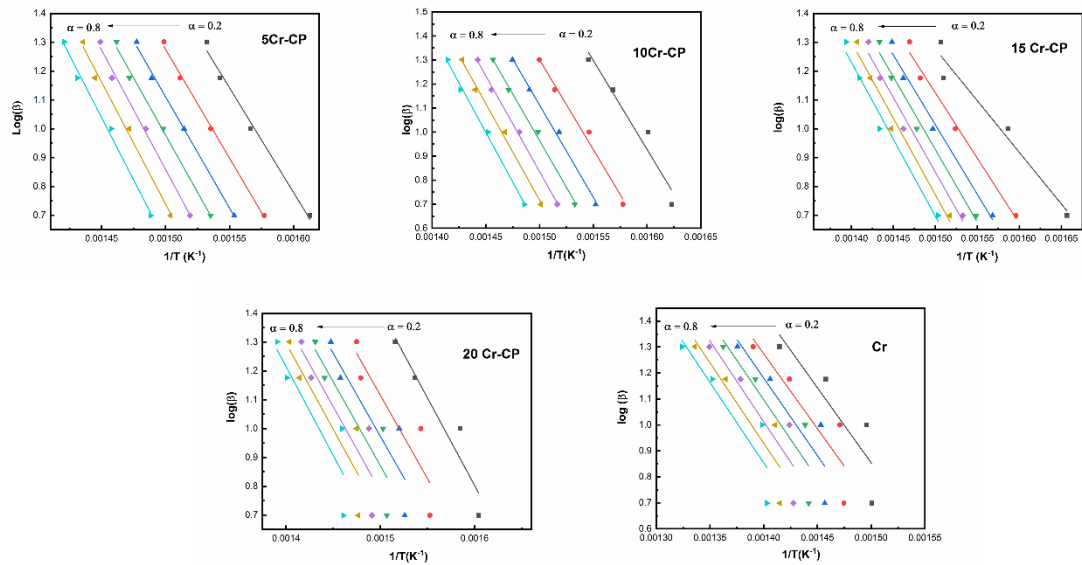


Figure A 9.1: Ozawa Plots of $\text{Cr}_x(x=0.05-0.2)$ $(\text{Ce}_{0.9}\text{Pr}_{0.1})_{1-x}\text{O}_{2-\delta}$ catalysts.

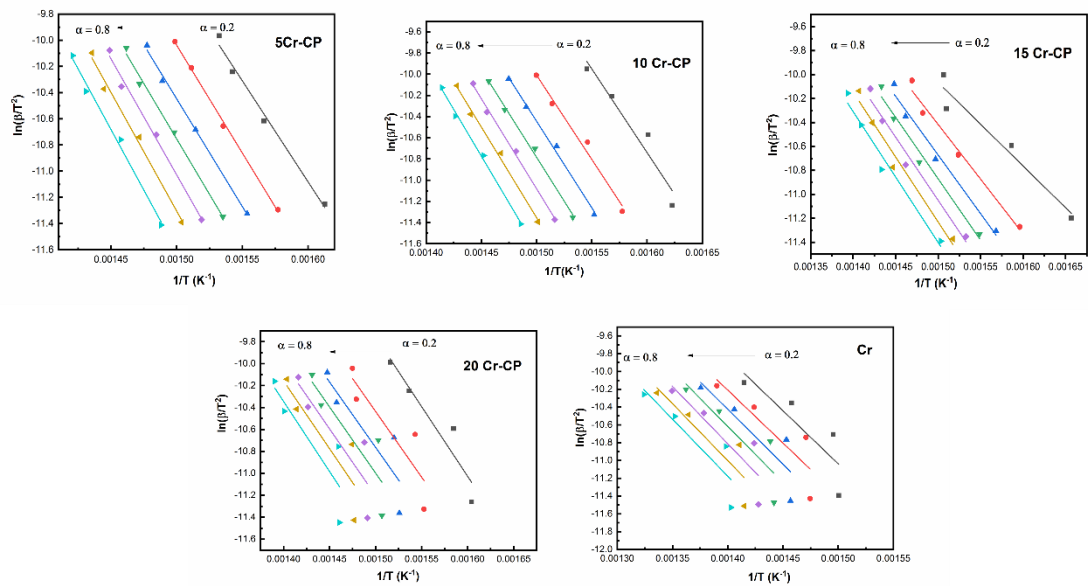


Figure A 9.2: KAS Plots of $\text{Cr}_x(x=0.05-0.2)$ $(\text{Ce}_{0.9}\text{Pr}_{0.1})_{1-x}\text{O}_{2-\delta}$ catalysts.

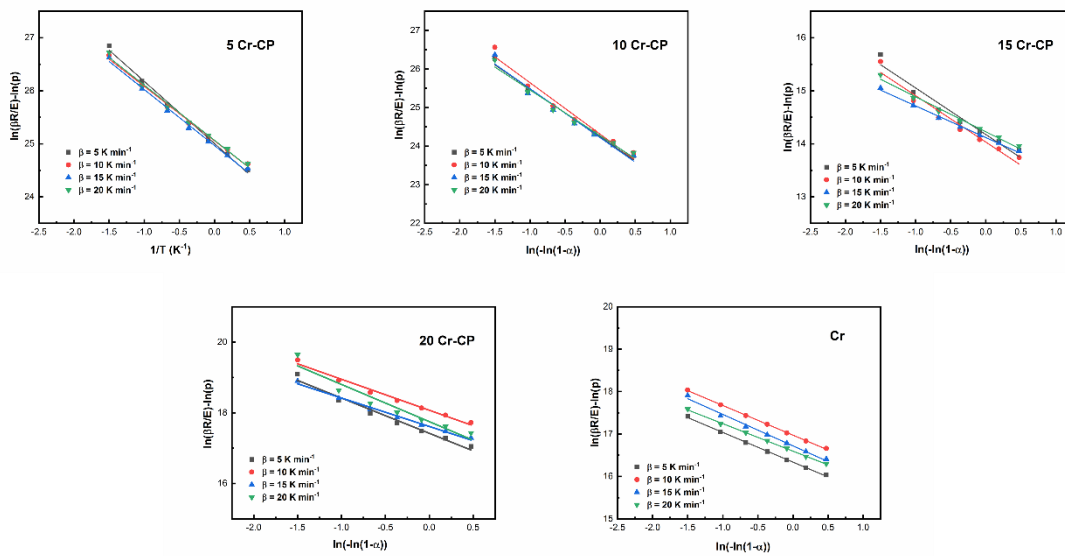


Figure A 9.3: Am Plots of $\text{Cr}_{x(x=0.05-0.2)} (\text{Ce}_{0.9}\text{Pr}_{0.1})_{1-x} \text{O}_{2-\delta}$ catalysts.

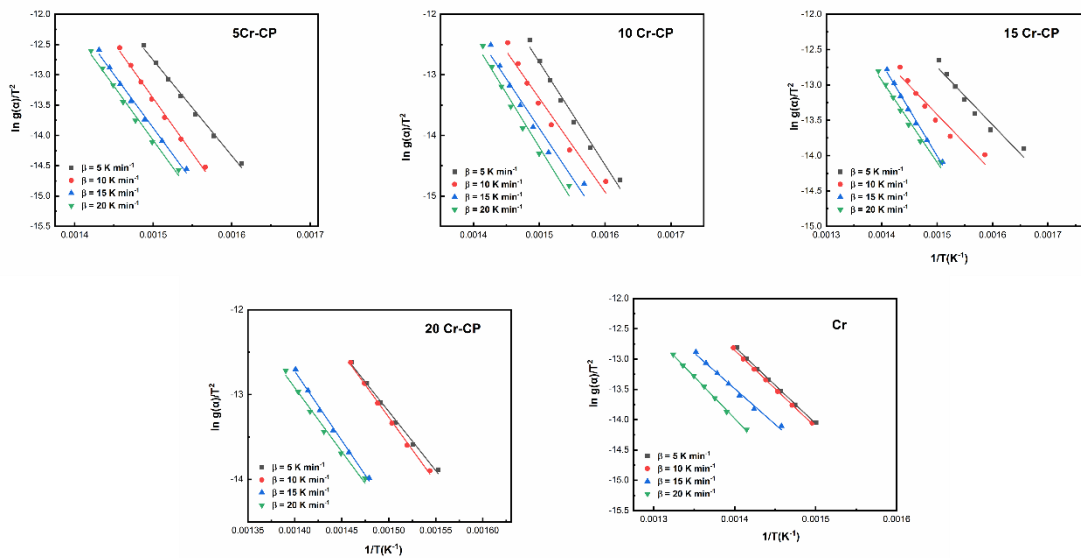


Figure A 9.4: CR Plots of $\text{Cr}_{x(x=0.05-0.2)} (\text{Ce}_{0.9}\text{Pr}_{0.1})_{1-x} \text{O}_{2-\delta}$ catalysts.

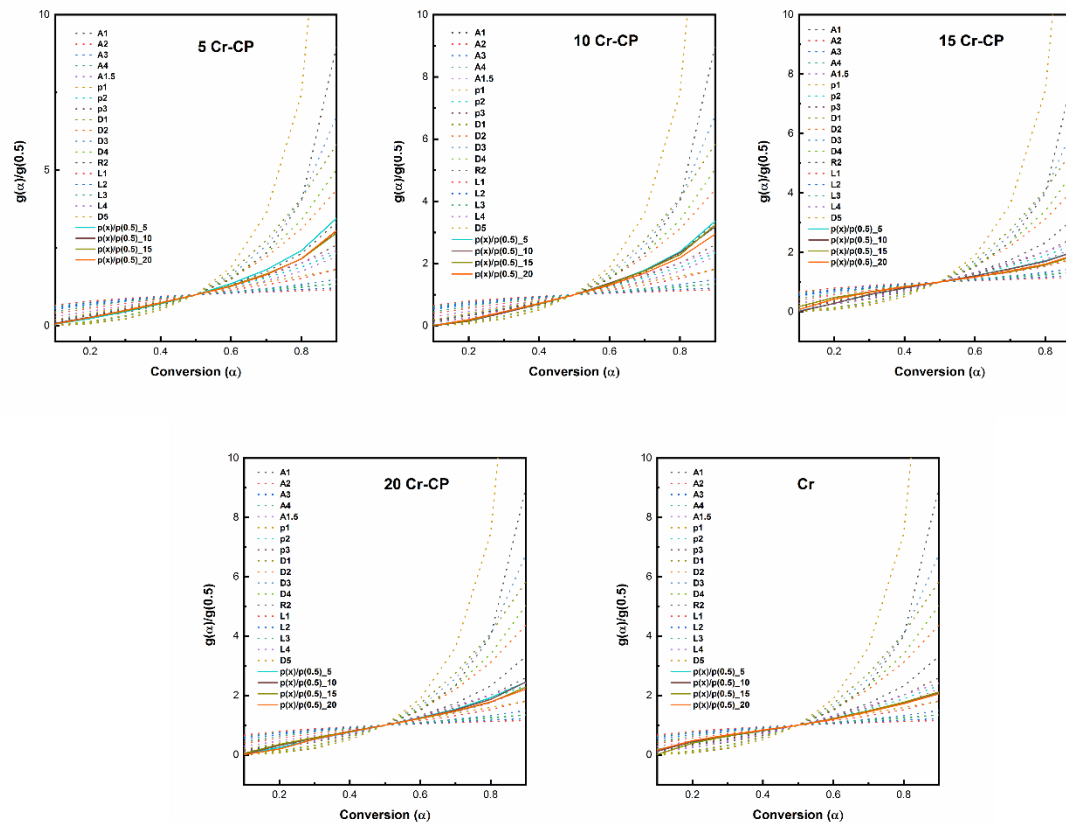


Figure A 9.5. Master Plots of $\text{Cr}_{x(x=0.05-0.2)}(\text{Ce}_{0.9}\text{Pr}_{0.1})_{1-x}\text{O}_{2-\delta}$ catalysts.

REFERENCES

Abdul Jameel, A. G., Han, Y., Brignoli, O., Telalović, S., Elbaz, A. M., Im, H. G., Roberts, W. L., and Sarathy, S. M. (2017). “Heavy fuel oil pyrolysis and combustion: Kinetics and evolved gases investigated by TGA-FTIR.” *J. Anal. Appl. Pyrolysis.*, 127, 183–195.

Aberkane, A. B., Yeste, M. P., Fayçal, D., Goma, D., and Cauqui, M. Á. (2019). “Catalytic soot oxidation activity of NiO-CeO₂ catalysts prepared by a coprecipitation method: Influence of the preparation pH on the catalytic performance.” *Materials (Basel).*, 12(20) 1-15.

Ahn, K., Yoo, D. S., Prasad, D. H., Lee, H., Chung, Y., and Lee, J. (2012). “Role of Multivalent Pr in the Formation and Migration of Oxygen Vacancy in Pr-Doped Ceria: Experimental and First-Principles Investigations.” *Chem. Mater.*, 24, 4261–4267.

Aliahmad, M., and Nasiri Moghaddam, N. (2013). “Synthesis of maghemite (γ -Fe₂O₃) nanoparticles by thermal-decomposition of magnetite (Fe₃O₄) nanoparticles.” *Mater. Sci. Pol.*, 31(2), 264–268.

Anantharaman, A. P., Dasari, H. P., Dasari, H., and Babu, G. U. B. (2018a). “Surface morphology and phase stability effect of Ceria-Hafnia (CH_x) binary metal oxides on soot oxidation activity.” *Appl. Catal. A Gen.*, 566, 181–189.

Anantharaman, A. P., Dasari, H. P., Lee, J. H., Dasari, H., and Babu, G. U. B. (2017). “Soot Oxidation Activity of Redox and Non-Redox Metal Oxides Synthesised by EDTA–Citrate Method.” *Catal. Letters*, 147(12), 3004–3016.

Anantharaman, A. P., Gadiyar, J., Surendran, M., Rao, A. S., Dasari, H. P., and Dasari, H. (2018b). “Effect of synthesis method on structural properties and soot oxidation activity of gadolinium-doped ceria.” *Chem Pap.* 72(12), 3179–3188.

References

Anantharaman, A. P., Geethu, J., P, M. R., and Prasad, H. (2018d). "Ceria-samarium binary metal oxides: A comparative approach towards structural properties and soot oxidation activity." *Mol. Catal.*, 451, 247-254.

Anantharaman, A. P., and Prasad, H. (2019). "Effect of ionic radius on soot oxidation activity for ceria - based binary metal oxides." *Asia Pacific J of Chem Engg*, 14, 1–11.

Andana, T., Piumetti, M., Bensaid, S., Russo, N., Fino, D., and Pirone, R. (2016). "CO and Soot Oxidation over Ce-Zr-Pr Oxide Catalysts." *Nanoscale Res. Lett.*, 278 (11), 1-9.

Andana, T., Piumetti, M., Bensaid, S., Veyre, L., Thieuleux, C., Russo, N., Fino, D., and Alessandra, E. (2018). "Nanostructured equimolar ceria-praseodymium for NO_x -assisted soot oxidation: Insight into Pr dominance over Pt nanoparticles and metal – support interaction." *Appl. Catal. B Environ.*, 226(226), 147–161.

Aneggi, E., Leitenburg, C. De, Dolcetti, G., and Trovarelli, A. (2006). "Promotional effect of rare earths and transition metals in the combustion of diesel soot over CeO₂ and CeO₂-ZrO₂." *Catal. Today*, 114, 40–47.

Aneggi, E., Leitenburg, C. De, Llorca, J., and Trovarelli, A. (2012). "Higher activity of Diesel soot oxidation over polycrystalline ceria and ceria-zirconia solid solutions from more reactive surface planes." *Catal. Today*, 197 (1), 119–126.

Aneggi, E., Llorca, J., Boaro, M., and Trovarelli, A. (2005). "Surface-structure sensitivity of CO oxidation over polycrystalline ceria powders." *J. of Catal.*, 234, 88–95.

Aneggi, E., Wiater, D., Leitenburg, C. De, Llorca, J., and Trovarelli, A. (2014a). "Shape-dependent activity of ceria in soot combustion." *ACS Catal.*, 4(1), 172–181.

References

Arumugam, S., Toku, Y., and Ju, Y. (2020). “Fabrication of γ -Fe₂O₃ Nanowires from Abundant and Low-cost Fe Plate for Highly Effective Electrocatalytic Water Splitting.” *Sci. Rep.*, 10(1), 1–11.

Aruna, S. T., and Mukasyan, A. S. (2008). “Combustion synthesis and nanomaterials.” *Curr. Opin. Solid State Mater. Sci.*, 12(3–4), 44–50.

Atribak, I. (2009). “Chemical Role of yttrium loading in the physicochemical properties and soot combustion activity of ceria and ceria–zirconia catalysts.” *J. Mol. Catal. A*, 300, 103–110.

Bedekar, V., Chavan, S. V, and Tyagi, A. K. (2007). “Highly sinter-active nanocrystalline RE₂O₃ (RE = Gd, Eu, Dy) by a combustion process, and role of oxidant-to-fuel ratio in preparing their different crystallographic modifications.” *J. Mater. Res.*, 22(3), 587–594.

Bedekar, V. V., Patra, S., Dutta, A., Basu, R. N., and Tyagi, A. K. (2010). “Ionic conductivity studies on neodymium-doped ceria in different atmospheres.” *Int. J. Nanotechnol.*, 7(9–12), 1178–1187.

Bensaid, S., Russo, N., and Fino, D. (2013). “CeO₂ catalysts with fibrous morphology for soot oxidation: The importance of the soot–catalyst contact conditions” *Catal Today* 216 (2013) 57– 63.

Bhabu, K. A., Theerthagiri, J., Madhavan, J., Balu, T., and Rajasekaran, T. R. (2016). “Investigations on acceptor (Pr³⁺) and donor (Nb⁵⁺) doped cerium oxide for the suitability of solid oxide fuel cell electrolytes.” *Ionics (Kiel)*, 2461–2470.

Bhardwaj, N., and Kundu, S. C. (2010). “Electrospinning : A fascinating fiber fabrication technique.” *Nanostructure Sci. and Tech.*, 28, 325–347.

References

- Bhardwaj, P., Singh, J., Kumar, R., Kumar, D., Verma, V., and Kumar, R. (2022). "Oxygen defects induced tailored optical and magnetic properties of $\text{Fe}_x\text{Cr}_{2-x}\text{O}_3$ ($0 \leq x \leq 0.1$) nanoparticles." *Appl. Phys. A Mater. Sci. Process.*, 128(2), 1–14.
- Bin, F., Song, C., Lv, G., Song, J., Wang, K., and Li, X. (2013). "Soot low-temperature combustion on Cu-Zr/ZSM-5 catalysts in O_2/He and $\text{NO}/\text{O}_2/\text{He}$ atmospheres." *Proc. Combust. Inst.*, 34(2), 2303–2311.
- Biswas, M., and Bandyopadhyay, S. (2013). "Synthesis of nanoscale Nd-doped ceria via urea-formaldehyde combustion method." *Metall. Mater. Trans. A.*, 44(11), 5251–5258.
- Braga, V. S., Garcia, F. A. C., Dias, J. A., and Dias, S. C. L. (2007). "Copper oxide and niobium pentoxide supported on silica-alumina : Synthesis, characterization, and application on diesel soot oxidation." *J. of Catalysis.*, 247, 68–77.
- Bratan, V., Vasile, A., Chesler, P., and Hornoiu, C. (2022). "Insights into the Redox and Structural Properties of CoOx and MnOx : Fundamental Factors Affecting the Catalytic Performance in the Oxidation Process of VOCs." *Catalysts.*, 12, 1-27.
- Cai, W., Zhong, Q., Ding, J., and Bu, Y. (2015). "Solvent effects during the synthesis of Cr/Ce_{0.2}Zr_{0.8}O₂ catalysts and their activities in NO oxidation." *Chem. Eng. J.*, 270, 1–8.
- Cao, C., Bishnoi, S. W., Proslie, T., Commission, A. E., and Albee, B. (2013a). "Detection of surface carbon and hydrocarbons in hot spot regions of niobium SRF cavities by Raman spectroscopy." *Physical review special topics - accelerators and beams.*, 16, 1-9.

References

- Cao, Z., Hu, Y., Li, J., Kai, Y., and Yang, W. (2013b). "Solubility of glycine in the binary system of ethanol+water solvent mixtures: Experimental data and thermodynamic modeling." *Fluid Phase Equilib.*, 360, 156–160.
- Casapu, M., Kro, O., Mehring, M., Nachtegaal, M., Borca, C., Harfouche, M., and Grolimund, D. (2010). "Characterization of Nb-Containing MnO_x - CeO_2 Catalyst for Low-Temperature Selective Catalytic Reduction of NO with NH_3 ." *J. Phys. Chem. C*, 114 (21) 9791–9801
- Chandrasekaran, A., Ramachandran, S., and Subbiah, S. (2017). "Determination of kinetic parameters in the pyrolysis operation and thermal behavior of *Prosopis juliflora* using thermogravimetric analysis." *Bioresour. Technol.*, 233, 413–422.
- Chang, S., Li, M., Hua, Q., Zhang, L., Ma, Y., Ye, B., and Huang, W. (2012). "Shape-dependent interplay between oxygen vacancies and Ag- CeO_2 interaction in Ag/ CeO_2 catalysts and their influence on the catalytic activity." *J. Catal.*, 293, 195–204.
- Charojrochkul, S., Waraporn Nualpaeng, N. L., and Assabumrungrat, S. (2012). "Combustion Synthesis of Nanoparticles CeO_2 and $\text{Ce}_{0.9}\text{Gd}_{0.1}\text{O}_{1.95}$." *Mater. Challenges Test. Supply Energy Resour.*, 1, 189–202.
- Chavan, S. V., Sastry, P. U. M., and Tyagi, A. K. (2008). "Combustion synthesis of nano-crystalline Nd-doped ceria and Nd_2O_3 and their fractal behavior as studied by small angle X-ray scattering." *J. Alloys Compd.*, 456(1–2), 51–56.
- Chen, D., Gao, X., and Dollimore, D. (1993). "A generalized form of the Kissinger equation." *Thermochimica Acta*, 215, 109–117.
- Chi, H., Zhang, P., Xiong, J., Wei, Y., Li, Y., and Zhao, Z. (2023). "Single-crystalline α - MnO_2 catalysts with tailored exposed crystal facets for boosting catalytic soot oxidation : The crystal facet-dependent activity." *Appl. Surf. Sci.*, 608, 155116.

References

- Chingakham, V. G., Jaison, C., and Sajith, J. V. (2020). “Enhancement of soot combustion in diesel particulate filters by ceria nanofiber coating.” *Appl. Nanosci.*, 10, 2429–2438.
- Chrissafis, K. (2009). “Kinetics of thermal degradation of polymers : Complementary use of isoconversional and model-fitting methods.” *J. Therm. Anal. Calorim.*, 95(1), 273–283.
- Christensen, J. M., Grunwaldt, J. D., and Jensen, A. D. (2016). “Importance of the oxygen bond strength for catalytic activity in soot oxidation.” *Appl. Catal. B Environ.*, 188, 235–244.
- Cordatos, H., Ford, D., and Gorte, R. J. (1996). “Simulated Annealing Study of the Structure and Reducibility in Ceria Clusters.” *J. Phys. Chem.*, 100(46), 18128–18132.
- Cousin, R., Capelle, S., Courcot, D., and Aboukaï, A. (2007). “Copper-vanadium-cerium oxide catalysts for carbon black oxidation.” *Appl. Catal. B Environ.*, 70, 247–253.
- Cui, Q., Dong, X., Wang, J., and Li, M. (2008). “Direct fabrication of cerium oxide hollow nanofibers by electrospinning.” *J. Rare Earths*, 26(5), 664–669.
- Deng, X., Li, M., Zhang, J., Hu, X., Zheng, J., Zhang, N., and Chen, B. H. (2017). “Constructing nano-structure on silver/ceria-zirconia towards highly active and stable catalyst for soot oxidation.” *Chem. Eng. J.*, 313, 544–555.
- Devaiah, D., Tsuzuki, T., Boningari, T., Smirniotis, P. G., and Reddy, B. M. (2015). “Ce_{0.80}M_{0.12}Sn_{0.08}O_{2-δ} (M= Hf, Zr, Pr, and La) ternary oxide solid solutions with superior properties for CO oxidation.” *RSC Adv.*, 5(38), 30275–30285.
- Drake, T., Ji, P., and Lin, W. (2018). “Site Isolation in Metal–Organic Frameworks Enables Novel Transition Metal Catalysis.” *Acc. Chem. Res.*, 51, 2129–2138.
- Duan, W., L. I. J., Xiaodong, W. U., and Zhichun, S. I. (2010). “NO_x -assisted soot oxidation over K / CuCe catalyst.” *J of Rare Earths.*, 28(4), 542–547.

References

- Dulgheru, P., and Sullivan, J. A. (2013). “Rare earth (La, Nd, Pr) doped ceria-zirconia solid solutions for soot combustion.” *Top. Catal.*, 56(1–8), 504–510.
- Durgasri, D. N., Vinodkumar, T., Lin, F., Alxneit, I., and Reddy, B. M. (2014a). “Gadolinium doped cerium oxide for soot oxidation: Influence of interfacial metal-support interactions.” *Appl. Surf. Sci.*, 314(x), 592–598.
- Ebrahimi-Kahrizsangi, R., and Abbasi, M. H. (2008). “Evaluation of reliability of Coats-Redfern method for kinetic analysis of non-isothermal TGA.” *Trans. Nonferrous Met. Soc. China.*, 18(1), 217–221.
- Al-Awadi Abdulrhman S., Mohamed El-Toni Ahmed., Al-Zahrani Saeed M., Abasaeed Ahmed E., and Khan Aslam (2020). “Synthesis, Characterization and Catalytic Evaluation of Chromium Oxide Deposited on Titania–Silica Mesoporous Nanocomposite for the Ethane Dehydrogenation with CO₂”, *Crystals.*, 322(10) 1-16.
- Fagg, D. P., Pe, D., Nu, P., Kharton, V. V, and Frade, J. R. (2003). “The effect of cobalt oxide sintering aid on electronic transport in Ce_{0.80} Gd_{0.20} O_{2-δ} electrolyte.” *Electrochimica Acta.*, 48(8) 1023-1029.
- Fan, L., Xi, K., Zhou, Y., Zhu, Q., Chen, Y., and Lu, H. (2017). “Design structure for CePr mixed oxide catalysts in soot combustion.” *RSC Adv.*, 7(33), 20309–20319.
- Farhadi, S., Javanmard, M., and Nadri, G. (2016). “Characterization of cobalt oxide nanoparticles prepared by the thermal decomposition of [Co(NH₃)₅(H₂O)](NO₃)₃ complex and study of their photocatalytic activity.” *Acta Chim. Slov.*, 63(2), 335–343.
- Farra, R., Garc, M., Eichelbaum, M., Hashagen, M., Frandsen, W., Allan, J., and Girgsdies, F. (2013). “Promoted Ceria: A Structural, Catalytic, and Computational Study.” *ACS Catalysis.*, 3, 2256–2268

References

- Fedunik-hofman, L., and Bayon, A. (2019). “Kinetics of Solid-Gas Reactions and Their Application to Carbonate Looping Systems.” *Energies*, 15(12), 1-35.
- Fu, M., Lin, J., Zhu, W., Wu, J., Chen, L., Huang, B., and Ye, D. (2014). “Surface reactive species on MnO_{x(0.4)}-CeO₂ catalysts towards soot oxidation assisted with pulse dielectric barrier discharge.” *J. Rare Earths*, 32(2), 153–158.
- Fu, S., Fang, Q., Li, A., Li, Z., Han, J., Dang, X., and Han, W. (2021). “Accurate characterization of full pore size distribution of tight sandstones by low-temperature nitrogen gas adsorption and high-pressure mercury intrusion combination method.” *Energy Sci. Eng.*, 9(1), 80–100.
- Ganiger, S., Patil, S. S., Dasari, H. P., Priyanka, R., and Kollimarla, S. (2022). “Printex-U soot oxidation kinetic behavior over Alumina and Quartz.” *Chem. Eng. Sci.*, 247, 1-11.
- Gao, H. (2006). “Synthesis and luminescence of europium doped yttria nano phosphors via a sucrose-templated combustion method.” *Nanotechnology*, 17, 4327-4331.
- Gao, J., Wang, Y., Wang, S., Li, X., Chang, X., Wang, X., Yang, C., and Xuan, R. (2022). “Effect of catalytic reactions on soot feature evolutions in the oxidation process.” *Chem. Eng. J.*, 443, 1-10.
- Garces, L. J., Hincapie, B., Zerger, R., and Suib, S. L. (2015). “The effect of temperature and support on the reduction of cobalt oxide: An in situ x-ray diffraction study.” *J. Phys. Chem. C*, 119(10), 5484–5490.
- García, A., and Atribak, I. (2008). “Thermally stable ceria – zirconia catalysts for soot oxidation by O₂.” *Cat. Comm*, 9, 250–255.
- Ghosh, S. K. (2020). “Diversity in the Family of Manganese Oxides at the Nanoscale: From Fundamentals to Applications.” *ACS Omega*, 5(40), 25493–25504.

References

Gotor, F. J., José, Criado, M., Malek, J., and Koga, N. (2000). “Kinetic analysis of solid-state reactions: The universality of master plots for analyzing isothermal and nonisothermal experiments.” *J. Phys. Chem. A*, 104(46), 10777–10782.

Govardhan, P., Anantharaman, A. P., Patil, S. S., Dasari, H. P., Dasari, H., and Shourya, A. (2022). “Effect of Ag loading on praseodymium doped ceria catalyst for soot oxidation activity.” *Korean J. Chem. Eng.*, 39(2), 328–342.

Grasselli, R. K. (2002). “Fundamental principles of selective heterogeneous oxidation catalysis.” *Topics in Catal.*, 21, 79–88.

Guangjun Zhai., Jinguo Wang., Zimei Chen., Shuaifeng Yang., Yong Men., (2019) "Highly enhanced soot oxidation activity over 3DOM $\text{Co}_3\text{O}_4\text{-CeO}_2$ catalysts by synergistic promoting effect." *J. of Hazardous Mat.*, 363, 214-226,

Guillén, C., and Herrero, J. (2021). “Structural Changes Induced by Heating in Sputtered NiO and Cr_2O_3 Thin Films as p-Type Transparent Conductive Electrodes.” *Electron. Mater.*, 2(2), 49–59.

Hansen, T. W., Delariva, A. T., Challa, S. R., and Datye, A. K. (2013). “Sintering of catalytic nanoparticles: Particle migration or Ostwald ripening” *Acc. Chem. Res.*, 46(8), 1720–1730.

Hernández-Giménez, A. M., Xavier, L. P. D. S., and Bueno-López, A. (2013). “Improving ceria-zirconia soot combustion catalysts by neodymium doping.” *Appl. Catal. A Gen.*, 462–463, 100–106.

Holgado, J. P., Alvarez, R., and Munuera, G. (2000). “Study of CeO_2 XPS spectra by factor analysis: Reduction of CeO_2 .” *Appl. Surf. Sci.*, 161(3), 301–315.

References

Huang, H., Zhang, X., Liu, J., and Ye, S. (2020). "Study on oxidation activity of Ce – Mn – K composite oxides on diesel soot." *Sci. Rep.*, (0123456789), 1–10.

ICCT Policy Update. (2016). "India Bharat stage VI emission standards." *Int. Counc. Clean Transp.*

Isabel, M., Argolo, S., and Educacionais, C. P. (2020). "Starch as a Sustainable Fuel for Solution Combustion Synthesis : Nanomaterials for Energy and Environmental Applications." *Current Nanoscience*, 17(4) 505-524.

Jamshidijam, M., Mangalaraja, R. V., Akbari-Fakhrabadi, A., Ananthakumar, S., and Chan, S. H. (2014). "Effect of rare earth dopants on structural characteristics of nanoceria synthesized by combustion method." *Powder Technol.*, 253, 304–310.

Jones, T. E., Rocha, T. C. R., Knop-Gericke, A., Stampfl, C., Schlögl, R., and Piccinin, S. (2015). "Insights into the Electronic Structure of the Oxygen Species Active in Alkene Epoxidation on Silver." *ACS Catal.*, 5(10), 5846–5850.

Kahlaoui, M., Chefi, S., Inoubli, A., Madani, A., and Chefi, C. (2013). "Synthesis and electrical properties of co-doping with La³⁺, Nd³⁺, Y³⁺, and Eu³⁺ citric acid-nitrate prepared samarium-doped ceria ceramics." *Ceram. Int.*, 39(4), 3873–3879.

Katta, L., Sudarsanam, P., Thrimurthulu, G., and Reddy, B. M. (2010). "Doped nanosized ceria solid solutions for low-temperature soot oxidation: Zirconium versus lanthanum promoters." *Appl. Catal. B Environ.*, 101(1–2), 101–108.

Kaus, I., Dahl, P. I., Mastin, J., Grande, T., and Einarsrud, M. A. (2006). "Synthesis and characterization of nanocrystalline YSZ powder by smoldering combustion synthesis." *J. Nanomater.*, 2006, 1–7.

References

Keck, J. D., and Wilcox, P. D. (1980). "Investigations of the effect of the morphology of Nb dopant on lead zirconate ceramic." *Ferroelectrics*, 27(1), 99–102.

Khaskheli, A. A., Xu, L., and Liu, D. (2022). "Manganese Oxide-Based Catalysts for Soot Oxidation : A Review on the Recent Advances and Future Directions." *Energy Fuels*, 36, 7362-7381.

Kim, K., Yoo, J. Do, Lee, S., Bae, M., Bae, J., Jung, W. C., and Han, J. W. (2017). "A Simple Descriptor to Rapidly Screen CO Oxidation Activity on Rare-Earth Metal-Doped CeO₂: From Experiment to First-Principles." *ACS Appl. Mater. Interfaces*, 9(18), 15449–15458.

Kreissl, H. T., Li, M. M. J., Peng, Y., Nakagawa, K., Hooper, T. J. N., Hanna, J. V, Shepherd, A., Wu, T., Soo, Y., and Tsang, S. C. E. (2017). "Structural Studies of Bulk to Nanosize Niobium Oxides with Correlation to Their Acidity." *J. of Americal Chem. Soc.* 139, 12670–12680.

Krishna, K., Bueno-López, A., Makkee, M., and Moulijn, J. A. (2007a). "Potential rare-earth modified CeO₂ catalysts for soot oxidation. Part III. Effect of dopant loading and calcination temperature on catalytic activity with O₂ and NO + O₂." *Appl. Catal. B Environ.*, 75(3–4), 210–220.

Kumar, P. A., Tanwar, M. D., Bensaid, S., Russo, N., and Fino, D. (2012a). "Soot combustion improvement in diesel particulate filters catalyzed with ceria nanofibers." *Chem. Eng. J.* 207/208, 258-266

Kumar, P. A., Tanwar, M. D., Russo, N., Pirone, R., and Fino, D. (2012b). "Synthesis and catalytic properties of CeO₂ and Co / CeO₂ nanofibres for diesel soot combustion." *Catal Today*, 184, 279–287.

References

- Kuwahara, Y., Kato, G., Fujibayashi, A., Mori, K., and Yamashita, H. (2020). “Diesel Soot Combustion over Mn_2O_3 Catalysts with Different Morphologies: Elucidating the Role of Active Oxygen Species in Soot Combustion.” *Chem. - An Asian J.*, 15(13), 2005–2014.
- Lebedev, O. I. (2007). “Structural and luminescence investigation on gadolinium gallium garnet nanocrystalline powders prepared by.” *Nanotechnology*, 18, 1-9.
- Lee, C., Jeon, Y., Kim, T., Tou, A., Park, J., and Einaga, H. (2018). “Ag-loaded cerium-zirconium solid solution oxide nano-fibrous webs and their catalytic activity for soot and CO oxidation.” *Fuel*, 212(October 2017), 395–404.
- Lee, C., Park, J., Shul, Y., Einaga, H., and Teraoka, Y. (2015). “Applied Catalysis B : Environmental Ag supported on electrospun macro-structure CeO_2 fibrous mats for diesel soot oxidation.” *Applied Catal. B, Environ.*, 174–175, 185–192.
- Lee, K. O., Seong, H., and Choi, S. M. (2013). “Detailed analysis of kinetic reactions in soot oxidation by simulated diesel exhaust emissions.” *Proc. Combust. Inst.*, 34(2), 3057–3065.
- Leitenburg, C. de, Trovarelli, A., Zamar, F., Maschio, S., Dolcetti, G., and Llorca, J. (1995). “A Novel and Simple Route To Catalysts With a High Oxygen Storage Capacity: the Direct Room-Temperature Synthesis of CeO_2 - ZrO_2 Solid-Solutions.” *J. Chem. Soc. Commun.*, 02(21), 2181–2182.
- Li, C., Sun, Y., and Zhang, A. (2015). “Binary Ce-Mn oxides confined in carbon nanotubes as efficient catalysts for ethylbenzene dehydrogenation in the presence of carbon dioxide.” *RSC Adv.*, 5(46), 36394–36403.
- Li, G., Zhang, X., Feng, W., Fang, X., and Liu, J. (2018). “Nanoporous CeO_2 -Ag catalysts prepared by etching the $CeO_2 / CuO / Al_2O_3$ mixed oxides for CO oxidation.” *Corrosion Sci.*, 134(17), 140–148.

References

- Li, M., Jiang, L., He, J. J., and Sun, J. H. (2019). “Kinetic triplet determination and modified mechanism function construction for thermo-oxidative degradation of waste polyurethane foam using conventional methods and distributed activation energy model method.” *Energy*, 175, 1–13.
- Li, X., Wei, S., Zhang, Z., Zhang, Y., Wang, Z., Su, Q., and Gao, X. (2011). “Quantification of the active site density and turnover frequency for soot combustion with O₂ on Cr doped CeO₂.” *Catal. Today*, 175(1), 112–116.
- Liang, H., Jin, B., Li, M., Yuan, X., Wan, J., Liu, W., Wu, X., and Liu, S. (2021). “Applied Catalysis B: Environmental Highly reactive and thermally stable Ag / YSZ catalysts with macroporous fiber-like morphology for soot combustion.” *Appl. Catal. B Environ.*, 294, 1-10.
- Liang, Q., Wu, A. X., Xiaodi, A., Ae, W., and Weng, D. (2007a). “Role of surface area in oxygen storage capacity of ceria–zirconia as soot combustion catalyst.” *Catal. Letters*, 119, 265–270.
- Liang, Q., Wu, X., Weng, D., and Lu, Z. (2008). “Selective oxidation of soot over Cu doped ceria / ceria – zirconia catalysts.” *Catal Comm*, 9(3), 202–206.
- Lin, F., Wu, X., and Weng, D. (2011a). “Effect of barium loading on CuOx – CeO₂ catalysts : NO_x storage capacity, NO oxidation ability, and soot oxidation activity.” *Catal. Today*, 175(1), 124–132.
- Liu, S., Wu, X., Liu, W., Chen, W., Ran, R., Li, M., and Weng, D. (2016). “Soot oxidation over CeO₂ and Ag / CeO₂ : Factors determining the catalyst activity and stability during reaction.” *J. of Catal.*, 337, 188–198.

References

- López-Fonseca, R., Elizundia, U., Landa, I., Gutiérrez-Ortiz, M. A., and González-Velasco, J. R. (2005). “Kinetic analysis of non-catalytic and Mn-catalysed combustion of diesel soot surrogates.” *Appl. Catal. B Environ.*, 61(1–2), 150–158.
- López-Fonseca, R., Landa, I., Elizundia, U., Gutiérrez-Ortiz, M. A., and González-Velasco, J. R. (2007). “A kinetic study of the combustion of porous synthetic soot.” *Chem. Eng. J.*, 129(1–3), 41–49.
- Maggi, F., Dossi, S., Paravan, C., Galfetti, L., Cianfanelli, S., and Marra, G. (2017). “Detailed properties of iron oxide solid propellant catalyst.” *Acta Astronautica.*, 158, 416-424.
- Mahofa, E. P., Narsaiah, T. B., and Kumar, P. (2014). “Catalytic Activity of CeO₂ -NiO for Low-Temperature Soot Combustion.” *Int. J. of Eng. Research and Tech*, 3(9), 48–51.
- Mahofa, E., Tumma, B. N., and Chidurala, S. (2018). “Catalytic Soot Oxidation Using Ceria, Cobalt and Copper.” *Mat. Research Soc Adv.* 1-8.
- Mallick, P., and Dash, B. N. (2013). “X-ray Diffraction and UV-Visible Characterizations of α -Fe₂O₃ Nanoparticles Annealed at Different Temperature.” *Nanosci. Nanotechnol.*, 3(5), 130–134.
- Mandal, B., Mondal, A., Ray, S. S., and Kundu, A. (2015). “Sm Doped Mesoporous CeO₂ Nanocrystals : Aqueous Solution-Based.” *Dalton Trans.*, 45, 1679-1692.
- Marbán, G., López, I., and Valdés-Solís, T. (2009). “Preferential oxidation of CO by CuO_x/CeO₂ nanocatalysts prepared by SACOP. Mechanisms of deactivation under the reactant stream.” *Appl. Catal. A Gen.*, 361(1–2), 160–169.
- Mary Mangaiyarkarasi, M. S., Vincent, S., Janarthanan, S., Subba Rao, T., and Tata, B. V. R. (2011). “Bioreduction of Cr(VI) by alkaliphilic *Bacillus subtilis* and interaction of the membrane groups.” *Saudi J. Biol. Sci.*, 18(2), 157–167.

References

- Meghana, S., and Kabra, P. (2015). “ Understanding the pathway of antibacterial activity of copper oxide nanoparticles .” *RSC Adv.*, 5, 12293–12299.
- Miceli, P., Bensaid, S., Russo, N., and Fino, D. (2014). “CeO₂-based catalysts with engineered morphologies for soot oxidation to enhance soot-catalyst contact.” *Nanoscale Res. Lett.*, 9(1), 1–10.
- Mimani, T., and Patil, K. C. (2001). “Solution Combustion of Nanoscale Oxides and Their Composites.” *Mater. Phys. Mech.*, 4, 134–137.
- Mira, J. G., Pérez, V. R., and Bueno-López, A. (2015). “Effect of the CeZrNd mixed oxide synthesis method in the catalytic combustion of soot.” *Catal. Today*, 253, 77–82.
- Mittal, M., Gupta, A., and Pandey, O. P. (2018). “Role of oxygen vacancies in Ag / Au doped CeO₂ nanoparticles for fast photocatalysis.” *Sol. Energy*, 165(January), 206–216.
- Mukherjee, D., Rao, B. G., and Reddy, B. M. (2016). “CO and soot oxidation activity of doped ceria: Influence of dopants.” *Appl. Catal. B Environ.*, 197, 105–115.
- Muroyama, H., Hano, S., Matsui, T., and Eguchi, K. (2010). “Catalytic soot combustion over CeO₂ -based oxides.” *Catal. Today*, 153(3–4), 133–135.
- Murugan, B., and Ramaswamy, A. V. (2005). “Nature of Manganese Species in Ce_{1-x}Mn_xO_{2-δ} Solid Solutions Synthesized by the Solution Combustion Route.” *Chem. Mater*, (10), 3983–3993.
- Naeem, R., Ali Ehsan, M., Yahya, R., Sohail, M., Khaledi, H., and Mazhar, M. (2016). “Fabrication of pristine Mn₂O₃ and Ag-Mn₂O₃ composite thin films by AACVD for photoelectrochemical water splitting.” *Dalt. Trans.*, 45(38), 14928–14939.

References

- Nascimento, L. F., Sousa Filho, P. C. De, Lima, J. F., and Serra, O. A. (2015). “Kinetic parameters of soot oxidation catalyzed by nanosized ZnO-CeO₂ solids.” *J. Braz. Chem. Soc.*, 26(7), 1315–1320.
- Neeft, J. P. A., Nijhuis, T. X., Smakman, E., Makkee, M., and Moulijn, J. A. (1997). “Kinetics of the oxidation of diesel soot.” *Fuel*, 76(12), 1129–1136.
- Neelapala, S. D., and Dasari, H. (2018a). “Catalytic soot oxidation activity of Cr-doped ceria (CeCrO_{2-δ}) synthesized by sol-gel method with organic additives.” *Mater. Sci. Energy Technol.*, 1(2), 155–159.
- Neelapala, S. D., Patnaik, H., and Dasari, H. (2018). “Enhancement of soot oxidation activity of manganese oxide (Mn₂O₃) through doping by the formation of Mn_{1.9}M_{0.1}O_{3-δ} (M = Co, Cu, and Ni).” *Asia-Pacific J. Chem. Eng.*, 13(5), 1–9.
- Niu, X., Li, M., Hao, B., and Li, H. (2016). “Hydrothermal synthesis of 3D hierarchical porous CeO₂ rugby-ball-like nanostructures with nanorods as building blocks.” *J. Mater. Sci. Mater. Electron.*, 27, 6845–6848.
- Okuhara, T. (2002). “Water-Tolerant Solid Acid Catalysts.” *Chem. Rev.* 102, 3641–3666
- Li Boyu., Raj Abhishek., C, Eric and Z, John Wen (2019). “Reactive Fe-O-Ce Sites in Ceria Catalysts for Soot Oxidation.” *Catalysts*, 9, 815 20–22.
- Ozawa, T. (1992). “Estimation of activation energy by isoconversion methods.” *Thermochim. Acta*, 203(C), 159–165.

References

Patil, S., and Dasari, H. P. (2019). "Materials Science for Energy Technologies Effect of fuel and solvent on soot oxidation activity of ceria nanoparticles synthesized by solution combustion method." *Mater. Sci. Energy Technol.*, 2(3), 485–489.

Patil, S. S., Prasad, H., and Dasari, H. (2019). "Effect of Nd-doping on soot oxidation activity of Ceria-based nanoparticles synthesized by Glycine Nitrate Process." *Nano-Structures & Nano-Objects*, 20, 1-7.

Paunovi, N. (2012). "Suppression of inherent ferromagnetism in Pr-doped CeO₂ nanocrystals", *Nanoscale*. 5469–5476.

Pengpanich, S., Meeyoo, V., and Rirksomboon, T. (2005). "Oxidation of methane over Nb-doped Ce_{0.75}Zr_{0.25}O₂ mixed oxide solid solution catalysts." *J. Chem. Eng. Japan*, 38(1), 49–53.

Poggio-Fraccari, E., Baronetti, G., and Mariño, F. (2018). "Pr³⁺ surface fraction in CePr mixed oxides determined by XPS analysis." *J. Electron Spectros. Relat. Phenomena*, 222, 1–4.

Poulose, A. C., Veerananarayanan, S., Mohamed, M. S., Aburto, R. R., Mitcham, T., Bouchard, R. R., Ajayan, P. M., Sakamoto, Y., Maekawa, T., and Kumar, D. S. (2016). "Multifunctional Cu_{2-x}Te Nanocubes Mediated Combination Therapy for Multi-Drug Resistant MDA MB *Sci. Rep.*, 453, 6, 1-13.

References

- Prabaharan, D. D. M., Sadaiyandi, K., Mahendran, M., and Sagadevan, S. (2017). "Precipitation method and characterization of cobalt oxide nanoparticles." *Appl. Phys. A Mater. Sci. Process.*, 123(4), 1–6.
- Pradier, C. M., Rodrigues, F., Marcus, P., Landau, M. V., Kaliya, M. L., Gutman, A., and Herskowitz, M. (2000). "Supported chromia catalysts for oxidation of organic compounds." *Appl. Catal. B Environ.*, 27(2), 73–85.
- Prasad, D. H., Park, S. Y., Ji, H.-I., Kim, H.-R., Son, J.-W., Kim, B.-K., Lee, H.-W., and Lee, J.-H. (2012a). "Structural Characterization and Catalytic Activity of $\text{Ce}_{0.65}\text{Zr}_{0.25}\text{RE}_{0.1}\text{O}_{2-\delta}$ Nanocrystalline Powders Synthesized by the Glycine-Nitrate Process." *J. Phys. Chem. C*, 116(5), 3467–3476.
- Prasad, D. H., Park, S. Y., Oh, E. O., Ji, H., Kim, H. R., Yoon, K. J., Son, J. W., and Lee, J. H. (2012c). "Synthesis of nano-crystalline $\text{La}_{1-x}\text{Sr}_x\text{CoO}_{3-\delta}$ perovskite oxides by EDTA–citrate complexing process and its catalytic activity for soot oxidation." *Appl. Catal. A Gen.*, 447–448, 100–106.
- Prasad, D. H., Son, J. W., Kim, B. K., Lee, H. W., and Lee, J. H. (2008). "Synthesis of nano-crystalline $\text{Ce}_{0.9}\text{Gd}_{0.1}\text{O}_{1.95}$ electrolyte by novel sol-gel thermolysis process for IT-SOFCs." *J. Eur. Ceram. Soc.*, 28(16), 3107–3112.
- Qayoom, M., Shah, K. A., Pandit, A. H., Firdous, A., and Dar, G. N. (2020). "Dielectric and electrical studies on iron oxide ($\alpha\text{-Fe}_2\text{O}_3$) nanoparticles synthesized by modified solution combustion reaction for microwave applications." *J. Electroceramics*, 45(1), 7–14.
- Qin, J., Long, Y., Wu, W., Zhang, W., Gao, Z., and Ma, J. (2019). "Amorphous Fe_2O_3 improved [O] transfer cycle of $\text{Ce}^{4+}/\text{Ce}^{3+}$ in CeO_2 for atom economy synthesis of imines at low temperature." *J. Catal.*, 371, 161–174.

References

- Qin, M., Du, X., Wang, J., Humail, I. S., and Qu, X. (2009). "Influence of carbon on the synthesis of AlN powder from combustion synthesis precursors." *J. of the European Ceramic Soc.*, 29, 795–799.
- Raba, A. M., Joya, M. R., and Santander, N. (2016). "Synthesis and Structural Properties of Niobium Pentoxide Powders : A Comparative Study of the Growth Process." *Mat. Research*, 19(6), 1-7.
- Rajvanshi, K., Patil, S. S., Lakhanlal, Dasari, H. P., Saidutta, M. B., and Dasari, H. (2020). "Promotional effect of nickel addition on soot oxidation activity of Ce_{0.9}Pr_{0.1}O₂ oxide catalysts." *Chem. Pap.*, 74(12), 4581–4592.
- Ramírez-Cabrera, E., Laosiripojana, N., Atkinson, A., and Chadwick, D. (2003). "Methane conversion over Nb-doped ceria." *Catal. Today*, 78, 433–438.
- Ranji-Burachaloo, H., Masoomi-Godarzi, S., Khodadadi, A. A., and Mortazavi, Y. (2016). "Synergetic effects of plasma and metal oxide catalysts on diesel soot oxidation." *Appl. Catal. B Environ.*, 182, 74–84.
- Rao, K. N., Venkataswamy, P., and Reddy, B. M. (2011). "Structural characterization and catalytic evaluation of supported copper-ceria catalysts for soot oxidation." *Ind. Eng. Chem. Res.*, 50(21), 11960–11969.
- Reddy, B. M., Bharali, P., Gode, A., Ae, T., Saikia, P., Lakshmi, A., Ae, K., and Park, S.-E. (2008). "Catalytic Efficiency of Ceria–Zirconia and Ceria–Hafnia Nanocomposite Oxides for Soot Oxidation." *Catal. Letters*, 123, 327–333.
- Reddy, B. M., and Rao, K. N. (2009). "Copper-promoted ceria-zirconia based bimetallic catalysts for low temperature soot oxidation." *Catal. Commun.*, 10(9), 1350–1353.

References

- Reddy, B. M., Thrimurthulu, G., and Katta, L. (2011). "Design of Efficient $Ce_xM_{1-x}O_{2-\delta}$ (M = Zr, Hf, Tb, and Pr) Nanosized Model Solid Solutions for CO Oxidation." *Catal. Letters*, 141, 572–581.
- Reddy, B. M., Thrimurthulu, G., Katta, L., and Park, S. (2009a). "Structural Characteristics and Catalytic Activity of Nanocrystalline Ceria - Praseodymia Solid Solutions." *J. Phys. Chem. C*, 15882–15890.
- Reddy, B. M., Thrimurthulu, G., Katta, L., Yamada, Y., and Park, S. E. (2009b). "Structural characteristics and catalytic activity of nanocrystalline ceria-praseodymia solid solutions." *J. Phys. Chem. C*, 113(36), 15882–15890.
- J, Chrzanowski and J.C. Irwin (1989) "Raman Scattering from Cupric Oxide," *Solid State Comm.*, 70, 11-14.
- Saikia, P., Allou, N. B., Borah, A., and Goswamee, R. L. (2017). "Iso-conversional kinetics study on thermal degradation of Ni-Al layered double hydroxide synthesized by 'soft chemical' sol-gel method." *Mater. Chem. Phys.*, 186, 52–60.
- Salavati-Niasari, M., Mir, N., and Davar, F. (2009). "Synthesis and characterization of NiO nanoclusters via thermal decomposition." *Polyhedron*, 28(6), 1111–1114.
- Santillán, J. M. J., Muñetón Arboleda, D., Coral, D. F., Fernández van Raap, M. B., Muraca, D., Schinca, D. C., and Scaffardi, L. B. (2017). "Optical and Magnetic Properties of Fe Nanoparticles Fabricated by Femtosecond Laser Ablation in Organic and Inorganic Solvents." *ChemPhysChem*, 18(9), 1192–1209.
- Sasmal, P., and Datta, P. (2019). "Tranexamic acid-loaded chitosan electrospun nano fibers as drug delivery system for hemorrhage control applications." *J. Drug Deliv. Sci. Technol.*, 52(February), 559–567.

References

- Sbirrazzuoli, N. (2013). "Thermochimica Acta Determination of pre-exponential factors and of the mathematical functions $f(\alpha)$ or $g(\alpha)$ that describe the reaction mechanism in a model-free way." *Thermochim. Acta*, 564, 59–69.
- Setten, B. A. A. L. Van, Makkee, M., and Moulijn, J. A. (2001). "Science and technology of catalytic diesel particulate filters." *Catal. Rev. - Sci. Eng.*, 43(4), 489–564.
- Shajahan, I., Ahn, J., Nair, P., Mediseti, S., Patil, S., Niveditha, V., Uday Bhaskar Babu, G., Dasari, H. P., and Lee, J. H. (2018). "Praseodymium doped ceria as electrolyte material for IT-SOFC applications." *Mater. Chem. Phys.*, 216, 136–142.
- Shannon, R. D. (1976). "Revised effective ionic radii and systematic studies of interatomic distances in halides and chalcogenides." *Acta Mater.*, A32, 751–767.
- Shenoy CS, Patil SS, Govardhan P, Shourya A, Dasari H, P., Saidutta, M, B., Dasari H (2019) Studies on the solid oxide cell perovskite electrode materials for soot oxidation activity. *Emiss Control Sci Technol.* 5:342–352.
- Shuang, L. I. U., Xiaodong, W. U., Duan, W., and Rui, R. A. N. (2015). "Ceria-based catalysts for soot oxidation : a review." *J. Rare Earths*, 33(6), 567–590.
- Shupack, S. I. (1991). "The chemistry of chromium and some resulting analytical problems." *Environ. Health Perspect.*, 92 (1), 7–11.
- Singhania, A. (2017). "High surface area M (M = La , Pr , Nd , and Pm) -doped ceria nanoparticles : Synthesis, characterization and activity comparison for CO oxidation" *Ind. Eng. Chem. Res.*, 56, 46, 13594–13601
- Starink, M. J. (2003). "The determination of activation energy from linear heating rate experiments: A comparison of the accuracy of isoconversion methods." *Thermochim. Acta*, 404(1–2), 163–176.

References

- Stegmayer, M. Á., Irusta, S., Miró, E. E., and Milt, V. G. (2022). “Electrospinning synthesis and characterization of nanofibers of Co, Ce and mixed Co-Ce oxides. Their application to oxidation reactions of diesel soot and CO.” *Catal. Today*, 383, 266–276.
- Stein, K. C., Feenan, J. J., Thompson, G. P., Shultz, J. F., Hofer, L. J. E., and Anderson, R. B. (1960). “An Approach to Air Pollution Control Catalytic Oxidation of Hydrocarbons.” *Ind. Eng. Chem.*, 52(8), 671–674.
- Suárez-Vázquez, S. I., Cruz-López, A., Molina-Guerrero, C. E., Sánchez-Vázquez, A. I., and Macías-Sotelo, C. (2018). “Effect of dopant loading on the structural and catalytic properties of Mn-doped SrTiO₃ catalysts for catalytic soot combustion.” *Catalysts*, 8(2) 1-11.
- Sudarsanam, P., Kuntaiah, K., and Reddy, B. M. (2014). “Promising ceria-samarium-based nano-oxides for low temperature soot oxidation: a combined study of structure-activity properties.” *New J. Chem.*, 38(12), 5991–6001.
- Tahmasebi, K., and Paydar, M. H. (2008). “The effect of starch addition on solution combustion synthesis of Al₂O₃ – ZrO₂ nanocomposite powder using urea as fuel.” *Mater Chemistry and Physics.*, 109, 156–163.
- Tan, T. L., and Lebron, G. B. (2012). “Determination of carbon dioxide, carbon monoxide, and methane concentrations in cigarette smoke by Fourier transform infrared spectroscopy.” *J. Chem. Educ.*, 89(3), 383–386.
- Thavasi, V., Singh, G., and Ramakrishna, S. (2008). “Electrospun nanofibers in energy and environmental applications.” *Energy & Environ. Sci.*, 1, 205–221.

References

- Thommes, M., Kaneko, K., Neimark, A. V., Olivier, J. P., Rodriguez-Reinoso, F., Rouquerol, J., and Sing, K. S. W. (2015). “Physisorption of gases, with special reference to the evaluation of the surface area and pore size distribution (IUPAC Technical Report).” *Pure Appl. Chem.*, 87(9–10), 1051–1069.
- Thrimurthulu, G., Rao, K. N., Devaiah, D., and Reddy, B. M. (2012). “Nanocrystalline ceria-praseodymia and ceria-zirconia solid solutions for soot oxidation.” *Res. Chem. Intermed.*, 38(8), 1847–1855.
- Tighe, C. J., Twigg, M. V., Hayhurst, A. N., and Dennis, J. S. (2016). “The kinetics of oxidation of Diesel soots and a carbon black (Printex U) by O₂ with reference to changes in both size and internal structure of the spherules during burnout.” *Carbon N. Y.*, 107, 20–35.
- Trovarelli, A. (1999). “Structural and oxygen storage/release properties of CeO₂-based solid solutions.” *Comments Inorg. Chem.*, 20(4–6), 263–284.
- Uslu, I., Aytimur, A., Öztürk, M. K., and Koçyigit, S. (2012). “Synthesis and characterization of neodymium doped ceria nanocrystalline ceramic structures.” *Ceram. Int.*, 38(6), 4943–4951.
- Valechha, D., Lokhande, S., Klementova, M., and Subrt, J. (2011). “Study of nano-structured ceria for catalytic CO oxidation.” 3718–3725.
- Varma, A., and Mukasyan, A. S. (2004). “Combustion synthesis of advanced materials: Fundamentals and applications.” *Korean J. Chem. Eng.*, 21(2), 527–536.
- Varma, A., Mukasyan, A. S., Rogachev, A. S., and Manukyan, K. V. (2016). “Solution Combustion Synthesis of Nanoscale Materials.” *Chem. Rev.*, 116(23), 14493–14586.

References

- Venkataswamy, P., Jampaiah, D., Mukherjee, D., Aniz, C. U., and Reddy, B. M. (2016a). "Mn-doped Ceria Solid Solutions for CO Oxidation at Lower Temperatures." *Catal. Letters*, 146(10), 2105–2118.
- Vilé, G., Teschner, D., Pérez-ramírez, J., and López, N. (2016). "Environmental Reactivity descriptors for ceria in catalysis." *Appl. Catal. B*, 197, 299–312.
- Vinod Kumar, T., Mukherjee, D., Subrahmanyam, C., and Reddy, B. M. (2018). "Investigation on the physicochemical properties of $Ce_{0.8}Eu_{0.1}M_{0.1}O_{2-\delta}$ ($M = Zr, Hf, La, \text{ and } Sm$) solid solutions towards soot combustion." *New J. Chem.*, 42(7), 5276–5283.
- Vinodkumar, T., Durgasr Naga, D., and Reddy, B. M. (2013). "Design of transition and rare earth metal doped ceria nanocomposite oxides for CO oxidation." *Int. J. Adv. Eng. Sci.*, 5(4), 224–231.
- Vinodkumar, T., Durgasri, D. N., Maloth, S., and Reddy, B. M. (2015). "Tuning the structural and catalytic properties of ceria by doping with Zr^{4+} , La^{3+} , and Eu^{3+} cations." *J. Chem. Sci.*, 127(7), 1145–1153.
- Vu, H., Nguyen, D., Fisher, J. G., Moon, W. H., Bae, S., Park, H. G., and Park, B. G. (2013). "CuO-based sintering aids for low temperature sintering of $BaFe_{12-19}$ ceramics." *J. Asian Ceram. Soc.*, 1(2), 170–177.
- Vyazovkin, S. (2020). "Kissinger Method in Kinetics of Materials: Things to Beware and Be Aware of." *Molecules*, 25(12) 1-18.
- Vyazovkin, S., Burnham, A. K., Criado, J. M., Pérez-Maqueda, L. A., Popescu, C., and Sbirrazzuoli, N. (2011). "ICTAC Kinetics Committee recommendations for performing kinetic computations on thermal analysis data." *Thermochim. Acta*, 520(1–2), 1–19.

References

- Wei, Y., Liu, J., Zhao, Z., Duan, A., Jiang, G., Xu, C., Gao, J., He, H., and Wang, X. (2011). “Three-dimensionally ordered macroporous $\text{Ce}_{0.8}\text{Zr}_{0.2}\text{O}_2$ -supported gold nanoparticles: Synthesis with controllable size and super-catalytic performance for soot oxidation.” *Energy Environ. Sci.*, 4(8), 2959–2970.
- Wei, Y., Zhang, Y., Zhang, P., Xiong, J., Mei, X., Yu, Q., Zhao, Z., and Liu, J. (2020). “Boosting the Removal of Diesel Soot Particles by the Optimal Exposed Crystal Facet of CeO_2 in Au/ CeO_2 Catalysts.” *Environ. Sci. Technol.*, 54, 3, 2002–2011
- Weidman, J., and Marshall, S. (2012). “Soot Pollution 101 What You Need to Know and How You Can Help Prevent It.” *Center for American Progress*, 2012–2015.
- Wu, X., Liang, Q., Weng, D., and Lu, Z. (2007a). “The catalytic activity of CuO-CeO_2 mixed oxides for diesel soot oxidation with a NO/O_2 mixture.” *Catal. Commun.*, 8(12), 2110–2114.
- Wu, X., Lin, F., Xu, H., and Weng, D. (2010). “Effects of adsorbed and gaseous NO_x species on catalytic oxidation of diesel soot with $\text{MnO}_x\text{-CeO}_2$ mixed oxides.” *Appl. Catal. B Environ.*, 96(1–2), 101–109.
- Wu, X., Liu, D., Li, K., Li, J., and Weng, D. (2007b). “Role of $\text{CeO}_2\text{-ZrO}_2$ in diesel soot oxidation and thermal stability of potassium catalyst.” *Catal. Commun.*, 8(8), 1274–1278.
- Wu, X., Liu, S., Weng, D., Lin, F., and Ran, R. (2011). “ $\text{MnO}_x\text{-CeO}_2\text{-Al}_2\text{O}_3$ mixed oxides for soot oxidation: Activity and thermal stability.” *J. Hazard. Mater.*, 187(1–3), 283–290.
- Xie, X., Li, Y., Liu, Z. Q., Haruta, M., and Shen, W. (2009). “Low-temperature oxidation of CO catalysed by Co_3O_4 nanorods.” *Nature*, 458(7239), 746–749.
- Xin, Y., Cao, H., Liu, C., Chen, J., Liu, P., Lu, Y., and Ling, Z. (2022). “A systematic spectroscopic study of laboratory synthesized manganese oxides relevant to Mars.” *J. Raman Spectrosc.*, 53(3), 340–355.

References

- Xing, L., Yang, Y., Ren, W., Zhao, D., Tian, Y., Ding, T., Zhang, J., Zheng, L., and Li, X. (2020). “Highly efficient catalytic soot combustion performance of hierarchically meso-macroporous $\text{Co}_3\text{O}_4/\text{CeO}_2$ nanosheet monolithic catalysts.” *Catal. Today*, 351, 83–93.
- Yafarova, L. V., Mamontov, G. V., Chislova, I. V., Silyukov, O. I., and Zvereva, I. A. (2021). “The effect of transition metal substitution in the perovskite-type oxides on the physicochemical properties and the catalytic performance in diesel soot oxidation.” *Catalysts*, 11(10), 1-10.
- Yang, D., Wang, L., Sun, Y., and Zhou, K. (2010). “Synthesis of one-dimensional $\text{Ce}_{1-x}\text{Y}_x\text{O}_{2-x/2}$ ($0 \leq x \leq 1$) solid solutions and their catalytic properties: The role of oxygen vacancies.” *J. Phys. Chem. C*, 114(19), 8926–8932.
- Yao, P., He, J., Jiang, X., Jiao, Y., Wang, J., and Chen, Y. (2020). “Factors determining gasoline soot abatement over $\text{CeO}_2\text{-ZrO}_2\text{-MnO}_x$ catalysts under low oxygen concentration condition.” *J. Energy Inst.*, 93(2), 774–783.
- Younis, A., Chu, D., and Li, S. (2016). “Cerium Oxide Nanostructures and their Applications.” *Funct. Nanomater.*, 53–68.
- Zhang, W., Niu, X., Chen, L., Yuan, F., and Zhu, Y. (2016a). “Soot combustion over nanostructured ceria with different morphologies.” *Nat. Publ. Gr.*, 6, 1-10.
- Zhang, Y., Zhang, H., Cao, Y., Yang, Y., Xu, B., Zhao, M., Gong, M., Xu, H., and Chen, Y. (2016b). “Promotional effect of cobalt addition on catalytic performance.” *Chem. Papers*, 70(10), 1370–1379.

References

Zhang, Z., Han, D., Wei, S., and Zhang, Y. (2010a). “Determination of active site densities and mechanisms for soot combustion with O₂ on Fe-doped CeO₂ mixed oxides.” *J. Catal.*, 276(1), 16–23.

Zhang, Z., Shao, C., Li, X., Wang, C., Zhang, M., and Liu, Y. (2010b). “ZnO Heterojunctions with Enhanced Photocatalytic Activity.” *Colloids and Surfaces A: Physicochemical and Engg. Aspects*, 2(10), 2915–2923.

Zhou, B., Xi, K., Fan, L. J., Zhou, Y., Wang, Y., Zhu, Q. L., and Lu, H. F. (2018). “A comparative study on Ce–Pr and Ce–Mn mixed oxide catalysts toward soot catalytic combustion.” *Appl. Catal. A Gen.*, 562, 1–10.

Zhu, S., Shi, S., Zheng, X., Wang, X., Yu, G., Jiang, Y., Feng, J., Zhu, L., and Zhang, G. (2022). “Enhanced Oxygen Vacancies in Ce-Doped SnO₂ Nanofibers for Highly Efficient Soot Catalytic Combustion.” *Catalysts*, 12(6), 1-16.

Zouaoui, N., Issa, M., Kehrlı, D., and Jeguirim, M. (2012). “CeO₂ catalytic activity for soot oxidation under NO / O₂ in loose and tight contact.” *Catal. Today*, 189(1), 65–69.

PUBLICATIONS

International Peer-Reviewed Journals (From Thesis)

Accepted

1. **Sunaina S Patil** and Hari Prasad Dasari, “An investigation on copper-loaded ceria-praseodymium catalysts for soot oxidation activity and its kinetics,” 2023, **Brazilian Journal of Chemical Engineering**, 1-17.
2. **Sunaina S Patil** and Hari Prasad Dasari et al., “A Negative Effect of Niobium-Doped Ceria on Soot Oxidation Activity,” 2022, **Chemical Engineering and Technology**, 517-525 .

Under Review

3. **Sunaina S Patil** and Hari Prasad Dasari, “Co-doped Ce- Pr catalysts for Soot Oxidation: Promotional Catalytic Effect and Kinetic studies,” 2023, **Kinetics and catalysis**.
4. **Sunaina S Patil** and Hari Prasad Dasari, “Synthesis and Characterization of Transitional Metal Doped Ceria-Praseodymium nanofibers and its Soot Oxidation Activity,” 2023, **Materials Today Communications**.

A Study on the Effect of Transition Metal Dopants in Ceria Praseodymium Catalysts for Soot Oxidation Activity and its Kinetics

Publications

In Submission

1. **Sunaina S Patil** and Hari Prasad Dasari, “Synthesis and Characterization of Iron Doped Ceria-Praseodymium catalysts and its Soot Oxidation Activity”.
2. **Sunaina S Patil** and Hari Prasad Dasari, “Soot Oxidation Activity and Kinetic Study of Manganese Doped Ceria-Praseodymium catalysts”.
3. **Sunaina S Patil** and Hari Prasad Dasari, “Soot Oxidation Activity and Kinetic Study of Chromium Doped Ceria-Praseodymium catalysts”.

Other Publications (Apart from thesis)

1. S Ganiger, **SS Patil**, HP Dasari, R Priyanka, S Kollimarla “ Printex-U soot oxidation kinetic behavior **SS Patil** over Alumina and Quartz **Chemical Engineering Science** 247, 117016, 2022.
2. P Govardhan, AP Anantharaman, **SS Patil**, HP Dasari, H Dasari,” Effect of Ag loading on praseodymium doped ceria catalyst for soot oxidation activity” **Korean Journal of Chemical Engineering**, 1-15, 2022.
3. MPA Vijay, **SS Patil**, DR Madhura, AP Anantharaman, P Gouramma, “ Effect of morphology and oxidation state of nickel on diesel soot oxidation activity” **Materials Today: Proceedings** 57, 1865-1870, 2022.
4. K Rajvanshi, SS Patil, HP Dasari, MB Saidutta, H Dasari “ Promotional effect of nickel addition on soot oxidation activity of $Ce_{0.9}Pr_{0.1}O_2$ oxide catalysts”, **Chemical Papers** 74, 4581-4592, 2020.

A Study on the Effect of Transition Metal Dopants in Ceria Praseodymium Catalysts for Soot Oxidation Activity and its Kinetics

Publications

-
5. CS Shenoy, **SS Patil**, P Govardhan, A Shourya, HP Dasari, MB Saidutta, “ Studies on the solid oxide cell perovskite electrode materials for soot oxidation activity” **Emission Control Science and Technology** 5, 342-352, 2019.
 6. **S Patil**, HP Dasari “Effect of fuel and solvent on soot oxidation activity of Ceria nanoparticles synthesized by solution combustion method” **Materials Science for Energy Technologies** 2 (3), 485-489, 2019.
 7. **SS Patil**, HP Dasari, H Dasari” Effect of Nd-doping on soot oxidation activity of Ceria-based nanoparticles synthesized by Glycine Nitrate Process, **Nano-Structures & Nano-Objects** 20, 100388, 2019.
 8. I Shajahan, J Ahn, P Nair, S Medisetti, **S Patil**, V Niveditha, GUB Babu, “Praseodymium doped ceria as electrolyte material for IT-SOFC applications” **Materials Chemistry and Physics** 216, 136-142, 2018.
 9. S Medisetti, J Ahn, **S Patil**, A Goel, Y Bangaru, GV Sabhahit, GUB Babu, “Synthesis of GDC electrolyte material for IT-SOFCs using glucose & fructose and its characterization” **Nano-Structures & Nano-Objects** 11, 7-12, 2017.

Conference / National Symposium attended

1. Pranathi S, **Sunaina S Patil**, Atmuri Shourya, Hari Prasad Dasari "Soot PM2.5 oxidation kinetics over CeO₂ synthesized using Saccharomyces Cerevisiae" International Conference on Biotechnology, Sustainable Bioresources and Bioeconomy (BSBB-2022) organized by IIT Guwahati from, December 7-11, 2022. (Presented Poster and Flash Talk).

2. **Sunaina S Patil**, Sahana Naik, Madhura D R, Harshini Dasari, Hari Prasad Dasari. "Effect of Niobium doped Ceria on soot oxidation activity" at International Chemical Engineering Conference 2021(100 Glorious Years of Chemical Engineering & Technology) organized by the Department of Chemical Engineering, Dr. B R Ambedkar National Institute of Technology, Jalandhar during September 16 -19, 2021. (Oral Presentation).
(won the "Best Paper Award")

3. **Sunaina S Patil**, Gouramma Pattanashetti, Kirti Rajvanshi, Hari Prasad Dasari" Effect of synthesis method for Nickel Oxide material on its soot oxidation activity" Environmental Pollution Prevention and Control: Future Perspective "EPPC-FP-2019", 23-25 August 2019, National Institute of Technology Karnataka Surathkal. (Oral Presentation).

A Study on the Effect of Transition Metal Dopants in Ceria Praseodymium Catalysts for Soot Oxidation Activity and its Kinetics

Biodata

BIODATA

PERSONAL DETAILS

Name	Sunaina S Patil
Date of Birth	10 th September 1989
Address	“AYODHYA”, B.C Road, Bantakal, Udupi-574114, Karnataka
Mobile	+91-9008483908
Email id	sunainapatil89@gmail.com ; sunaina.197ch001@nitk.edu.in

EDUCATION

2019 – Till Date	Ph.D. in Chemical Engineering National Institute of Technology Karnataka, Surathkal Department of Chemical Engineering
2017-2019	M-Tech (by Research) in Industrial Pollution Control National Institute of Technology Karnataka, Surathkal Department of Chemical Engineering
2013-2015	M-Tech in Chemical Plant Design National Institute of Technology Karnataka, Surathkal Department of Chemical Engineering
2007-2011	B-Tech in Biotechnology Nagarjuna College of Engg. & Tech. Bangalore, Karnataka, India (Under VTU, Belgaum) Department of Biotechnology

A Study on the Effect of Transition Metal Dopants in Ceria Praseodymium Catalysts for Soot Oxidation Activity and its Kinetics

Biodata

PUBLICATION DETAILS

International Journals	02 (Accepted From thesis) 09 (Apart from thesis)
International Conference	02
National Symposium	01

WORK EXPERIENCE

Year	Role	Institute/ Agency /Company	Funding	Project Title	Publications
2015-16	Project Assistant	NITK Surathkal, DST, India		Future Materials in Solid Oxide Fuel Cells	02
2016-17	Project Assistant	NITK Surathkal, KIST, Korea		Decreasing the sintering temperature of Solid-Oxide Fuel Cell Electrolytes	01
2017-19	Project Assistant / M.Tech (Research)	NITK Surathkal, KIST, Korea		Development of Quaternary Ceria-based catalysts for soot oxidation activity.	05
2011-2013	Scientific Analyst	Molecular Connections Pvt. Ltd. Bengaluru.		MCPAIRS	-

A Study on the Effect of Transition Metal Dopants in Ceria Praseodymium Catalysts for Soot Oxidation Activity and its Kinetics